Twist angle and proximity spin-orbit coupling in graphene-based heterostructures: an ab-initio approach

DISSERTATION

zur Erlangung des
Doktorgrades der Naturwissenschaften (Dr. rer. nat.)
der Fakultät für Physik der Universität Regensburg

vorgelegt von

Thomas Naimer

aus Regensburg

2024

Das Promotionsgesuch wurde eingereicht am 17.6.2024.

Die Arbeit wurde angeleitet von Prof. Dr. Jaroslav Fabian.

Prüfungsausschuss:
Vorsitzender: PD Dr. Jonathan Eroms
Erstgutachter: Prof. Dr. Jaroslav Fabian
Zweitgutachter: Prof. Dr. Ferdinand Evers
Weiterer Prüfer: Prof. Dr. Christoph Lehner

Contents

Abbreviations v

1 Introduction 1

2 Motivation 3
- 2.1 Quantum spin Hall effect . . . 4
- 2.2 Giant anisotropic spin relaxation & spin field-effect transistor . . . 5
- 2.3 Charge-to-spin conversion & spin-orbit torque . . . 7

3 Materials 11
- 3.1 Graphene . . . 11
- 3.2 Transition-metal dichalcogenides . . . 12
  - 3.2.1 Semiconducting TMDCs: $MoSe_2$, MoS_2, WSe_2, WS_2 . . . 13
  - 3.2.2 $NbSe_2$ . . . 15
- 3.3 3D Topological insulators Bi_2Se_3 and Bi_2Te_3 . . . 15
- 3.4 Van der Waals heterostructures & proximity effects . . . 17

4 Methods 19
- 4.1 Constructing heterostructure supercells . . . 19
  - 4.1.1 Construction of an (n,m) supercell . . . 19
  - 4.1.2 Generalized backfolding rules . . . 21
  - 4.1.3 Combining two supercells . . . 24
- 4.2 Density functional theory . . . 24
  - 4.2.1 Fundamentals . . . 25
  - 4.2.2 Methodological choices & further approximations . . . 26
- 4.3 Theoretical modeling of graphene . . . 29
  - 4.3.1 Tight binding Hamiltonian . . . 29
  - 4.3.2 Model Hamiltonian . . . 31
- 4.4 Interlayer interaction via generalized Umklapp processes . . . 33
  - 4.4.1 Notation . . . 34
  - 4.4.2 Interaction rules . . . 35
  - 4.4.3 Modifying the coupling by twist angle and strain . . . 38
  - 4.4.4 Symmetry considerations . . . 40
- 4.5 Combating unwanted strain effects in DFT . . . 43
  - 4.5.1 The effects of strain . . . 44

4.5.2 Control knobs . . . 48
4.6 Charge-to-spin conversion efficiencies from linear response theory . . . 54
4.6.1 Derivation . . . 54
4.6.2 Application to the graphene Hamiltonian . . . 55
4.6.3 Fermi energy dependence . . . 56
4.6.4 Scaling with different parameters . . . 59

5 Twist-angle dependent proximity spin-orbit coupling in heterostructures of graphene and semiconducting TMDCs 61
5.1 Twisted supercells . . . 62
5.2 Band structures . . . 64
5.3 Extracted SOC parameters . . . 67
5.3.1 Angle dependence of λ_R and λ_VZ . . . 67
5.3.2 Gauging the effects of strain and the effectiveness of the approach 69
5.3.3 Comparison with literature . . . 71
5.4 Charge-to-spin conversion efficiencies . . . 73
5.5 Summary . . . 74

6 Twist-angle dependent proximity spin-orbit coupling in heterostructures of graphene and topological insulators 77
6.1 Twisted supercells . . . 78
6.2 Band structures . . . 81
6.3 Extracted SOC parameters $0° \leq \Theta \lessapprox 20°$ . . . 83
6.4 Extracted SOC parameters 30° . . . 85
6.4.1 Distinguishing 'type 1' and 'type 2' band pairs . . . 85
6.4.2 Spin texture & fitting method . . . 87
6.4.3 Extracted model parameters . . . 88
6.5 Charge-to-spin conversion efficiencies . . . 91
6.6 Summary . . . 92

7 Twist-angle dependent proximity spin-orbit coupling in heterostructures of graphene and $\mathrm{NbSe_2}$ 97
7.1 Twisted supercells . . . 98
7.2 Band structures & energetic alignments . . . 101
7.3 Challenges regarding the metallic states . . . 103
7.4 Extracted SOC parameters . . . 105
7.5 Charge-to-spin conversion . . . 108
7.6 Summary . . . 109

A Proving the inverse of the statement about backfolding from Subsec. 4.4.2 111

B Derivation of the Bloch function based linear response susceptibilities in the weak disorder limit 115

References 137

List of publications 139

Acknowledgements 141

Abbreviations

2D	two-dimensional
3D	three-dimensional
BHZ	Bernevig-Hughes-Zhang
BZ	Brillouin zone
CDW	charge density wave
CSC	charge-to-spin conversion
CVD	chemical vapor deposition
DFT	density functional theory
FET	field-effect transistor
GGA	generalized gradient approximation
KM	Kane-Mele
LDA	local density approximation
MBE	molecular beam epitaxy
MRAM	magnetoresistive random-access memory
PAW	projector augmented wave
PBE	Perdew-Burke-Ernzerhof
QL	quintuple layer
QHE	quantum Hall effect
QSHE	quantum spin Hall effect
REE	Rashba-Edelstein effect
SDE	superconducting diode effect
SFET	spin field-effect transistor
SHE	spin Hall effect
SOC	spin-orbit coupling
SOT	spin-orbit torque
STT	spin-transfer torque
TI	topological insulator (in the context of this thesis always 3D topological insulator)
TMDC	transition-metal dichalcogenide
UREE	unconventional Rashba-Edelstein effect
VZ	valley-Zeeman

1 Introduction

In recent years, the study of atomically thin two-dimensional (2D) materials has found widespread attention, continuously demonstrating new physics and opening the frontiers of technological advances [1]. Graphene is certainly the forerunner and model student amongst the 2D materials [2, 3, 4], often even used as a synonym for 2D materials in general. The discovery of graphene demonstrated just how different the properties and applications of bulk materials and their 2D counterparts can be. Soon after graphene, the exfoliation and study of other 2D materials, like transition-metal dichalcogenides (TMDCs) [5, 6], followed. Meanwhile, most phenomena witnessed in 3D materials found their counterparts in the 2D world. Furthermore, these properties can even be transferred onto other 2D materials by proximity effects in so called van der Waals heterostructures [1]. These structures consist of multiple 2D materials stacked on top of each other, being held together by van der Waals forces. Neighbouring layers can then adopt properties from one another by sheer proximity.

The most relevant application of this principle is likely proximity-induced spin-orbit coupling (SOC) in graphene, which can be used with great effect to construct novel devices within the context of spintronics – a research field aiming to rethink electronics by replacing the charge degree of freedom with the spin degree of freedom [7, 8, 9]. The very weak SOC exhibited by graphene leads to long spin lifetimes and has hence proven to be useful for transporting spin currents [10, 11]. However, at the same time, the weak SOC is also detrimental for spin manipulation, i.e. the reading and writing of spins. Bringing the graphene in contact with high-SOC materials can change this and give researchers control over graphene's potential for spin manipulation. However, it is not that simple – the SOC can come in various forms (or flavours), each of which lends itself to different applications. Control over both the magnitude and the flavour of the proximity SOC in graphene has been a prominent goal of research in the last decade. In order to achieve this control, theoretical investigations of such heterostructures are highly relevant. They can be done for example by using tight binding models or by employing density functional theory (DFT) [12], a state of the art *ab-initio* method. Pioneering DFT studies by Gmitra et al. [13, 14] on heterostructures of graphene and semiconducting TMDCs (like WSe_2 or MoS_2) paved the way for such investigations. Although these TMDCs are the most frequently used materials for inducing SOC in graphene, there are multiple other high-SOC 2D materials, which can also induce their SOC in graphene.

Ever since the discovery of superconductivity in magic angle twisted bilayer graphene [15, 16, 17, 18], the twist angle has been recognized as a major tuning knob in van der Waals heterostructures. This culminated in the birth of a new field of research – twistronics. While former investigations (both theoretical and experimental) paid little to no attention to the relative twist angle between two layers and how it can affect their interaction, it is meanwhile widely recognized that it can play a major role, especially for proximity effects. Theoretical investigations by means of tight binding calculations predicted significant control over both magnitude and flavour of the proximity SOC by varying the twist angle [19, 20, 21].

In this thesis, we aim to give an extensive DFT perspective on the topic of twist-angle dependent SOC in graphene-based heterostructures. To this end, we employ DFT calculations on a multitude of twisted heterostructure supercells consisting of graphene and high-SOC materials. In the tradition of Gmitra et al., we utilize a model Hamiltonian of the low energy Dirac cone states in order to extract the SOC parameters. The extracted SOC parameters are then compared based on the twist angle of the heterostructure supercell. We uncover a great potential for tuning both the flavour and magnitude of the proximity SOC in graphene by twisting and gating, confirming the findings of the tight binding calculations. The underlying mechanisms behind the witnessed effects are further explained by employing the theory of generalized Umklapp processes [22]. Furthermore, the investigation of twisted heterostructures reveals the possibility for a radial in-plane spin texture, which is forbidden by symmetry in the commonly used untwisted heterostructures. The consequence of this radial spin texture is the emergence of an unconventional form of charge-spin-interconversion, which we capture by defining a figure of merit based on calculations within linear response theory. Unfortunately, employing DFT for the investigations of heterostructures yields one major problem – as commensurate heterostructure supercells are needed, it is inevitable to artificially strain one of the layers, resulting in potential distortion of the results. Arguably the most detrimental effect of this strain is a change in band offset between the layers. In order to remedy this problem, we utilize external electric fields, correcting the band offsets. We extensively discuss this issue of strain related effects in order to clarify and justify our approach.

2 Motivation

Spin-orbit coupling (SOC) – the interaction between an electron's spin and its orbital degree of freedom – is an inherently relativistic phenomenon; it appears only after describing the system using the Dirac equation instead of the Schrödinger equation. Hence, in an atom, SOC is most relevant, if the electrons travel close to the speed of light. The velocities of the orbiting electrons are dictated by the atom's atomic number Z and in fact the SOC strength can be approximated to show a Z^2 dependence [23, 24, 25, 26, 27], meaning heavier atoms exhibit substantially more SOC. The light carbon atoms of graphene are therefore one reason for its very small SOC. An additional factor, hampering the possibility of graphene to exhibit SOC, is the orbital composition of the Dirac cone states, which are close to the Fermi level and hence govern the relevant physics (e.g. transport). These states predominantly consist of p_z-orbitals forming π-bonds. As p_z-orbitals have no net out-of-plane orbital momentum and hence cannot exhibit the symmetry-allowed SOC, there are only two pathways for the Dirac states to display SOC [28, 29, 30]: either by mixing of the π-bonds with the underlying sp^2 hybridized σ-bonds (as e.g. in graphene nanotubes or rippled graphene) or by virtual tunneling processes through d- (or higher) orbitals. While for flat pristine graphene the σ-π-mixing is suppressed, the d-orbitals can provide a SOC on the order of 10μeV [30, 31, 32, 33].

Equipping graphene with more substantial (meV scale) SOC has various applications; this chapter is dedicated to shining light on some of the most relevant ones. Besides topological physics (quantum spin Hall effect (QSHE) [34, 35] and pseudohelical states [36]), the main field of applications of graphene with enhanced SOC is spintronics [7, 9]. While in conventional electronics information is transmitted, processed and stored using the charge of an electron, in spintronics its spin is used. This approach can have many benefits: information can be stored without loss of power (non-volatility), operations are less power consuming, data can be stored more densely and switching of states can be performed more rapidly [37]. In spintronics, there is both the need for spin transport and for spin manipulation (reading and writing of spins). Graphene's weak SOC allows for only very limited spin relaxation (i.e. high spin life times), making graphene excellent for spin transport. Although the low SOC is beneficial for spin transport, it is detrimental for spin manipulation. To fix this problem, parts of graphene sheets can be decorated by heavy adatoms [38, 39] or proximitized by high-SOC materials [13, 40, 41, 21] (like TMDCs), to locally increase the potential for spin manipulation. Depending on the setup, different kinds of SOC (see Sec. 4.3) can be induced in graphene. Which of those flavours is demanded, depends on the concrete application. In this chapter, we discuss three different relevant applications for the three different kinds of SOC described by the model employed by us (see Eq. (4.43)):

1. Kane-Mele SOC λ_{KM} is the key factor in enabling the QSHE, entailing spin-momentum-locked topological surface states.
2. Valley-Zeeman SOC λ_{VZ} is crucial in enabling highly anisotropic spin relaxation, where in-plane spins relax much faster than the out-of-plane spins do.
3. Rashba SOC λ_{R} is the driving parameter for the Rashba-Edelstein effect (REE) and the unconventional REE (UREE), which present an efficient way of realizing charge-to-spin conversion (CSC).

Since the different flavours of SOC are relevant for different applications and can even be detrimental to other applications, it is a highly relevant endeavour to not only tune the magnitude of the SOC, but also the kind of SOC. In order to exercise control over the SOC, different controlling knobs can be used in experiment. This includes interlayer distance (tunable by pressure), transverse electric field (realized by a gate voltage), strain and twist angle (the latter two can be determined in the manufacturing process). While interlayer distance almost exclusively influences the general strength of the SOC, the latter three show great potential for tuning the SOC flavour as well. In Sec. 4.5 the interplay between gate voltage, strain and twist angle is discussed in more detail. It is the goal of this thesis to demonstrate how these tuning knobs can be used to control the SOC parameters and therefore the effects discussed in the following.

2.1 Quantum spin Hall effect

Akin to the quantum Hall effect (QHE), the QSHE is a topological state of matter occurring in 2D systems. However, the QSHE is time reversal symmetric, whereas the QHE requires an external magnetic field, breaking the time reversal symmetry. Like the QHE, the QSHE comes with one dimensional edge states (see Fig. 2.1) robust against backscattering by impurities, allowing for dissipationless transport; in the case of the QSHE these impurities have to be non-magnetic, in order to preserve the time-reversal symmetry. Where in the QHE any integer number of edge states (equal to the Chern number, a $\mathbb{Z}$ invariant) wrap around the sample, in the QSHE there are always exactly two non-trivial edge states propagating in opposite directions. As these states have opposite spin (spin-momentum locking), backscattering between them is only allowed by scattering off of magnetic impurities. The topological invariant of the QSHE is a $\mathbb{Z}_2$ invariant, meaning it is always either 0 or 1, i.e. topologically trivial or non-trivial. Edge states will always arise at a border between a non-trivial (e.g. graphene with sufficiently high λ_{KM}) and trivial (e.g. vacuum) zone.

The original proposal of the QSHE, made by Kane and Mele [34, 35], includes graphene as the material of choice. However, this requires sufficiently high SOC, inducing a topologically non-trivial gap in the Dirac cone, within which the edge states reside. Since

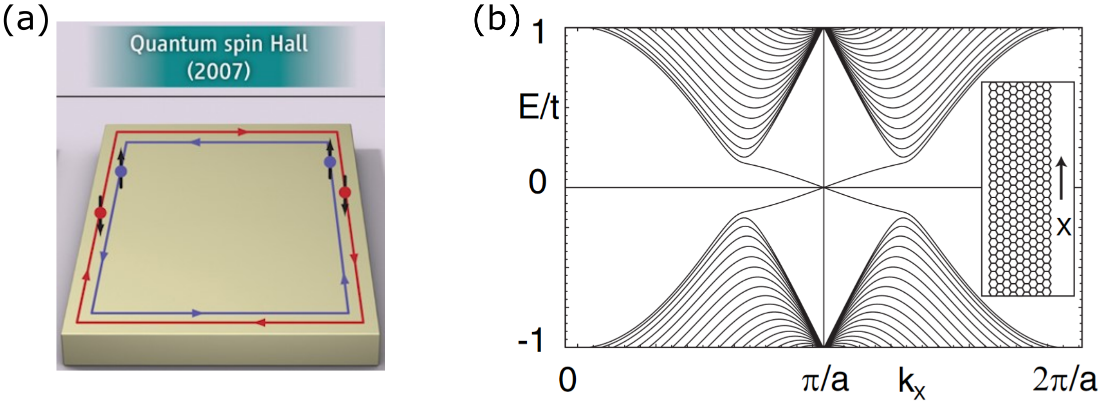

Figure 2.1: (a) Schematic illustration of the QSHE edge states winding around the 2D sample (taken from [47]). (b) Graphene ribbon band structure with edge states within the bulk band gap (taken from [34]).

the SOC of pristine graphene is not enough to stabilize the QSHE, proximity-induced SOC was sought to solve the problem. Unfortunately, the kind of SOC needed in order to stabilize the QSHE is the Kane-Mele SOC λ_{KM}, while most practical ways of inducing SOC in graphene result in a mixture of Rashba SOC and valley-Zeeman SOC. DFT calculations suggest that Kane-Mele SOC can be induced in a certain graphene/topological insulator (TI) heterostructure (see Refs. [42, 43, 41, 44] and Sec. 6.4). Although experimental hints of the QSHE in this particular situation are sparse [45], the QSHE has been experimentally verified in other materials, like HgTe quantum wells [46]. Our DFT results suggest a strong tunability by gate voltage of the magnitude and even sign of the Kane-Mele SOC λ_{KM} in graphene/TI heterostructures. Since this is the mass term in the QSHE, gate control could be used to selectively locally induce the QSHE in graphene and create the edge states within the graphene sheet based on the gating.

2.2 Giant anisotropic spin relaxation & spin field-effect transistor

In spin transport, the spin lifetime describes how long the electrons involved in the spin transport can propagate before scattering and losing their spin-orientation. As previously stated, graphene has a very high spin lifetime and is therefore excellent for spin transport, since the spins keep their orientation for a long distance. Enhancing graphene's SOC, enhances the scattering rates and therefore decreases the spin lifetime, so why would we be interested in doing so? By specifically increasing only the valley-Zeeman SOC, we can specifically decrease the spin lifetime of in-plane spins [48], further expanding on the ability to control the spins. The result is a large difference between the lifetimes of

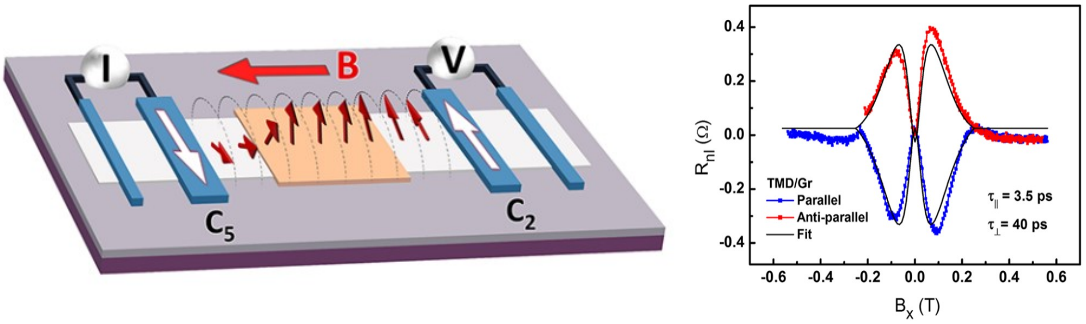

Figure 2.2: Experimental setup for measuring the spin-relaxation anisotropy through Hanle precession in a non-local spin transport measurement (taken from Ref. [49]).

spins pointing in different directions, a spin lifetime anisotropy

$$\xi = \frac{\tau_{s,\perp}}{\tau_{s,||}} = \frac{\lambda_{\mathrm{VZ}}^2}{\lambda_{\mathrm{R}}^2} \cdot \frac{\tau_{iv}}{\tau_p} + \frac{1}{2}, \tag{2.1}$$

with spin lifetimes out of plane $\tau_{s,\perp}$ and in-plane $\tau_{s,||}$. In the extreme situation, where graphene exclusively acquires valley-Zeeman SOC (λ_{VZ}), all Dirac states are purely spin-polarized in z-direction. Here, the spin relaxation anisotropy is highest (within formula Eq. (2.1) even infinite). Adding Rashba SOC (λ_{R}), induces an in-plane component to the spin texture, opening up the possibility of scattering into in-plane polarized spins. But even for $\lambda_{\mathrm{R}} \approx \lambda_{\mathrm{VZ}}$, due to the interplay of two different scattering mechanism (inter-valley scattering τ_{iv} and momentum scattering τ_p), ξ is nevertheless enhanced. Estimations on these scattering mechanisms [48] suggest $\frac{\tau_{iv}}{\tau_p} \approx 5$. In experiments [49, 50, 51] large spin relaxation anisotropies of $\xi > 10$ can be measured. In Fig. 2.2 an experimental setup for measuring the spin-relaxation anisotropy is shown: In-plane spins are induced in the graphene through the magnetic contact C_2. The spins propagate to the opposing magnetic contact C_5 resulting in a signal in the non-local resistance R_{nl}. Then, an external magnetic field B is applied, changing the spins' direction through Hanle precession [52, 49, 53, 54]. Since the spins are now (partially) oriented out-of-plane, their lifetime increases. Therefore, the signal measured at C_5 first increases with magnetic field B. Increasing B further, however, the dephasing effect takes over and the signal decays again. Fitting this curve to the results of the Bloch equations gives estimates for the in-plane and out-of-plane spin lifetimes [49].

Another scheme, where the proximity-induced SOC selectively decreases the spin lifetimes, is the proposed spin-orbit valve system by Gmitra et al. [55, 56, 57] capable of functioning as a spin field-effect transistor (SFET). The concept of a SFET was originally proposed by Datta and Das [58]. It describes the spintronics analogue of a field-effect transistor (FET). The difference to a FET is, that in a SFET, the gate allows for electrical control not over the flowing charge current between source and drain, but over the spin

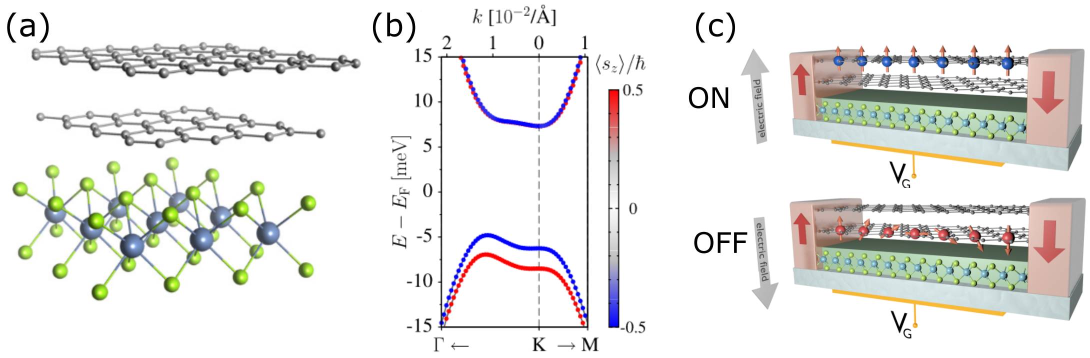

Figure 2.3: (a) Bilayer graphene proximitized by TMDC. (b) Zoom to the low-energy spectrum of the proximitized bilayer graphene; the spin splitting (effect of the SOC) is limited to the valence band, if no external electric field is applied. (c) ON and OFF configuration of the bilayer graphene-based SFET (all figures are taken from Ref. [55]).

current. The setup proposed by Gmitra et al. is the following: Using bilayer graphene instead of monolayer graphene results in a situation, where one of the graphene sheets (the one closer to the substrate) exhibits substantially more proximity SOC. An external gate can then be used to tune the layer polarization of the Dirac cone states (i.e. whether the states near the Fermi level live in the high-SOC or the low-SOC layer). This control over the layer polarization then in turn enables control over the spin transport properties of the device: it can be in one of two states:

1. ON-state, the graphene layer further away from the substrate is contributing to transport; high spin lifetimes
2. OFF-state, the graphene layer close to the substrate is contributing to transport; low spin lifetimes.

Coherent spin transport between source and drain is then only possible, if the system is in an ON-state and hence the spin lifetimes are high. Such a device (as illustrated in Fig. 2.3(c)) would then constitute such a SFET, presenting a major step for the field of spintronics. There is already experimental evidence supporting this idea [56, 57].

2.3 Charge-to-spin conversion & spin-orbit torque

Any physical process that translates a charge current or charge accumulation into a spin current or spin accumulation can be considered CSC. The inverse effect (a spin-to-charge conversion) can usually be achieved in the same system. Therefore, sometimes both effects are referred to under the umbrella term charge-spin-interconversion. The two most prominent examples for such an effect are the spin Hall effect (SHE) [59] and the REE [60, 61, 62]. The efficiencies of both can be calculated rather easily with a simple approach within linear response theory [63, 64, 65, 66] (more elaborate approaches can for example be found in Refs. [62, 67, 68]). In Sec. 4.6, we elaborate in detail how to calculate such CSC efficiencies for the REE. The effect is illustrated in Fig. 2.4(a)-(c): an external electric field introduces a bias in the occupation of the electric states in the proximitized graphene's Dirac cone. Because spin and momentum of the newly populated states are locked, a spin imbalance is achieved. The direction of these spins can be perpendicular (REE) or collinear (UREE) to the charge current $\mathbf{j}$, depending on the specific in-plane spin texture of the Dirac cone. The UREE is especially interesting, since it is less common and has often been ignored in the interpretation of spin transport experiments. The same spin-momentum locking exhibited by proximitized graphene is also observed in the surface states of 3D TIs (see Sec. 3.3). However, instead of the two subbands with opposite spins (but different k-radius) in Fig. 2.4(b) and (c), the 3D TI's surface states are degenerate, but located at different surfaces and therefore only one of them will be relevant at any given surface. In Fig. 2.4(d) a typical experimental setup for measuring spin-to-charge conversion is shown: Non-equilibrium spin densities are created through the magnetic contact (blue rectangle). They propagate towards the proximitized region and lead to a measurable charge density response.

In spintronics, the spin accumulation can be used with great effect to exert a spin-orbit torque (SOT) on a nearby magnetic layer [69, 70], switching its magnetization. Since in a magnetoresistive random-access memory (MRAM) system the magnetization direction represents the information of a bit (0 or 1), one can thereby establish control over the bit. Such a SOT-driven process constitutes a new step in the development of spintronics MRAM, potentially replacing the spin-transfer torque (STT) [70, 7, 71] devices. Fig. 2.4(e) and (f) illustrate the design of STT-MRAM and SOT-MRAM, respectively. The STT works in a very similar way, with the key difference that the charge current used to flip the spin (writing) has to flow through the magnetic layers. The electrons first run through the fixed layer, where they acquire spin polarization, which they maintain, while passing the tunneling barrier. In the free layer, the spin current exerts a torque on the magnetization of the free layer and flips it. As the current used to read the magnetization also runs in the same direction (just with a smaller current), STT-MRAMs can display problems with reliability, as the magnetization can accidentally be flipped in the reading process. The SOT-MRAMs avoid this problem by separating the writing- and reading-lines. Here, the material in which the CSC occurs (CSC-material) is directly adjacent to the free layer. Therefore, while in the writing process current runs along the CSC-material, producing a spin accumulation exerting torque on the free layer, in the reading process the current runs perpendicular to the CSC-material and hence the free layer is not subject to any torque. Furthermore, control over the directions of the spins can aid in creating space-efficient device designs. While CSC by means of the SHE creates out-of-plane spins, REE and UREE create in-plane spins (perpendicular or collinear to the current, respectively).

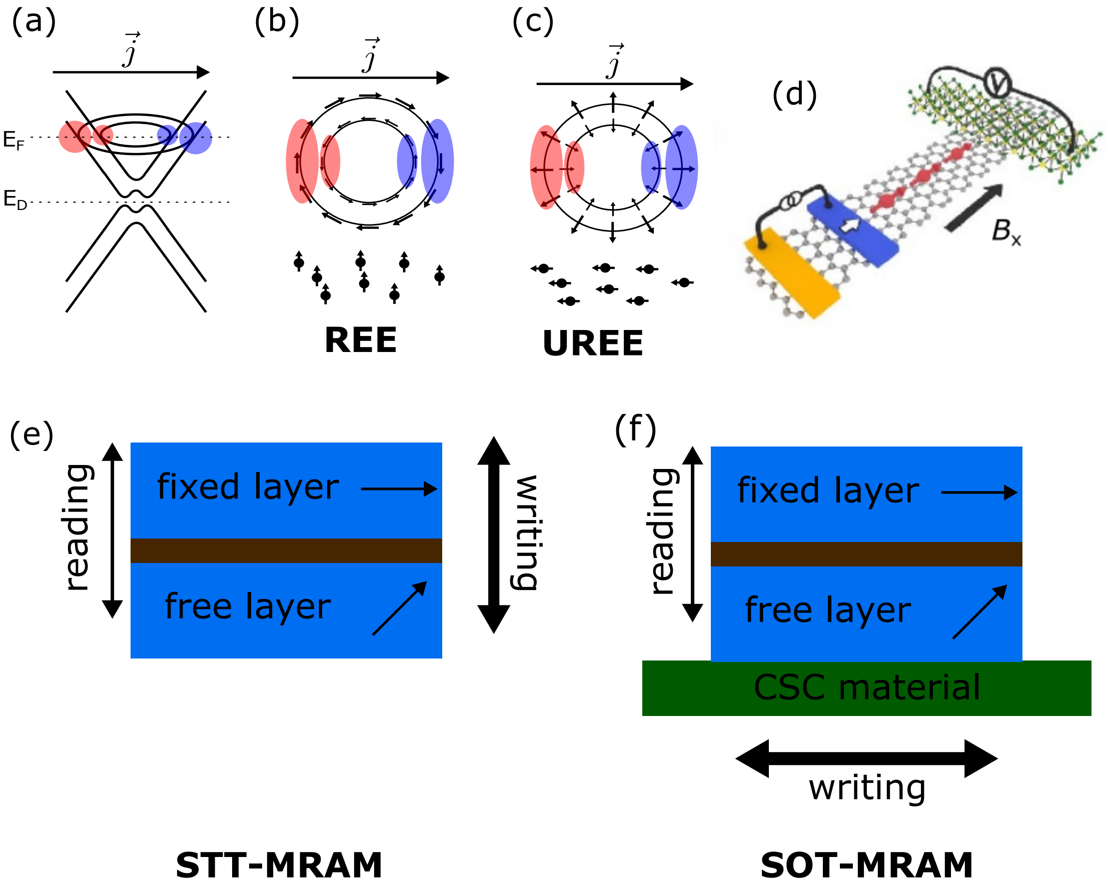

Figure 2.4: (a) Dirac cone with a mixture of Rashba and valley-Zeeman SOC. The Dirac cone energy E_D and the Fermi energy E_F are drawn. By applying a voltage (resulting in a current $\mathbf{j}$) the states at the given Fermi energy are redistributed to favour the ones marked with red. (b) Cut through the Fermi energy of the Dirac cone shown in (a). The tangential in-plane spin texture in combination with the redistribution of states leads to a spin imbalance; the direction of the spins is perpendicular to $\mathbf{j}$. (c) Same as (b), but for a radial in-plane spin texture; the direction of the spins is perpendicular to $\mathbf{j}$. (b) and (c) demonstrate the REE and the UREE, respectively. (d) An example of an experimental setup for probing spin-to-charge conversion (taken from Ref. [72]). (e) and (f) show schematics of the STT and SOT, respectively. The brown layer is a tunneling barrier.

3 Materials

In van der Waals heterostructures [1], different 2D materials can be joined together, imprinting their properties on the neighbouring layers through proximity effects. In this thesis, we investigate heterostructures of graphene with other 2D materials (sometimes loosely called substrates throughout the thesis). This chapter is mainly dedicated to introducing the individual materials, which were used: First, graphene as the template material, which will be imprinted with proximity spin-orbit coupling (SOC), is discussed. Then, the two material classes (transition-metal dichalcogenides (TMDCs) and topological insulators (TIs)) serving as substrates, are introduced. For all materials, we present both the real space and reciprocal space structures and their most important physical properties and applications are highlighted. We conclude the chapter by briefly discussing the procedure of combining the materials into van der Waals heterostructures.

3.1 Graphene

Graphene is a 2D sheet of carbon atoms in a honeycomb arrangement. Its 3D counterpart is regular graphite, which simply consists of millions of graphene layers stacked on top of each other. In 2004, graphene was first isolated using the scotch-tape method [2, 3, 73]. This simple method of mechanically exfoliating graphene ('top-down' method) is still widely used, although 'bottom-up' methods [74, 75, 76] have become more popular, providing a scalable alternative for industrial purposes. Astonishingly, although graphene is only the 2D format of such a simple and widely spread material like graphite, it has gathered a lot of attention due to its outstanding properties. This does not only include its high electron mobility [77, 78, 4] and mechanical robustness [79, 80, 3, 81], but also its long spin lifetimes [10, 11]. The latter makes it a material suitable for spintronics applications [7, 9]. Moreover, its 2D structure ensures that its properties can be easily manipulated by proximity effects in van der Waals heterostructures. It also comes in several derivative forms like carbon nanotubes [82, 3], fullerene [83, 3] or graphene nanoribbons [3, 4, 36]. To describe the electronic structure of graphene we use both a full tight binding model and a model Hamiltonian linearized around the K/K' point, which will be introduced in Sec. 4.3. The hexagonal structure of graphene is described by the two lattice vectors

$$\mathbf{a}_1 = \begin{pmatrix} 1 \\ 0 \end{pmatrix} \cdot a, \quad \mathbf{a}_2 = \begin{pmatrix} 1/2 \\ \frac{\sqrt{3}}{2} \end{pmatrix} \cdot a \tag{3.1}$$

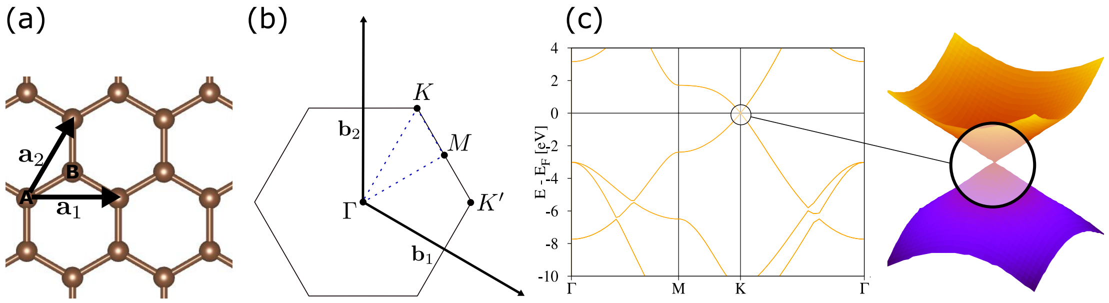

Figure 3.1: Graphene structure in real and k space. (a) The real space lattice of graphene with lattice vectors $\mathbf{a}_1$ and $\mathbf{a}_2$. (b) 1st Brillouin zone (BZ) of graphene with high symmetry points Γ, K, K' and M. (c) DFT band structure along a high symmetry path indicated as blue dotted line in (b) with a zoom to the Dirac cone at K.

in combination with the two basis atoms — which build the two sublattices A and B — sitting at

$$\mathbf{r}_1 = \begin{pmatrix} 0 \\ 0 \end{pmatrix} \cdot a, \quad \mathbf{r}_2 = \frac{1}{3}\mathbf{a}_1 + \frac{1}{3}\mathbf{a}_2 = \begin{pmatrix} 0.5 \\ \frac{1}{2\sqrt{3}} \end{pmatrix} \cdot a. \tag{3.2}$$

This results in an equally hexagonal structure in reciprocal space. The reciprocal lattice vectors are

$$\mathbf{b}_1 = \begin{pmatrix} 1 \\ -\frac{1}{\sqrt{3}} \end{pmatrix} \cdot \frac{2\pi}{a}, \quad \mathbf{b}_2 = \begin{pmatrix} 0 \\ \frac{2}{\sqrt{3}} \end{pmatrix} \cdot \frac{2\pi}{a} \tag{3.3}$$

with the K/K' point sitting at

$$\mathbf{K} = \frac{1}{3} \cdot \mathbf{b}_1 - \frac{1}{3} \cdot \mathbf{b}_2, \quad \mathbf{K}' = -\frac{1}{3} \cdot \mathbf{b}_1 + \frac{1}{3} \cdot \mathbf{b}_2. \tag{3.4}$$

and the M/M' point sitting at

$$\mathbf{M} = -\frac{1}{2} \cdot \mathbf{b}_1, \quad \mathbf{M}' = \frac{1}{2} \cdot \mathbf{b}_2. \tag{3.5}$$

The real space and reciprocal space structures are depicted in Fig. 3.1(a) and (b), respectively. In order to describe the band structure along the high symmetry points Γ, K and M both DFT or tight binding model might be used.

3.2 Transition-metal dichalcogenides

TMDCs are a class of layered materials used for a wide range of applications. This includes valleytronics [84, 85, 86], straintronics [87, 88], optoelectronics [89, 90] and not least spintronics [7, 9]. A monolayer TMDC usually occurs in the 2H phase, which means it has the same hexagonal structure as graphene, with a metal atom (e.g. W or Nb) sitting at sublattice A and two vertically shifted chalcogenide atoms (e.g. S or Se) sitting at sublattice B (see Fig. 3.2(a) and (b)). Its structure is defined by the lattice parameter a and its thickness d_{XX} (distance between the chalcogen atoms). Although all TMDCs discussed in this thesis have this structure, TMDCs can also occur in other configurations, like the 1T configuration [91, 92].

Due to their metal atoms, all TMDCs have strong SOC, resulting in huge (up to more than 400 meV) spin splittings, with opposite signs at opposing points in k space (most prominent at the valleys at Q, K and K', see Fig. 3.2(e)). Since, additionally, most TMDCs are semiconducting, their optical properties are of great interest and have been investigated thoroughly, especially exciton physics [93, 94, 95, 96]. Furthermore, the TMDCs' 2D nature makes them easy to implement in heterostructures. On the one hand, this opens the possibility for further modifying their optical properties by interlayer excitons [97, 98, 99, 100], dielectric screening [101, 102, 103, 104] and hybridization effects [105]. On the other hand, they can transfer their properties through proximity effects onto another material. In this thesis we focus on investigating such proximity effects, in particular the proximity SOC. As chapter 5 and chapter 6 are dealing with semiconducting TMDCs ($MoSe_2$, MoS_2, WSe_2, WS_2) and a metallic TMDC ($NbSe_2$), respectively, we discuss these further in the following.

3.2.1 Semiconducting TMDCs: $MoSe_2$, MoS_2, WSe_2, WS_2

As already mentioned, semiconducting TMDCs have exceptional optical properties. Their band gaps are indirect in the bulk and direct in the monolayer (see Fig. 3.2(c)) and range mostly between 1 eV and 2 eV [84, 88]. Due to their broken inversion symmetry (in monolayers), they show optical selection rules (see Fig. 3.2(d)): Depending on the handedness of the circularly polarized light (σ^+ or σ^-), shined on the sample, excitations can occur either at the K or K' valley. This means one can specifically produce valley- and spin-polarized excited electrons. This opens up the field of valleytronics – the selective manipulation of the valley degree of freedom. Furthermore, 2D materials in general and TMDCs in specific represent an excellent platform for exciton physics [93, 94, 95, 96]. The reduced dielectric screening of 2D materials increases the excitons' binding energies and the large spin splitting of TMDCs additionally introduces different types of excitons (type A and type B). On top of that, in bilayers of TMDC the electron and hole forming an exciton can come from different layers, creating so called interlayer excitons. These interlayer excitons depend both on the twist angle and the stacking configuration of the layers, enriching the possibilities even further [97, 98, 99, 100]. In order to tune the optical properties, different knobs can be used. Strain can for instance be used to great effect in order to tune the size and position in k space of the TMDC band gap [88]. This effect can be witnessed in bubbles, forming in experimental setups [87]. Furthermore, encapsulation (e.g. with hBN or graphene) can manipulate the dielectric environment of the TMDC and therefore both the band gap and the exciton binding energy [101, 102, 103, 104]. On top of these rather well known effects, proximity to graphene in particular can change the g-factors of the excitons via a multistep process driven by a hybridization of the layers'

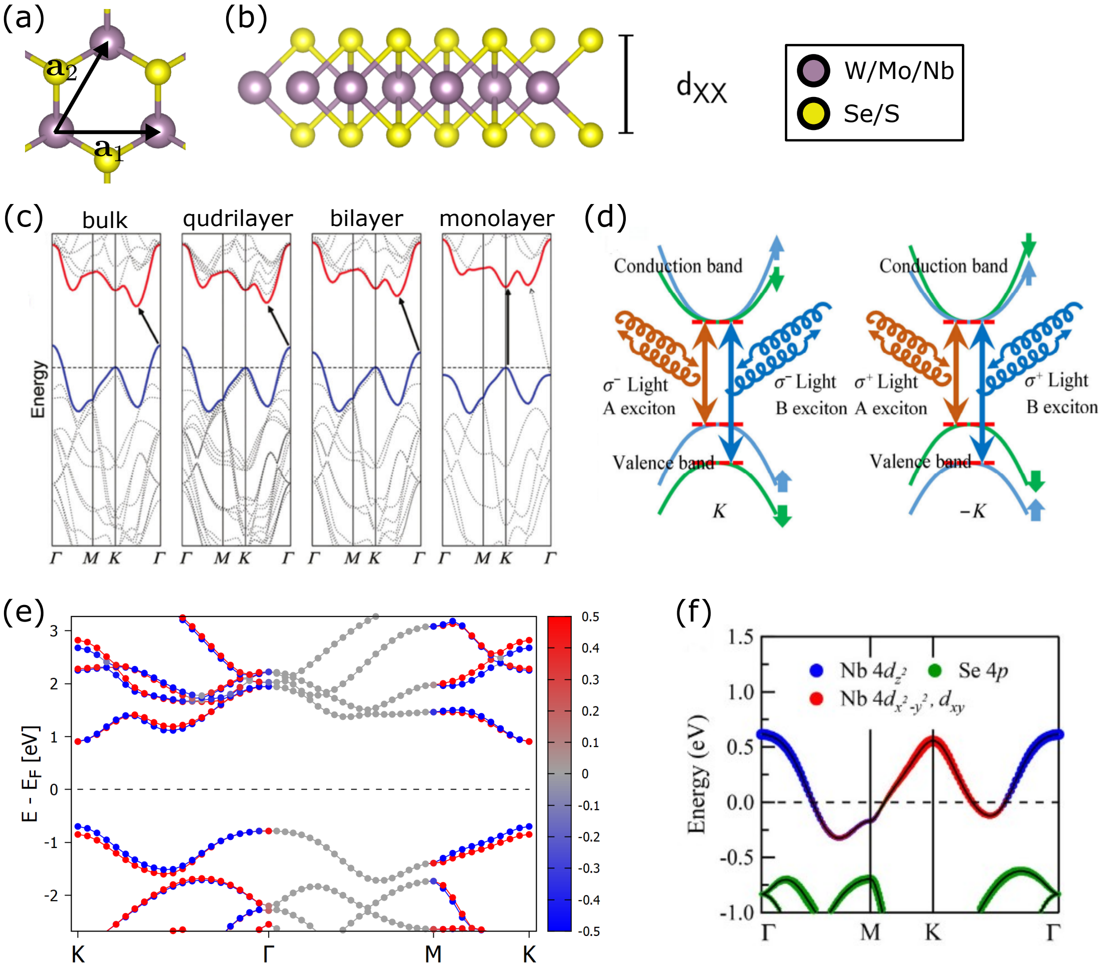

Figure 3.2: (a) Top view and lattice vectors $\mathbf{a}_1$ and $\mathbf{a}_2$ of the TMDCs. (b) Side view of a TMDC with indicated chalcogen-chalcogen distance d_{XX}. (c) Transition from indirect band gap (bulk, Γ to Q-valley) to direct band gap (monolayer, K to K) for MoS_2 without SOC. (d) Schematic depiction of the optical selection rules in semiconducting TMDCs. (c) and (d) are adapted from Ref. [84]. (e) Band structure of monolayer MoS_2 along high symmetry points as calculated by DFT. Spin-z expectation values are color coded from blue (spin down) to red (spin up). (f) $NbSe_2$ band structure along high symmetry points with orbital decomposition (blue Γ states are more out of plane, while red K states are more in-plane); adapted from Ref. [106].

wavefunctions [105]. In Chap. 5 graphene/TMDC heterostructures are discussed. Here, the band gaps are also crucial, since they ensure that (as long as the graphene Dirac cone sits within the band gap, which it usually does) the transport will occur exclusively through the graphene.

3.2.2 $NbSe_2$

In contrast to the semiconducting TMDCs, monolayer $NbSe_2$ has metallic bands near the Fermi level (see Fig. 3.2(f)). In combination with its SOC, this opens up the possibility for charge-to-spin conversion (CSC) [107, 72, 108]. However, in heterostructures (e.g. graphene/$NbSe_2$) this can complicate the transport properties, as it opens up an additional channel for the current. Additionally, $NbSe_2$ shows superconducting behaviour [109, 110] at low temperatures and can even equip graphene with superconductivity via proximity effect [111, 112, 113, 66]. Although superconducting graphene has been discussed intensely in recent years, it was mainly in the context of twisted bilayer graphene [15, 16, 17, 18]. Yet, proximity to $NbSe_2$ could simultaneously provide graphene with both superconductivity and SOC, both of which could be modulated via twist angle [111, 66]. Such superconducting graphene with both tuneable SOC and tuneable superconductivity might be relevant for applications involving the superconducting diode effect (SDE) [114, 115, 116, 117, 118], in which a mixture of (Rashba) SOC and superconductivity leads to a Josephson junction, in which the supercurrent can run only in one direction. Another phenomenon observed in monolayer $NbSe_2$ is the charge density wave (CDW) [119, 120, 106], a periodic modulation of both the electron ground state density and the atomic lattice. The typical periodicity of this CDW in $NbSe_2$ is that of a 3×3 supercell. In Chap. 7 our DFT calculations on twisted graphene/$NbSe_2$ heterostructures are discussed. There, we find that the metallic states of the $NbSe_2$ do not present a major problem to the extraction of the SOC parameters, as they do not hybridize with the Dirac cone so strongly as to distort it. Furthermore, the $NbSe_2$ can be manipulated by the strain in the graphene in a meaningful way, shifting offset between the $NbSe_2$ Γ- and K-bands.

3.3 3D Topological insulators Bi_2Se_3 and Bi_2Te_3

Another class of materials, which has introduced plenty of new and interesting physics, are topological materials [121]. An experimentally viable one [122, 123, 124, 125, 126] is the 3D topological insulator (3D TI, referred to simply as TI throughout the thesis) as described by the Bernevig-Hughes-Zhang (BHZ) model [127, 128]. Here, a material with a small band gap and large SOC can achieve a so called band inversion. This means that valence and conduction bands partially switch their orbital decomposition, i.e. the valence band obtains the 'nature' of the conduction band, and vice versa. This manifests in a non-trivial topological invariant in the bulk, the Hamiltonian of the 3D TI bulk cannot be connected to the vacuum adiabatically without closing the band gap. At the surface of such a material (where the non-trivial material meets the trivial vacuum) the band gap needs to be closed – the topological surface state arises. This is called the bulk-boundary correspondence [121]. In contrast to trivial surface states, the topological state cannot be lifted or destroyed easily (only by magnetic impurities) and is therefore very robust. In the 3D TI, this surface state takes the form of a Dirac cone at the Γ point (see Fig. 3.3(c)). The fact that its spin and momentum are locked to each other prevents electrons from being backscattered [121, 122]. Additionally, it can provide a platform for effective CSC by the Rashba-Edelstein effect (REE, see Sec. 2.3) through its in-plane spin texture [129, 130, 131] (see Fig. 3.3(d)).

Two of the most widely used materials for realizing a 3D TI are Bi_2Se_3 and Bi_2Te_3. Although the primitive unit cell (containing 5 atoms) of their bulk versions is rhombohedral, their layered structure is best captured in their hexagonal unit cell (15 atoms). This hexagonal unit cell can be described by the two lattice parameters a and c in combination with the atomic constants u and v. This unit cell contains 3 quintuple layers (QL) of Bi_2Se_3 (or Bi_2Te_3), see Fig. 3.3(b). From this bulk unit cell it is easy to construct heterostructures of thin layers (few QLs) of TI. In this quasi-2D form, the 3D TIs can show finite-size effects. If the films are thin enough, the surface states from the bottom and top surfaces (which decay exponentially into the bulk) can overlap slightly, introducing a gap in the surface state. How this finite size gap evolves with decreasing thickness of the 3D TI layer can be seen in Fig. 3.3(c). One can generally say that at 5-6 QLs the surface states are fully formed and show only minimal hybridization with each other [126, 132, 133, 134].

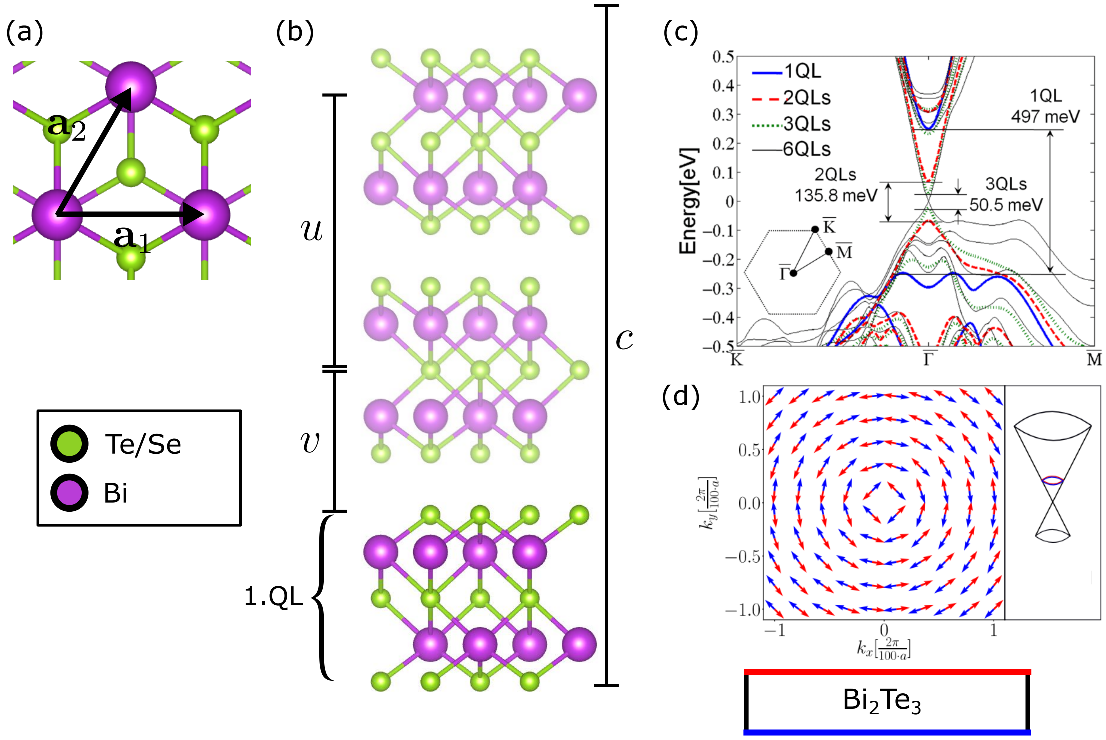

Figure 3.3: (a) Top view and lattice vectors $\mathbf{a}_1$ and $\mathbf{a}_2$ of the hexagonal Bi_2Te_3 (or Bi_2Se_3) unit cell. (b) Side view of 3QL of the TI with structural parameters u, v and c. (c) Band structure of 1-6 QLs of Bi_2Se_3; the surface state fully forms while increasing the number of QLs; adapted from Ref. [135]. (d) In-plane spin texture of a cut through the surface states of 6QL Bi_2Te_3. Red and blue arrows stem from states living at opposing surfaces.

3.4 Van der Waals heterostructures & proximity effects

In the previous sections, we discussed different layered materials, i.e. 2D or quasi 2D materials, which can be repeatedly stacked on top of each other, building their 3D equivalents (e.g. graphene to graphite). Since the only forces holding together these layered 3D structures are van der Waals forces (as opposed to chemical bonds), one can easily combine the different 2D materials creating so called van der Waals heterostructures [1]. In such structures, the materials' wavefunctions hybridize very slightly, introducing qualities of one layer to a neighbouring one by sheer proximity. Hence, such an effect is called a proximity effect. A prominent example of this are graphene/TMDC heterostructures — here the TMDC's large SOC is transferred to the graphene (see e.g. Ref. [13, 136, 137, 19, 40] and Chap. 5), but also the large g-factor of graphene enhances the TMDC g-factors (see Ref. [105]). The scope of possible proximity effects, however, is much bigger, as meanwhile an extensive list of 2D materials exists.

In this list, a large range of material classes and effects are represented: this includes magnets (e.g. CrI_3), large-gap semiconductors (e.g. hBN), high-SOC materials (e.g. TMDCs), superconductors (e.g. $NbSe_2$), topological insulator (e.g. Bi_2Se_3) etc.

Experimentally, these heterostructures can be manufactured in many ways, which can all be classified in two categories [138]:

1. 'Bottom-up' (e.g. chemical vapor deposition (CVD), molecular beam epitaxy (MBE)): Here, one 2D material is assembled from smaller constituents (i.e. grown) on top of another in some fashion. The two layers are likely to form a commensurate structure, despite the resulting strain on one or both of the layers. Some twist angles are more likely than others, since the corresponding configurations involve less strain.

2. 'Top-down' (e.g. exfoliation, wet transfer): Here, one existing 2D material (usually extracted from its 3D version) is transferred on top of another 2D material. The two materials brought together might have been manufactured either in a 'top-down' or in a 'bottom-up' fashion in the first place. However, the process of joining them combines two already existing layers. Therefore, change of lattice constant by adaption is very limited, even if the material is annealed afterwards. Also, the resulting twist angle between the layers is in most cases random.

It is possible to determine the twist angle of a sample of such a van der Waals heterostructure in experiment after the manufacturing process. This can be done for example by second-harmonic generation [139, 137] or by the orientation of the flakes, grown on a substrate [139, 140].

4 Methods

4.1 Constructing heterostructure supercells

In order to ensure periodicity in the DFT calculations on heterostructures, commensurate supercells of the combined materials need to be constructed; we call them heterostructure supercells. Since all materials discussed in this thesis have a hexagonal unit cell, we can easily combine them [141, 142, 143]. The construction of heterostructure supercells involving mixed lattice types would be more complicated, as it would require uniaxial strain. The method we employ works as follows: First, we construct a supercell for each of the two layers in a way that the supercells of both layers have a similar supercell lattice constant. By straining one (or both) of the supercells by a small margin, we can then put them together into one commensurate supercell. In this section, we will discuss the construction and properties of such a heterostructure supercell in detail.

4.1.1 Construction of an (n, m) supercell

Let us first start with constructing a general (n, m) supercell of a 2D material. We start from the primitive hexagonal unit cell of the material, e.g. graphene in Sec. 3.1. Note that in order to keep the integers n and m mostly positive, we assume unit cells with an acute angle between the lattice vectors $\mathbf{a}_1 \measuredangle \mathbf{a}_2 = 60°$. For unit cells with an obtuse angle $\mathbf{a}_1 \measuredangle \mathbf{a}_2 = 120°$, the scheme also works. However, the formulas are inconsistent with those presented here. Using the integers n and m, we define the lattice vectors $\mathbf{a}^{S,1}_{(n,m)}$ and $\mathbf{a}^{S,2}_{(n,m)}$ as a linear combination of the primitive lattice vectors $\mathbf{a}_1$ and $\mathbf{a}_2$ (see Fig. 4.1(a)):

$$\mathbf{a}^{S,1}_{(n,m)} = n \cdot \mathbf{a}_1 + m \cdot \mathbf{a}_2 \tag{4.1}$$

$$\mathbf{a}^{S,2}_{(n,m)} = -m \cdot \mathbf{a}_1 + (n + m) \cdot \mathbf{a}_2. \tag{4.2}$$

We assign attributes (n, m) to such a new supercell. The fact that its lattice vectors are linear combinations of the primitive lattice vectors ensures that the supercell is commensurate with the underlying lattice. $\mathbf{a}^{S,2}_{(n,m)}$ was simply obtained by rotating $\mathbf{a}^{S,1}_{(n,m)}$ by 60°. For this, we use the general rotation matrix

$$R_\Theta = \begin{pmatrix} \cos(\Theta) & -\sin(\Theta) \\ \sin(\Theta) & \cos(\Theta) \end{pmatrix} \tag{4.3}$$

for twist angle $\Theta = 60°$:

$$R_{60^\circ} = \begin{pmatrix} \cos(60^\circ) & -\sin(60^\circ) \\ \sin(60^\circ) & \cos(60^\circ) \end{pmatrix} = \begin{pmatrix} 0.5 & -\frac{\sqrt{3}}{2} \\ \frac{\sqrt{3}}{2} & 0.5 \end{pmatrix}. \tag{4.4}$$

Since we know that the primitive lattice vectors enclose an angle of 60° (i.e. $\mathbf{a}_2 = R_{60^\circ}\mathbf{a}_1$), we can express $\mathbf{a}^{S,2}_{(n,m)}$ as:

$$\begin{aligned}
\mathbf{a}^{S,2}_{(n,m)} &= R_{60^\circ}(n\mathbf{a}_1 + m\mathbf{a}_2) \\
&= nR_{60^\circ}\mathbf{a}_1 + mR^2_{60^\circ}\mathbf{a}_1 \\
&= \left[n \begin{pmatrix} 0.5 & -\frac{\sqrt{3}}{2} \\ \frac{\sqrt{3}}{2} & 0.5 \end{pmatrix} + m \begin{pmatrix} -0.5 & -\frac{\sqrt{3}}{2} \\ \frac{\sqrt{3}}{2} & -0.5 \end{pmatrix} \right] \mathbf{a}_1 \\
&= \left[(n+m) \begin{pmatrix} 0.5 & -\frac{\sqrt{3}}{2} \\ \frac{\sqrt{3}}{2} & 0.5 \end{pmatrix} - 2m \begin{pmatrix} 0.5 & 0 \\ 0 & 0.5 \end{pmatrix} \right] \mathbf{a}_1 \\
&= (n+m)R_{60^\circ}\mathbf{a}_1 - m\mathbf{a}_1 \\
&= -m \cdot \mathbf{a}_1 + (n+m) \cdot \mathbf{a}_2.
\end{aligned} \tag{4.5}$$

This makes it apparent that every (n, m) supercell has the same form as the primitive unit cell, just rotated by some angle Θ and enlarged by some scaling factor s. How much it is enlarged can be determined by examining the supercell lattice constant

$$\begin{aligned}
a^S_{(n,m)} = |\mathbf{a}^{S,1}_{(n,m)}| = |\mathbf{a}^{S,2}_{(n,m)}| &= \sqrt{n^2\mathbf{a}_1^2 + m^2\mathbf{a}_2^2 + 2nm\mathbf{a}_1\mathbf{a}_2} \\
&= \sqrt{n^2a^2 + m^2a^2 + 2nm \cdot a^2 \cdot \cos(60^\circ)} \\
&= a \cdot \sqrt{(n^2 + m^2) + n \cdot m} = a \cdot s.
\end{aligned} \tag{4.6}$$

Here, $a = |\mathbf{a}_1| = |\mathbf{a}_2|$ is the lattice constant of the primitive unit cell. The number of atoms in such a supercell is $N_{\text{at}} = N_{\text{at,prim}} \cdot (n^2 + m^2 + n \cdot m)$, with $N_{\text{at,prim}}$ being the number of atoms in the primitive unit cell.

Now, we determine the relative twist angle $\Theta_{(n,m)}$ with respect to the primitive unit cell, i.e. the angle between the old lattice vector $\mathbf{a}_1$ and the new lattice vector $\mathbf{a}^{S,1}_{(n,m)}$. In order to do so, we compare a rotated and enlarged version of $\mathbf{a}_1$ with the new lattice vector $\mathbf{a}^{S,1}_{(n,m)}$:

$$R_{\Theta_{(n,m)}}\mathbf{a}_1 \cdot s \overset{!}{=} \mathbf{a}^{S,1}_{(n,m)} \tag{4.7}$$

$$= n\mathbf{a}_1 + m\mathbf{a}_2 \tag{4.8}$$

$$= \left[n + mR_{60^\circ} \right] \mathbf{a}_1 \tag{4.9}$$

with the scaling factor from Eq. (4.6) $s = \sqrt{n^2 + m^2 + nm}$. Inserting the rotation matrices, we find

$$\begin{pmatrix} \cos(\Theta_{(n,m)}) & -\sin(\Theta_{(n,m)}) \\ \sin(\Theta_{(n,m)}) & \cos(\Theta_{(n,m)}) \end{pmatrix} \mathbf{a}_1 \cdot s \overset{!}{=} \left[n + m \begin{pmatrix} 0.5 & \frac{-\sqrt{3}}{2} \\ \frac{\sqrt{3}}{2} & 0.5 \end{pmatrix} \right] \mathbf{a}_1. \tag{4.10}$$

Comparing the two sides elementwise, we find:

$$\cos(\Theta_{(n,m)}) = \left(n + \frac{m}{2}\right) \cdot \frac{1}{s} \quad \text{and} \quad \sin(\Theta_{(n,m)}) = \left(\frac{\sqrt{3}m}{2}\right) \cdot \frac{1}{s}. \tag{4.11}$$

Dividing these two equations gives the angle $\Theta_{(n,m)}$ between a (n, m) supercell and the primitive unit cell:

$$\Theta_{(n,m)} = \arctan\left(\frac{\sqrt{3}m}{2n + m} \right). \tag{4.12}$$

4.1.2 Generalized backfolding rules

When working with a supercell of a material, one has to consider the backfolding of the primitive unit cell's 1st Brillouin zone (BZ) into the supercell's 1st BZ. Since we are focused on extracting the properties of the Dirac cone, which resides at K/K' in the BZ of the primitive unit cell, we will now determine where this K/K' point is folded back to in the supercell's 1st BZ. Determining this backfolding is not only important in order to find the Dirac cone in k space. More importantly, it is crucial in deciding whether the extracted Dirac cone stems from K or K'. This information is necessary to determine the correct sign of the valley-Zeeman spin-orbit coupling (SOC). For simple supercells like a 2×2 ($n = 2$, $m = 0$), 3×3 ($n = 3$, $m = 0$) or $\sqrt{3} \times \sqrt{3}$ ($n = m = 1$), this backfolding is already well known. To determine this backfolding rule for a general (n, m) supercell, we first need to know an expression for the general reciprocal lattice vectors. It can easily be shown that

$$\mathbf{b}^{S,1}_{(n,m)} = \frac{1}{(n^2 + m^2 + nm)} \cdot \left[(n + m) \cdot \mathbf{b}_1 + m \cdot \mathbf{b}_2 \right] \tag{4.13}$$

$$\mathbf{b}^{S,2}_{(n,m)} = \frac{1}{(n^2 + m^2 + nm)} \cdot \left[-m \cdot \mathbf{b}_1 + n \cdot \mathbf{b}_2 \right] \tag{4.14}$$

fulfill $\mathbf{b}^{S,i}_{(n,m)} \cdot \mathbf{a}^{S,j}_{(n,m)} = 2\pi\delta_{i,j}$ for all $n, m \in \mathbb{Z}$ and can therefore be used as the reciprocal lattice vectors. The condition for backfolding is, that it exists a vector $\mathbf{G}^S_{(n,m)}$, such that:

$$\mathbf{k} \overset{!}{=} \mathbf{k}^S + \mathbf{G}^S_{(n,m)}, \tag{4.15}$$

where $\mathbf{k}$ is the k point within the 1st BZ of the primitive unit cell which is backfolded and $\mathbf{k}^S$ is the k point within the 1st BZ of the supercell where the $\mathbf{k}$ is backfolded to. $\mathbf{G}^S_{(n,m)}$ is

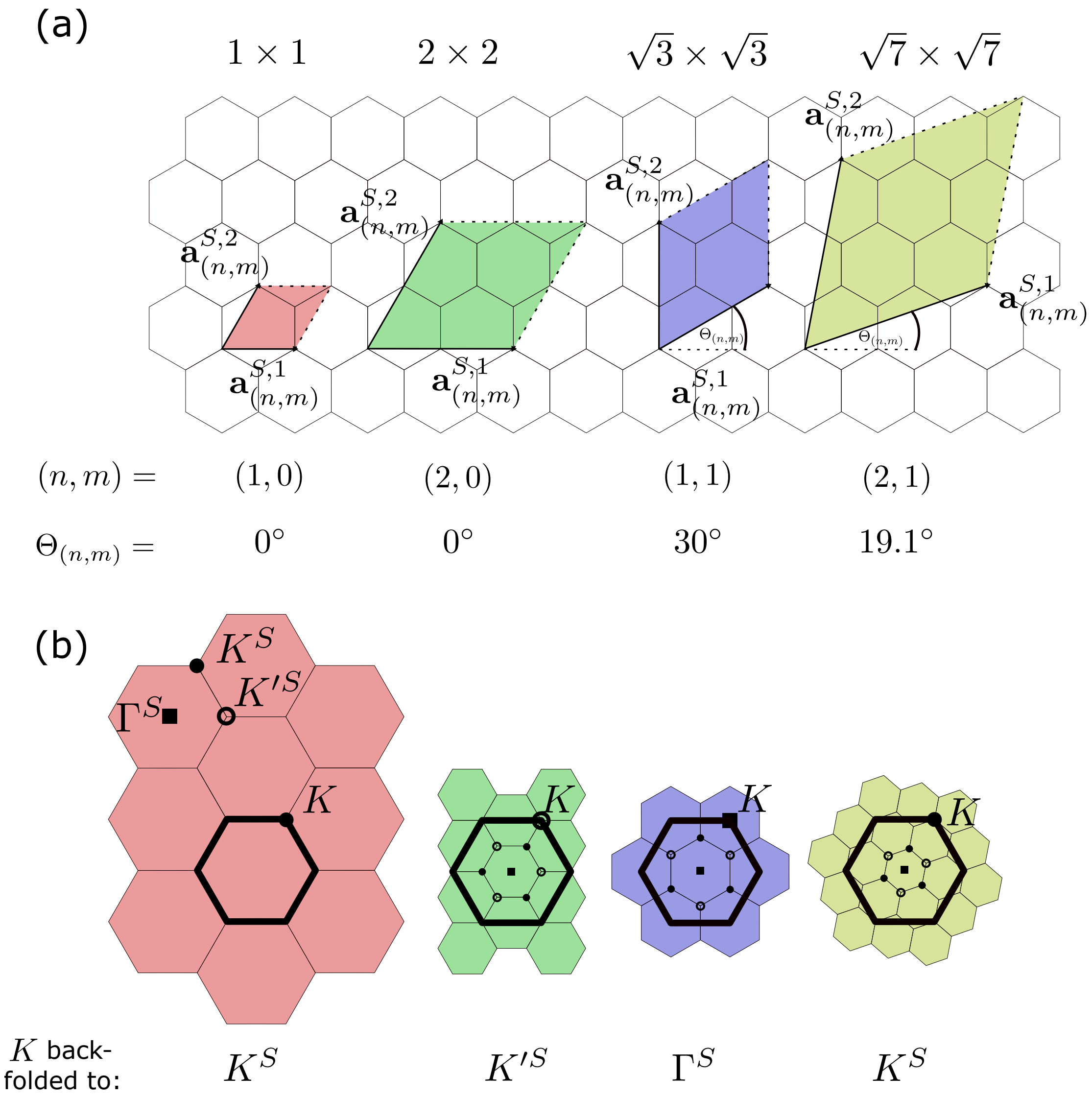

Figure 4.1: Four examples (1×1, 2×2, $\sqrt{3} \times \sqrt{3}$ and $\sqrt{7} \times \sqrt{7}$) of (n,m) supercells in real space (a) and their corresponding k space structures (b). (a) The hexagonal background represents the hexagonal structure of a graphene sheet. However, the supercell generation and backfolding rules work for any structure with a hexagonal primitive unit cell independent of the basis atoms. For each of the four (n,m)- supercells, we show the supercells' lattice vectors $\mathbf{a}^{S,1}_{(n,m)}$ and $\mathbf{a}^{S,2}_{(n,m)}$. Additionally we display the angle $\Theta_{(n,m)}$ between the supercells and the underlying primitive unit cell. (b) The hexagonal backgrounds represent the k space of the four supercells divided into hexagonal BZs. The Γ, K and K' points of these BZs (Γ^S, K^S and K'^S) are marked as squares, dots and circles, respectively. For all four hexagonal supercells of (a), we draw the 1st BZ of the primitive unit cell above the grid centered around one of the supercell BZs. We especially mark the K point of the primitive cell's 1st BZ, and note where it falls on the underlying lattices, which provides information about the backfolding.

a general reciprocal lattice vector for a (n, m) supercell

$$\mathbf{G}^{S}_{(n,m)} = k \cdot \mathbf{b}^{S,1}_{(n,m)} + l \cdot \mathbf{b}^{S,2}_{(n,m)}, \tag{4.16}$$

with $k, l \in \mathbb{Z}$. The position of K in the 1st BZ of the primitive unit cell is

$$\mathbf{K} = \frac{1}{3}\mathbf{b}_1 - \frac{1}{3}\mathbf{b}_2. \tag{4.17}$$

By graphically analyzing this issue, we presume that backfolding of K is only possible to K, K' and Γ of the supercell. Therefore, we now determine when $\mathbf{K}$ coincides with the vectors $\mathbf{K}^S$, $\mathbf{K}'^S$ or $\mathbf{\Gamma}^S$, which are the K, K' and Γ points of the supercell's 1st BZ:

$$\begin{aligned} \mathbf{K}^S &= \frac{1}{3}\mathbf{b}^{S,1}_{(n,m)} - \frac{1}{3}\mathbf{b}^{S,2}_{(n,m)} && (4.18) \\ \mathbf{K}'^S = -\mathbf{K}^S &= -\frac{1}{3}\mathbf{b}^{S,1}_{(n,m)} + \frac{1}{3}\mathbf{b}^{S,2}_{(n,m)} && (4.19) \\ \mathbf{\Gamma}^S &= 0. && (4.20) \end{aligned}$$

Hence, from Eq. (4.15) we know that backfolding occurs, if:

$$\begin{aligned} \mathbf{K} \overset{!}{=} \mathbf{K}^S + \mathbf{G}^S_{(n,m)} &= (k + \frac{1}{3}) \cdot \mathbf{b}^{S,1}_{(n,m)} + (l - \frac{1}{3}) \cdot \mathbf{b}^{S,1}_{(n,m)} && (4.21) \\ \mathbf{K} \overset{!}{=} \mathbf{K}'^S + \mathbf{G}^S_{(n,m)} &= (k - \frac{1}{3}) \cdot \mathbf{b}^{S,1}_{(n,m)} + (l + \frac{1}{3}) \cdot \mathbf{b}^{S,1}_{(n,m)} && (4.22) \\ \mathbf{K} \overset{!}{=} \mathbf{\Gamma}^S + \mathbf{G}^S_{(n,m)} &= k \cdot \mathbf{b}^{S,1}_{(n,m)} + l \cdot \mathbf{b}^{S,1}_{(n,m)}. && (4.23) \end{aligned}$$

The solutions of the ensuing systems of equation are:

$$\begin{aligned} \text{for } \mathbf{K}^S: \quad & k = \frac{(n - m - 1)}{3}, \quad & l = \frac{-2m - n + 1}{3} = -k - m && (4.24) \\ \text{for } \mathbf{K}'^S: \quad & k = \frac{(n - m + 1)}{3}, \quad & l = \frac{-2m - n - 1}{3} = -k - m && (4.25) \\ \text{for } \mathbf{\Gamma}^S: \quad & k = \frac{(n - m)}{3}, \quad & l = \frac{-2m - n}{3} = -k - m. && (4.26) \end{aligned}$$

Since k and l need to be integers, we can find suitable l and k (and therefore have backfolding to the given k point (K, K' or Γ)), if and only if the following backfolding rules are fulfilled:

$$\begin{aligned} \text{backfolding to } \Gamma \text{ for: } n - m &= 0 + 3 \cdot p \\ \text{backfolding to K for: } n - m &= 1 + 3 \cdot p \qquad (4.27) \\ \text{backfolding to K' for: } n - m &= 2 + 3 \cdot p \end{aligned}$$

with $p \in \mathbb{Z}$. As we see, this covers all possible (n, m) supercells. Therefore our assumption that checking only K, K' and Γ is enough has proven to be correct. Example for these foldings can be found in Fig. 4.1(b).

4.1.3 Combining two supercells

The last step is to combine a (n, m) supercell of one material with a (n', m') supercell of another materials. In heterostructures, the lattice constants of the supercells can never match exactly, which necessitates the introduction of strain. Whether layer 1 or layer 2 are strained or whether the strain is distributed between the two layers depends on the specific materials and the details of the manufacturing process. When performing DFT calculations, this is a choice up to the researcher. It depends on factors like the materials' robustness against strain and the effects one would like to study. In our calculations, we choose to always strain graphene, since it is more resilient to strain than the other materials [79, 80, 144, 145, 146]. Assuming that we put all the stain on layer 1 (lattice constant a_1, (n, m) supercell) and leave layer 2 (lattice constant a_2, (n', m') supercell) unstrained, the strain can be calculated as:

$$\epsilon = \frac{a_2 \cdot \sqrt{n'^2 + m'^2 + n'm'}}{a_1 \cdot \sqrt{n^2 + m^2 + nm}} - 1. \tag{4.28}$$

With this, the twist angle between the supercells and the primitive unit cells (Eq. (4.12)) can now be used to determine the relative twist angle between the two layers of the heterostructure. The relative twist angle between the two layers is

$$\Theta = \Theta_{(n', m')} - \Theta_{(n, m)} = \arctan\left(\frac{\sqrt{3}m'}{2n' + m'}\right) - \arctan\left(\frac{\sqrt{3}m}{2n + m}\right). \tag{4.29}$$

Note that in Chap. 5 the interlayer twist angle Θ is defined with an additional minus sign, hence the formula differs from the one presented.

4.2 Density functional theory

The main method employed in this thesis is density functional theory (DFT) [12]. It is an *ab-initio* technique (i.e. it operates from first principles, in principle without any external parameters) used to calculate the zero-temperature ground state band structure of a system. As we use the well established QUANTUM ESPRESSO code [147] with standard settings, we limit ourself to a brief overview of the DFT method. We refer to more in depth explanations of DFT in Refs. [148, 149, 150], which inspired and informed this section. After introducing the fundamental theoretical background in Subsec. 4.2.1, we discuss various options and the concrete flavour of DFT we employ in Subsec. 4.2.2. Some further details on our DFT calculations (electric field, relaxation, strain distribution) are discussed in Sec. 4.5.

4.2.1 Fundamentals

Employing only the Born-Oppenheimer approximation, i.e. assuming that the Hamiltonians describing atom cores and electrons are decoupled, one can write the electron part of a non-relativistic many-body Hamiltonian of a given system (without an external magnetic field) as [150]:

$$\hat{H} = \hat{T} + \hat{V} + \hat{V}_{\text{ext}} \tag{4.30}$$

$$\text{with} \quad \hat{T} = -\frac{\hbar^2}{2m} \sum_i \nabla^2_{\mathbf{r}_i} \tag{4.31}$$

$$\hat{V} = \frac{e^2}{8\pi\epsilon_0} \sum_{i \neq j} \frac{1}{\mid \mathbf{r}_i - \mathbf{r}_j \mid} \tag{4.32}$$

$$\hat{V}_{\text{ext}} = -\frac{1}{4\pi\epsilon_0} \sum_{i,j} \frac{e^2 Z_i}{\mid \mathbf{R}_i - \mathbf{r}_j \mid} + V_0. \tag{4.33}$$

Here, $\hat{T}$ is the many-body kinetic energy operator with $\nabla_{\mathbf{r}_i}$ acting on the electron coordinates $\mathbf{r}_i$ of electron i, and m is the electron mass. The Coulomb interaction between the electrons is captured in $\hat{V}$, with elementary charge e and electric constant ϵ_0. $\hat{V}_{\text{ext}}$ represents the external potential given by the atom cores, with atomic number Z_i and coordinates $\mathbf{R}_i$ of atom i. The potential V_0 arises from the interaction of the atom cores and is a constant within the Born-Oppenheimer approximation. This Hamiltonian constitutes the starting point for DFT.

Hohenberg Kohn theorems

The theorems of Hohenberg and Kohn, formulated in 1964 [12], are fundamental to DFT. The first one states that there is a one-to-one correspondence between the electron ground state density

$$\rho(\mathbf{r}) = \langle\Phi| \sum_i \delta(\mathbf{r} - \mathbf{r}_i) |\Phi\rangle \tag{4.34}$$

and the external potential $\hat{V}_{\text{ext}}$ (up to a constant). As an immediate consequence, the ground state expectation value of any observable $\hat{O}$ is a unique functional of $\rho(\mathbf{r})$:

$$O[\rho] = \langle\Phi| \hat{O} |\Phi\rangle . \tag{4.35}$$

The second theorem is concerned with the case in which this operator $\hat{O}$ is the Hamiltonian $\hat{H}$. Here, one can see that the first part – the Hohenberg-Kohn density functional $F_{\text{HK}}[\rho]$

– is universal for all systems, as all system-specific parts are concentrated in $\hat{V}_{\text{ext}}$:

$$\begin{aligned} E_{V_{\text{ext}}}[\rho] = \langle\Phi|\,\hat{H}\,|\Phi\rangle &= \langle\Phi|\,\hat{T}+\hat{V}\,|\Phi\rangle + \langle\Phi|\,\hat{V}_{\text{ext}}\,|\Phi\rangle \\ &= \quad F_{\text{HK}}[\rho] \quad + \quad V_{\text{ext}}[\rho]. \end{aligned} \tag{4.36}$$

Furthermore, $E_{V_{\text{ext}}}[\rho]$ has its minimum if ρ is the real ground-state density corresponding to V_{ext}. Using the density $\rho(\mathbf{r})$ instead of individual electron coordinates reduces the degrees of freedom from $3N$ (where N is the number of electrons in the system) to only 3.

Kohn Sham formalism

Unfortunately, the exact Hohenberg-Kohn density functional $F_{\text{HK}}[\rho]$ is not known. It is the idea of Kohn and Sham [151] to map the many-body problem onto a non-interacting effective single-body problem with the same ground-state density. In this new form, all effects of the interaction are represented in an effective potential, the exchange-correlation potential. This amounts to recasting Eq. (4.36):

$$\begin{aligned} E_{V_{\text{ext}}}[\rho] &= \overbrace{(T_0[\rho] + V_{\text{c}}[\rho])}^{T[\rho]} + \overbrace{(V_{\text{H}}[\rho] + V_{\text{x}}[\rho])}^{V[\rho]} + V_{\text{ext}}[\rho] \\ &= T_0[\rho] + V_H[\rho] + V_{\text{xc}}[\rho] + V_{\text{ext}}[\rho]. \end{aligned} \tag{4.37}$$

The correlation energy $V_{\text{c}}[\rho]$ is separated from the kinetic energy term, leaving only the kinetic energy of a single particle problem $T_0[\rho]$. The $V[\rho]$ is split into a Hartree-term $V_{\text{H}}[\rho]$, representing the Coulomb interaction of a many-electron density with itself, and an exchange term $V_{\text{x}}[\rho]$. The exchange-correlation functional $V_{\text{xc}}[\rho]$ now encompasses both the exchange and the correlation features of the system. Finding a suitable approximation for this term is an endeavour crucial to DFT.

Self-consistency problem

As the initial many-body problem is now reduced to an effective single-body problem, it is a feasible endeavour to calculate ground state properties. However, the Hamiltonian involves the ground state density itself, and as a consequence the equations have to be solved iteratively. After an initial guess for the wave functions is made, the equations are solved and the new value for the density is used. This is repeated until a self-consistent solution is achieved.

4.2.2 Methodological choices & further approximations

After introducing the fundamentals of DFT, we now discuss some details of how DFT is realized in an actual practical calculation and clarify which additional approximations and modifications are employed in our calculations.

Exchange-correlation functionals

As already discussed, the exchange-correlation functional is the last unknown piece of the DFT formalism. Here we present some widely used approximations:

1. Local density approximation (LDA): The exchange-correlation functional $V_{\text{xc}}[\rho]$ is approximated to be of the form
$$V_{\text{xc}}[\rho] = \int d\mathbf{r}\; \rho(\mathbf{r})\epsilon_{\text{xc}}(\rho(\mathbf{r})), \tag{4.38}$$
where $\epsilon_{\text{xc}}(\rho(\mathbf{r}))$ is the exchange-correlation energy of a homogeneous electron gas, which is numerically known [150, 152].
2. Generalized gradient approximation (GGA): The GGA is similar to LDA, only additionally including the local gradient of $\rho(\mathbf{r})$.
3. Hybrid functionals: The idea of hybrid functionals is to replace some fraction of the exchange-correlation energy by the (exact) Hartree-Fock exchange energy [153]:
$$V_{\text{x}}^{\text{HF}} = -\frac{1}{2}\int d\mathbf{r}_1 \int d\mathbf{r}_2 \frac{\Phi_i^*(\mathbf{r}_1)\Phi_j(\mathbf{r}_1)\Phi_j^*(\mathbf{r}_2)\Phi_i(\mathbf{r}_2)}{\mid \mathbf{r}_1 - \mathbf{r}_2 \mid} \tag{4.39}$$
Although this increases accuracy, it comes with a substantial increase of the computational cost.

Throughout all of our calculations, the Perdew-Burke-Ernzerhof (PBE) functional [154] is employed. This is a widely used GGA exchange-correlation functional.

Plane wave basis and k-grid

Several options for the basis set of the wave functions can be chosen, each with their own advantages and disadvantages. The three most widely employed options are atomic orbitals, Gaussian-type orbitals and plane waves [155]. This choice certainly depends on the system one aims to describe. For extended structures like the 2D structures we investigate, the natural option are plane waves. In order to limit the number of basis states, we need to define a cutoff for the wave functions. The cutoffs for our calculations are presented in Tab. 4.1. Also, a grid in k space needs to be defined, covering the 1st BZ. For this, we use a $n_k \times n_k$ Monkhorst grid [156], where the n_k is chosen based mostly on the size of the supercell. We list the values for n_k for all calculations in Chap. 5 here, in Tab. 4.2. The n_k of the other cases are listed alongside their respective supercells (Tabs. 6.2 and 7.1) in the respective chapters.

Pseudopotentials and projector augmented wave method

One problem which arises when using plane waves is that, in order to describe the strongly oscillating wave functions close to the atom cores, a large cutoff would be

Table 4.1: Computational details: Used charge density cutoff energy E_ρ and wave function kinetic energy cutoff E_{wfc} for the calculations of Chap.5, Chap.6 and Chap. 7.

	MoS_2	WS_2	MoSe_2	WSe_2	$\mathrm{Bi}_2\mathrm{Se}_3$	$\mathrm{Bi}_2\mathrm{Te}_3$	NbSe_2
E_ρ[Ry]	55	70	60	65	58	48	60
E_{wfc}[Ry]	350	500	350	550	480	480	350

Table 4.2: Computational details: k-grid density (we used a $n_k \times n_k$ grid) for the supercells listed in Tab. 5.2. For calculations with electric fields, the grid was sometimes adjusted, those are listed with a tilde over the material. The supercells are in the same order as in Tab. 5.2.

	MoS_2	$\widetilde{\mathrm{MoS}_2}$	WS_2	$\widetilde{\mathrm{WS}_2}$	MoSe_2	$\widetilde{\mathrm{MoSe}_2}$	WSe_2	$\widetilde{\mathrm{WSe}_2}$
0°	21	21	15	15	21	15	21	15
0°	3	9	3	9	3	9	3	9
5.2°	21	-	21	15	21	15	21	21
6.6°	21	21	-	-	18	12	18	12
9.5°	21	18	-	-	18	18	-	-
10.9°	-	-	-	-	21	-	21	-
13.9°	21	21	3	9	21	15	-	-
13.9°	9	15	-	-	-	-	-	-
13.9°	21	-	-	-	6	12	3	3
19.1°	30	30	30	30	21	21	21	21
22.7°	21	18	-	-	18	12	-	-
23.4°	-	-	-	-	18	-	21	12
27°	21	-	15	15	21	15	21	21
30°	39	39	21	36	21	21	21	21
30°	21	-	-	-	6	-	-	-

needed, entailing large computational costs. To tackle this problem, the principle of pseudopotentials has proven to be very helpful. With this method, only the outer shell electrons are described correctly within DFT, while the inner shell electrons are joined with the atom core forming a screened potential. This way, the resulting wave functions have less nodes in the region close to the atom cores than the actual wave function. This lowers the computational cost at the price of misrepresenting the wave functions close to the core, where no relevant physics occurs. We employ an extension of this idea – the projector augmented wave (PAW) method [157]. Here, within a given radius around the atom core, the all-electron wave functions (i.e. the correct wave functions) are mapped to smooth pseudo wave functions via a linear transformation.

Empirical van der Waals corrections

The long ranged van der Waals forces are not well described within DFT. As these are the forces holding together the systems we want to describe, it is apparent that these forces should be incorporated. In order to do so, we deviate from the pure *ab-initio* approach and add a term based on empirical data to our model. This term has the form:

$$V_{\mathrm{vdW}} = \sum_{i,j} \frac{C_{i,j}}{r_{i,j}^6} f(r_{i,j}). \tag{4.40}$$

It connects all atoms in a pairwise fashion, with atoms i and j separated by a distance $r_{i,j}$. $C_{i,j}$ are the dispersion coefficients of atom pairs and $f(r_{i,j})$ is a damping function. There are several different implementations of this method; we use the Grimme-D2 van der Waals corrections for all of our calculations [158, 159, 160].

4.3 Theoretical modeling of graphene

Describing a system using DFT gives us a very accurate picture without demanding any parameters (ab initio). However, it does not give us a clear picture of the underlying processes. Representing the system in a simpler form can give us more insight into what mechanisms are at play and, combined with DFT results, allows us to quantify them accordingly. To this end, one can use a tight binding model (or the linearized model Hamiltonian) describing the system (or a part of it). As such models are not ab-initio, some parameters need to be defined. We can combine the strengths of both approaches by fitting a model Hamiltonian to the DFT data, thereby providing us with reasonable values for the parameters. In this section, we introduce the full tight binding Hamiltonian and the model Hamiltonian capable of describing graphene with the most relevant SOC effects.

4.3.1 Tight binding Hamiltonian

In graphene, the s- and $p_{x/y}$-orbitals build the strong in-plane sp^2 hybridized honeycomb lattice connecting the C atoms (σ-bonds). States formed by those orbitals are energetically far away from the Fermi level and are not actively participating in transport. The p_z-orbitals on the other hand constitute the relevant physics near the Fermi level (π-bonds). Therefore, the tight binding model constructed to emulate these physics is described by hoppings between the p_z-orbitals. In its simplest form, the tight binding Hamiltonian consists of hoppings (with strength t) between nearest neighbours sites in the hexagonal structure:

$$H_0 = t \sum_{\langle ij \rangle, s} c_{is}^{\dagger} c_{js} \tag{4.41}$$

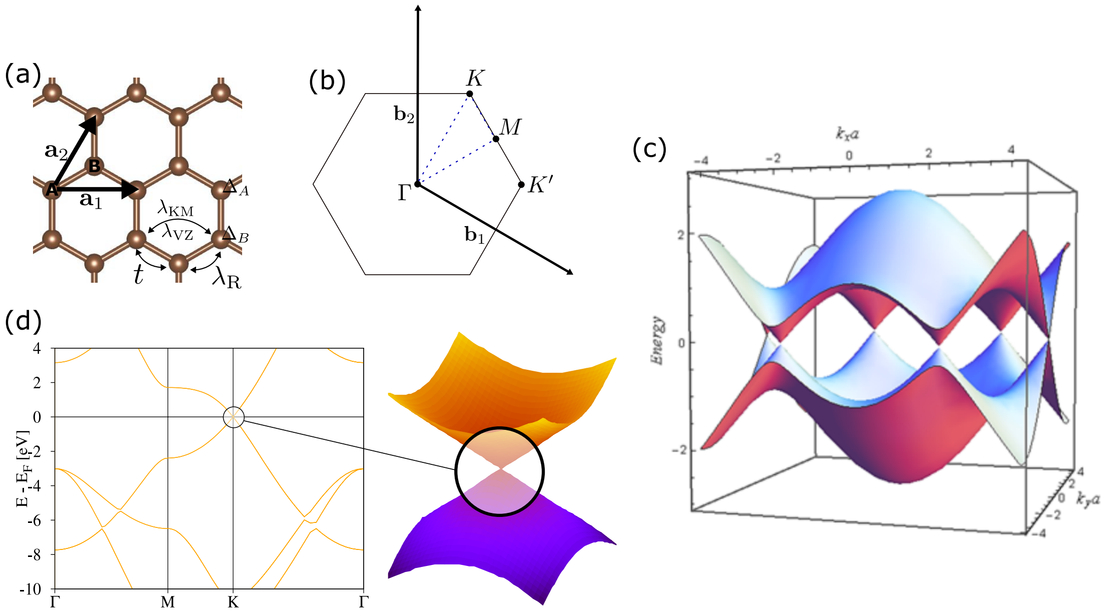

Figure 4.2: Graphene structure in real and k space. (a) The real space lattice of graphene with lattice vectors $\mathbf{a}_1$ and $\mathbf{a}_2$ with indicated sublattice A and B atoms. We also show the on-site potentials and hoppings in the tight binding Hamiltonian from Eq. (4.42). (b) 1st BZ of graphene with high symmetry points Γ, K, K' and M. (c) Tight binding band structure (taken from Ref. [161]). (d) DFT band structure along a high symmetry path indicated as blue dotted line in (b).

We now additionally incorporate on-site potentials and, to include spin-orbit effects, we add hoppings representing the most relevant SOC terms [14, 162]:

$$\begin{aligned} H = H_0 &+ \sum_{i,s} \Delta_i c_{is}^\dagger c_{is} \\ &+ \frac{i}{3\sqrt{3}} \sum_{\langle\langle ij \rangle\rangle, ss'} c_{is}^\dagger c_{js'} (\lambda_{\mathrm{KM}} + \xi \lambda_{\mathrm{VZ}}) [\nu_{ij} s_z]_{ss'} \\ &+ \frac{2i\lambda_{\mathrm{R}}}{3} \sum_{\langle ij \rangle, ss'} c_{is}^\dagger c_{js'} \left[\exp\left(-i\Phi \frac{s_z}{2}\right) [\hat{\mathbf{z}} \cdot (\mathbf{s} \times \mathbf{d}_{ij})] \exp\left(i\Phi \frac{s_z}{2}\right) \right]_{ss'} . \end{aligned} \tag{4.42}$$

The single brackets constitute sums over nearest neighbours and the double brackets constitute sums over next nearest neighbours. $c_{is}^\dagger$ and c_{is} are the creation and annihilation operators of an electron at site i with spin s, $\mathbf{d}_{i,j}$ is a unit vector pointing from site j to nearest neighbour site i, $\mathbf{s}$ is a vector containing the Pauli matrices, ν_{ij} is equal to +1 for clockwise and equal to -1 for counterclockwise hoppings from site j to i, ξ is +1 for sublattice A and -1 for sublattice B, $\hat{\mathbf{z}}$ is the unit vector in z-direction. The first term describes a series of on-site potentials Δ_i. The second term describes Kane-Mele and valley-Zeeman SOC. The third term describes a Rashba SOC related to an electric field in z-direction. λ_{R}, λ_{KM} and λ_{VZ} constitute the three main flavours of SOC discussed in the thesis. We will give more information on them in the context of the model Hamiltonian in the next subsection. This Hamiltonian is not exactly the general C_{3v}-symmetric Hamiltonian from Ref. [162], it was modified to suit our calculations. That is why, on the one hand, it additionally includes the Rashba angle Φ (breaking C_{3v}-symmetry), but on the other hand does not include PIA (pseudospin inversion asymmetry) SOC; this holds true for both the tight binding and the model Hamiltonian version.

Translating this model into k space produces a decent representation of the graphene band structure, which can be seen in Fig. 4.2(c). At K and K' we see the most relevant feature, the Dirac cone, located at the Fermi energy (half filling in the tight binding model). For low energies it has a nearly isotropic linear dispersion. In the case without SOC ($\lambda_{\mathrm{KM}} = \lambda_{\mathrm{VZ}} = \lambda_{\mathrm{R}} = 0$), its states are doubly degenerate. Adding these terms will give more complexity to the low energy band structure, which is discussed in the following.

4.3.2 Model Hamiltonian

Linearizing the Fourier-transformed version of Eq. (4.42) around the K/K' point produces a simpler version [14, 19], capturing the physics of the Dirac cone:

$$H(\mathbf{k}) = H_{\mathrm{orb}}(\mathbf{k}) + H_{\mathrm{so}} = H_{\mathrm{orb}}(\mathbf{k}) + H_{\mathrm{so,I}} + H_{\mathrm{so,R}}. \tag{4.43}$$

The orbital part describes the dispersion of the Dirac cone; it is linearized around the K/K' point, therefore $\mathbf{k}$ is the electron wave vector measured from K/K':

$$H_{\text{orb}}(\mathbf{k}) = \hbar v_F(\kappa\sigma_x k_x + \sigma_y k_y) + \Delta\sigma_z. \tag{4.44}$$

Here, v_F is the Fermi velocity of the Dirac electrons and σ_x,σ_y and σ_z are the Pauli matrices operating on the sublattice (A/B) space. The parameter κ determines, whether the Hamiltonian describes the band structure near K or K' ($\kappa = 1$ for K and $\kappa = -1$ for K'). The on-site potentials Δ_i are reduced to a staggered potential Δ, describing the difference in potential between A- and B-sublattice. Although this is no spin-orbit term, it is often needed in order to take into account any asymmetrical influence of the substrate on the graphene A- and B-sublattice. The intrinsic spin-orbit Hamiltonian

$$H_{\text{so,I}} = \left[\lambda_{\text{KM}}\sigma_z + \lambda_{\text{VZ}}\sigma_0\right]\kappa s_z, \tag{4.45}$$

and the Rashba spin-orbit Hamiltonian

$$H_{\text{so,R}} = -\lambda_{\text{R}} \exp\left(-i\Phi\frac{s_z}{2}\right)\left[\kappa\sigma_x s_y - \sigma_y s_x\right] \exp\left(i\Phi\frac{s_z}{2}\right), \tag{4.46}$$

both include spin Pauli matrices s_x, s_y and s_z acting on the spin space; λ_{VZ} and λ_{KM} are the valley-Zeeman [13, 40] SOC and the Kane-Mele [34, 35] SOC, respectively. The Rashba SOC term is defined by two parameters: the magnitude λ_{R} and the Rashba (phase) angle Φ [163, 21]. The effects of the different flavours of SOC are depicted in Fig. 4.3(a)-(c). They can be summarized as:

1. The Kane-Mele SOC (λ_{KM}) is the SOC which is already present in pristine graphene, although only on the μeV scale. It introduces a mass term (and therefore a gap) to the Dirac cone. In contrast to the trivial gap induced by Δ, it has different signs for K and K'. Hence, if it is large enough, it can produce a quantum spin Hall state [34, 35].

2. The valley-Zeeman SOC (λ_{VZ}) splits the degenerate bands into a spin-up and a spin-down band just like a Zeeman field. Since time-reversal symmetry has to be conserved, this effective magnetic field has opposite signs at K and K'. It can enable pseudohelical states [36] and is the main driving force for spin-relaxation anisotropy [48].

3. The Rashba SOC (λ_{R},Φ) originates from a breaking of the inversion symmetry by a substrate. It is the same term arising in e.g. bilayer graphene when applying an out-of-plane electric field. Through Rashba SOC, the Dirac cone acquires an in-plane spin-texture (see Fig. 4.3(c)), which enables charge-to-spin (or spin-to-charge) conversion. The Rashba angle Φ determines the radial part of the spin texture (from a purely tangential spin texture at $\Phi = 0°$ to a purely radial one at $\Phi = 90°$). We choose to limit the Rashba parameter to positive values $\lambda_{\text{R}} > 0$.

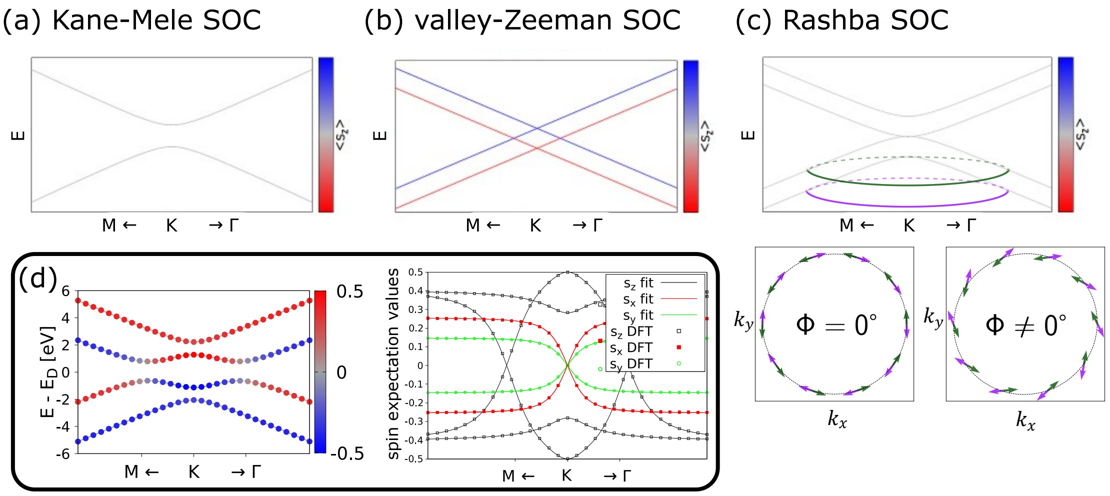

Figure 4.3: (a)-(c) The Dirac cone as obtained by the model Hamiltonian (Eq. (4.43)) with only one flavour of SOC. The only non-zero spin-orbit parameter is λ_{KM} (a), λ_{VZ} (b) or λ_{R} (c). For (c), we additionally show the in-plane spin texture within circles around the K point for the purely tangential case ($\Phi = 0$) and mixed tangential and radial case ($\Phi \neq 0$). (d) The Dirac cone of a $\Theta = 0°$ graphene/$\mathrm{Bi_2Se_3}$ heterostructure as calculated by DFT (dots) and the model Hamiltonian fit (solid lines). Both energies and spin expectation values can be captured in the fit.

A sign change of λ_{R} then corresponds to an additional phase shift of Φ by a half rotation, i.e. $\Phi \to \Phi + 180°$.

The model Hamiltonian can be used with great effect to fit the results of the DFT calculations near the Dirac cone energy. Both spins and energies can be usually described very accurately with the model Hamiltonian (see Fig. 4.3(d)).

4.4 Interlayer interaction via generalized Umklapp processes

Apart from the DFT approach we use, the effect of the twist angle can be described by other means, most importantly tight binding [19, 20, 21]. Tight binding models incorporate the twist angle into their calculations through generalized Umklapp processes. In this section, we present the general interlayer interaction in layered systems via generalized Umklapp processes as discussed by Koshino in Ref. [22]. The main insight this theory offers is which k points of the individual layer's 1st BZ can interact with each other and how this can be varied using the interlayer twist angle and strain. This knowledge can be very helpful in interpreting DFT results. Although in Ref. [22] incommensurate lattices are discussed, the theory is equally valid for the commensurate systems used in DFT.

4.4.1 Notation

Firstly, we will introduce the notations adapted from Ref. [22] describing an incommensurate bilayer system. We assume a heterostructure of two layers with different lattice vectors $\mathbf{a}_1$ and $\mathbf{a}_2$ (layer 1) and $\tilde{\mathbf{a}}_1$ and $\tilde{\mathbf{a}}_2$ (layer 2). The corresponding reciprocal lattice vectors of the two layers are $\mathbf{b}_1$ and $\mathbf{b}_2$ (layer 1) and $\tilde{\mathbf{b}}_1$ and $\tilde{\mathbf{b}}_2$ (layer 2). The system is described within tight binding with the atomic orbitals and sublattices noted by the index $X = A, B, \ldots$ (for layer 1) and $\tilde{X} = \tilde{A}, \tilde{B}, \ldots$ (for layer 2). These orbitals are localized at the position $\boldsymbol{\tau}_X$ (or $\boldsymbol{\tau}_{\tilde{X}}$ for layer 2) within each unit cell. Note that $\boldsymbol{\tau}_X$ and $\boldsymbol{\tau}_{\tilde{X}}$ can have both in-plane and out-of-plane components and the interlayer distance separating the two layers is encoded in the $\boldsymbol{\tau}_X$ (or $\boldsymbol{\tau}_{\tilde{X}}$). Hence, all atomic positions are given by

$$\mathbf{R}_X = n_1\mathbf{a}_1 + n_2\mathbf{a}_2 + \boldsymbol{\tau}_X \quad \text{for layer 1} \tag{4.47}$$

$$\mathbf{R}_{\tilde{X}} = \tilde{n}_1\tilde{\mathbf{a}}_1 + \tilde{n}_2\tilde{\mathbf{a}}_2 + \boldsymbol{\tau}_{\tilde{X}} \quad \text{for layer 2} \tag{4.48}$$

with $n_1, n_2, \tilde{n}_1, \tilde{n}_2 \in \mathbb{Z}$. Furthermore, $|\mathbf{R}_X\rangle \equiv \Phi_X(\mathbf{r} - \mathbf{R}_X)$ and $|\mathbf{R}_{\tilde{X}}\rangle \equiv \Phi_{\tilde{X}}(\mathbf{r} - \mathbf{R}_{\tilde{X}})$ are the atomic states (with sublattice and atomic orbital determined by X or $\tilde{X}$) localized at $\mathbf{R}_X$ in layer 1 and layer 2, respectively. The transfer integral between two sites

$$-T_{\tilde{X},X}(\mathbf{R}_{\tilde{X}} - \mathbf{R}_X) \tag{4.49}$$

depends only on the relative position $\mathbf{R}_{\tilde{X}} - \mathbf{R}_X$ between the sites and their different orbitals $\tilde{X}$ and X. The Bloch states of the two layers are the defined as

$$\left|\mathbf{k}, X\right\rangle = \frac{1}{\sqrt{N}} \sum_{\mathbf{R}_X} \exp\left(i\mathbf{k}\mathbf{R}_X\right) |\mathbf{R}_X\rangle \quad \text{for layer 1} \tag{4.50}$$

$$\left|\tilde{\mathbf{k}}, \tilde{X}\right\rangle = \frac{1}{\sqrt{\tilde{N}}} \sum_{\mathbf{R}_{\tilde{X}}} \exp\left(i\tilde{\mathbf{k}}\mathbf{R}_{\tilde{X}}\right) |\mathbf{R}_{\tilde{X}}\rangle \quad \text{for layer 2,} \tag{4.51}$$

with $\mathbf{k}$ and $\tilde{\mathbf{k}}$ in-plane Bloch wave-vectors of layer 1 and 2, respectively, and N and $\tilde{N}$ number of unit cells (of layer 1 and 2, respectively) in the (large, but finite) total system area S_{tot}.

Using the transfer integral $-T_{\tilde{X},X}(\mathbf{R}_{\tilde{X}} - \mathbf{R}_X)$, we now define the interlayer Hamiltonian in real space as

$$U = -\sum_{X,\tilde{X}} T_{\tilde{X},X}(\mathbf{R}_{\tilde{X}} - \mathbf{R}_X) |\mathbf{R}_{\tilde{X}}\rangle \langle \mathbf{R}_X| + \text{h.c.} \tag{4.52}$$

The main piece of the formalism is the k space interlayer Hamiltonian. For a detailed derivation of it, we refer to Ref. [22]. It can be written as

$$U_{\tilde{X},X}(\tilde{\mathbf{k}},\mathbf{k}) = \left\langle \tilde{\mathbf{k}},\tilde{X}\middle| U \middle|\mathbf{k},X\right\rangle \tag{4.53}$$

$$= -\sum_{\mathbf{G},\tilde{\mathbf{G}}} t_{\tilde{X},X}(\mathbf{k}+\mathbf{G}) \exp\left(-i\mathbf{G}\cdot\boldsymbol{\tau}_X + i\tilde{\mathbf{G}}\cdot\boldsymbol{\tau}_{\tilde{X}}\right)\delta_{\mathbf{k}+\mathbf{G},\tilde{\mathbf{k}}+\tilde{\mathbf{G}}}. \tag{4.54}$$

with in-plane Fourier transform of the transfer integral

$$t_{\tilde{X},X}(\mathbf{q}) = \frac{1}{\sqrt{S\tilde{S}}}\int T_{\tilde{X},X}(\mathbf{r}+z_{\tilde{X}X}\mathbf{e}_z)\exp(-i\mathbf{q}\mathbf{r})d^2r. \tag{4.55}$$

Here, we define the out-of plane distance of orbitals X and $\tilde{X}$ as $z_{\tilde{X}X} = (\boldsymbol{\tau}_{\tilde{X}} - \boldsymbol{\tau}_X)\cdot\mathbf{e}_z$ using the out-of-plane unit vector $\mathbf{e}_z$. The integral is performed in 2D, covering the system area S_{tot}. S and $\tilde{S}$ are the unit cell's area of the layers 1 and 2, respectively. $\mathbf{G}$ and $\tilde{\mathbf{G}}$ are general reciprocal lattice vectors (i.e. linear combinations of the reciprocal lattice vectors) of layers 1 and 2, respectively:

$$\mathbf{G} = s\cdot\mathbf{b}_1 + t\cdot\mathbf{b}_2, \tag{4.56}$$

$$\tilde{\mathbf{G}} = \tilde{s}\cdot\tilde{\mathbf{b}}_1 + \tilde{t}\cdot\tilde{\mathbf{b}}_2, \tag{4.57}$$

with $s,t,\tilde{s},\tilde{t}\in\mathbb{Z}$.

4.4.2 Interaction rules

The k space interlayer Hamiltonian $U_{\tilde{X},X}(\tilde{\mathbf{k}},\mathbf{k})$ from Eq. (4.54) is the main result of the approach as it can be used e.g. in explicit tight binding calculations within perturbation theory to determine proximity SOC terms [19, 20, 21]. However, even without assuming explicit atomic orbits and transfer integrals, we can draw conclusions from it, namely which k points of the two layers couple with each other. For this we only need the two sets of lattice vectors $\{\mathbf{a}_1,\mathbf{a}_2\}$ and $\{\tilde{\mathbf{a}}_1,\tilde{\mathbf{a}}_2\}$ (including the relative twist angle) and the assumption that all transfer integrals between orbitals decay exponentially with the distance $(\mathbf{R}_{\tilde{X}} - \mathbf{R}_X)$. The two most relevant parts of $U_{\tilde{X},X}(\tilde{\mathbf{k}},\mathbf{k})$ are

1. the condition for k point matching $\delta_{\mathbf{k}+\mathbf{G},\tilde{\mathbf{k}}+\tilde{\mathbf{G}}}$ and
2. the Fourier-transformed transfer integral $t_{\tilde{X},X}(\mathbf{q})$.

k matching condition

Let us first discuss $\delta_{\mathbf{k}+\mathbf{G},\tilde{\mathbf{k}}+\tilde{\mathbf{G}}}$. It imposes the condition

$$\mathbf{k}+\mathbf{G} = \tilde{\mathbf{k}}+\tilde{\mathbf{G}} \tag{4.58}$$

on the k points. This means one needs to find a $\mathbf{G}$ and a $\tilde{\mathbf{G}}$, such that somewhere in the extended k space (i.e. extended beyond the 1st BZ) the vectors $\mathbf{k}+\mathbf{G}$ (in layer 1) and $\tilde{\mathbf{k}}+\tilde{\mathbf{G}}$

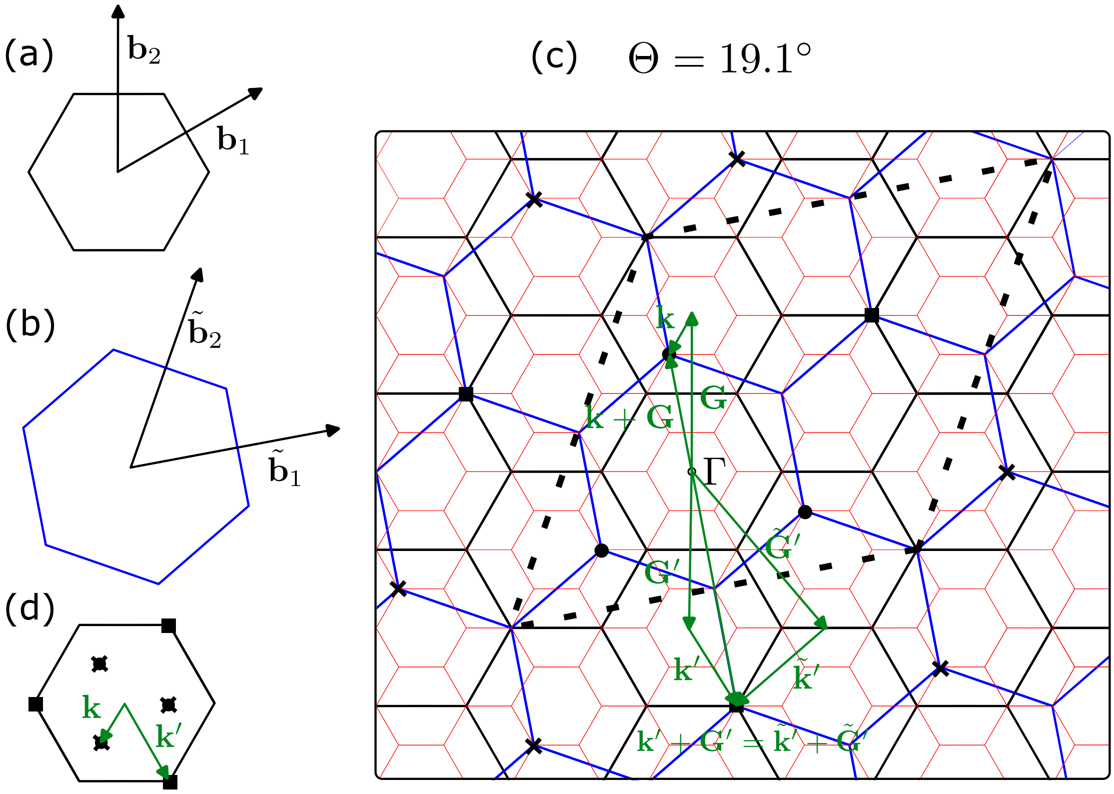

Figure 4.4: Visualizing the k point matching condition for the example of a $\Theta = 19.1^\circ$ commensurate graphene/transition-metal dichalcogenide (TMDC) supercell. (a) and (b) show the 1st BZ of layer 1 (TMDC) and layer 2 (graphene) with the corresponding reciprocal lattice vectors. The main subfigure (c) shows the extended reciprocal structures of layer 1 (black) and layer 2 (blue) on top of the underlying reciprocal structure of the supercell (red). k points, which fulfil the matching condition between the layer 2 K point and any k point in layer 1 are marked with dots ('first order'), squares ('second order') and crosses ('third order'). The higher the order, the farther away the k point is from the origin of the extended k space (marked as Γ). The dotted lines indicate a 'unit cell', which forms a repeating pattern (for both layer 1 and layer 2 reciprocal structures) throughout the extended reciprocal space. The green vectors show for two examples ('first order' dot without prime and 'second order' square marked with prime) how the vectors of Eq. (4.58) look like. For the 'first order' case $\tilde{\mathbf{k}} = \tilde{\mathbf{K}}$ and $\tilde{\mathbf{G}} = \mathbf{0}$ are omitted. (d) shows the points discussed in (c), which fulfil the matching condition, drawn within the 1st BZ of layer 1.

(in layer 2) match (see Fig. 4.4(c)). For the incommensurate structures (as discussed in the tight binding models), this condition alone would be trivially fulfilled: somewhere in the extended k space the points will inevitably match, since the incommensurate combination of $\mathbf{G} - \tilde{\mathbf{G}}$ is able to cover the whole 2D k plane. For commensurate structures (as used in DFT), however, going further away from the origin of k space, the k space structures of layer 1 and 2 will eventually form a repeating pattern (dotted lines in Fig. 4.4(c)). Therefore, no further new matching pairs of $\mathbf{k}$ and $\tilde{\mathbf{k}}$ can arise from this point forward.

Let us now discuss the case of commensurate systems, as they appear in DFT calculations. Here, there are three relevant 1st BZs: the one of layer 1, the one of layer 2 and the one of the commensurate heterostructure supercell. They are depicted as black, blue and red, respectively, in Fig. 4.4(c). If the matching condition Eq. (4.58) is fulfilled, the two k points $\mathbf{k}$ (1st BZ of layer 1) and $\tilde{\mathbf{k}}$ (1st BZ of layer 2) automatically fold back to the same point in the 1st BZ of the supercell. This can be seen in Fig. 4.4(c), where all k points fulfilling the matching condition are residing at one of the K points of the underlying supercell extended reciprocal structure (red hexagonal grid). A proof for this statement works as follows: The k point in the extended k space that fulfills the matching condition can always be represented using a k point $\mathbf{k}^S$ within the supercell system's 1st BZ and a reciprocal lattice vector $\mathbf{G}^\mathbf{S}$ of the supercell system:

$$\mathbf{k} + \mathbf{G} = \tilde{\mathbf{k}} + \tilde{\mathbf{G}} = \mathbf{k}^S + \mathbf{G}^S. \tag{4.59}$$

As both $\mathbf{G}$ and $\tilde{\mathbf{G}}$ can be interpreted as linear combinations of reciprocal lattice vectors of the supercell system as well, we can incorporate them into $\mathbf{G}^S$:

$$\mathbf{k} = \mathbf{k}^S + (\mathbf{G}^S - \mathbf{G}) = \mathbf{k}^S + \mathbf{G}^S_{\text{new},1} \tag{4.60}$$

$$\tilde{\mathbf{k}} = \mathbf{k}^S + (\mathbf{G}^S - \tilde{\mathbf{G}}) = \mathbf{k}^S + \mathbf{G}^S_{\text{new},2}. \tag{4.61}$$

Using the backfolding condition Eq. (4.15), this proves that both $\mathbf{k}$ and $\tilde{\mathbf{k}}$ fold back to the same point $\mathbf{k}^S$ in the 1st BZ of the supercell system.

Proving the inverse, namely that, if $\mathbf{k}$ and $\tilde{\mathbf{k}}$ fold back to the same point $\mathbf{k}^S$ in the supercell system's 1st BZ, they automatically fulfill the matching condition Eq. (4.58), is a bit more cumbersome and requires an additional condition. This condition is that the heterostructure supercell in question is the smallest possible one describing this exact heterostructure system (same twist angle and same strain). Another way of phrasing this, is that the heterostructure cannot be viewed as a supercell of another heterostructure supercell. If this condition is not met, for example when combining a 15 × 15 and a 10 × 10 supercell (instead of a 3 × 3 supercell and a 2 × 2 supercell), we have practically formed a 'supercell of a supercell'. Therefore, bands could be folded on top of each other without being linked by the matching condition Eq. (4.58). However, for all supercells used in this thesis, this condition is fulfilled, as artificially enlarging the supercells only increases the computational cost without providing any benefit. We perform the proof for this inverse statement under said condition in App. A.

Fourier-transformed transfer integral $t_{\tilde{X},X}(\mathbf{q})$

The second important term of $U_{\tilde{X},X}(\tilde{\mathbf{k}},\mathbf{k})$ is $t_{\tilde{X},X}(\mathbf{q})$. It is the Fourier transform of the transfer integral $-T_{\tilde{X},X}(\mathbf{R}_{\tilde{X}} - \mathbf{R}_X)$. Naturally, the real space transfer integral decays with increasing distance $r = |\mathbf{R}_{\tilde{X}} - \mathbf{R}_X|$ between orbitals. In the literature, the real space transfer integral is commonly assumed to decay exponentially [19]. Hence, (ignoring the direction dependence induced by the different orbitals) we describe the dependence of $-T_{\tilde{X},X}(\mathbf{R}_{\tilde{X}} - \mathbf{R}_X)$ on the distance r by some function

$$f(r) = \exp(-\alpha(r - r_0)), \tag{4.62}$$

with decay strength α and equilibrium distance r_0. It can be shown that the 2D Fourier transform of this function is

$$f(q) = \mathcal{F}(f(r)) = \frac{\sqrt{2\pi}\alpha \exp(\alpha r_0)}{(\alpha^2 + |q|^2)^{3/2}}. \tag{4.63}$$

If another decaying function was assumed, the Fourier transform $t_{\tilde{X},X}(\mathbf{q})$ would still decay with $|q|$ in some fashion. This decaying behaviour of $t_{\tilde{X},X}(\mathbf{q})$ means, that although $\mathbf{k}$ and $\tilde{\mathbf{k}}$ are allowed to couple by the matching condition, because $\mathbf{G}$ and $\tilde{\mathbf{G}}$ exist, so that

$$\mathbf{k} + \mathbf{G} = \tilde{\mathbf{k}} + \tilde{\mathbf{G}}, \tag{4.64}$$

the coupling might be suppressed if the needed vectors $\mathbf{G}$ and $\tilde{\mathbf{G}}$ are so large that $|\mathbf{k} + \mathbf{G}|$ is too far away from the origin of the 2D k space. For the parameters chosen in Ref. [22] for bilayer graphene, the values of $t_{\tilde{X},X}(\mathbf{q})$ for the 'first order' (points with the lowest $|\mathbf{k} + \mathbf{G}|$) and the 'second order' (points with the second lowest $|\mathbf{k} + \mathbf{G}|$) are separated by almost two orders of magnitude. Hence, all contributions beyond this 'first order' are usually neglected.

4.4.3 Modifying the coupling by twist angle and strain

Introducing a twist angle between the two layers in real space, the corresponding reciprocal structures will twist as well with regard to each other. If we twist layer 1 by a twist angle Θ using the rotation matrix R_Θ, this amounts to transforming the real space and k space vectors of layer 1 as follows:

$$\{\mathbf{a}_1, \mathbf{a}_2\} \rightarrow \{R_\Theta \mathbf{a}_1, R_\Theta \mathbf{a}_2\} \tag{4.65}$$

$$\{\mathbf{b}_1, \mathbf{b}_2\} \rightarrow \{R_\Theta \mathbf{b}_1, R_\Theta \mathbf{b}_2\}. \tag{4.66}$$

This has consequences for the interaction between the two layers. Namely, that for a fixed k point $\tilde{\mathbf{k}}$ in the 1st BZ of layer 2, different k points $\mathbf{k}$ in the 1st BZ of layer 1 now couple to it. More precisely, as the twist angle Θ increases, the points $\mathbf{k}$ follow a circular path

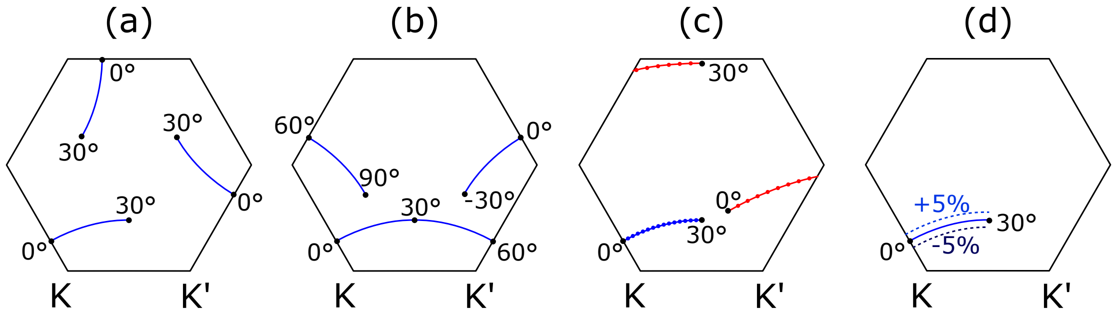

Figure 4.5: ’Path of interaction’ of the graphene K point within the 1st BZ of the neighbouring WS_2 layer when varying twist and strain in the incommensurate heterostructure. (a) The paths of all three points of ’first order’ interaction (connected by C_3 symmetry) from $0° \leq \Theta \leq 30°$. In all following subfigures only one of the three paths is shown. (b) One of the paths from (a) for range $-30° \leq \Theta \leq 90°$. (c) One ’first order’ (blue) and one ’second order’ (red) path for $0° \leq \Theta \leq 30°$. The blue (or red) dots are separated by a twist angle of $\Delta\Theta = 2°$. (d) The same ’first order’ path, with additional dotted lines indicating the alternative paths with $\epsilon = +5\%$ (light blue) and $\epsilon = -5\%$ (dark blue) strain on the graphene.

continually exiting and reentering the 1st BZ (see Fig. 4.5(b)). Throughout the thesis we will occasionally refer to such a path as ’path of interaction’. The radius of this circular path grows with $|\mathbf{k} + \mathbf{G}|$ and therefore with the ’order’ of the layer interaction. Hence, with increasing ’order’ the paths appear as increasingly straight lines through the 1st BZ (see Fig. 4.5(c)).

Additionally, the interlayer interaction can be varied by changing the structure through the introduction of strain. Surely, the modifications to the system by strain are plentiful and we offer a comprehensive discussion in Sec. 4.5. One of these effects is that – similar to the twist angle – the point of interaction between the layers is modified by the strain. Straining the real space lattice of layer 1 by the margin ϵ will result in a transformation

$$\{\mathbf{a}_1, \mathbf{a}_2\} \rightarrow \{(1 \pm \epsilon)\mathbf{a}_1, (1 \pm \epsilon)\mathbf{a}_2\} \tag{4.67}$$

$$\{\mathbf{b}_1, \mathbf{b}_2\} \rightarrow \{\frac{1}{(1 \pm \epsilon)}\mathbf{b}_1, \frac{1}{(1 \pm \epsilon)}\mathbf{b}_2\}. \tag{4.68}$$

of the real space and k space vectors, respectively. While increasing the twist angle will lead to a circular path, increasing the strain will lead to a straight path. This path is always locally perpendicular to the circular one induced by twist. Combining both twist angle and strain as degrees of freedom and limiting them to a certain range of values therefore opens up an annular sector within the 1st BZ (see Fig. 4.5(d)).

4.4.4 Symmetry considerations

Based on these interlayer interaction rules [22], there have been subsequent tight binding calculations of a concrete graphene-based system [19, 20, 21]. These use perturbation theory in order to determine the twist-angle dependence of the proximity SOC in graphene. Without discussing the concrete tight binding results (which depend on details of the tight binding description of the substrate), one can use this approach to deduce symmetry rules regarding the twist angle for the proximity SOC (i.e. the model Hamiltonian parameters of Eq. (4.43)) in graphene. Although these rules can be mostly understood using the symmetries of the real space structures as well, we discuss them here, as they were first introduced in Ref. [19, 20, 21]. Also, the 'path of interaction' the k points take through the substrate's 1st BZ often nicely illustrates the symmetries. In this subsection, we consider the case of graphene (layer 1) on a substrate with a hexagonal 1st BZ (layer 2, e.g. TMDC) and discuss how the graphene Dirac cone at the K point of layer 1 couples to different parts of the 1st BZ of layer 2 with varying twist angle. In the following, we only consider the path that one of the three 'first order' k points takes with increasing twist angle, as these three points are connected by C_3 symmetry (see Fig. 4.5(a)).

Symmetry rules for twisting by $60°$

As the twist angle changes from $\Theta = 0°$ to $\Theta = 60°$, the path of 'first order' interaction (depicted in Fig. 4.5(b)) goes from a point close to the K point to one close to the K' point. For $60° < \Theta < 120°$, this path is repeated in a similar way starting from a point close to the K' point and ending at one close to the K point. This illustrates that twisting by 60° from any situation leads to the same interlayer coupling with a switch $K \rightarrow K'$. The ensuing symmetry rules for the SOC parameters are:

$$\lambda_{\mathrm{VZ}}(\Theta + 60°) = -\lambda_{\mathrm{VZ}}(\Theta) \tag{4.69}$$

$$\lambda_{\mathrm{R}}(\Theta + 60°) = \lambda_{\mathrm{R}}(\Theta) \tag{4.70}$$

$$\Phi(\Theta + 60°) = \Phi(\Theta). \tag{4.71}$$

This can be understood as follows: twisting graphene by 60° leaves us with the same structure, only sublattice label 'A' and 'B' are exchanged. Consequently only the SOC parameter λ_{VZ} has to change its sign, as it is sensitive to this relabeling.

Symmetry rules for twisting clockwise/counterclockwise

From tight binding calculations, we can conclude that twisting from $\Theta = 0°$ clockwise or counterclockwise yields mostly the same results. Only the Rashba angle Φ shows a sensitivity to this change, which can be used with great effect in trilayer systems in order to create purely radial Rashba SOC [21, 164]. The symmetry rules capturing this behaviour can be written as:

$$\lambda_{\mathrm{VZ}}(-\Theta) = \lambda_{\mathrm{VZ}}(\Theta) \tag{4.72}$$
$$\lambda_{\mathrm{R}}(-\Theta) = \lambda_{\mathrm{R}}(\Theta) \tag{4.73}$$
$$\Phi(-\Theta) = -\Phi(\Theta). \tag{4.74}$$

These rules can be proven using the explicit form of the reflection operator R_x converting $(x,y,z) \to (-x,y,z)$ (which connects $\Theta \to -\Theta$) from Ref. [19]:

$$R_x = -i\sigma_0 s_x \tau_x \tilde{R}_x, \tag{4.75}$$

with σ_0 and s_x acting on the sublattice- and spin-space, respectively, as always. Additionally, τ_x acts on the valley-space (K/K') and $\tilde{R}_x$ represents the reflection operator for the envelop function by the x-axis. It is now a straight forward task to show that for the valley-Zeeman and Rashba terms

$$H_{\mathrm{so,VZ}}(\lambda_{\mathrm{VZ}}) = \lambda_{\mathrm{VZ}}\sigma_0 s_z \tau_z \tag{4.76}$$
$$H_{\mathrm{so,R}}(\lambda_{\mathrm{R}},\Phi) = -\lambda_{\mathrm{R}} \exp\left(-i\Phi\frac{s_z}{2}\right)\left[\sigma_x s_y \tau_z - \sigma_y s_x \tau_0\right] \exp\left(i\Phi\frac{s_z}{2}\right) \tag{4.77}$$
$$= -\frac{\lambda_{\mathrm{R}}}{2}\left[\cos(\Phi)(\sigma_x s_y \tau_z - \sigma_y s_x \tau_0) - \sin(\Phi)(\sigma_x s_x \tau_z + \sigma_y s_y \tau_0)\right] \tag{4.78}$$

the reflection operator fulfills the equations

$$R_x H_{\mathrm{so,VZ}}(\lambda_{\mathrm{VZ}}) R_x^{-1} = H_{\mathrm{so,VZ}}(\lambda_{\mathrm{VZ}}) \tag{4.79}$$
$$R_x H_{\mathrm{so,R}}(\lambda_{\mathrm{R}},\Phi) R_x^{-1} = H_{\mathrm{so,R}}(\lambda_{\mathrm{R}},-\Phi), \tag{4.80}$$

proving the (anti-)symmetry rules in Eq. (4.72) to Eq. (4.74).

Zero points of λ_{VZ} and Φ

From the rules above, one can easily deduce that

$$\lambda_{\mathrm{VZ}}(\Theta = 30^\circ) \overset{(4.72)}{=} \lambda_{\mathrm{VZ}}(\Theta = -30^\circ) \overset{(4.69)}{=} -\lambda_{\mathrm{VZ}}(\Theta = 30^\circ) = 0 \tag{4.81}$$

We find this also in our DFT calculations and it can easily be understood in the following way: At $\Theta = 30^\circ$ the interlayer coupling takes place at a k point directly between K and K', therefore inheriting the exact amount of spin-splitting from K and K' just with a different sign. In a similar fashion we can establish the rules

$$\Phi(0^\circ) \overset{(4.74)}{=} -\Phi(-0^\circ) \qquad \to \Phi(0^\circ) = 0 + n \cdot 180^\circ \tag{4.82}$$
$$\Phi(30^\circ) \overset{(4.74)}{=} -\Phi(-30^\circ) \overset{(4.71)}{=} -\Phi(30^\circ) \to \Phi(30^\circ) = 0 + m \cdot 180^\circ. \tag{4.83}$$

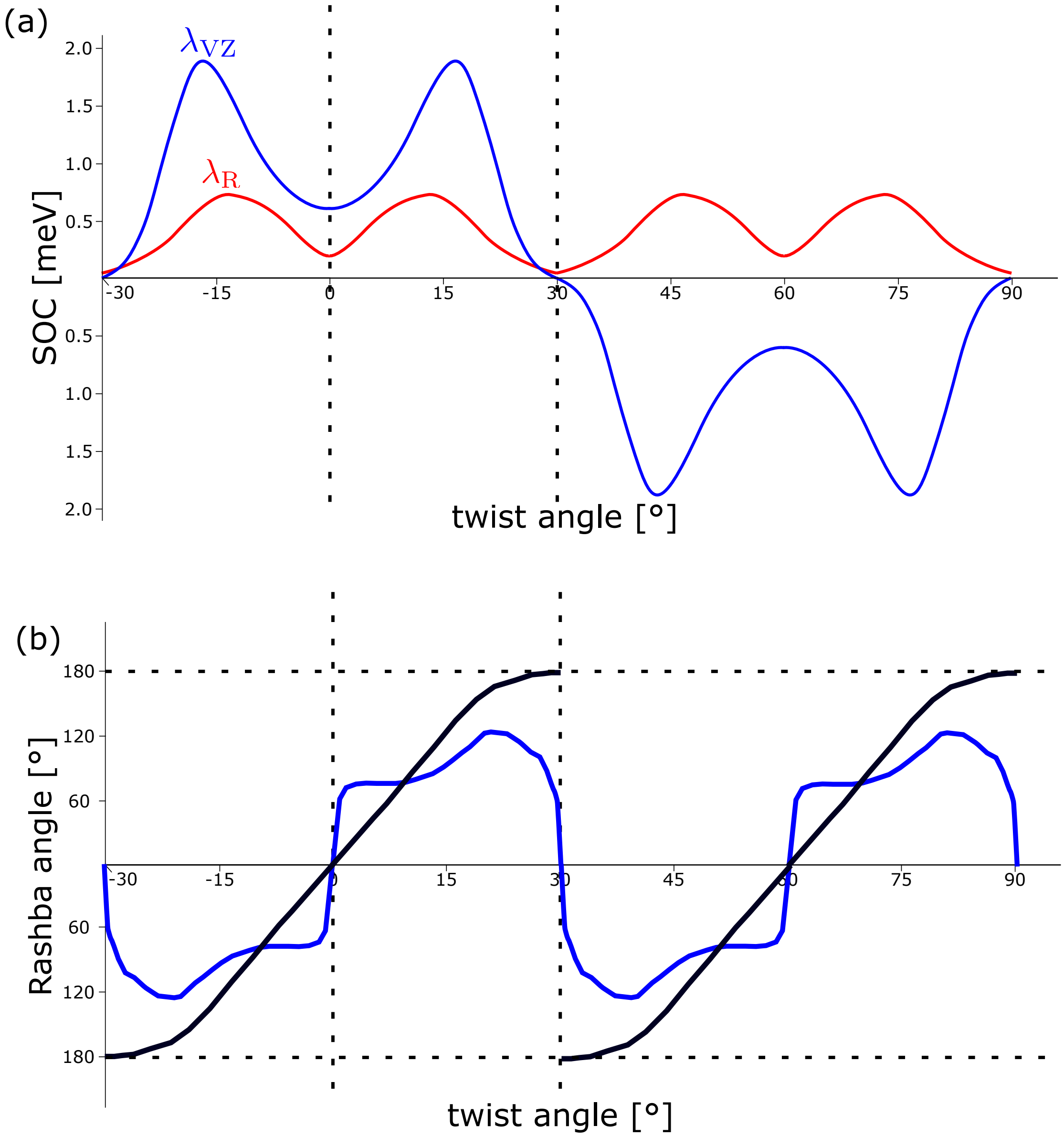

Figure 4.6: The twist-angle dependent SOC parameters of graphene/MoS_2 heterostructures from Ref. [19] expanded beyond the initial (irreducible) range $0° \leq \Theta \leq 30°$ using the symmetry relations. (a) shows valley-Zeeman SOC λ_{VZ} (blue) and Rashba SOC λ_R (red). (b) shows Rashba angle Φ from two different tight binding approaches: Ref. [19] (blue) and Ref. [21] (black). The vertical dotted line marks the initial twist-angle range. The horizontal lines in (b) mark the $\Phi = -180°$ and $\Phi = 180°$ values, which constitute the same physical situation as Φ is defined only modulo 2π.

with $n, m \in \mathbb{Z}$. This means that there are two separate zero points where Φ can be either 0° or 180°, both entailing an exclusively tangential in-plane spin texture, i.e. for all $l, k \in \mathbb{Z}$ it holds:

$$\begin{aligned} \Phi(l \cdot 60^\circ) = \Phi(0^\circ) = \Phi(60^\circ) = \ldots &= \begin{cases} 0^\circ \\ 180^\circ \end{cases} \\ \Phi(30^\circ + k \cdot 60^\circ) = \Phi(-30^\circ) = \Phi(30^\circ) = \ldots &= \begin{cases} 0^\circ \\ 180^\circ \end{cases} . \end{aligned} \tag{4.84}$$

The reason for the possibility of $\Phi = 180^\circ$ is that Φ is defined only modulo 2π. The symmetry enforced zero points (or 180° points) of Φ are also witnessed in DFT calculations [163, 67, 64]. They can alternatively be derived from the reflection symmetries converting $(x, y, z) \to (-x, y, z)$ and $(x, y, z) \to (x, -y, z)$ at $\Theta = 0^\circ$ and $\Theta = 30^\circ$, respectively [19]. Using all the above symmetry rules, it is sufficient to discuss the twist-angle range $0^\circ \leq \Theta \leq 30^\circ$, as the SOC parameters for all other twist angles can be deduced using these symmetry rules. Fig. 4.6 illustrates this by expanding the SOC parameters of the usual $0^\circ \leq \Theta \leq 30^\circ$ beyond that range.

4.5 Combating unwanted strain effects in DFT

In the previous section we mentioned Refs. [19, 20, 21], where a tight binding model is used to describe the influence of the twist angle on the proximity SOC and establish a quantitative twist-angle dependency of the SOC parameters. In order to check if this notion can be validated by an ab-initio perspective and to obtain more realistic values going beyond the (tight binding) model approach, we use density functional theory (DFT). The basic formalism and idea behind DFT were already layed out in Sec. 4.2. Contrary to the tight binding approach, the heterostructures used for DFT calculations need to be commensurate. How to generate commensurate heterostructure supercells with specific twist angles was discussed in Sec. 4.1. We reiterate that such commensurate supercells always involve strain in one or multiple layers. If we want to emulate heterostructures with specific commensurate structures (as they appear in 'bottom-up' sample fabrication, e.g. CVD or MBE), this specific combination of strain and twist angle (e.g. 30° supercell in Chap. 6) is a natural part of the situation that we aim to describe. However, as most of the experimental setups involve incommensurate structures without significant strain due to 'top-down' fabrication (e.g. exfoliation), we mostly view the strain as an artifact introduced by DFT. This means in order to establish a relation that links twist angle to the SOC parameters, we need to combat the effects of the strain — specifically the effects on the SOC. Since the effects of different parameters are entangled, we need to consider the interconnected effects of several parameters (see Fig. 4.7): twist angle, strain, relaxation, interlayer distance, external electric field and lateral shift between the layers. Within the DFT approach, there are several choices and control knobs that need to be taken into account. In this section, we present our specific approach of implementing twisted heterostructures in DFT and the problems and choices of parameters that come with it and compare it to the literature (see Tab. 4.4). Although our argumentation assumes graphene-based heterostructures, most of it can be reformulated to fit general heterostructures.

4.5.1 The effects of strain

Every heterostructure supercell comes not only with a certain twist angle, but also with a certain strain. This means the parameters twist angle and strain are linked, i.e. we only have one degree of freedom (the choice of the supercell) instead of two degrees of freedom (twist angle and strain). For a few cases, there are two supercells with the same twist angle and different strains, or the same strain and different twist angles. These supercells can help us in gauging the effectivity of our approach. But as they are the exception, we mostly cannot tune the twist angle without simultaneously changing the strain and vice versa. This shows how important it is to know the effects of the strain on the properties of the heterostructure, especially on the proximity SOC. It is here that a first choice needs to be made. Namely, how should the strain be distributed? We could either put tensile strain on the slightly smaller supercell or compressive strain on the slightly larger supercell or distribute the strain equally among both layers. In our approach, we choose to always put the strain on the graphene layer, as its properties under strain are rather well known and it is resilient to strain [79, 80, 144, 145, 146]. In the following, we identify four main effects of the strain on graphene, although we cannot fully exclude that there are other effects of the strain.

Change of Dirac cone Fermi velocity

The first effect is the change of the graphene band structure induced by the strain. As the applied strain is biaxial, there is no change in crystal symmetries and therefore the only relevant effect is an effective scaling of the Fermi velocity (slope) of the Dirac cone [80, 144]. This can be easily understood within the tight binding model of graphene. The hopping term t scales with the distance between the carbon atoms and therefore with the applied strain; for tensile strain the atoms move apart leading to decreasing t, while for compressive strain they move closer leading to increasing t. Since the Fermi velocity is directly linked to this hopping parameter $v_F = \frac{\sqrt{3}}{2\hbar} a \cdot t$ [162], it will scale accordingly. Although there is the additional effect due to the change of the lattice constant a, this effect is overshadowed by the change of t, resulting in an approximately linear dependency of the Fermi velocity on the strain [80]. Since the rescaling of the Fermi velocity itself is not influencing the SOC, we do not need any measures to counteract this effect. As the SOC in graphene can also be described as hoppings, it is reasonable to assume that the SOC might scale with the strain in a similar way. However, none of our data supports this hypothesis. We assume that, as the electron follows a virtual tunneling process through the substrate layer, it does not scale in the same fashion.

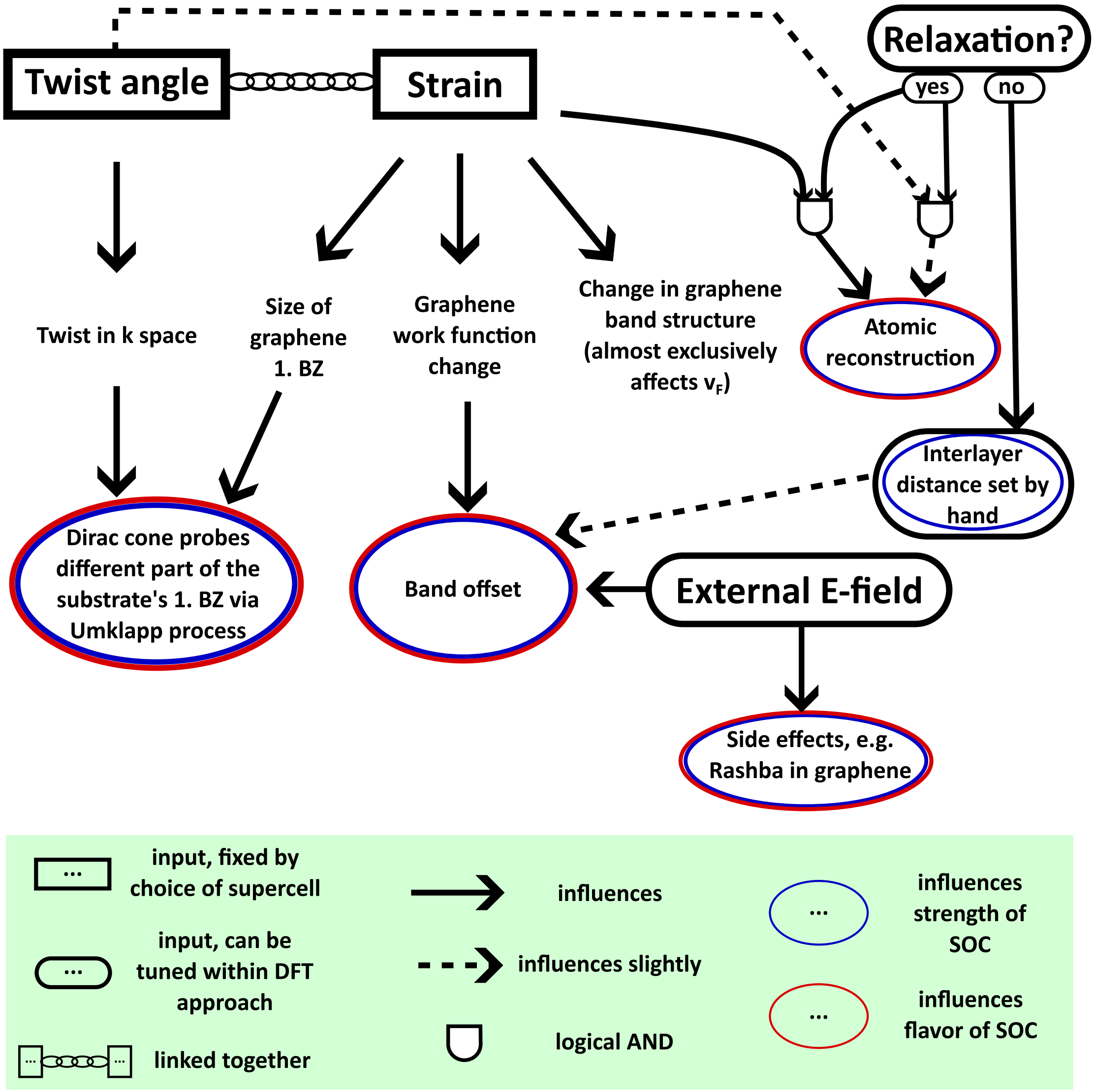

Figure 4.7: Overview of all different parameters and how they affect the proximity SOC of graphene.

k-space probed by Umklapp process

The second effect of the strain does not concern the graphene itself, but rather the interaction between the two layers of the heterostructure. In Sec. 4.4 we describe how the twist angle between the layers will influence what regions of the substrate (e.g. TMDC) 1st BZ are probed by the Dirac cone — the k point, which the Dirac interacts with, will describe a certain 'path of interaction' through the 1st BZ as the twist angle is tuned (see Fig. 4.5). Straining graphene changes the size of graphene's 1st BZ, which will in turn shift said path. Allowing for a range of strains will accordingly open the path to an annular sector (see Fig. 4.5(d)). Contrary to the other effects, this effect is both inevitable and affects the SOC. It cannot be avoided by putting the strain on the other layer, as it only depends on the ratio of lattice constants of the layers $\frac{a_{\text{layer 1}}}{a_{\text{layer 2}}}$. Counteracting it might be possible by estimating corrections based on the tight binding models of Ref. [19, 20]. However, we do not follow this path, as it would rely heavily on details of the specific tight binding approach.

Rippling

The third effect of the strain in graphene is the rippling of graphene for strong compressive strains. It is a very common (see Tab. 4.4) procedure to calculate atomic forces and allow for atomic relaxation within the DFT unit cell, before the actual self consistent calculations. During such a relaxation process, graphene supercells with large compressive strains will form ripples in order to minimize the forces on the atoms. For large strains (up to 10%), these ripples can be as big as 2 Å (for example for a supercell with $\epsilon = -6.64\%$ strain, see Fig. 4.8(b)). But already for smaller strains (up to 3%), a significant rippling of about 0.3 Å can still be observed (for example for a supercell with $\epsilon = -2.9\%$ strain, see Fig. 4.8(a)). In Ref. [163], we find the main consequence of these ripples in graphene/TMDC heterostructures to be an increase in the staggered potential Δ and the Kane-Mele SOC λ_{KM}, which are the two fitting parameters, which are close to zero for the unrelaxed structures. The emergence of these two parameters is reasonable, as the rippling can plausibly induce both an asymmetrical potential on the A/B-sublattices (emergence of Δ) and a σ-π-mixing, i.e. mixing of the sp^2 hybridized in-plane states and the p_z-orbitals dominated out-of-plane states (emergence of λ_{KM}).

Graphene work function and band offsets

The fourth effect we attribute to the strain is a change in band offsets, i.e. the energetic shift between the band structures of the two layers. Assuming an otherwise rigid band structure of the two layers, it is determined by the difference in energy between some fix points within the two band structures. For example, the band offset between graphene and a TMDC substrate can be measured as the difference between the energy of the Dirac cone and the energy of the valence band edge $\Delta E = E_D - E_{\text{TMDC,val}}$. The work function of graphene changes approximately linear [80, 165] with a small quadratic

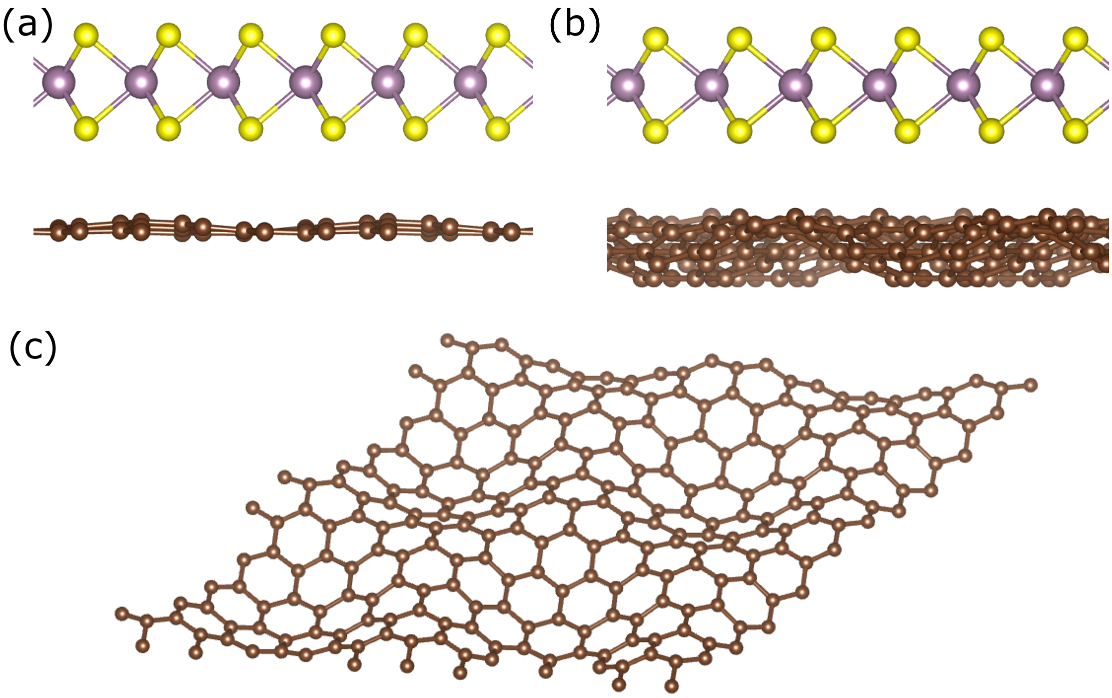

Figure 4.8: Rippling in compressively strained graphene: (a)-(b) Side view of relaxed graphene/MoS_2 heterostructure with (a) medium strain ($\epsilon = -2.9\%$) and (b) large strain ($\epsilon = -6.64\%$). (c) Angled view of graphene layer from (b) without MoS_2.

Table 4.3: Extrapolated zero-strain band offsets $\Delta E^0_{\text{material,F}}$ and deformation potential α_{material} for graphene-based heterostructures involving all investigated materials. The fix points F are: valence band edge for the semiconducting TMDCs, conduction band edge of the surface state remnant for the topological insulators (TIs), the upper band edge of the states (at Γ) near the Fermi level for $NbSe_2$.

	MoS_2	WS_2	$MoSe_2$	WSe_2	Bi_2Te_3	Bi_2Se_3	$NbSe_2$
$\Delta E^0_{\text{material,F}}$[meV]	1365	1027	680	290	396	671	-109
α_{material} [meV/%]	-74	-79	-78	-89	-52	-50	-35

correction [145] (see Fig. 4.9(a)). For compressive strain, the work function shrinks, while for tensile strain it grows. The slope of this change in work function as determined by Ref. [145] ($\alpha_{\text{WF,ref}} \approx 86\frac{\text{meV}}{\%}$), nicely aligns with the one we find ($\alpha_{\text{WF}} \approx 89\frac{\text{meV}}{\%}$) from fitting the data of our DFT calculations in Fig. 4.9(a). As the band offsets are in part determined by the work functions of the two layers, this approximately linear change in work function translates to an approximately linear change in band offsets for graphene-based heterostructures. We witness this result in all of our calculations. When plotting strain against the band offsets for an array of different heterostructure supercells of the same material combination, we see a clear correlation (see Fig. 4.9(b)-(d)). Fitting it with a linear fit gives us two values: the estimated zero-strain band offset between the graphene Dirac cone and some fixpoint F in the substrate band structure $\Delta E^0_{\text{material,F}}$ and the deformation potential α_{material}. Both depend on the material that graphene is proximitized with (substrate), while $\Delta E^0_{\text{material,F}}$ additionally depends on our choice of the fixpoint F (e.g. valence band edge) in the substrate band structure. We list a table of the offsets and deformation potentials in Tab. 4.3. We see that, while the work function change fully translates into a band offset change for graphene/WSe_2 heterostructures ($\alpha_{\text{WF}} \approx \alpha_{\text{WSe}_2}$), for most heterostructures α_{WF} constitutes an upper limit to the band offset change. As the vicinity of the Dirac cone to the substrate's bands (and therefore also the band offset) is crucial for the acquired proximity SOC, there is the need for a method, which can eliminate this error. Luckily, in DFT we can easily correct for these strain-induced changes in band offset by applying an electric field perpendicular to the heterostructure, as it will be presented in the next subsection.

4.5.2 Control knobs

In the following, we present certain control knobs within DFT that can be used in order to combat the problems induced by the strain. Also, potential problems that might go along with these solutions are discussed.

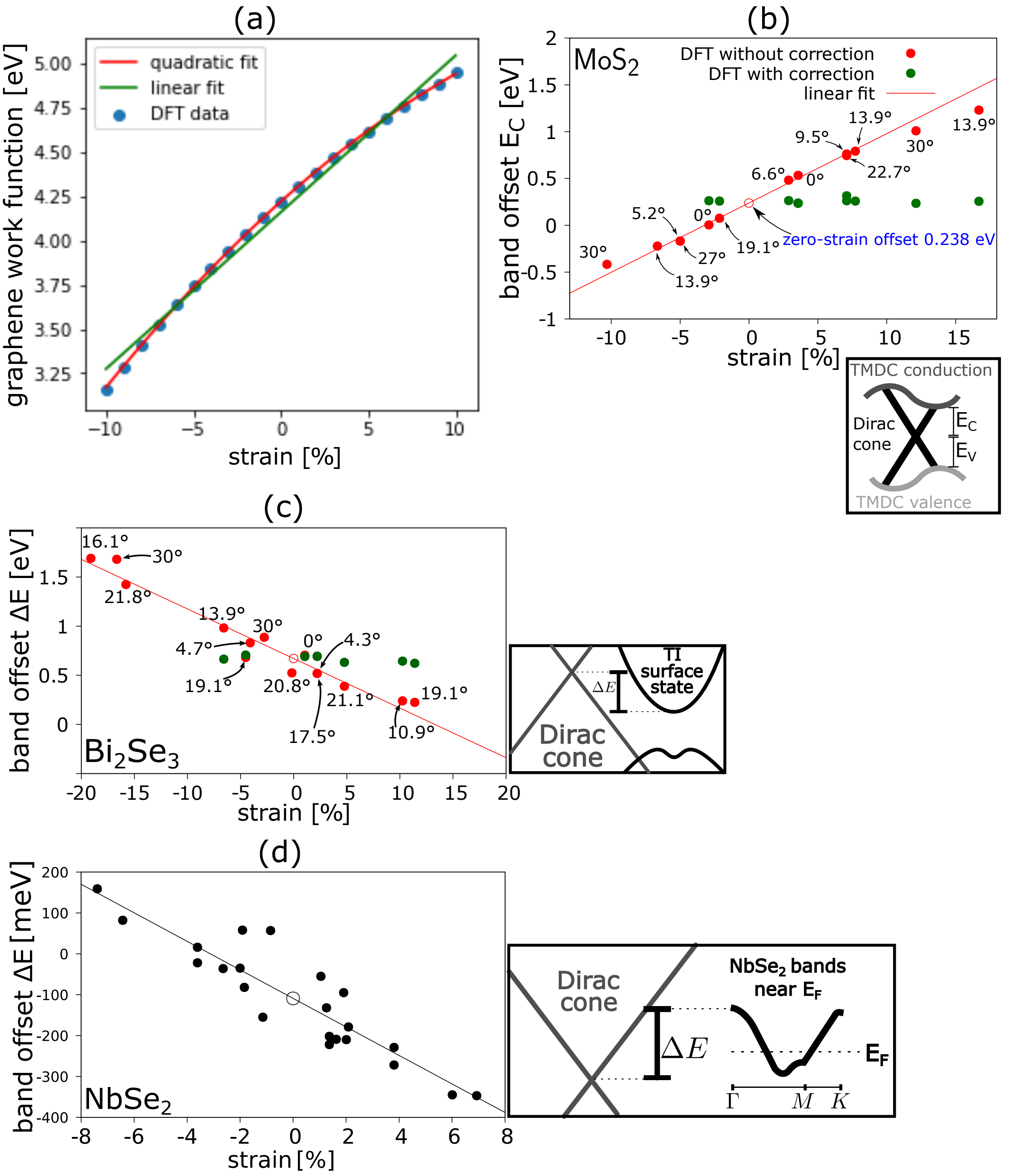

Figure 4.9: (a) Work function of graphene for different strains (blue dots represent DFT calculations, green curve is the linear fit and red curve is the quadratic fit). (b)-(d) Strain-dependent band offsets for different graphene-based heterostructures (dots represent DFT data, lines are linear fits): (b) graphene/MoS$_2$, (c) graphene/Bi$_2$Se$_3$, (d) graphene/NbSe$_2$. Adjacent pictograms illustrate the way the band offsets are measured. In (b) the slope of the curve is positive, because the band offsets are measured as positive, if the Dirac cone is positioned under the conduction band edge. In (b) and (c) we additionally indicate the twist angles for each data point in order to demonstrate that the twist angle has no significant influence on the offsets. Also in (b) and (c) we additionally show the band offsets after correction through the electric field in green.

External electric field

One of the problems induced by the strain in graphene is the change in band offsets due to the strain-dependent work function of graphene. These band offsets can be adjusted using an external electric field perpendicular to the 2D plane of the heterostructure (z-direction). This electric field can be realized in DFT by adding an artificial sawtooth potential to the exchange-correlation potential. The potential rises along the z-direction with a constant slope equal to the strength of the electric field over the heterostructure and rapidly drops in the vacuum region. As long as it is ensured that the overlap between the heterostructure's wave function and the region of the dropping potential is minimized, this method can be used to effectively introduce an electric field. The main effect of the electric field is the adjustment of the band offsets — the two layers of the heterostructure are set to different potentials and therefore we can correct the band offsets between the layers by tinkering with the electric field. However, the side effect of this approach is that the layers themselves are also subject to the electric field and therefore their electronic structures are altered as well. Thin layers like graphene exhibit a very small effect, e.g. even the strongest fields used in our calculations would produce a Rashba SOC of only $\lambda_\mathrm{R} = 60\mu\mathrm{eV}$ [166, 31]. Thick layers, on the other hand, can feel more drastic changes, e.g. the surface states of 8 quintuple layers of the TI $\mathrm{Bi_2Te_3}$ will split by 6.5 meV per $1\frac{\mathrm{mV}}{\mathrm{nm}}$ [167]. However, as we are mainly interested in proximity effects and these are short ranged, the relevant parts of the substrate are the ones close to the graphene layer. For the example of $\mathrm{Bi_2Te_3}$, this means: since the graphene can only interact with the nearby surface state anyways, the splitting between the surface state will not be too relevant for the proximity SOC. Keeping the potential side effects in mind, we can nevertheless use this method to ensure a consistent band offset for all heterostructure supercells. In Fig. 4.9(b) and (c), we additionally show the band offsets after the corrections with the electric field, demonstrating roughly equal band offsets throughout all twist angles.

Atomic relaxation

The heterostructure supercells constructed in Sec. 4.1 are idealized structures. This means, although we used sensible structural parameters taken either from other DFT calculations or experimental studies, there can be forces on the atoms due to induced strain or the influence of the layers on each other. In order to minimize these forces, one can perform relaxation calculations within DFT. In these calculations forces on the atoms are calculated and small changes in the atomic positions are made accordingly. Then, forces are calculated again and the process repeats until all the forces on the atoms are below a certain threshold. This procedure is very commonly used (see Tab. 4.4) and can lead to more realistic results. However, as discussed prior, excessive strain in graphene will lead to massive rippling of the graphene. Assuming zero strain, allowing for a relaxation of the heterostructure supercell will incorporate subtle effects of the twist angle on the electronic structure through atomic reconstruction (this can in principle also affect the SOC, but probably to a rather small degree [163, 67]). However, in

reference	Naimer [163]	PEF [105]	Naimer [66]	Zollner [67]	Gmitra [14]
code	QE	QE&W2k	QE	QE	QE
materials	MoS_2, $MoSe_2$, WS_2, WSe_2	MoS_2, WS_2	$NbSe_2$	MoS_2, $MoSe_2$, WS_2, WSe_2	MoS_2, $MoSe_2$, WS_2, WSe_2, $MoTe_2$, WTe_2
N_{twist}	8	2	13	11	1
relaxation	sample	yes	sample	yes	yes
interlayer distance	3.3Å	-	3.3Å	-	-
max. strain $\lvert\epsilon_{\max}\rvert$	10%	3.11%	5%	2.5%	7.8%
strain distribution	on GR	on GR	on GR	on GR	on both
E-field corrections	yes	no	no	no	no
lateral shift	yes	yes	no	no	yes
reference	Hou [168]	Lee [64]	Pezo [169]	Di Felice [170]	Wang [143]
code	VASP	VASP	SIESTA	Fireball	VASP
materials	PdS_2, PtS_2	WSe_2	WSe_2, $MoTe_2$	MoS_2	MoS_2
N_{twist}	4	8	7	4	4
relaxation	yes	yes	yes	yes	yes
interlayer distance	-	-	-	-	-
max. strain	5.2%	2%	3.55%	5.9%	5.4%
strain distribution	on GR	on TMDC	on TMDC	on both	on both
E-field corrections	no	no	no	no	no
lateral shift	no	no	no	no	no
reference	Naimer [44]	Song [41]	Zollner [171]	Jin [172]	Popov [173]
code	QE	VASP	QE	VASP	VASP
materials	Bi_2Se_3, Bi_2Te_3	Bi_2Se_3	Bi_2Se_3, Bi_2Te_2Se	Sb_2Te_3	Bi_2Se_3
N_{twist}	9	2	1	1	1
relaxation	no	yes	no	yes	no
interlayer distance	3.5Å	-	3.5Å	-	2.2Å-3Å
max. strain	10%	3%	1.06%	1%	2.3%
strain distribution	on GR	on GR	on GR	on GR	on TI
E-field corrections	yes	no	no	no	no
lateral shift	yes	yes	no	yes	no

Table 4.4: Comparison of different DFT studies on graphene-based heterostructures and their approaches. The first author of the paper is listed under 'reference'. We list the employed DFT codes (QUANTUM ESPRESSO (QE) [147], Wien2k (W2k) [174], Vienna ab initio simulation package (VASP) [175], Spanish Initiative for Electronic Simulations with Thousands of Atoms (SIESTA) [176] or Fireball [177]). Furthermore, we list the materials they use as substrates for graphene, the number of investigated twist angles N_{twist}, whether the authors choose to relax the structure (if not, what was set as interlayer distance), how the strain was distributed among the layers, the maximal strain used $|\epsilon_{\max}|$ (if the strain was distributed between the layers, we nevertheless list the total strain, as if the strain was only put on one layer), whether band offsets were corrected by an electric field corrections and whether lateral shifts were considered. The entry 'sample' for relaxations means that although the main results come from unrelaxed structures, relaxation calculations were performed and evaluated for a few samples.

situations including rippled graphene, although there might be atomic reconstruction due to the neighbouring layer, this effect is often overshadowed by the consequences of the rippling. Consequently, for large strains in graphene, it is more representative of the true twist-angle physics to skip the relaxation process in order to eliminate this pathway of strain-related error, although this means simultaneously also eliminating the legitimate pathways of twist-angle physics through the means of atomic reconstruction. In Fig. 4.7 this is indicated by the fact that the effect of 'strain' on 'atomic reconstruction' is depicted as solid arrow, while the effect of 'twist angle' on 'atomic reconstruction' is only depicted as a dotted arrow.

Interlayer distance

One structural parameter which can be determined during the relaxation process is the (average) interlayer distance, as the layers can move freely towards each other or away form each other. Skipping the relaxation process prohibits this natural way of determining an (average) interlayer distance. Instead, it is usually set using values from literature or estimated from relaxation calculations on exemplary supercells. However, the main effect of the interlayer distance is its influence on the general strength of the SOC, while it hardly effects the weight of the different SOC flavors. The only route by which the SOC flavour can be tuned is via the slight influence of the interlayer distance on the band offsets — changing the interlayer distance will change the built-in electric field of the heterostructure and hence the band offsets, which in turn can influence the SOC. In experiment, the interlayer distance can be tuned by subjecting the heterostructure to hydrostatic pressure [136].

Lateral shift

As a final control knob, we want to list the lateral shift between the layers. By shifting the two layers laterally with respect to each other, different microscopic atomic registries can be realized. In graphene-based structures the nomenclature usually refers to the position of nearby atoms with respect to the graphene ('Top', 'Hollow' or 'Bridge' position). The heterostructure supercells we use, however, are usually large enough that many individual local stacking orders occur. A lateral shift then causes all of these local stacking orders to change, which on average does not lead to any significant change of the SOC parameters [13, 163]. However, for very small heterostructures (as in Sec. 6.4 or Refs. [44, 41]) or for homobilayers [164], the effects of lateral shifts on the proximity SOC can be highly relevant. Examples for different lateral shifts and their effects on the graphene Dirac cone are given in Fig. 4.10.

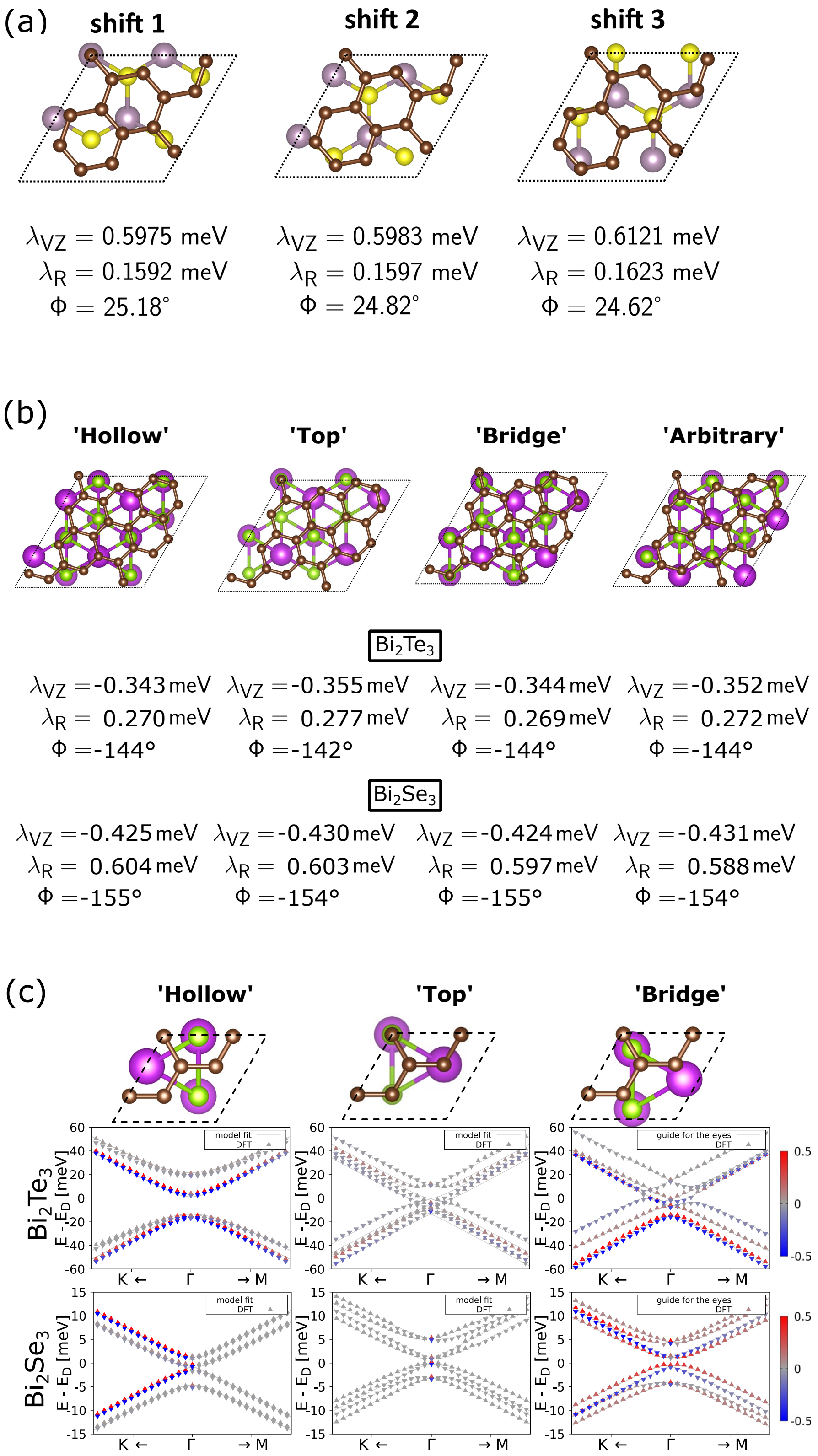

Figure 4.10: Effects of different shiftings on the graphene Dirac cone: (a) graphene/MoS_2 19.1° supercell, (b) graphene/TI 13.9° supercell, (c) graphene/TI 30° supercell. For (a) and (b) the supercells are big enough for averaging, therefore the small changes to the Dirac cone are given in the form of fitting parameters, whereas for (c) the changes are clearly visible in the Dirac cone.

4.6 Charge-to-spin conversion efficiencies from linear response theory

In Chap. 2, we introduced the REE and the UREE as possible mechanisms for charge-spin interconversion, which can be used in spintronics. In order to give quantified estimates for the efficiencies of such charge-to-spin (or spin-to-charge) processes, we utilize the Kubo formula [178, 179] in the Smrcka-Streda decomposition [63, 180, 181]. We first give a short derivation of the formulas in Subsec. 4.6.1, followed by the application to the Dirac cone model Hamiltonian in Subsec. 4.6.2. Then, in Subsec. 4.6.3, we describe the dependence of the efficiencies on the chosen Fermi level and in Subsec. 4.6.4 we discuss the scaling of the charge-to-spin conversion (CSC) efficiencies with different (SOC) parameters.

4.6.1 Derivation

The Kubo formula describes the linear response of the system in an observable (A, with operator $\hat{A}$), when a perturbation, a time-dependent external change in the Hamiltonian ($\delta\hat{H} = \hat{B} \cdot f(t)$), is added. The change in A can be expressed as

$$\delta A = \frac{-i}{\hbar}\int_{t_0}^{t} dt' \Big\langle \big[\hat{A}(t), \delta\hat{H}\big] \Big\rangle = \frac{-i}{\hbar}\int_{t_0}^{t} dt' \Big\langle \big[\hat{A}(t), \hat{B}(t')\big] f(t') \Big\rangle, \tag{4.85}$$

where t_0 is the point in time, the perturbation takes action and $\langle\cdot\rangle$ is the equilibrium average with respect to the unperturbed Hamiltonian. The external change δH in the Hamiltonian consist of an operator $\hat{B}$ and $f(t)$. The former is needed to form the correlator between $\hat{A}$ and $\hat{B}$, which ends up as the susceptibility χ_{AB}. In the following we will omit the index B, because we always consider the response to an electric field in x-direction, and therefore use $\hat{B} = \hat{j}_x$. The second part ($f(t)$) contains the electric field E. In the setup we are using, we are interested in the spin response (A) of a system to an external electric field (B). However, using the Onsager relations, the CSC efficiencies we extract with this setup are the same as the spin-to-charge efficiencies.

In the Smrcka-Streda decomposition [63, 180, 181], the change in A can be expressed as $\delta A = \left[\chi_A^{\mathrm{I}} + \chi_A^{\mathrm{II}}\right] \cdot E$ in such a situation. Here E is the strength of the electric field and $\chi_A^{\mathrm{I/II}}$ are the susceptibilities given by

$$\chi_A^{\mathrm{I}} = \frac{\hbar}{2\pi}\int d\epsilon \frac{\partial f(\epsilon)}{\partial \epsilon} \mathrm{Re}\Big(Tr(\hat{A}\hat{G}^r\hat{B}(\hat{G}^r - \hat{G}^a))\Big), \tag{4.86}$$

$$\chi_A^{\mathrm{II}} = \frac{\hbar}{2\pi}\int d\epsilon f(\epsilon) \mathrm{Re}\Big(Tr(\hat{A}\hat{G}^r\hat{B}\frac{\partial \hat{G}^r}{\partial \epsilon} - \hat{A}\frac{\partial \hat{G}^r}{\partial \epsilon}\hat{B}\hat{G}^r)\Big). \tag{4.87}$$

Here, $f(\epsilon)$ is the Fermi-Dirac function, $\hat{A}$ and $\hat{B}$ are the operators corresponding to the observables A and B, respectively, and $\hat{G}^{r/a} = \lim_{\gamma\to\infty} \frac{1}{\epsilon - \hat{H} \pm i\gamma}$ is the retarded/advanced

Green's function of the system. We use a similar decomposition given by Bonbien et al. [181], dividing the terms into Fermi sea and Fermi surface terms:

$$\delta A = \left[\chi_A^{\mathrm{I}} + \chi_A^{\mathrm{II}}\right] \cdot E = \left[\chi_A^{\mathrm{surf}} + \chi_A^{\mathrm{sea}}\right] \cdot E \quad \text{with} \tag{4.88}$$

$$\chi_A^{\mathrm{surf}} = \frac{\hbar}{4\pi} \int d\epsilon \frac{\partial f(\epsilon)}{\partial \epsilon} \mathrm{Re}\Big(Tr(\hat{A}(\hat{G}^r - \hat{G}^a)\hat{B}(\hat{G}^r - \hat{G}^a))\Big) \tag{4.89}$$

$$\chi_A^{\mathrm{sea}} = \frac{\hbar}{2\pi} \int d\epsilon f(\epsilon) \mathrm{Re}\Big(Tr(\hat{A}(\hat{G}^r - \hat{G}^a)\hat{B}(\frac{\partial \hat{G}^r}{\partial \epsilon} + \frac{\partial \hat{G}^a}{\partial \epsilon}))\Big). \tag{4.90}$$

Further assuming a constant scattering (given by γ) in the weak disorder limit and using a Bloch basis for the Hamiltonian, we can rewrite the terms to be more practical for calculations (for details see App. B):

$$\chi_A^{\mathrm{surf}}(\mathbf{k}) = \frac{\hbar}{\pi} \sum_{n,m} \frac{\gamma^2 \mathrm{Re}\Big(\langle n\mathbf{k}| \hat{A} |m\mathbf{k}\rangle \langle m\mathbf{k}| \hat{B} |n\mathbf{k}\rangle\Big)}{\Big((\epsilon_F - \epsilon_{n\mathbf{k}})^2 + \gamma^2\Big)\Big((\epsilon_F - \epsilon_{m\mathbf{k}})^2 + \gamma^2\Big)} \tag{4.91}$$

$$\chi_A^{\mathrm{sea}}(\mathbf{k}) = \hbar \sum_{n,m} (f(\epsilon_{n\mathbf{k}}) - f(\epsilon_{m\mathbf{k}})) \frac{\mathrm{Im}\Big(\langle n\mathbf{k}| \hat{A} |m\mathbf{k}\rangle \langle m\mathbf{k}| \hat{B} |n\mathbf{k}\rangle\Big)}{(\epsilon_{n\mathbf{k}} - \epsilon_{m\mathbf{k}})^2}, \tag{4.92}$$

where $|n\mathbf{k}\rangle$ and $\epsilon_{n,\mathbf{k}}$ are the eigenstate and eigenenergy of the Hamiltonian $H(\mathbf{k})$ with band number n at a certain position $\mathbf{k}$ in k space, ϵ_F is the Fermi energy and γ is the broadening of the states by scattering. Notice, that χ_A^{sea} is now independent of γ as we have taken the limit $\gamma \rightarrow 0$. While the terms we derived here are the same as used in Refs. [181, 182, 65], Ref. [64] reintroduces γ to χ_A^{sea} as a broadening for the numerical calculations. χ_A^{surf} and χ_A^{sea} are called Fermi surface and Fermi sea term, respectively. This terminology comes from the fact that the states around the Fermi level (here $(\epsilon_F - \epsilon_{n/m})$ is minimal) constitute the main contribution to χ_A^{surf}, while χ_A^{sea} only includes occupied $(f(\epsilon_n) - f(\epsilon_m) \neq 0)$ states.

4.6.2 Application to the graphene Hamiltonian

The system we aim to describe is graphene with SOC, as described in Sec. 4.3 either by a full tight binding model or the low-energy model Hamiltonian. Since the only relevant physics in our system will come from the Dirac cone, we use the low-energy model Hamiltonian described in Eq. (4.43) as the starting point unperturbed Hamiltonian $\hat{H}$. Ref. [64] uses the full tight binding Hamiltonian (Eq. (4.42)) arriving at very similar results, underpinning our assumption that focusing on the Dirac cone is sufficient.

Since the Hamiltonian and therefore the eigenstates are $\mathbf{k}$-dependent, we have to integrate over the 1st BZ

$$\delta A = \int \frac{d^2\mathbf{k}}{4\pi^2} \left[\chi_A^{\mathrm{surf}}(\mathbf{k}) + \chi_A^{\mathrm{sea}}(\mathbf{k})\right] \cdot E \tag{4.93}$$

in order to obtain the total response of the system. In our case the integration takes place over two square grids covering the K and the K' point. It needs to be large enough to cover the Dirac cone for the highest used Fermi level and its grid needs to be dense enough to resolve all relevant physics. We use a 151×151 square grid with a side length of $\Delta k = 0.03\frac{1}{v_F\hbar} \approx 2.5 \cdot 10^{-3}\frac{2\pi}{a}$, sufficiently fulfilling the two conditions. In Fig. 4.11(b) we show how a smaller and less dense grid would entail less accurate results. While the more coarse grid density only results in slight noise, the too small size will lead to a breakdown of the results at high Fermi levels. This can simply be attributed to the fact that the outer band leaves the integration grid at higher Fermi levels. For computationally more demanding situations an adaptive integration region (e.g. a ring covering only the cut through the Dirac cone) could be applied in order to be computationally more efficient.

The next question is how the operators $\hat{A}$ and $\hat{B}$ are chosen. In our case we are only interested in the spin responses due to a charge current. Therefore, without loss of generality, we set our perturbation as an electric field in x direction, hence

$$\hat{B} = \hat{j}_x = -e\hat{v}_x = -e\frac{1}{\hbar}\frac{\partial H}{\partial k_x} = -ev_F\kappa\sigma_x. \tag{4.94}$$

And the relevant observables to measure are

$$\begin{aligned} \hat{A} &= \hat{s}_x = \frac{\hbar}{2}\sigma_x && (4.95)\\ \hat{A} &= \hat{s}_y = \frac{\hbar}{2}\sigma_y && (4.96)\\ \hat{A} &= \hat{B} = \hat{j}_x = -ev_F\kappa\sigma_x. && (4.97) \end{aligned}$$

Eq. (4.95) and Eq. (4.96) give us the collinear and perpendicular spin density responses, respectively. Eq. (4.97) is used to find the conductivity, which we use to define the normalized figures of merit

$$\begin{aligned} \alpha_{\mathrm{REE}} &= \frac{v_F e}{\hbar}\frac{\delta s_y}{\delta j_x} = \frac{v_F e}{\hbar}\frac{\delta s_y}{\sigma_{x,x}} && (4.98)\\ \alpha_{\mathrm{UREE}} &= \frac{v_F e}{\hbar}\frac{\delta s_x}{\delta j_x} = \frac{v_F e}{\hbar}\frac{\delta s_x}{\sigma_{x,x}}, && (4.99) \end{aligned}$$

which we use to quantify the Rashba-Edelstein effect (REE) and the unconventional REE (UREE), respectively. We will refer to α_{REE} and α_{UREE} as the REE and UREE efficiencies throughout the thesis.

4.6.3 Fermi energy dependence

Naturally, the efficiencies α_{REE} and α_{UREE} will depend on the Fermi energy E_F we set for the calculations. A typical Fermi level dependence is depicted in Fig. 4.11(a). It shows the following features, which are congruent with Refs. [64, 62, 67]:

- The (U)REE signal is antisymmetric with respect to the middle of the Dirac cone gap. We will therefore in the following describe the signal starting from the gap and moving (either up or down) in energy to $E_F \rightarrow \pm\infty$.
- Within the gap there is a residual signal.
- At the onset of the first band we usually see an initial peak of the signal, due to a certain flatness of this first band.
- After this initial peak, it follows a plateau that stretches until the Fermi energy hits the second band. In this plateau $\delta s_{x/y}$ and δj_x grow at the same rate, as both depend linearly on the k-radius at which the Fermi energy cuts the Dirac cone.
- As soon as both bands contribute to the signal, $\delta s_{x/y}$ will stay constant, since the additional contribution from the first and second band cancel out. Because δj_x continuous to increase, the (U)REE signal $\alpha_{\mathrm{(U)REE}}$ vanishes for $E_F \rightarrow \pm\infty$.

In order to assign a general (U)REE efficiency, independent of the Fermi level, to a system, one might follow different approaches:

- One could use the Fermi level as determined by the DFT calculations. However, this Fermi level can depend on details of the DFT calculation. Furthermore, the Fermi level can be tuned in experiment. Hence, we argue that this approach is the least sensible.
- As the Fermi level can be tuned in experiment, another option is to use the Fermi energy, which yields the maximal (U)REE signal $\alpha_{\mathrm{(U)REE}}$. However, with this approach, the height of the initial peak will prevail as the only relevant measure, ignoring the size of the plateau. Experimental realization of this peak (U)REE efficiency would require fine tuning of the Fermi level more precise than the meV range. Moreover, as Fig. 4.11(b) shows, the height of the peak depends heavily on the disorder parameter γ, further complicating the analysis in this approach.
- The last approach is averaging $\alpha_{\mathrm{(U)REE}}$ over a certain range of E_F. As long as this range is chosen in a sensible manner, covering the region where the (U)REE signal constitutes a relevant contribution, this approach presents the most reasonable solution.

We choose to use the last approach and average over a certain range of E_F throughout the entirety of the thesis. In Fig. 4.11 we compare the last two approaches, indicating them with 'max. REE' and 'avg. REE', respectively. If not mentioned otherwise, we use the range from $E_F = 0$ meV to $E_F = 12$ meV. Hence, if the Rashba angle is $\Phi = 0$, a negative REE efficiency is always expected. Similarly, for a positive Rashba angle $0 < \Phi < 180$ a positive UREE is expected.

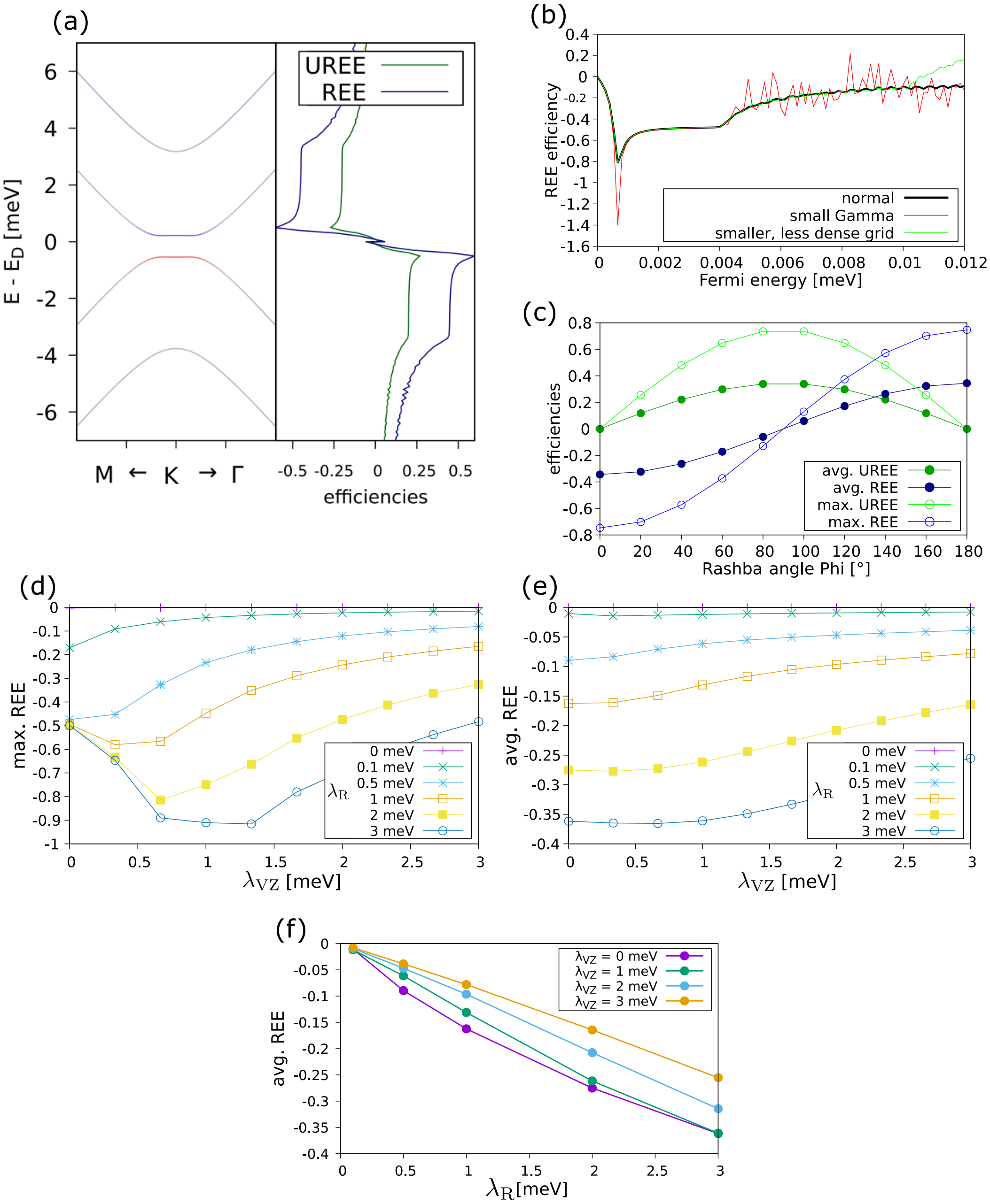

Figure 4.11: (a) Example of a graphene Dirac cone modelled by the model Hamiltonian Eq. (4.43) and the Fermi energy dependence of its subsequent CSC efficiencies for REE and UREE. The model Hamiltonian parameters are $\Phi = -24°$, $\Delta = -0.018$ meV, $\lambda_{\mathrm{KM}} = 0.067$ meV, $\lambda_{\mathrm{VZ}} = 0.366$ meV and $\lambda_{\mathrm{R}} = 1.726$ meV. (b) Fermi energy dependence of REE efficiency for different scenarios: standard parameters as given in the main text (black line), standard parameters with reduced $\gamma = 0.01$ meV (instead of $\gamma = 0.1$ meV) (red), standard parameters with smaller (side length reduced by 20%) and less dense (101×101 instead of 151×151) square grid used for integration (green line). The model Hamiltonian parameters are chosen as $\Phi = \Delta = \lambda_{\mathrm{KM}} = 0$, $\lambda_{\mathrm{VZ}} = 0.667$ meV and $\lambda_{\mathrm{R}} = 2$ meV. (c) (U)REE efficiencies (using maximal value or averaging over Fermi energies) for varying Φ. Other model Hamiltonian parameters are chosen as $\Delta = \lambda_{\mathrm{KM}} = 0$, $\lambda_{\mathrm{VZ}} = 1$ meV and $\lambda_{\mathrm{R}} = 3$ meV. (d) and (e) show the maximal (d) and Fermi-energy averaged (e) REE efficiency for increasing λ_{VZ} for different values of λ_{R}. (f) shows the averaged REE efficiencies for increasing λ_{R} for different values of λ_{VZ}. For (d)-(f) all other model Hamiltonian parameters are zero.

4.6.4 Scaling with different parameters

In the following, we will examine, how different parameters affect the CSC efficiencies. After briefly discussing the role of the averaged scattering rate γ, we explain how the actual SOC parameters λ_R (Rashba SOC), λ_VZ (valley-Zeeman SOC) and Φ (Rashba angle) translate into CSC efficiencies. We do not explicitly discuss the effects of the parameters λ_KM (Kane-Mele SOC) and Δ (staggered potential), as they are very close to zero for most of our fitting results from the DFT calculations.

The role of γ

Contrary to the Fermi sea term χ_A^sea, the Fermi surface term χ_A^surf inherently scales with the averaged scattering γ. However, the quantities we extract (spin accumulation $\delta s_{x/y}$ and induced charge density δj_x) both exclusively show contributions by Fermi surface terms. Therefore, in the CSC efficiencies $\alpha_\mathrm{(U)REE} = \frac{v_F e}{\hbar} \frac{\delta s_{x/y}}{\delta j_x}$ the γ dependencies of the two terms cancel out and hence $\alpha_\mathrm{(U)REE}$ does not scale with γ. Nevertheless, there are effects of the choice of γ that can be witnessed (see Fig. 4.11(b)). The first consequence of adding a finite broadening γ is the attenuation of the initial peak before the plateau in the Fermi-level dependence. Additionally, the broadening aids in smoothing the irregularities of the Fermi-energy dependence arising from using k space grids with finite density.

Rashba SOC λ_R

The Rashba SOC λ_R is responsible for the in-plane spin texture. Therefore, if we set $\lambda_\mathrm{R} = 0$, the CSC efficiencies automatically vanish. If we introduce finite λ_R to an otherwise unmodified Dirac cone (all other parameters zero), the valence and conduction bands both split into two bands with opposite spin textures, creating the plateaus in the Fermi-energy dependence. The (U)REE efficiencies scale roughly linear with λ_R, because the energy split of the bands (i.e. the length of the plateau) scales linear with λ_R, while the plateau's height stays constant. The tail towards higher Fermi energies, however, distorts this picture, especially for small λ_R. The scaling can be seen in Fig. 4.11(f) for different values of λ_VZ.

Valley-Zeeman SOC λ_VZ

Although the driving force of (U)REE is the Rashba SOC λ_R, the valley-Zeeman SOC λ_VZ also plays a role, albeit a more subtle one. On one hand, the addition of a finite λ_VZ reduces the in-plane spin expectation values of the Dirac cone bands by inducing out-of-plane ones, thereby reducing the (U)REE efficiencies. On the other hand, the λ_VZ can bring about more flat bands, creating the initial peak at the onset of the bands. Fig. 4.11(d) and (e) show this ambiguity. If only the maximum value of the (U)REE efficiencies is tracked (Fig. 4.11(d)), a certain amount of λ_VZ can be beneficial for the (U)REE. However, plotting the more relevant observable, namely (U)REE efficiencies averaged over a certain range of E_F (Fig. 4.11(e)), it is revealed that λ_{VZ} is detrimental to the (U)REE.

Rashba angle Φ

The effect of the Rashba angle is rather simple. Assuming all other parameters to be fixed at any value, increasing the Rashba angle from $\Phi = 0°$ to $\Phi = 360°$ simply rotates the in-plane spin texture once. In this fashion, one can alternate between REE and UREE, without impacting the total magnitude $\alpha_{\mathrm{tot}} = \sqrt{\alpha_{\mathrm{REE}}^2 + \alpha_{\mathrm{UREE}}^2}$. As (according to our definition) we have the case of pure REE for $\Phi = 0$, we can write the CSC efficiencies [68] as

$$\alpha_{\mathrm{REE}} = \mp\alpha_{\mathrm{tot}} \cos(\Phi) \tag{4.100}$$

$$\alpha_{\mathrm{UREE}} = \pm\alpha_{\mathrm{tot}} \sin(\Phi), \tag{4.101}$$

where the ± indicates, whether the valence ($E_F < 0$) or conduction bands ($E_F > 0$) are examined. Fig. 4.11(c) shows this simple sine-cosine behaviour.

5 Twist-angle dependent proximity spin-orbit coupling in heterostructures of graphene and semiconducting TMDCs

The most frequently employed materials for inducing spin-orbit coupling (SOC) in graphene are certainly transition-metal dichalcogenides (TMDCs). There are plenty of theoretical works using both tight binding models [19, 20, 21, 183, 184] and DFT [163, 13, 14, 169, 67, 64] in order to investigate the proximity SOC in such systems. Experimental studies confirm many of the proposed properties: The general notion of enhanced graphene SOC in graphene/TMDC heterostructures has been thoroughly confirmed [185, 40, 186, 187, 188, 51, 189, 190, 191, 54, 136, 192, 137, 193, 194]. Beyond that, the different proposed applications layed out in Chap. 2 have been witnessed in heterostructures of graphene and TMDCs. This includes giant spin-relaxation anisotropy [51, 49, 50], the spin field-effect transistor proposal [57, 56], and conventional and unconventional charge-to-spin conversion (CSC) [72, 193, 194, 137]. However, there are only few experiments explicitly specifying the twist angle [137]. While tight binding calculations can easily incorporate the twist angle in a continuous way, in DFT studies a set of commensurate heterostructure supercells needs to be constructed. Although there are a few references using this approach [143, 168, 170], it is only recently that there has been an effort to systematically use this procedure in order to extract SOC parameters depending on the twist angle [163, 67, 169, 64].

Most studies focus on semiconducting TMDCs (e.g. WSe_2). These materials are especially relevant, since the graphene Dirac cone will reside within the band gap of the semiconducting TMDC, as demonstrated by many studies (e.g. [14, 163, 67, 170, 143]). This does not only guarantee that the Dirac cone is clearly visible and that its nature is preserved and not distorted by excessive hybridization. It also provides easy access for studying the effects of proximity SOC on transport through the graphene. As heterostructures of graphene and semiconducting TMDCs additionally provide an excellent platform for studying optical phenomena, there are plenty of studies exploring this side of their nature [105, 101, 195, 104], further providing us with a large expertise to draw from.

This chapter is based on Ref. [163] and is structured as follows. First, in Sec. 5.1, we introduce the twisted supercells, which were used. After this, we discuss the band structures of the different twisted supercells and their features as calculated by DFT in Sec. 5.2. In Sec. 5.3 the extracted SOC parameters and especially their twist-angle dependences are presented. The subsequent CSC efficiencies are shown in Sec. 5.4.

5.1 Twisted supercells

In this chapter we discuss heterostructures of graphene and the semiconducting TMDCs WSe_2, WS_2, $MoSe_2$ and MoS_2. The structures of the separate graphene and TMDC monolayers were already shown in Fig. 3.1 and Fig. 3.2, respectively. Their structural parameters are listed in Tab. 5.1. In order to evaluate the twist-angle dependence of the proximity SOC of the heterostructure within DFT, we need to construct an array of different heterostructure supercells with different twist angles. In Sec. 4.1, we discuss in detail, how such supercells can be generated. In this scheme each heterostructure supercell is defined by two pairs of integers for the two layers of the heterostructure ((n, m) for graphene and (n', m') for TMDC). The lattice vectors of a supercell defined by the pair of integers (n, m) are linear combinations of that layers primitive lattice vectors $\mathbf{a}_1$ and $\mathbf{a}_2$, such that:

Table 5.1: Unstrained geometries of the primitive unit cells of graphene and the four selected semiconducting TMDCs, as determined by relaxation calculations in Ref. [88]. Note that in our calculations, the structure of the TMDCs stay unchanged, while the graphene layers are strained by a margin ϵ listed in Tab. 5.2 to ensure commensurability in the supercell setup.

	Graphene	MoS_2	WS_2	$MoSe_2$	WSe_2
a[Å]	2.46	3.185	3.18	3.319	3.319
d_{XX}[Å]	-	3.138	3.145	3.357	3.364

$$\mathbf{a}^{S,1}_{(n,m)} = n \cdot \mathbf{a}_1 + m \cdot \mathbf{a}_2 \tag{5.1}$$

$$\mathbf{a}^{S,2}_{(n,m)} = -m \cdot \mathbf{a}_1 + (n + m) \cdot \mathbf{a}_2. \tag{5.2}$$

As discussed in Sec. 4.1, we can assign a twist angle Θ to the combined heterostructure:

$$\Theta = \Theta_{(n,m)} - \Theta_{(n',m')} = \arctan\left(\frac{\sqrt{3}m}{2n + m}\right) - \arctan\left(\frac{\sqrt{3}m'}{2n' + m'}\right). \tag{5.3}$$

Note that this notation differs by the one in Eq. (4.29) by a minus sign. The sizes of the k-grids, employed in the DFT calculations are given in Tab. 4.2. In Subsec. 4.4.4, we argue that due to the symmetries of the systems, it is sufficient to use supercells within a range of $\Theta = 0°$ to $\Theta = 30°$ (see Fig. 4.6), since the properties of all other twist angles can be deduced from the symmetry relations given in Eq. (4.69) to Eq. (4.74).

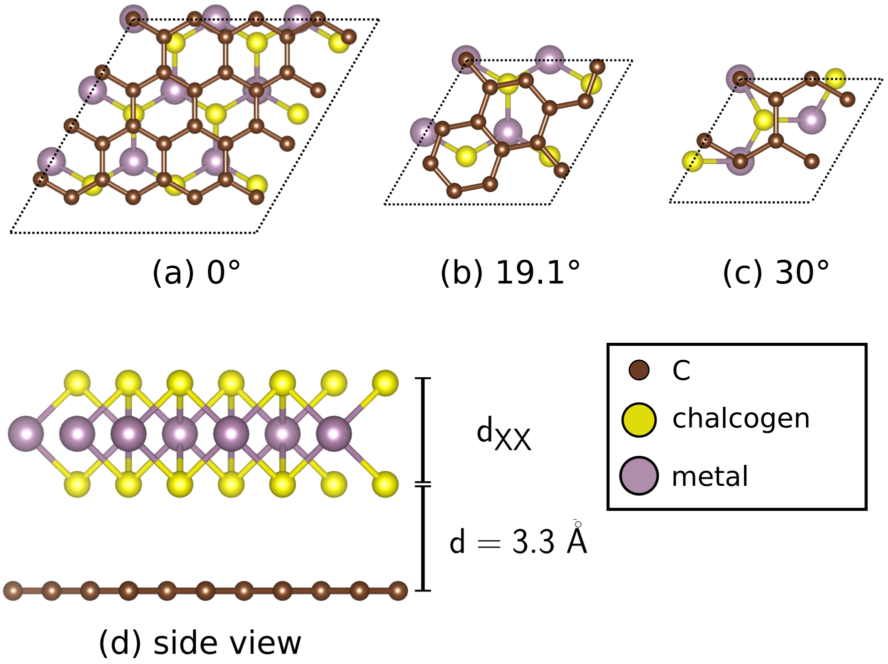

Figure 5.1: (a)-(c) Bottom view of three graphene/TMDC heterostructure supercells with the twist angles $|\Theta| = 0°, 19.1°, 30°$. (d) Side view of the 0° unit cell. The interlayer distance was chosen to be $d = 3.3$ Å and the chalcogen-chalcogen distance d_{XX} can be found in Tab. 5.1.

We note that in these relations the only parameter susceptible to a change of the sign in the twist angle is the Rashba angle Φ. Since the Rashba angle was not the focus of this investigation (Ref. [163]), we did not pay attention to use supercells with uniform signs of the twist angle. Therefore, we mostly only list the absolute value $|\Theta|$ of the twist angle. As discussed in Sec. 4.5, the construction of commensurate periodic heterostructure supercells for DFT typically leads to strain, which needs to be applied in either of the layers. We put all strain on graphene, as it is more resilient to strain [79, 80, 144, 145, 146]. Hence, in all cases the TMDCs remain unstrained. Tab. 5.2 shows all heterostructure supercells used in the calculations. In Sec. 4.5 we argued that for investigations with high-strain cases, it is sensible to skip atomic relaxation. Because the strain in the evaluated structures (up to $\epsilon = 10\%$) is very high, we in do not relax our structures. Although the lateral shift does apparently not influence the extracted parameters for large supercells in a relevant way (see Subsec. 4.5.2), we adhere to the following convention for the lateral shift of the two layers: In the corner of our supercells a carbon atom of graphene will always sit directly beneath a metal atom of the TMDC. Fig. 5.1 shows the heterostructure supercells for few exemplary twist angles.

Table 5.2: Structural information of the investigated heterostructure supercells of graphene and semiconducting TMDCs. For each supercell we list the supercell attributes (n,m) of graphene and (n',m') of the TMDC. Additionally, we list the absolute value of the twist angle $|\Theta|$, the strain ϵ^{TMDC} in graphene (depending on the specific choice of TMDC) and the number of atoms (N_{at}) in the heterostructure supercell. In the cases, where the strain is written in grey, the supercells were not investigated for this specific material. These supercells usually either had too much built-in strain or entailed computational difficulties (e.g., convergence problems) and are listed only for completeness. The sizes of the k-grids employed in the DFT calculations of the supercells can be found in Tab. 4.2

$\lvert\Theta\rvert$ [°]	(n,m)	(n',m')	$\epsilon^{\mathrm{MoS_2}}$ [%]	$\epsilon^{\mathrm{WS_2}}$ [%]	$\epsilon^{\mathrm{MoSe_2}}$ [%]	$\epsilon^{\mathrm{WSe_2}}$ [%]	N_{at}
0.0	(4,0)	(3,0)	-2.9	-3.05	1.19	1.19	59
0.0	(0,5)	(0,4)	3.58	3.41	7.93	7.93	98
5.2	(3,1)	(2,1)	-4.99	-5.14	-1.0	-1.0	47
6.6	(3,2)	(2,2)	2.89	2.73	7.22	7.22	74
9.5	(3,2)	(3,1)	7.1	6.93	11.6	11.6	77
10.9	(2,1)	(1,1)	-15.24	-15.37	-11.67	-11.67	23
13.9	(3,1)	(3,0)	7.73	7.56	12.26	12.26	53
13.9	(0,4)	(1,3)	16.7	16.52	21.61	21.61	71
13.9	(5,0)	(3,1)	-6.64	-6.78	-2.71	-2.71	89
19.1	(2,1)	(2,0)	-2.13	-2.28	1.99	1.99	26
22.7	(3,2)	(1,3)	7.1	6.93	11.6	11.6	77
23.4	(3,2)	(3,0)	-10.89	-11.03	-7.14	-7.14	65
27.0	(3,1)	(1,2)	-4.99	-5.14	-1.0	-1.0	47
30.0	(2,0)	(1,1)	12.13	11.95	16.84	16.84	17
30.0	(5,0)	(2,2)	-10.3	-10.44	-6.53	-6.53	86

5.2 Band structures

Performing DFT calculations (see Sec. 4.2) on these heterostructure supercells provides us with their corresponding band structures. In Fig. 5.2 we show some examples with different twist angles and for the four different TMDCs. The backfolding rules of an (n,m) supercell (see Eq. (4.27)) hold true for both the graphene layer and the TMDC layer. However, the backfolding of the TMDC is of little interest for us. The much more relevant backfolding occurs for the graphene: If

$$n - m = 0 + 3 \cdot p, \text{ with } p \in \mathbb{Z} \tag{5.4}$$

and consequently both K and K' (of the primitive 1st Brillouin zone (BZ)) fold back to the Γ point, an extraction of the SOC parameters is hampered. Concretely, the sign of the

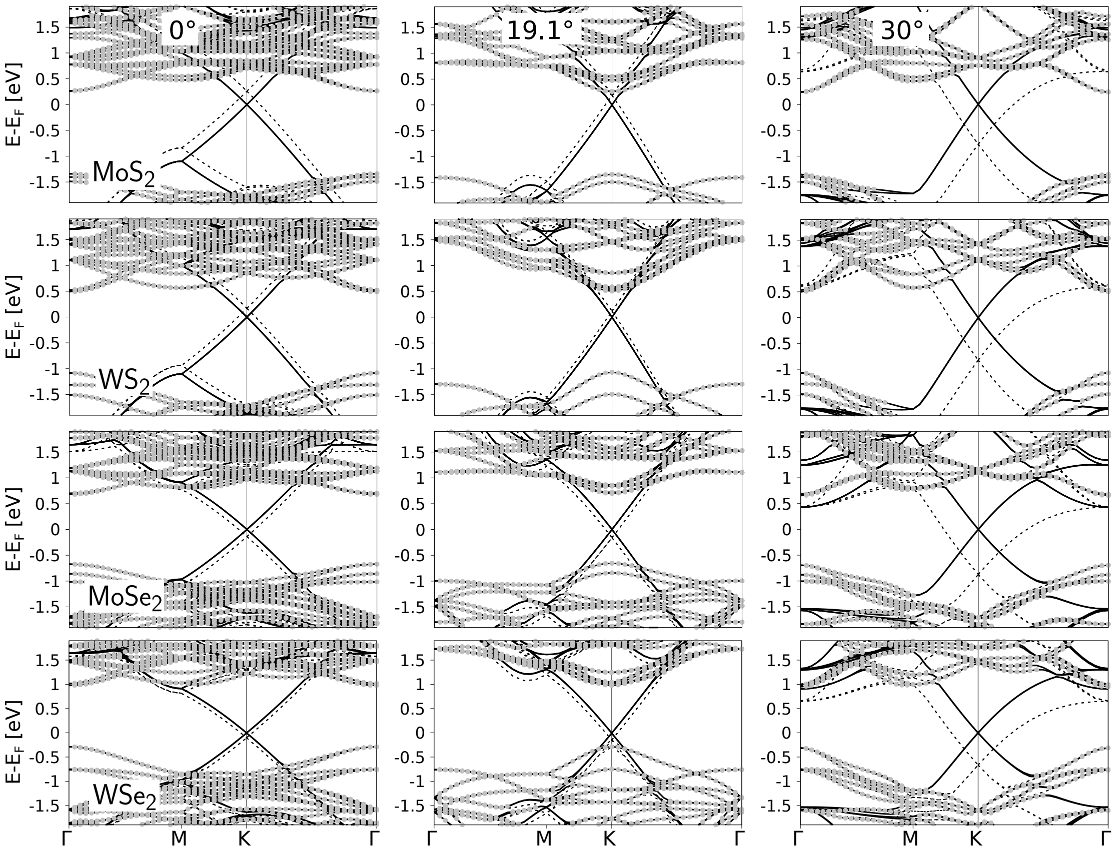

Figure 5.2: Band structures along high symmetry lines for selected graphene/TMDC supercells as calculated by DFT. For each of the four semiconducting TMDCs, we show the band structures of supercells with three different angles: $|\Theta| = 0°, 19.1°, 30°$, as indicated. The grey dots stem from TMDC orbitals, while the solid lines come from graphene states. The dotted lines show the graphene bands without the electric field corrections. Note that band folding effects change the positions of the TMDC valence band maxima and conduction band minima in k space. Nevertheless, the global TMDC band gap stays intact.

valley-Zeeman SOC λ_{VZ} cannot be determined as it is opposite at K and K'. Therefore, we constructed the supercells in Tab. 5.2 in a way that

$$n - m = 1 + 3 \cdot p \tag{5.5}$$

$$\text{or} \quad n - m = 2 + 3 \cdot p. \tag{5.6}$$

In the former case K simply folds back to K, whereas in the latter case K folds back to K' (and vice versa). Therefore it is crucial for us to know, which of the two cases applies, in order to correctly determine the sign of λ_{VZ}.

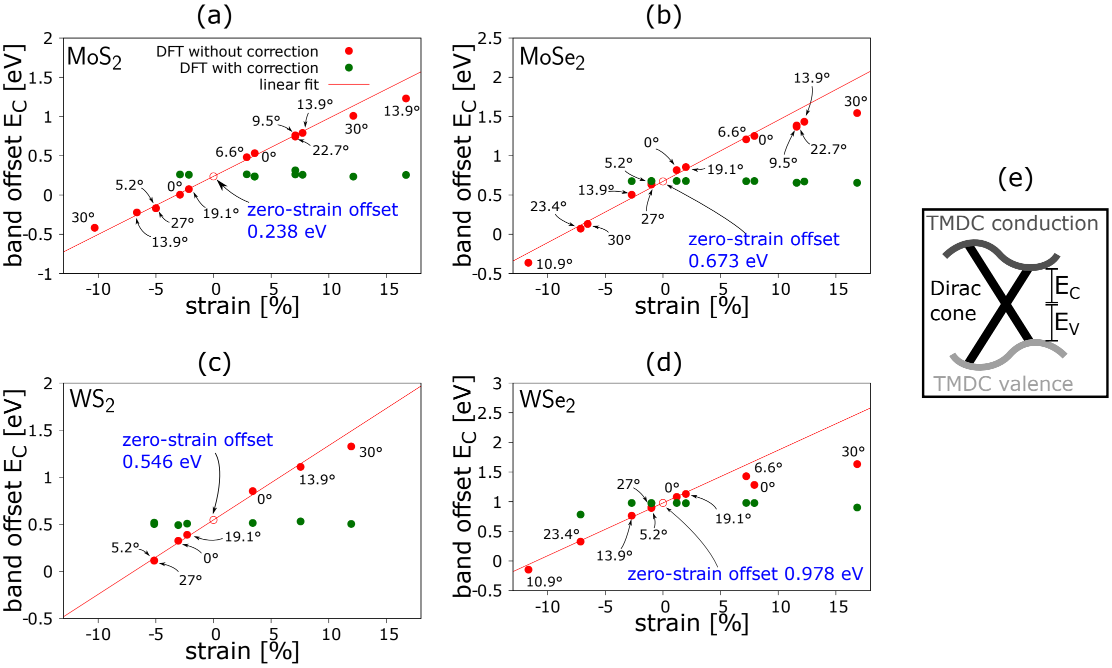

Figure 5.3: Strain induced band offsets and correcting for the strain. For all investigated supercells of graphene with (a) $\mathrm{MoS_2}$, (b) $\mathrm{MoSe_2}$, (c) $\mathrm{WS_2}$ and (d) $\mathrm{WSe_2}$ monolayers we plot the band offsets E_C of the Dirac cone with respect to conduction band against the strain ϵ on graphene; $\epsilon > 0$ indicates tensile strain while $\epsilon < 0$ indicates compressive strain. Every data point (red dots) is annotated with the twist angle of the corresponding supercell. From the linear fit (red line) we extract the (apparent) zero-strain band offsets (empty red circles) which can be found in Tab. 4.3. Green circles show the band offsets after the correction by electric field, employed to compensate the influence of strain (see Sec. 4.5.2). We excluded supercells with strains above 10% or below -10% and supercells with negative band offsets ($E_C < 0$) from the linear fit. The illustration in (e) portrays how E_C and E_V are defined.

In Sec. 4.5.1 we already showed that the graphene work function increases linearly with strain (see Fig. 4.9(a)). As a consequence, the band offset between graphene and the

TMDCs changes linearly with strain as well (see Fig. 5.3). We define the band offsets as the energy difference between the Dirac cone energy and the valence (E_V) or conduction band edge (E_C) as Fig. 5.3(e) shows. Hence, adding E_V and E_C will always yield the TMDC band gap, i.e. $E_C + E_V = E_{\text{gap}}$. Using a linear fit, we give an estimate for the zero-strain band offsets, i.e. the band offsets we expect for unstrained graphene. For the parameters extracted from the fit (zero-strain band offsets and deformation potentials) see Tab. 4.3. Because the strain of the supercells used in this chapter can be up to 10%, we then use an electric field to counteract this effect and bring the band offsets of all supercells to the zero-strain band offset (see Sec. 4.5). The graphene Dirac cone resides within the TMDC band gap for most of our calculations, i.e. $E_V > 0$ and $E_C > 0$. Although there are high-strain cases where the Dirac cone resides within the conduction or valence bands (without band offset corrections), the Dirac cone will be pushed inside the TMDC band gap by the band offset corrections through the external electric field. The Dirac cone can hence be easily extracted. Fig. 5.4 shows zooms of the band structures near the Dirac cone. We find that the Dirac cones are highly isotropic and that the bands can be fitted using the effective model Hamiltonian (Eq. (4.43)) with high precision. In the next section, we discuss these fitting parameters.

5.3 Extracted SOC parameters

The key question we try to answer is, how the twist angle Θ between the layers affects the proximity SOC in the graphene. By plotting the SOC fitting parameters of all heterostructure supercells against their twist angle, we can now give a reasonable answer from a DFT perspective on this question. This sort of plot is shown in Fig. 5.5, for the calculations without band offset corrections in (a) and for the ones with band offset corrections in (b). Data points with excessive strain of $|\epsilon| > 10\%$ can be considered as heavily distorted (see Sec. 4.5), but are nevertheless plotted in a de-emphasized way (transparent, light color) for completeness. For supercells, where the band offset corrections were not possible, because excessive electric fields would have been needed, distorting the TMDC band structure too much, data points are excluded completely for both the corrected and uncorrected plots. The fitting parameters Δ and λ_{KM} are omitted, because they are negligibly small for most supercells. We performed additional calculations on relaxed structures (see Ref. [163]), showing that (in accordance with e.g. Ref. [14]) Δ and λ_{KM} are non-zero for the relaxed structures. The overall values for both λ_{R} and λ_{VZ} are comparable to values from other DFT calculations [14, 67, 64].

5.3.1 Angle dependence of λ_{R} and λ_{VZ}

The main results – the angle dependence of λ_{R} and λ_{VZ} – can be seen in Fig. 5.5 and are summarized in Tab. 5.3 and Tab. 5.4. Let us focus first on the results with corrected band offsets (Fig. 5.5(b)). The valley-Zeeman SOC λ_{VZ} vanishes for $\Theta = 30°$; here the system has a pure Rashba SOC. The reason for this is that the Dirac cone couples

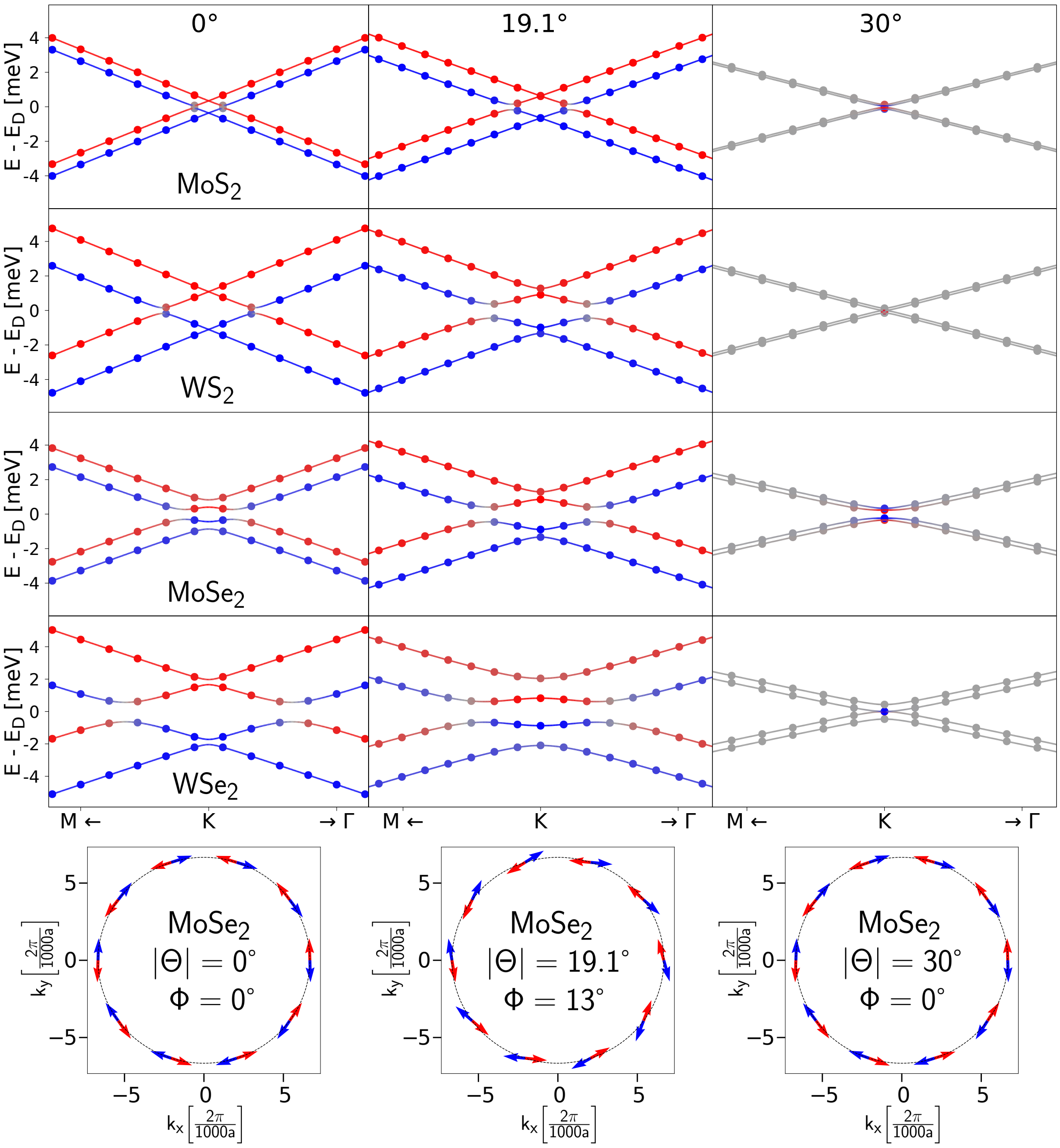

Figure 5.4: Zoom to the Dirac band structures with proximity SOC at the K point (after band offset corrections). The shown results are from all four used semiconducting TMDCs and for heterostructure supercells with different angles $|\Theta| = 0°$, $19.1°$, and $30°$. The dots represent the DFT data, while the solid line represent the effective model Hamiltonian fit (see Eq. (4.43)). The color codes show spin-z expectation values and go from $\langle s_z \rangle = -0.5$ (spin down; blue) over $\langle s_z \rangle = 0$ (unpolarized; grey) to $\langle s_z \rangle = 0.5$ (spin up; red). The extracted parameters can be found in Tab. 5.4. In the last row we show the in-plane spin texture of the spin-up (red arrows) and spin-down (blue arrows) valence bands of the graphene/MoSe$_2$ supercells. The k-path (dotted line) goes along a circular path around the K point. We also present the extracted Rashba angle Φ, measuring the uniform deviation of the spin texture from tangential.

with a point in the TMDC 1st BZ (see Subsec. 4.4.4), which lies in the middle of its K and K' point. Therefore, it does not show spin splitting and in consequence does also not transfer any proximity valley-Zeeman SOC. Apart from this very general fact of the matter, the λ_{VZ} shows a very different angle dependence in heterostructures with Mo-based and W-based TMDCs. For the Mo-based structures, we see the following behaviour. For small twist angles $0° \leq \Theta \leq 15°$ the values of λ_{VZ} stay at an intermediate level. After this, a relatively sharp peak at about $\Theta \approx 20°$ arises, which is then followed by a rapid decline toward $\lambda_{\mathrm{VZ}} = 0$ at $\Theta = 30°$. This behaviour is very much in line with the predictions of the tight binding model of Ref. [19], where the peak is explained by the fact that the Dirac cone couples with the Q-valley of the TMDCs through interlayer interaction. The W-based structures on the other hand show a different behaviour. Their maximum value of λ_{VZ} can be found at $\Theta = 0°$, with an almost monotonous decrease, which is only interrupted by a very small peak at about $\Theta \approx 15°$ (WS_2) or $\Theta \approx 20°$ (WSe_2). In general it can be said that the values of both λ_{VZ} and λ_{R} are on average much higher for the W-based heterostructures. This is a natural consequence of the fact that W has a higher atomic number than Mo and therefore exhibits more SOC.

The Rashba SOC λ_{R} has a more subtle angle dependence. For most cases it tends to be stronger in the middle of the $0° \leq \Theta \leq 30°$ range, than at $\Theta = 0°$ or $\Theta = 30°$. There seems to be a maximum at $\Theta \approx 25°$ followed by a sharp drop toward $\Theta = 30°$ for the W-based structures. However, as these are rather small features, the variance of the λ_{R} is lower than the one of λ_{VZ}. Another parameter which can be extracted from the Dirac cones is the Rashba angle Φ, whose main role it is to determine the angle between applied voltage and induced spin density in the (unconventional) Rashba-Edelstein effect ((U)REE). We extracted Φ only for a few heterostructures discussed in this chapter (see Fig. 5.5(c)). However, the picture is nevertheless congruent with more detailed DFT calculations [67, 64] and experiment [137]. It follows the symmetry rules Eq. (4.84), i.e. $\Phi = 0°$ (or $\Phi = 180°$) at both $\Theta = 0°$ and $\Theta = 30°$. The data point at $\Theta = 180°$ has to be regarded as less reliable, as it exhibits very high strain and has a very small supercell making it prone to effects by lateral shifting. In between $\Theta = 0°$ and $\Theta = 30°$, there is a rather small ($|\Phi| \leq 50°$) deviation from the $\Phi = 0°$ case. This however contradicts the findings of Ref. [21], which predicts much higher values of Φ and for some parameters even $\Phi = \pm 90°$, promising a realization of a pure UREE with purely collinear CSC.

5.3.2 Gauging the effects of strain and the effectiveness of the approach

Comparing the SOC parameters before (Fig. 5.5(a)) and after (Fig. 5.5(b)) the band offset corrections via electric field can give valuable insights into the effectiveness of these corrections. We can see that some features can be observed in both versions, e.g. the peak of λ_{VZ} at $\Theta = 19.1°$ for MoS_2 or the disappearance of λ_{VZ} for $\Theta = 30°$. Also, the subtle structure of the Rashba SOC is not strongly influenced. However, in the uncorrected version we see more drastic fluctuations including some serious outlier data points (e.g.

(a) SOC parameters with uncorrected band offsets

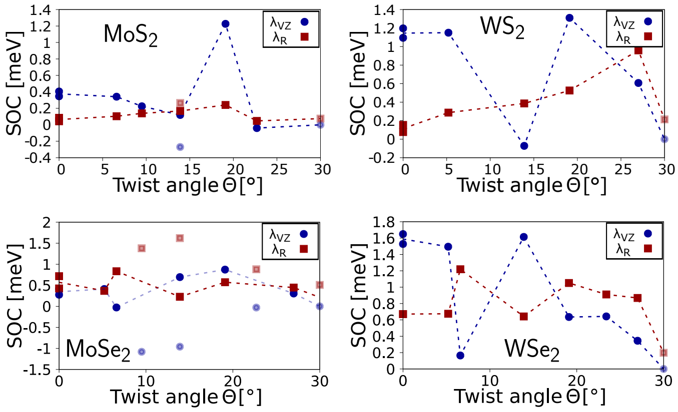

(c) Rashba angle for a few different twist angles

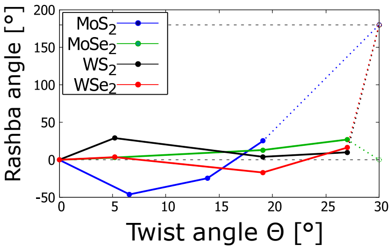

(b) SOC parameters with corrected band offsets

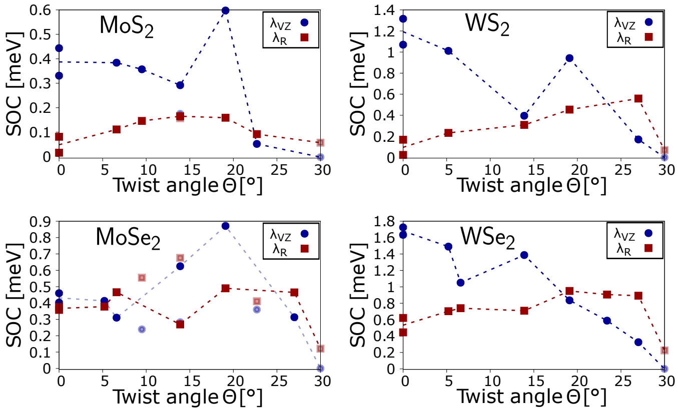

(d) tuning SOC parameters of 19.1° MoS$_2$ supercell

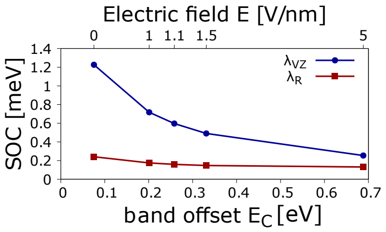

Figure 5.5: Twist-angle dependence of the SOC parameters. Both (a) and (b) show λ_R (red squares) and λ_{VZ} (blue dots) as function of the twist angle. The uncorrected SOC parameters are shown in (a), while (b) shows the SOC parameters after the band offset corrections with an external electric field. We de-emphasize (transparent, light red/blue) data points from supercells with excessive built-in strain of $|\epsilon| > 10\%$, deeming them less reliable. The dotted line is a guide for the eyes. (c) Rashba angle Φ for a few twist angles. The data around $\Theta = 30°$ is depicted as dotted point and line as this data point is rather unreliable due to high strain and small supercell size. Dotted horizontal lines mark $\Phi = 0°$ and $\Phi = 180°$, both showing purely tangential in-plane spin texture. (d) Evolution of the SOC parameters λ_R and λ_{VZ} of the 19.1° MoS$_2$ supercell for increasing band offset E_C to the conduction band.

$\Theta = 6.6°$ for WSe_2), delivering an overall much less clear picture. The example of the peak in λ_{VZ} at $\Theta = 19.1°$ nicely illustrates these outliers and how they can be adjusted using the band offset corrections. For the uncorrected band offsets, this peak is much more prevalent; compared to the value at $\Theta = 0°$ an increase by the factor 3 can be noted as compared to the factor 1.5 for the corrected case. The reason for this is, that in the uncorrected band structure for the $\Theta = 19.1°$ supercell the Dirac cone is very close in energy to the conduction band ($E_C = 75$ meV). Although this is also the case for example for the $\Theta = 0°$ supercell ($E_C = 4$ meV), the relevant measure is the distance to the nearest bands interacting with the Dirac cone through the generalized Umklapp process in the first order (see Sec. 4.4). This distance is 500 meV for $\Theta = 0°$ and only 288 meV for $\Theta = 19.1°$. The vicinity to these bands strongly enhances the proximity SOC and over-emphasizes this peak. Applying the electric field corrects the band offset, decreases the proximity SOC (see Fig. 5.5(d)) and brings about a more realistic peak structure.

We note that at $\Theta = 0°$ a situation arises, where two data points (with reasonable strain $|\epsilon| < 10\%$) have the same twist angle, but different strains. These points can be used to gauge the error arising due to strain. If the strain was not the source of any error, these two supercells should always yield the same SOC parameters. From our results we can say that the extracted SOC parameters are similar, but still apart by some margin. Even for the cases without band offset corrections the two data points mostly seems to fit very well except for λ_R in the case of $MoSe_2$. Here the two data points deviate from their average value by ±26%. For the corrected cases, the worst matching data point pairs are λ_{VZ} for MoS_2 and WS_2, deviating by ±14% and ±10%, respectively. This showcases again that, although the overall accuracy of the calculations (as measured by the matching of these two data points) is not drastically improved by the band offset corrections, especially outlier data points can be readjusted to more reasonable values.

5.3.3 Comparison with literature

As the proximity SOC in heterostructures of semiconducting TMDCs and graphene are of great interest to the scientific community, there are several other references explicitly studying the twist-angle dependence as well. In this subsection, we will place our results in the context of varying other publications, using different approaches. This includes tight binding calculations [19, 20, 21] (Fig. 5.6(a) and (b)), other DFT calculations [67, 64] (Fig. 5.6(c) and (d)) and finally experiment [137] (Fig. 5.6(e)). Fig. 5.6(a) and (b) show results from Ref. [19] and Ref. [21], respectively, both of which use a very similar tight binding approach. However, the subtle differences of their approaches and employed parameters apparently lead to relevant differences of the outcome. One prominent feature, which both exhibit is the peak of λ_{VZ} at $\Theta \approx 20°$ for graphene/MoS_2, which shows up in our calculations of the Mo-based heterostructures as well. The twist-angle dependence of λ_R of our calculations decently matches the one of Ref. [19] (Fig. 5.6(a)) for most cases. A feature appearing solely in Ref. [21] (Fig. 5.6(b)) is the sign change of λ_{VZ}, which is at odds with our results. Regarding the Rashba angle Φ, both tight binding references predict sufficiently higher values of Φ, with Ref. [20] (Fig. 5.6(b)) even predicting a swap

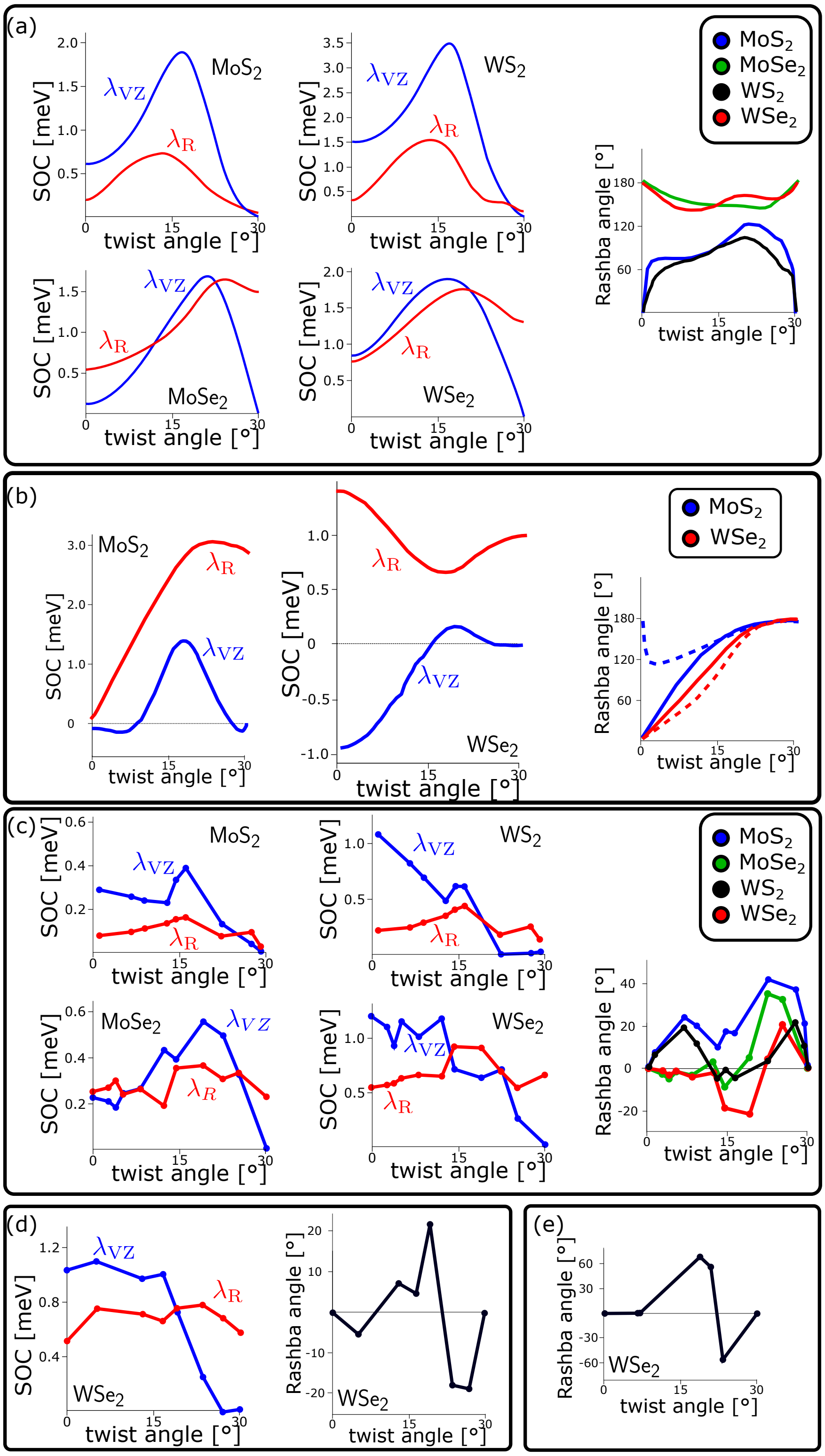

Figure 5.6: Overview of proximity SOC parameters from different references. Ref. [19] (a) and Ref. [21] (b) employed tight binding models. Ref. [67] (c) and Ref. [64] (d) employed DFT. In (e) we show experimental results from Ref. [137]. The Rashba angles from (a) are drawn from private communication with the authors of Ref. [19]. All plots were recreated using a uniform style. There might be inconsistent signs or shifts by 180° of the Rashba angle as the calculations might use different conventions (direction of z-axis, direction of the twist).

of the Rashba sign (180° shift) from $\Theta = 0°$ to $\Theta = 30°$. In our calculations, this sign swap is only observed, if the less reliable $\Theta = 30°$ is taken into account.

Fig. 5.6(c) and (d) show results from Ref [67] and Ref. [64], respectively, both of which use a DFT approach. Results of Ref. [169] are not discussed here, as their results are heavily dependent on the strain, complicating any possible comparison. Details of the DFT approaches can be found in Tab. 4.4. The results of the DFT-based calculations are much more congruent with our results. The peak of λ_{VZ} for the Mo-based structures, the declining λ_{VZ} for the W-based structures and the subtle dependence of λ_{R} with a small bump at $\Theta \approx 15°$ are all reproduced. Although the exact twist-angle dependence of Φ is differing, the general magnitude of Φ and the presence of sign changes are also in agreement with both DFT references. The decent consensus between the calculations is remarkable as the strain on graphene, which is allowed in Refs. [67, 64] is significantly smaller than the ones allowed in our calculations.

The only experimental reference explicitly plotting proximity SOC parameters against the twist angle Θ is Ref. [137]. The twist-angle dependence of the Rashba angle Φ in graphene/WSe$_2$ heterostructures (which is the only SOC parameters they discuss) is generally compatible with the DFT results (especially of Refs. [67, 64]). The magnitude of Φ (up to $|\Phi| = 70°$) seems to represent a middle ground between the DFT (up to $|\Phi| = 50°$) and the tight binding predictions (up to $|\Phi| = 180°$). Possible reasons for this are plentiful and include for example the notoriously incorrect bands gaps of the DFT calculations as well as incorrect band offsets.

5.4 Charge-to-spin conversion efficiencies

In Sec. 4.6 we introduced a scheme by which we can calculate CSC efficiencies (REE and UREE) of graphene-based systems based on the fitting parameters from the model Hamiltonian Eq. (4.43) within linear response theory. We can now use the extracted parameters from the band offset corrected calculations of heterostructures of graphene and the semiconducting TMDCs (see Tab. 5.4 and Fig. 5.5(b)) in order to give such estimates for the discussed heterostructures. Due to the fact that we did not extract the Rashba angle Φ for all calculations, we cannot differentiate between REE and UREE efficiencies for all twist angles. Therefore, we only give the total CSC efficiency defined as $\alpha_{\mathrm{tot}} = \sqrt{\alpha_{\mathrm{REE}}^2 + \alpha_{\mathrm{UREE}}^2}$.

The twist-angle dependencies of this quantity are plotted in Fig. 5.7. It paints a clear picture: The curves for all four materials (MoS$_2$, MoSe$_2$, WS$_2$ and WSe$_2$) follow for the most part the curves of the Rashba SOC (see Fig. 5.5). All deviation from these forms can be readily explained by the detrimental effects of adding valley-Zeeman SOC (as can be seen in Fig. 4.11(e)). An example of this is the following: the maximal Rashba SOC λ_{R} of the graphene/WSe$_2$ heterostructure can be found at $\Theta = 19.1°$. However, the maximal CSC efficiency α_{tot} is located at $\Theta = 27°$, which can be explained by the lower value of the valley-Zeeman SOC λ_{VZ} for this twist angle.

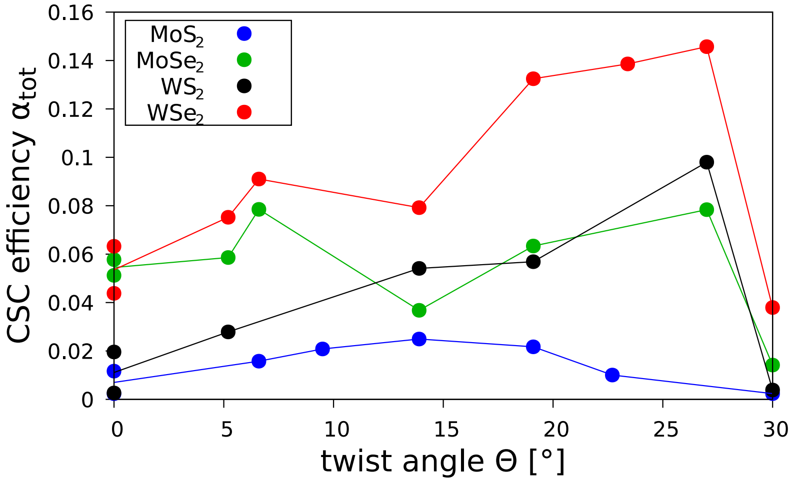

Figure 5.7: CSC efficiencies of graphene proximitized by MoS$_2$, MoSe$_2$, WS$_2$ and WSe$_2$ as determined by the Kubo formula approach from Sec. 4.6. Because of a lack of data for the Rashba angle Φ, we show only the total CSC efficiency $\alpha_{\text{tot}} = \sqrt{\alpha_{\text{REE}}^2 + \alpha_{\text{UREE}}^2}$.

5.5 Summary

We constructed several twisted supercells of heterostructures of graphene with semiconducting TMDCs MoS$_2$, MoSe$_2$, WS$_2$ and WSe$_2$ and performed DFT calculations on them. Their strain-dependent band offsets were corrected by using a transverse electric field and the apparent zero-strain band offsets were extracted. Fitting the low energy Dirac states of the resulting band structures to a model Hamiltonian yielded relevant SOC parameters ranging in the meV range consistent with other calculations. The twist-angle dependence of these parameters was examined and parallels to existing literature were drawn. Most notably, we found valley-Zeeman SOC peaking at $\Theta \approx 20^\circ$ (for Mo-based structures) and vanishing at $\Theta = 30^\circ$, which was also predicted by tight binding calculations [19]. We evaluated the Rashba angle for some twist angles, finding a small deviation from $\Phi = 0^\circ$ of up to $|\Phi| = 50^\circ$ with varying sign and without a clear structure. For all systems, we found the twist-angle dependencies to be in accordance with more refined, computationally more expensive calculations with less strain [67]. This indicates the effectiveness of our measures mitigating the effects of strain presented in Sec. 4.5. Furthermore, we used the extracted model Hamiltonian parameters to calculate CSC efficiencies within linear response theory. The results of these calculations nicely illustrate how the Rashba SOC translates to CSC, with a small attenuating effect of the valley-Zeeman SOC. Experimental evidence of the effects of the twist angle are scarce, as the twist angle is seldomly determined in experimental setups. However, the experimental results of Ref. [137] seem to somewhat align with the theoretical predictions.

Table 5.3: Model Hamiltonian parameters (staggered potential Δ, Kane-Mele SOC λ_{KM}, valley-Zeeman SOC λ_{VZ} and Rashba SOC λ_{R}) extracted from the band structure calculations (without band offset corrections) for all used heterostructure supercells. We additionally list band offsets E_V and E_C of the Dirac cone with respect to the valence and conduction band, respectively. The parameters for the calculations with band offset corrections can be found in Tab. 5.4.

$\lvert\Theta\rvert$	ϵ	Δ	λ_{KM}	λ_{VZ}	λ_{R}	E_V	E_C
[°]	[%]	[meV]	[meV]	[meV]	[meV]	[eV]	[eV]
MoS$_2$							
0	-2.9	0.014	0.000	0.346	0.085	1.598	0.004
0	3.58	-0.005	-0.003	0.405	0.043	1.066	0.533
5.2	-4.99	0.022	-0.001	0.456	0.165	1.773	-0.169
6.6	2.89	0.054	0.000	0.341	0.104	1.118	0.482
9.5	7.1	0.023	0.000	0.225	0.139	0.838	0.761
13.9	7.73	0.017	-0.001	0.120	0.168	0.809	0.791
13.9	16.7	0.037	0.000	-0.270	0.265	0.377	1.230
13.9	-6.64	0.124	-0.023	8.730	1.251	1.828	-0.222
19.1	-2.13	0.023	-0.003	1.227	0.241	1.532	0.075
22.7	7.1	-0.005	0.000	-0.040	0.047	0.859	0.745
27	-4.99	-0.004	0.001	0.458	0.531	1.773	-0.168
30	12.13	0.000	0.000	0.000	0.075	0.596	1.009
30	-10.3	0.000	-0.062	0.000	1.774	1.868	-0.418
WS$_2$							
0	-3.05	0.021	-0.000	1.094	0.154	1.248	0.325
0	3.41	-0.097	0.004	1.197	0.077	0.717	0.853
5.2	-5.14	0.000	-0.002	1.150	0.287	1.459	0.114
13.9	7.56	0.866	-0.004	-0.072	0.386	0.463	1.110
19.1	-2.28	0.004	-0.006	1.310	0.526	1.185	0.389
27	-5.14	-0.052	0.001	0.607	0.959	1.459	0.116
30	11.95	0.000	0.004	0.000	0.214	0.237	1.327
MoSe$_2$							
0	1.19	0.034	0.001	0.417	0.425	0.535	0.817
0	7.93	-0.625	0.005	0.276	0.717	0.098	1.252
5.2	-1	0.024	0.000	0.412	0.368	0.708	0.645
6.6	7.22	0.069	0.003	-0.026	0.834	0.142	1.209
9.5	11.6	0.038	-0.019	-1.080	1.380	-0.051	1.386
10.9	-11.67	0.244	0.137	4.769	1.011	1.719	-0.363
13.9	12.26	0.029	-0.035	-0.958	1.621	-0.069	1.433
13.9	-2.71	0.024	-0.001	0.695	0.227	0.850	0.503
19.1	1.99	-0.015	0.000	0.873	0.573	0.496	0.856
22.7	11.6	-0.013	0.001	-0.028	0.881	-0.026	1.370
23.4	-7.14	-0.002	0.002	-0.211	0.253	1.284	0.071
27	-1	-0.012	0.001	0.306	0.446	0.721	0.633
30	16.84	0.000	0.005	0.000	0.509	-0.178	1.544
30	-6.53	0.000	-0.004	0.000	0.213	1.224	0.131
WSe$_2$							
0	1.19	0.042	0.002	1.649	0.671	0.186	1.081
0	7.93	0.219	0.009	1.528	0.671	-0.018	1.282
5.2	-1	0.034	0.001	1.494	0.675	0.360	0.907
6.6	7.22	0.090	0.004	-0.165	1.219	-0.164	1.429
10.9	-11.67	0.014	-0.013	3.198	1.051	1.417	-0.147
13.9	-2.71	0.023	-0.002	1.614	0.642	0.504	0.764
19.1	1.99	0.009	0.005	0.636	1.051	0.138	1.123
23.4	-7.14	-0.004	-0.002	0.643	0.911	0.943	0.326
27	-1	0.000	0.002	0.345	0.868	0.375	0.894
30	16.84	0.001	0.018	-0.001	0.198	-0.349	1.633

Table 5.4: Model Hamiltonian parameters (staggered potential Δ, Kane-Mele SOC λ_{KM}, valley-Zeeman SOC λ_{VZ} and Rashba SOC λ_{R}) extracted from the band structure calculations (with band offset corrections) for all used heterostructure supercells. We additionally list band offsets E_V and E_C of the Dirac cone with respect to the valence and conduction band, respectively and the electric field used in the band offset corrections. The parameters for the calculations without band offset corrections can be found in Tab. 5.3.

$\lvert\Theta\rvert$ [°]	ϵ [%]	E-field [V/nm]	Δ [meV]	λ_{KM} [meV]	λ_{VZ} [meV]	λ_R [meV]	E_V [eV]	E_C [eV]
MoS_2								
0	-2.9	1.499	0.009	0.000	0.331	0.081	1.341	0.262
0	3.58	-1.748	0.130	0.002	0.444	0.016	1.358	0.236
5.2	-4.99	-	-	-	-	-	-	-
6.6	2.89	-1.301	0.032	0.000	0.384	0.111	1.334	0.264
9.5	7.1	-2.962	0.026	-0.001	0.357	0.146	1.322	0.262
13.9	7.73	-3.183	0.010	-0.001	0.292	0.165	1.331	0.258
13.9	16.7	-6.154	-0.327	0.001	0.175	0.157	1.381	0.256
13.9	-6.64	-	-	-	-	-	-	-
19.1	-2.13	1.107	0.031	-0.005	0.597	0.159	1.336	0.258
22.7	7.1	-2.564	-0.004	0.000	0.052	0.092	1.242	0.315
27	-4.99	-	-	-	-	-	-	-
30	12.13	-6.582	0.059	0.002	0.000	0.057	1.359	0.235
30	-10.3	-	-	-	-	-	-	-
WS_2								
0	-3.05	0.951	0.014	-0.002	1.070	0.168	1.082	0.492
0	3.41	-1.969	-0.047	0.004	1.316	0.024	1.053	0.514
5.2	-5.14	2.234	0.008	-0.001	1.011	0.233	1.056	0.518
13.9	7.56	-3.416	-0.263	-0.002	0.396	0.309	1.035	0.531
19.1	-2.28	0.662	0.005	-0.005	0.942	0.454	1.067	0.507
27	-5.14	2.195	0.010	0.001	0.170	0.559	1.073	0.503
30	11.95	-4.973	-0.001	0.004	0.000	0.069	1.067	0.504
$MoSe_2$								
0	1.19	-0.863	0.017	0.001	0.403	0.370	0.673	0.679
0	7.93	-3.754	0.101	0.003	0.460	0.358	0.667	0.678
5.2	-1	0.209	0.016	0.000	0.413	0.378	0.674	0.679
6.6	7.22	-3.453	-0.006	0.001	0.310	0.466	0.672	0.676
9.5	11.6	-5.101	0.038	0.000	0.239	0.555	0.687	0.657
10.9	-11.67	-	-	-	-	-	-	-
13.9	12.26	-5.150	-0.051	0.002	0.283	0.676	0.675	0.672
13.9	-2.71	1.080	-0.016	-0.001	0.625	0.269	0.676	0.677
19.1	1.99	-1.048	0.000	-0.001	0.871	0.490	0.655	0.678
22.7	11.6	-4.958	0.033	0.000	0.360	0.411	0.696	0.655
23.4	-7.14	-	-	-	-	-	-	-
27	-1	0.288	-0.012	0.000	0.313	0.465	0.677	0.677
30	16.84	-6.515	-0.236	0.003	0.000	0.121	0.675	0.655
30	-6.53	-	-	-	-	-	-	-
WSe_2								
0	1.19	-0.636	0.056	0.001	1.634	0.621	0.289	0.978
0	7.93	-3.445	0.084	0.003	1.725	0.445	0.286	0.977
5.2	-1	0.449	0.033	0.001	1.490	0.703	0.291	0.977
6.6	7.22	-3.137	0.073	0.001	1.051	0.740	0.285	0.979
13.9	-2.71	1.327	-0.022	-0.000	1.388	0.709	0.290	0.978
19.1	1.99	-0.920	0.014	0.001	0.835	0.950	0.294	0.974
23.4	-7.14	3.085	0.000	0.000	0.588	0.906	0.427	0.783
27	-1	0.555	0.000	0.003	0.326	0.892	0.294	0.975
30	16.84	-6.065	0.003	0.009	0.000	0.225	0.313	0.901

6 Twist-angle dependent proximity spin-orbit coupling in heterostructures of graphene and topological insulators

Although the most prevalent materials to be combined with graphene are transition-metal dichalcogenides (TMDCs), there is another promising class of materials, used to modify the spin-orbit coupling (SOC) in graphene — three-dimensional topological insulators (3D TIs). Such materials (like Bi_2Se_3, Bi_2Te_3, Bi_2Te_2Se, Sb_2Te_3 etc.) [122, 123, 124, 125, 126] are mostly known for their topological surface states. One crucial property responsible for the band inversion, and therefore the surface states, is the strong SOC of these materials. This simultaneously makes them ideal candidates for inducing said SOC in graphene by proximity in graphene/TI heterostructures. Using 3D TIs instead of TMDCs not only promises stronger proximity SOC [41, 171], it also introduces new and interesting physics: since the topological surface state of the 3D TI resides on its surface, it can be expected to hybridize strongly with the graphene layer. The ramifications of such an interaction are not fully understood yet, but there are signs that it could be the reason for the Kane-Mele SOC, which has been proposed to occur in commensurate graphene/TI heterostructures with a 30° twist angle [44, 41]. This constitutes a special case, as usually only a combination of Rashba SOC and valley-Zeeman SOC are induced by proximity in graphene. Hence, graphene/TI heterostructures might constitute a unique platform for the quantum spin Hall effect (QSHE) [34, 35] in graphene. The fact that this effect apparently only occurs at a specific twist angle underlines the necessity for twist angle resolved studies.

Experimentally, such a commensurate heterostructure can be effectively realized in 'bottom-up' fabricated samples [140, 42, 139, 196], e.g. by CVD. Using such procedures, the resulting structures will most likely exhibit a twist angle corresponding to an energetically favourable commensurate supercell. For graphene/TI heterostructures, the most commonly found twist angles are 0° or 30° [139, 140]. DFT calculations on graphene/TI supercells mainly focus on the 30° supercell [43, 172, 197, 42, 198, 199, 173, 200] or the 0° supercell [171, 41]. However, many experiments use 'top-down' fabrication [201, 197, 202, 203, 200, 204, 205] (e.g. by exfoliation) of heterostructures, resulting in incommensurate structures, mostly with random twist angle. These intermediate twist angles are especially relevant as they allow for the emergence of radial components of the in-plane spin texture and therefore the unconventional Rashba-Edelstein effect (UREE).

This chapter is based on Ref. [44] and is structured as follows. First, in Sec. 6.1, we establish what twisted supercells were used. After this, we discuss the heterostructure band structures as calculated by DFT in Sec. 6.2. In Sec. 6.3 the extracted SOC parameters for twist angles $0^\circ \leq \Theta \lessapprox 20^\circ$ are discussed. In Sec. 6.4 the special case of the highly commensurate 30° twist angle case is discussed in great detail. The SOC parameters are then used as a starting point to calculate charge-to-spin conversion (CSC) efficiencies in Sec. 6.5.

6.1 Twisted supercells

We now introduce the heterostructures of graphene and 3D TIs Bi_2Te_3 and Bi_2Se_3 used throughout the chapter. The structures of the separate materials were already depicted in Fig. 3.1 and Fig. 3.3 and their structural parameters are listed in Tab. 6.1. One open parameter is the thickness of the used TI layer, which is measured in quintuple layers (QL). For thin TIs, the TI surface state is gaped out by finite size effects and only fully forms at about 5QL thickness (see Fig: 3.3(c)). As the proximity effects we are investigating are short ranged, it is reasonable to assume, that increasing the number of QLs is mostly influencing the proximity effects via the change of the TI surface state. Hence, we use only 1QL for the cases with $0^\circ \leq \Theta \lessapprox 20^\circ$, where the surface state is mostly not influencing the graphene band structure according to the rules of the generalized Umklapp processes (see Sec. 4.4). For the special case of the $\Theta = 30^\circ$ supercell, where the surface state directly influences the graphene Dirac cone, we discuss two cases, the 1QL and the 3QL case.

Table 6.1: Lattice constants and atomic constants of unstrained primitive unit cells of graphene and TIs Bi_2Te_3 and Bi_2Se_3, as taken from Ref. [206]. The structure of the TIs stays unchanged in the graphene/TI supercells we use, while the graphene layers are strained by the factors ϵ listed in Tab. 6.2 to ensure commensurability.

	a[Å]	c[Å]	u[Å]	v[Å]
Graphene	2.46	-	-	-
Bi_2Te_3	4.386	30.497	$0.4000 \cdot c$	$0.2097 \cdot c$
Bi_2Se_3	4.143	28.636	$0.4008 \cdot c$	$0.2117 \cdot c$

As in Chap. 5, we use the scheme layed out in Sec. 4.1, in order to create heterostructure supercells with integer pairs (n, m) (graphene) and (n', m') (TI). We define the twist angle

Table 6.2: Structural information of the investigated graphene/TI heterostructures. We list the supercell attributes (n,m) (for graphene) and (n',m') (for the TI), the twist angle Θ between the two layers and the strain ϵ^{TI} imposed on the graphene (depending on the specific choice of TI). Additionally, we list the number of atoms N_{at}, which the heterostructure supercell contains for the cases with 1 and 3 QLs of TI. For completeness, we also list strains and N_{at} corresponding to supercells, which were not investigated, in grey. These supercells, which were not investigated, either had too much built-in strain, too many atoms or entailed computational difficulties (e.g., convergence problems). Additionally, we list the k-mesh densities of the $n_k \times n_k \times 1$ meshes employed in the self-consistent calculations.

Θ [°]	(n,m)	(n',m')	$\epsilon^{\mathrm{Bi_2Te_3}}$ [%]	$\epsilon^{\mathrm{Bi_2Se_3}}$ [%]	N_{at} (1QL)	N_{at} (3QL)	n_k (1QL)	n_k (3QL)
0.0	(0 2)	(0 1)	-10.85	-15.79	13	23	15	-
0.0	(0 5)	(0 3)	6.98	1.05	95	185	6	-
4.3	(2 3)	(1 2)	8.22	2.22	73	143	9	3
4.7	(4 3)	(2 2)	1.54	-4.09	134	254	3	-
8.9	(1 5)	(0 3)	-3.93	-9.26	107	197	3	-
10.9	(2 1)	(1 1)	16.72	10.25	29	95	15	9
13.9	(1 3)	(0 2)	-1.1	-6.58	46	86	15	9
16.1	(3 1)	(1 1)	-14.35	-19.1	41	71	15	-
17.5	(3 2)	(1 2)	8.22	2.22	73	143	9	-
19.1	(4 0)	(2 1)	17.93	11.4	67	137	12	-
19.1	(5 0)	(2 1)	-5.66	-10.88	85	155	6	-
19.1	(2 4)	(0 3)	1.08	-4.52	101	191	3	-
20.8	(4 3)	(1 3)	5.68	-0.17	139	269	3	-
21.1	(5 1)	(2 2)	10.93	4.78	122	242	3	-
21.8	(4 2)	(1 2)	-10.85	-15.79	91	161	6	-
30.0	(1 1)	(0 1)	2.94	-2.77	11	21	45	45
30.0	(7 0)	(2 2)	-11.77	-16.66	158	278	3	-

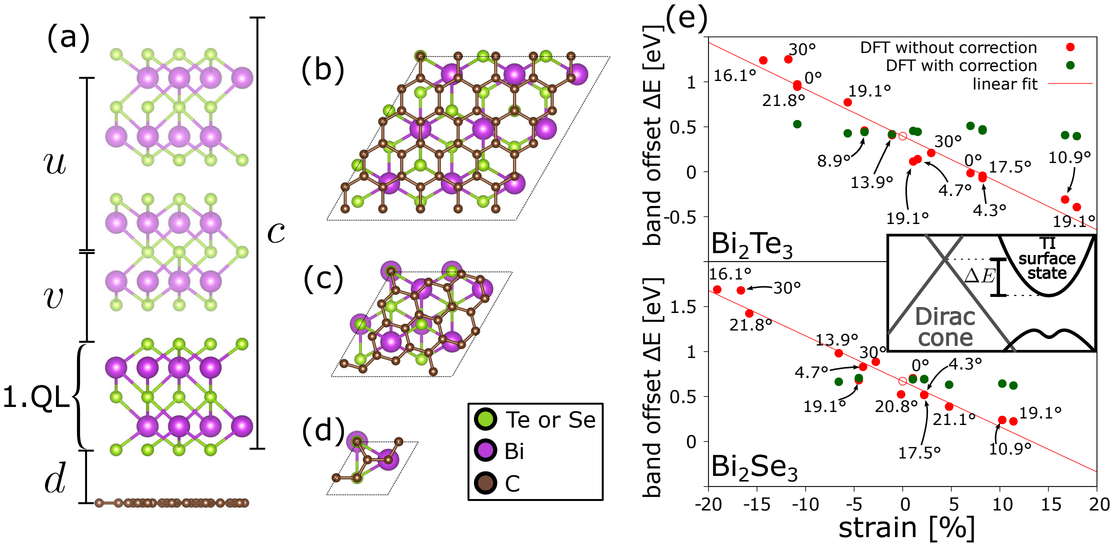

Figure 6.1: (a) Side view of the 13.9° unit cell with indicated interlayer distance d, atomic constants u and v and out-of-plane lattice constant c. The upper two QLs are depicted as transparent, since for the most part only the first QL is used in our calculations. (b)-(d) Bottom view of the graphene/TI heterostructure supercells with twist angles $\Theta = 0°, 13.9°$, and $30°$, respectively. (e) Correcting the strain induced band offset changes: For all investigated supercells of graphene and 1QL of Bi_2Te_3 and Bi_2Se_3, we plot band offsets ΔE of the Dirac cone with respect to the TI surface state remnant (see inset) against the strain ϵ on graphene. Each data point (red solid circles) is annotated with the twist angle of the corresponding supercell. From a linear fit (red line) we extract the (apparent) zero-strain band offsets (empty red circles). The green circles show band offsets after the electric field corrections.

of a supercell as:

$$\Theta = \Theta_{(n',m')} - \Theta_{(n,m)} = \arctan\left(\frac{\sqrt{3}m'}{2n'+m'}\right) - \arctan\left(\frac{\sqrt{3}m}{2n+m}\right). \tag{6.1}$$

In the creation of the commensurate supercells a strain ϵ is inevitably induced in one of the layers. As in chapter. 5, this strain is fully put on the graphene layer, due to its resilience towards strain [79, 80, 144, 145, 146]. As this strain can be very high ($|\epsilon| = 10\%$), we do not relax the structure, as argued in Sec. 4.5. We use a fixed interlayer distance of $d = 3.5$ Å. For a list of all heterostructure supercells see Tab. 6.2, and for depictions of examples see Fig. 6.1.

6.2 Band structures

Performing DFT calculations provides us with band structures of all twisted heterostructure supercells, examples of which can be found in Fig. 6.2 (for the 1QL case only). It additionally shows the zooms to the Dirac cones and their in-plane spin textures. The first notable feature is that at Γ, the TI bands (grey dots) do indeed not exhibit a fully formed surface state, but rather the remnant of a surface state, i.e. a surface state with a large gap induced by finite size effects. Let us first analyze the band structure of the twist-angle range $0^\circ \leq \Theta \lessapprox 20^\circ$. Here, the graphene Dirac cone always resides at the K point of the supercell's 1st Brillouin zone (BZ), as we again do not allow for heterostructure supercells with backfolding to Γ. Energetically, the Dirac cone neither resides within the gap of the surface state, nor within the TI bulk band gap. Nevertheless, it is locally within a band gap, i.e. there are no TI states close in energy folded back on top of it. Hence, there is no strong hybridization with the TI states, rather proximity effects comparable to those in graphene/TMDC heterostructures. For the $\Theta = 30^\circ$ case, the situation is different. Here, the Dirac cones of K and K' both fold back to Γ forming an eight-band Dirac cone, which sits somewhere above the TI surface state (for the 1QL case: in an energy gap between the surface state and bulk bands; in the 3QL case: between two bulk bands). The consequences of this for the proximity SOC will be discussed in detail in Sec. 6.4.

We define a band offset between the TI's and the graphene's band structure as the energy difference between the Dirac cone and the 'conduction band' minimum of the TI surface state remnant (see inset in Fig. 6.1(e)). Note that, in the heterostructure this 'conduction band' is technically no longer the conduction band, as the Fermi level rises due to charge transfer effects from the graphene, hence the quotes. As discussed in Subsec. 4.5.1, the strain ϵ has a major influence on the band offset in the heterostructure. Hence we use (in the same fashion as in Chap. 5) an electric field to counteract this effect. Fig. 6.1(e) shows the corrected band offsets as green dots. They are aimed towards representing the zero-strain offsets (as extracted from the linear fits), which are $\Delta E = 396$ meV for Bi_2Te_3 and $\Delta E = 671$ meV for Bi_2Se_3.

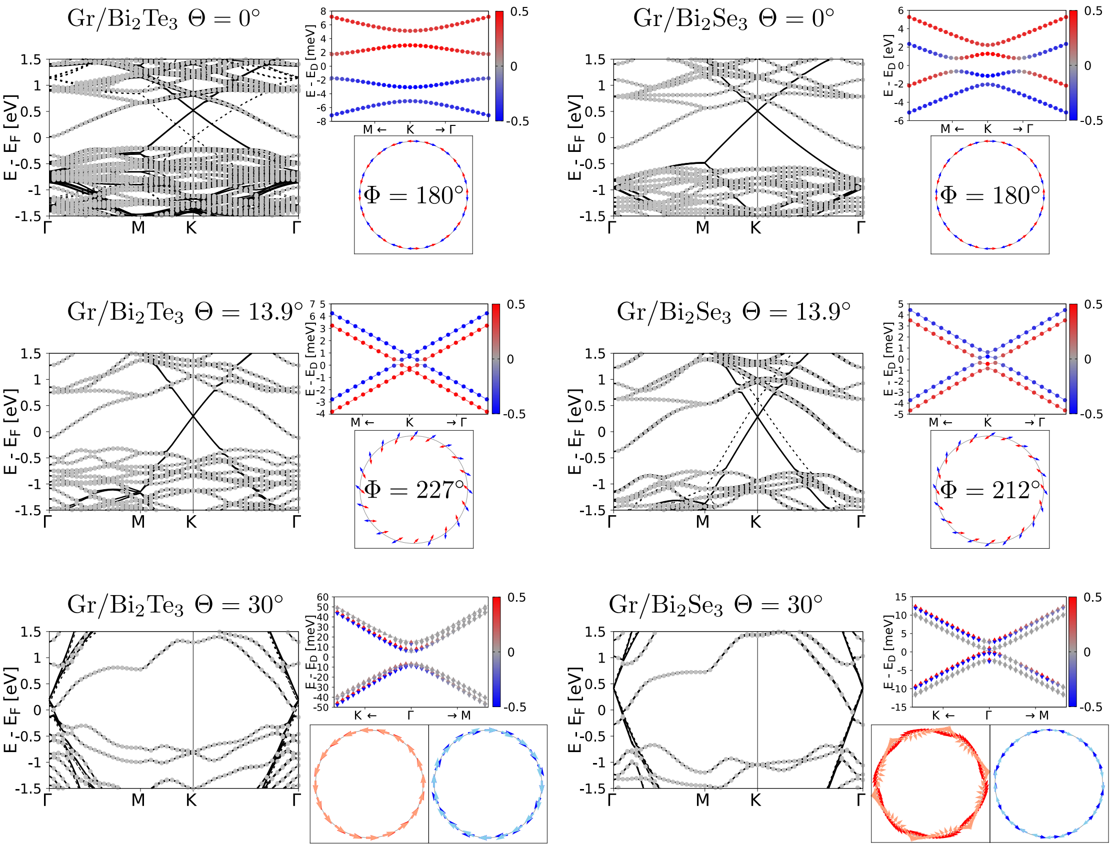

Figure 6.2: DFT band structures of graphene/TI heterostructures using Bi_2Te_3 (first column) and Bi_2Se_3 (second column), and for three different selected twisting angles $\Theta = 0°, 13.9°, 30°$. On the left of each panel we show the band structures along high symmetry lines. Here, TI orbitals are shown in grey, while the solid (dashed) lines come from graphene states with (without) the electric field corrections. The Fermi energy E_F used in the scale is taken from the cases without electric field correction. In addition to that, zooms to the (electric-field corrected) Dirac cone (with color coded spin-z) and their in-plane spin-textures are shown. In the former, dots indicate DFT data, while solid lines represent the fits from the model Hamiltonian (Eq. (4.43)). In the latter, red (blue) arrows indicate in-plane spin in the energetically lower (higher) valence band. Since for the $\Theta = 30°$ cases the band structure comprises eighth bands, we show two plots: one with red and orange arrows for the energetically lower pair of valence bands and one with blue and light-blue arrows for the energetically higher pair of valence bands. In this case, the conduction bands show the same structure. We extract the Rashba angle Φ for all, but the $\Theta = 30°$ case. Note that the zoomed band structures of the $\Theta = 30°$ cases use an enlarged k window (by a factor of 3 for Bi_2Se_3 and 15 for Bi_2Te_3).

6.3 Extracted SOC parameters $0^\circ \leq \Theta \lessapprox 20^\circ$

In the following, the extracted SOC parameters with band offset corrections (see Fig. 6.3 and Tab. 6.4) for the twist-angle range $0^\circ \leq \Theta \lessapprox 20^\circ$ are discussed. In this range, the interlayer interaction (see Sec. 4.4) connects the Dirac cone almost exclusively to bulk states. Furthermore, the Dirac cone is always located locally within a band gap (after electric field corrections). Hence, the SOC is both in magnitude and flavor akin to the SOC in graphene/TMDC heterostructures (see Chap. 5). This means that both λ_{KM} and Δ are negligibly small, leaving Rashba and valley-Zeeman SOC as dominating SOC parameters.

Fig. 6.3(b) and (c) show parameters λ_{R}, λ_{VZ} and Φ as function of the twist angle. The first notable feature is the sign switch of λ_{VZ} at $\Theta \approx 10^\circ$ for both $\mathrm{Bi_2Te_3}$ and $\mathrm{Bi_2Se_3}$. Actually, this change of sign does not only appear when sweeping the twist angle Θ, but also when sweeping the strain ϵ, as illustrated by Fig. 6.3(a). It shows the TI's 1st BZ and – for each heterostructure supercell – the k point, with which the Dirac cone interacts and inherits its SOC from. As discussed in Sec. 4.4, the location of this point depends on both the twist angle and the strain. As each point is color coded with the sign of λ_{VZ} extracted from this supercell, one can easily see a sign switch at high positive strains $\epsilon \approx 10\%$ (for $\mathrm{Bi_2Te_3}$) or $\epsilon \approx 5\%$ (for $\mathrm{Bi_2Se_3}$) for twist angles $10^\circ \lessapprox \Theta \lessapprox 25^\circ$. The magnitude of the Rashba SOC λ_{R} starts with intermediate magnitude at $\Theta = 0^\circ$ and then is very weak for $5^\circ \lessapprox \Theta \lessapprox 20^\circ$. Only for the data point $\Theta = 21.1^\circ$ of the $\mathrm{Bi_2Se_2}$ based structures, a sharp rise in λ_{R} is witnessed. This is the same data point, where also a sharp sign change of λ_{VZ} occurs. Both of these irregularities are likely related to the vicinity of its 'point of interaction' to the surface state (see the green line in Fig. 6.3(a)). We additionally find that the Rashba angle Φ is significantly more susceptible to the twist angle than it is the case for graphene/TMDC heterostructures (see Chap. 5 and Chap. 7). For small twist angles $0^\circ < \Theta \lessapprox 15^\circ$, Φ increases slowly, only to then rapidly rise up to values of $\Phi \approx 400^\circ$. This means that almost all values $0^\circ \leq \Phi \leq 360^\circ$ (or $180^\circ \leq \Phi \leq 540^\circ$) can be realized by adjusting the twist angle Θ. Hence, in principle both REE and UREE can be readily realized in graphene/TI systems. We discuss the ramifications on those CSC effects in Sec. 6.5.

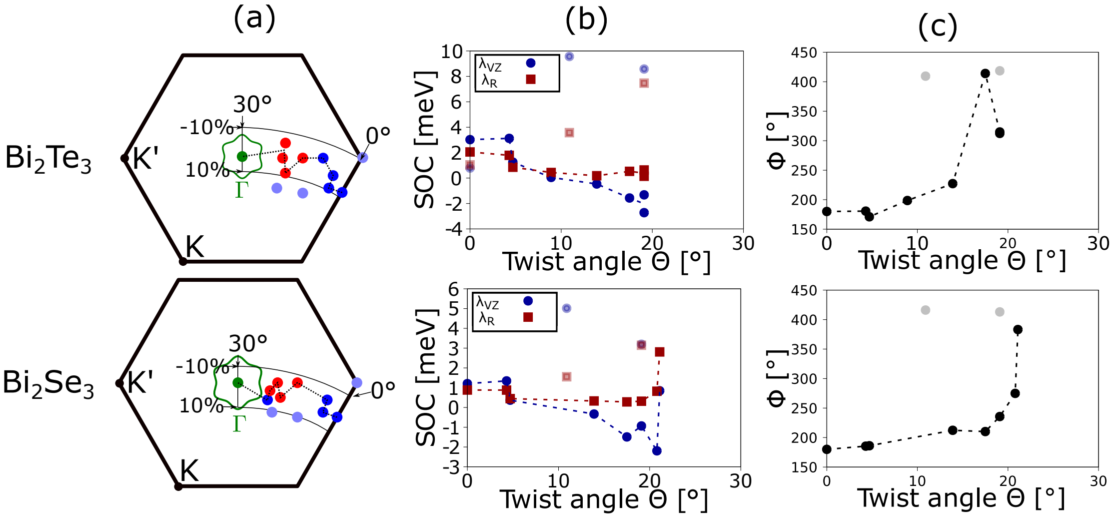

Figure 6.3: Extracted SOC parameters of the graphene Dirac cone in graphene/Bi$_2$Te$_3$ and graphene/Bi$_2$Se$_3$ heterostructures with electric field corrections. (a) shows the TI BZ and the annular sector (as in Fig. 4.5) in which interlayer interaction of the Dirac cone can take place for a given range of twist angle ($0° \leq \Theta \leq 30°$) and strain ($-10\% \leq \epsilon \leq 10\%$). For each heterostructure supercell, the filled circle indicates the region in which the Dirac cone couples to the TI Bloch states. Blue (red) circles correspond to supercells, where positive (negative) valley-Zeeman SOC was extracted. The green circle represents the Γ point as well as the 30° supercell connecting to it. The green line indicates the cut of the (band offset corrected) Dirac cone energy through the surface state remnant. The dotted line connects the relevant points with ascending twist angle in the same order as the guide to the eyes in (b) and (c). (b) shows Rashba SOC λ_R (red squares) and valley-Zeeman SOC λ_{VZ} (blue circles) as function of the twist angle Θ. Data points from supercells with excessive built-in strain of $|\epsilon| > 10\%$ are de-emphasized (transparent). The dotted line is a guide for the eyes. (c) shows the twist-angle dependence of the Rashba angle Φ. Again, data points with $|\epsilon| > 10\%$ are de-emphasized (grey).

6.4 Extracted SOC parameters 30°

The combination of a graphene $\sqrt{3} \times \sqrt{3}$ supercell ($n = m = 1$) and a TI 1×1 supercell ($n' = 0, m' = 1$) results in a supercell with interesting properties. We refer to it as the $\Theta = 30°$ supercell, although one can in principle also construct other possible heterostructure supercells with the same twist angle. However, as these all have either too high strain or involve too many atoms (resulting in too high computational cost), we could not use them for extracting SOC parameters. Additionally, this specific highly commensurate supercell is appearing in experiments [139, 140] utilizing 'bottom-up' manufacturing of the samples (e.g. CVD). There are three relevant properties by which this cell differs from the ones discussed in Sec. 6.3.:

1. It is a notably small supercell. As discussed in Sec. 4.5, the lateral shift has almost no influence on the proximity SOC in heterostructure supercells beyond a certain size. For this small supercell, however, shifting plays an important role.

2. Since $n - m = 0$, we find that the K and K' point of the primitive graphene unit cell fold back to the Γ point in the supercell's 1st BZ.

3. Furthermore, the Dirac cone is not only folded back on top of the TI surface states at the Γ point, but it is also connected to it via interlayer interaction (as discussed in Sec. 4.4).

In accordance with the first point, we find that the form of the proximitized Dirac cone varies greatly with the lateral shift between the layers (see Fig. 6.4). We show the results for three different shiftings 'Hollow', 'Top' and 'Bridge'. The 'Hollow' position is special as its symmetry demands that all graphene sites experience the same on-site potential. As a consequence, the eight-band Dirac cone consists of four almost-degenerate band pairs with only μeV splittings within them. We emphasize that, although these splittings are very small, they are no numerical artifacts and no symmetry of the system demands that they are exactly degenerate. However, the on-site potentials, which seem to be the main driving forces for splitting up these bands, are missing in this case. For all other shifting situations there are eight well-separated bands (except for the Γ point, where the degeneracy is demanded by Cramer's rule). Since the 'Hollow' shifting is also the energetically most favourable one, we will only use this configuration from now on.

6.4.1 Distinguishing 'type 1' and 'type 2' band pairs

Further analyzing the Dirac cone of this 'Hollow' case, we find that the almost-degenerate band pairs fall into either one category. Forward from here, we will call them band pair of 'type one' and 'type two'. Our results show that a Dirac cone will always consist of two band pairs of each type, occurring in an alternating fashion, i.e. the band pairs (going from energetically low to high) will follow one of two patterns: 1-2-1-2 or 2-1-2-1. It should be noted that which of these two patterns occurs can be changed for example by

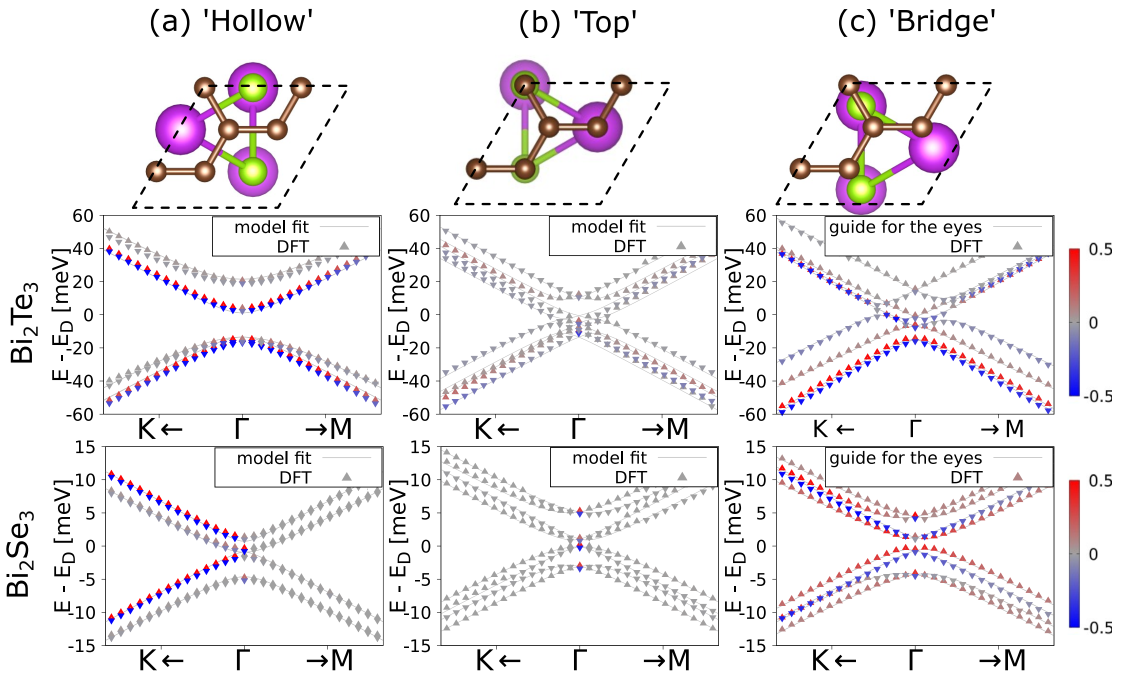

Figure 6.4: Different laterally shifted supercells for the $\Theta = 30°$ case and their low energy band structures with color coded spin-z. The triangles represent DFT data. The upwards and downwards pointing triangles represent DFT data from the almost degenerate band pairs. If the triangles are just touching, the two bands are degenerate. The lines in (a) come from a fit assuming a four-band Hamiltonian, while the lines in (b) come from an eighth-band Hamiltonian fit including different on-site potentials (see Ref. [44]). The lines in (c) are merely a guide to the eyes.

increasing the thickness of the TI or by applying an external electric field (see Ref. [44]). But how exactly do ’type one’ and ’type two’ differ? In Fig. 6.5, the differences between the two types are illustrated. The key differences are:

1. On the one hand, ’type one’ band pairs show barely any out-of-plane spin texture. The spin-z expectation values of ’type two’ band pairs, on the other hand, show a strong polarization, which is anisotropic. The bands are most polarized moving towards the K point, but unpolarized moving towards the M point (see Fig. 6.5(a) and (d)).

2. The splittings within each band pair is also different for the two types. Although for both types the splittings are (close to the Dirac cone) on the μeV scale, the splittings of the ’type one’ band pairs are usually larger by at least one order of magnitude (see Fig. 6.5(c)).

3. We showed examples of the in-plane spin textures in the last row of plots in Fig. 6.2. These are also tied to the type of band pair and repeat in an alternating fashion.

This is especially astonishing as in-plane spin textures caused by usual Rashba SOC would follow a different sequence (namely 1-2-2-1).

4. The hybridization with the TI states is significantly higher for the 'type one' bands (see Fig. 6.5(e)). Furthermore, in relative terms, 'type one' bands hybridize more with the surface states (higher *s*-orbital content) and 'type two' bands more with TI states lying deeper in the valence or conduction bands (higher content of *p*-orbitals with $m_j = \pm 3/2$), as shown in Fig. 6.5(b). Therefore, the out-of-plane spin texture of the 'type two' bands is akin to those of the deep-lying TI bulk states (Fig. 6.5(f)).

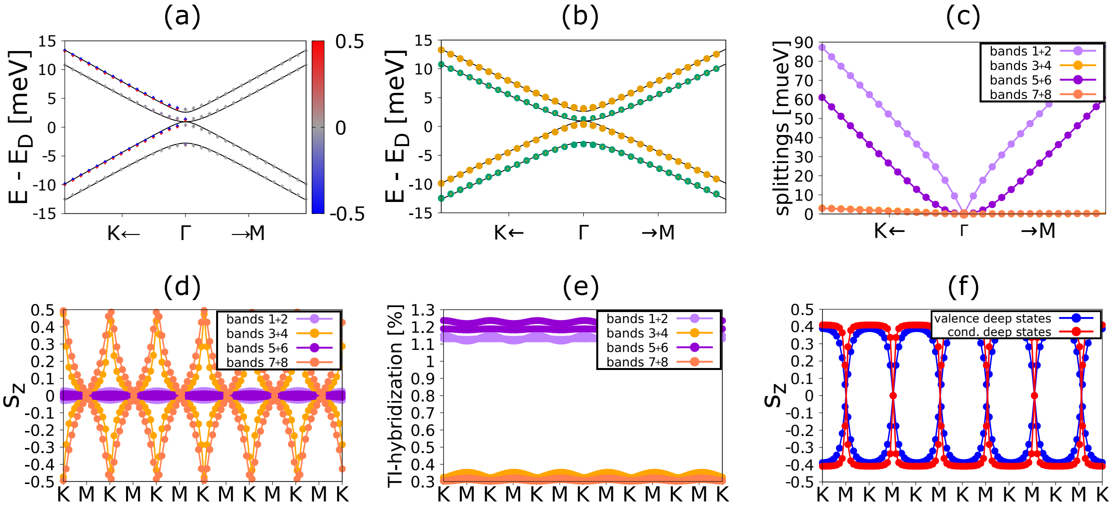

Figure 6.5: The two types of band pairs of the eight-band Dirac cone for $\Theta = 30°$ for the case of graphene on 1QL Bi_2Se_3 without electric field correction. (a) and (b) show the Dirac cone, with color coded spin-z (a) and color coded orbital decomposition (b). In (b) green dots show TI s-orbital contribution, while yellow dots show p-orbital contribution with $m_j = \pm 3/2$. (c) shows the (μeV) splittings within the band pairs. Plots (d)-(f) are concerned with the properties along a circular path around the Dirac cone 55 meV above the Dirac point. Here, labels 'K' and 'M' indicate whether the k point on the path lies on the Γ-K or Γ-M connection line, respectively. (d) and (f) show spin-z expectation values of the Dirac cone and a selected TI bulk states (far inside the TI valence and conduction band), respectively. (e) shows the contribution of TI orbitals to the Dirac cone states. Labeling of the bands is energetically ordered, e.g. 'band 1+2' refers to the energetically lowest valence band pair.

6.4.2 Spin texture & fitting method

Fitting the 30° case Dirac cones is a challenging task, as the spin textures are very unusual. The out-of-plane spin texture (as also found and discussed in Ref. [41]) is based on a

μeV splitting and is therefore very elusive. The in-plane spin texture seems to align in some cases with what might be expected from usual Rashba SOC. However, the mentioned ordering of the bands (1-2-1-2 instead of 1-2-2-1) is inconsistent with the model Hamiltonian. Since for $\Theta = 30°$, symmetry demands both $\lambda_{\text{VZ}} = 0$ and $\Phi = 0$, it is apparent that these spin textures come from the special highly commensurate shifting-sensitive nature of the supercell. One can get similar results for both the out-of-plane and in-plane spin textures by using a full tight binding Hamiltonian (see Eq. (4.42)) and adding terms taking into account the full real space nature ($\sqrt{3} \times \sqrt{3}$ supercell) of the heterostructure. This has been done in Ref. [41] and we also used such a Hamiltonian in the appendix of Ref. [44]. However, none of the models were able to describe the specific ordering based on the two types of band pairs, but can only describe the spin texture of one band pair at a time.

As we only use the 'Hollow' case band structures, we can simplify the task of fitting by simply using the same four-band model Hamiltonian (see Eq. (4.43)) and ignoring one band of each band pair. The upside of this approach is that the results are easily comparable to the ones for cases $0° \leq \Theta \lessapprox 20°$. The downside of this approach is that we explicitly do not attempt to describe any spins and use only energies for fitting. However, a comparison of the fitting results for the four-band model Hamiltonian and the eight-band tight-binding Hamiltonian shows, that the parameters are very much comparable, with two differences: Firstly, the usual Rashba SOC is replaced by an in-plane Rashba SOC corresponding to a specific real space arrangement of electric fields. Secondly, there is an additional Kekule distortion. For details of this, see Ref. [44]. Hence, we choose this simple model Hamiltonian fit approach, arguing that even though the complicated spin texture is not represented, some key aspects of the Dirac cone band structure can nevertheless be captured.

6.4.3 Extracted model parameters

General remarks

In the following, we will analyse the results of the fitting. Firstly, since the heterostructure supercell in question has a twist angle of $\Theta = 30°$, symmetry rules (see Subsec. 4.4.4) demand $\lambda_{\text{VZ}} = 0$. Furthermore, as we are concerned with the 'Hollow' case, all graphene atoms experience the same on-site potential, therefore we find $\Delta = 0$ as well. More surprisingly, we do find a very substantial amount of Kane-Mele SOC (in accordance with Ref. [41]). Hence, the only two non-zero parameters are λ_{R} and λ_{KM}, which both appear in the meV scale. According to Ref. [19], Kane-Mele SOC is not allowed in incommensurate structures. Although all heterostructure supercells discussed in this thesis are commensurate, a non-negligible λ_{KM} does not occur in any other structure except this one. The reason for this might either be its special highly-commensurate structure or its connection to the TI surface state. The former seems plausible, as it is the incommensurability, which prohibits λ_{KM} in the tight binding calculations. However, this proposition is somewhat discredited by the fact that one of the $\Theta = 30°$ cases of the graphene/TMDC structures (see Chap. 5) has a similar size and does not show any relevant λ_{KM}. Furthermore, apart from this one case, there is no correlation between supercell size and λ_{KM} in any of the data. The latter proposition (connection of Dirac cone and TI surface state) is also reasonable, especially as the Kane-Mele SOC is very sensitive to the position of the Dirac cone within the TI surface state (remnant), as will be discussed in the following.

Electric field dependence

As discussed previously, for the $\Theta = 30°$ case, the Dirac cone folds back on top of the TI surface state and interacts with it directly through interlayer interaction (see Sec. 4.4). Consequently, both the concrete form of the surface state and its relative position (band offset) to the Dirac cone will have a much more pronounced impact on the proximity SOC than for the cases with $0° \leq \Theta \lessapprox 20°$. While the form of the surface state is changed by the thickness of the TI slab, the band offset can be varied by applying an external transverse electric field. Therefore, we investigated the electric field dependence of the SOC parameters for two TI slab thicknesses (1QL and 3QL) for the $\Theta = 30°$ case. In order to analyze further, which TI bands provide the proximity SOC to the Dirac cone, we additionally provide an orbital analysis of both the Dirac cone and the TI bands.

Fig. 6.6 shows the SOC parameters and orbital composition of the Dirac cone states, while shifting it in energy through the TI band structure within the range marked in black. We find that, when the Dirac cone approaches one of the TI bands, the total SOC becomes larger, with both SOC parameters reaching up to 20 meV. A very remarkable feature is the change of sign for λ_{KM}, which occurs during the energetic shifting. This behaviour can be observed in three out of the four scenarios. In experiment the band offset can be easily tuned by gating. Such a gate control of the Kane-Mele SOC opens up tremendous opportunities for spintronics, as the surface states of the QSHE can be activated at will. Furthermore, one could even engineer edge states within a graphene sheet between two regions of opposite sign of λ_{KM}.

Analyzing the orbital decomposition (see Fig. 6.6, 'orbital decomposition'), we find that, unsurprisingly, the general overlap with TI states (black curve 'TI content') of the Dirac cone states increases, when the Dirac cone is moved in close vicinity to a nearby TI state. This 'TI-content' of the Dirac states mostly consists of TI p-orbitals ($\approx 90\%$) and to a lesser degree of TI s-orbitals ($\approx 10\%$, dark-green curve). We see, that this s-orbital content increases, when moving the Dirac cone towards the surface state in most cases. d-orbital contribution is negligible. The p-orbitals can further be split into those with $m_j = \pm 1/2$ and $m_j = \pm 3/2$. This distinction is similar to the distinction between p_z-orbitals (corresponding to $m_j = \pm 1/2$) and $p_{x/y}$-orbitals (corresponding to $m_j = \pm 3/2$) for the spinless case. We find that a decent amount ($\approx 20\%$, orange curve) of the p-orbitals have $m_j = \pm 3/2$. This percentage is surprisingly high, considering that the Dirac cone consists of p_z orbitals and that the states with high $m_j = \pm 3/2$ content are not energetically close. When the Dirac cone is brought close to nearby TI states, however, it acquires more of their $m_j = \pm 1/2$ character, lowering the orange curve. In conclusion, the

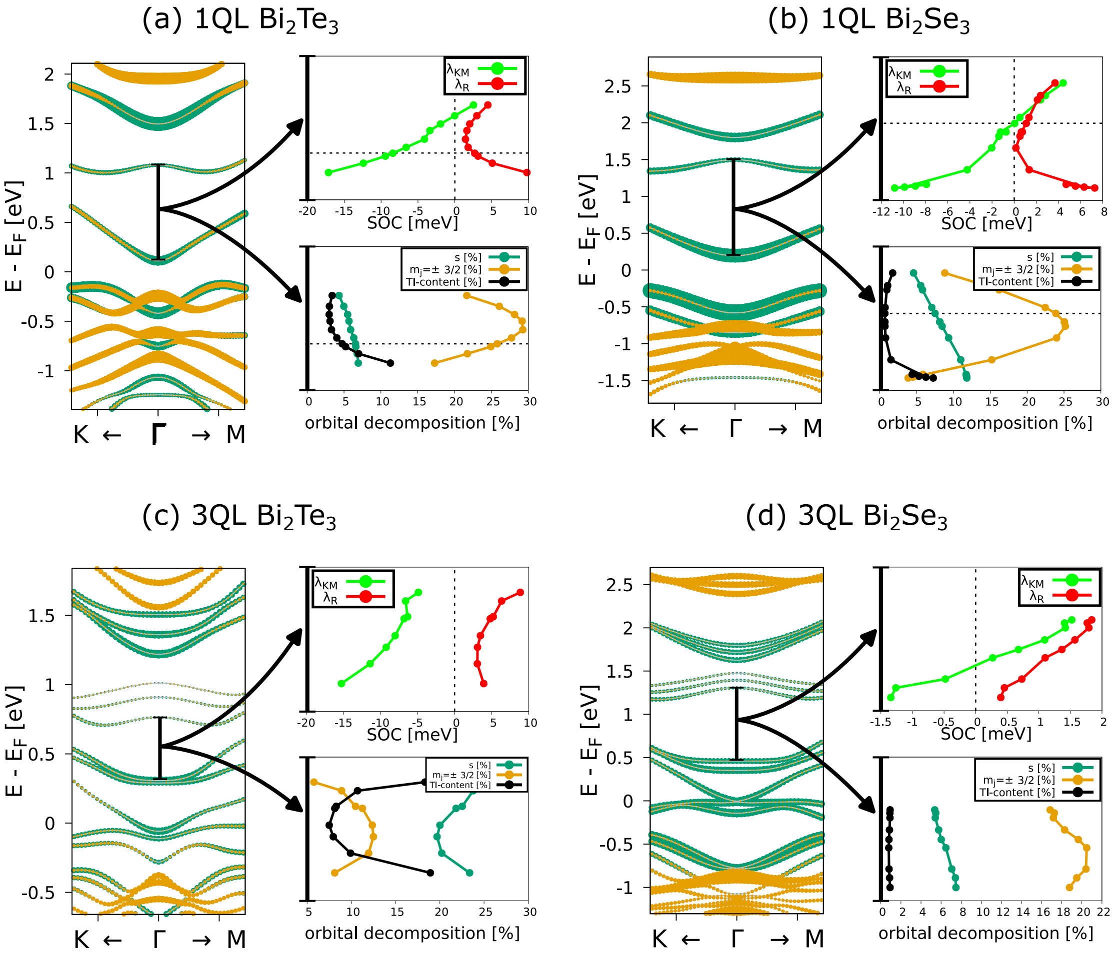

Figure 6.6: Electric field dependence of the SOC parameters for the 30° case: The four panels show the four cases (1QL or 3QL; Bi_2Te_3 or Bi_2Se_3). The left plot in each panel shows the TI band structure around the Γ point. The projection of each state onto the TI s-orbitals are depicted as green dots and the projection onto p-orbitals with $m_j = \pm 3/2$ as yellow dots. The graphene Dirac cone is shifted (within the energy range depicted as black bar) using an electric field in the corresponding graphene/TI heterostructure. We show the development of the SOC parameters (top right of the panel) and the orbital decomposition (bottom right of the panel) of the Dirac cone states during this shifting. For the orbital composition, we use states along the high symmetry path around K and average over a k range of $0.04\frac{1}{\text{Å}}$ (for Bi_2Te_3) or $0.004\frac{1}{\text{Å}}$ (for Bi_2Se_3). For the 1QL cases (a) and (b) the horizontal dotted lines indicate the position of the Dirac cone in the electric field corrected band structure (zero-strain band offset). Hence, the parameters at this line correspond to the zooms in the last line of plots in Fig. 6.2. In the 'orbital decomposition' plot, the black curves show the content of TI-orbitals in the Dirac cone states. The dark-green curve shows, how much of those contributing TI states are TI s-orbitals. The yellow curve shows, how much of the contributing TI p-orbitals have quantum number $m_j = \pm 3/2$.

orbital composition of the proximitized Dirac cone suggests that the Dirac cone draws its proximity SOC from the nearby TI states (e.g. surface state, dominated by s-orbitals and p-orbitals with $m_j = \pm 1/2$) to a lesser degree than expected. Rather, it hybridized very well with the more deep-lying TI states (more than 2 eV away, dominated by p-orbitals with $m_j = \pm 3/2$).

6.5 Charge-to-spin conversion efficiencies

The Rashba angles depicted in Fig. 6.3(c) show a great tunability and are hence very promising for realizing UREE in graphene/TI heterostructures. Therefore, we will in the following analyze the CSC (REE and UREE) efficiencies of our heterostructure supercells as determined by linear response theory (see Sec. 4.6). As model Hamiltonian parameters we use the SOC parameters after electric field correction (see Fig. 6.3 and Tab. 5.4). Fig. 6.7 shows the REE and UREE efficiencies as function of the twist angle Θ for the angle range $0° \leq \Theta \lessapprox 20°$ for graphene proximitized with either Bi_2Te_3 or Bi_2Se_3. In the case of Bi_2Te_3 one can clearly see that although the rising Φ promises great UREE yields, these are very much diminished, as at the same time λ_R is dropping, reducing both REE and UREE efficiencies drastically. While the same things seems to happen in the case of Bi_2Se_3 at first, the last data point shows a sign change and sharp increase in total value of both REE and UREE. The reason for this, as discussed in Sec. 6.3, is probably that it couples to a k point close to the TI surface state. Overall, it is not possible to discern a clear trend for these cases.

In the $\Theta = 30°$ case it is not possible to calculate reliable CSC efficiencies with our approach, as in our fitting procedure spins were neglected. In principle, one could extract the energies and matrix elements in Eq. (4.91) and Eq. (4.92) directly from DFT instead of the model Hamiltonian. However, our code is not designed to do so and we hence limit ourself to a qualitative argument. The most outstanding property of the CSC in the $\Theta = 30°$ systems is that, due to its unusual ordering of the in-plane spin textures of the bands (1-2-1-2 instead of 1-2-2-1), the (U)REE efficiencies will be symmetric with respect to the Fermi level. This is in stark contrast to the antisymmetric structure witnessed in graphene with usual Rashba SOC (see Fig. 4.11(a)). Since the TI surface state shows such a symmetric structure in the CSC as well, this property is clearly inherited from the TI surface state. Therefore, one has to call into question the approach of distinguishing CSC from TI surface states and from proximitized graphene by examining its gate dependence in graphene/TI heterostructures [204, 205]. Another question which arises is, whether such structures support a conventional REE, a UREE or a mixture of both. Judging from the DFT in-plane spin textures (see last row of plots in Fig. 6.2), it appears that only REE is occurring, as is the case in graphene/TMDC structures with $\Theta = 30°$.

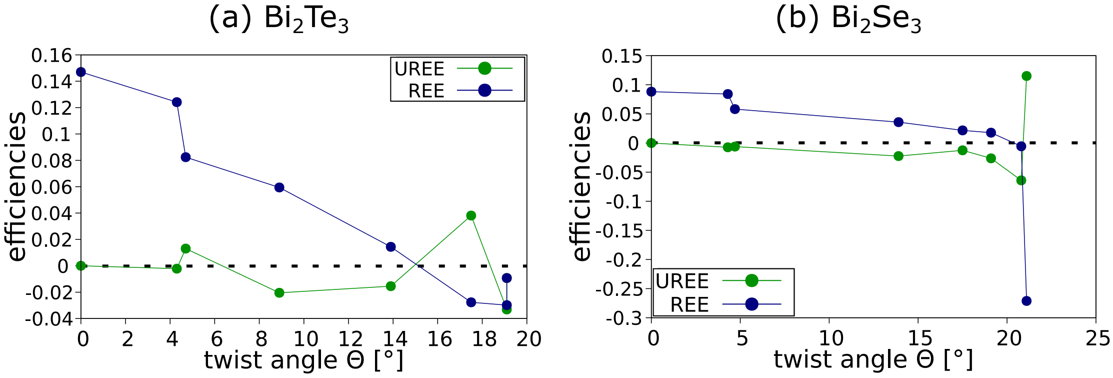

Figure 6.7: Twist-angle dependencies of the REE and UREE efficiencies of graphene on 1QL Bi_2Te_3 (a) and 1QL Bi_2Se_3 (b) for the range $0° \leq \Theta \lessapprox 20°$ as determined by linear response theory (see Sec. 4.6).

6.6 Summary

We generated an array of twisted graphene/Bi_2Se_3 and graphene/Bi_2Te_3 heterostructure supercells and performed DFT calculations on them, determining their band structure and especially Dirac cone properties. After band offset corrections with an electric field, the low energy spectra were fitted to a model Hamiltonian and the resulting extracted SOC parameters were plotted against the twist angles. Here, a distinction between the $0° \leq \Theta \lessapprox 20°$ twist-angle range and the special highly commensurate $\Theta = 30°$ case had to be made. For most cases with $0° \leq \Theta \lessapprox 20°$ the influence of the TI surface state is very limited. Hence, we observed SOC parameters akin to the ones of the graphene/TMDC heterostructures, i.e. a combination of Rashba SOC and valley-Zeeman SOC. A special feature that could be witnessed is the change of sign of λ_{VZ} at $\Theta \approx 10°$ for both graphene/Bi_2Se_3 and graphene/Bi_2Te_3. Another feature is the large tunability of the Rashba angle Φ. Although this seems promising for realizing UREE, subsequent CSC calculations utilizing linear response theory suggest that (due to the low overall magnitude of λ_R for intermediate twist angles) high values of UREE could only be achieved for one graphene/Bi_2Se_3 heterostructure supercell with $\Theta = 21.1°$. This supercell's special properties might arise from the fact that its Dirac cone couples to a point close to the TI surface state.

For the highly-commensurate case $\Theta = 30°$, the Dirac cone couples directly to the TI surface state via interlayer interaction. As this small supercell is very susceptible to lateral shifting, we use only the low energy and high-symmetry 'Hollow' case, in order to simplify the considerations. The eight bands of its Dirac cone form four almost-degenerate band pairs, which can be categorized into two types differing in spin texture and TI hybridization. We find that these different band pairs occur in an alternating fashion. This is especially remarkable as the in-plane spin textures also follow this alternating ordering, which should result in a CSC symmetric around the Dirac cone energy. Such behaviour is known rather from TI surface states, all the more demonstrating the hybridization between the Dirac cone and the TI surface state. Although its complicated and elusive spin texture cannot be captured by our model Hamiltonian, we find that fitting it only by using the energies still gives valuable insight into its nature. That is, most outstandingly, that it involves Kane-Mele SOC, which opens up the possibility for realizing the QSHE. Moreover, we find that the sign of this Kane-Mele SOC can be changed by applying a transverse electric field and therefore changing the band offsets between the TI and the graphene. This opens up a possible route of engineering the QSHE by controlling the gate voltage.

Table 6.3: Parameters extracted from the band structure calculations before correcting the band offset with an electric field. For both Bi_2Te_3 and Bi_2Se_3 and for all supercells of Tab. 6.2 the twist angle Θ and strain ϵ are listed alongside the model Hamiltonian parameters, except if the band offset is too large, shifting the Dirac cone into the TI bands. Extracted model Hamiltonian (Eq. (4.43)) parameters are: staggered potential Δ, Kane-Mele SOC λ_{KM}, valley-Zeeman SOC λ_{VZ}, magnitude of the Rashba SOC λ_{R} and Rashba angle Φ. We additionally list the band offset ΔE of the Dirac cone with respect to the TI surface band.

Θ	ϵ	Φ	Δ	λ_{KM}	λ_{VZ}	λ_{R}	ΔE
[°]	[%]	[°]	[meV]	[meV]	[meV]	[meV]	[eV]
Bi_2Te_3							
0	-10.85	180	2.325	0.698	1.256	1.452	0.972
0	6.98	180	0.002	-0.004	1.934	0.748	-0.015
4.3	8.22	152	0.000	-0.006	2.038	0.512	-0.072
4.7	1.54	146	0.002	-0.003	1.019	0.557	0.141
8.9	-3.93	199	0.418	-0.002	-0.319	0.342	0.458
10.9	16.72	19	-0.067	0.271	13.694	7.140	-0.309
13.9	-1.1	-130	0.010	0.011	-0.464	0.178	0.407
17.5	8.22	-10	0.001	0.154	3.513	2.897	-0.044
19.1	1.08	-42	-0.001	0.024	-0.814	0.980	0.114
19.1	17.93	-	-	-	-	-	-0.393
19.1	-5.66	-	-	-	-	-	0.772
30	2.94	-	0.000	-12.400	0.000	5.089	0.255
Bi_2Se_3							
0	-15.79	180	1.496	0.252	0.726	0.816	1.423
0	1.05	180	0.002	-0.007	1.217	0.901	0.704
4.3	2.22	-178	-0.001	-0.006	1.195	0.621	0.518
4.7	-4.09	190	0.001	-0.005	0.381	0.616	0.831
10.9	10.25	47	-0.049	0.002	3.175	1.024	0.240
13.9	-6.58	-155	0.004	0.007	-0.496	0.623	0.982
17.5	2.22	17	0.080	0.027	-0.552	0.076	0.519
19.1	11.4	47	0.035	0.006	2.304	2.217	0.225
19.1	-4.52	-120	0.005	0.002	-0.917	0.299	0.682
20.8	-0.17	-41	0.001	-0.007	-1.258	0.468	0.524
21.1	4.78	23	0.022	-0.028	0.600	1.680	0.388
30	-2.77	-	0.000	0.517	0.000	1.340	0.754

Table 6.4: Parameters extracted from the band structure calculations after correcting the band offset with an electric field. For both Bi_2Te_3 and Bi_2Se_3 and for all supercells of Tab. 6.2 the twist angle Θ and strain ϵ are listed alongside the model Hamiltonian parameters, except if the band offset is too large, shifting the Dirac cone into the TI bands. Extracted model Hamiltonian (Eq. (4.43)) parameters are: staggered potential Δ, Kane-Mele SOC λ_{KM}, valley-Zeeman SOC λ_{VZ}, magnitude of the Rashba SOC λ_{R} and Rashba angle Φ. We additionally list the band offset ΔE of the Dirac cone with respect to the TI surface band and the electric field used to correct the band offsets.

Θ [°]	ϵ [%]	E-field [V/nm]	Φ [°]	Δ [meV]	λ_{KM} [meV]	λ_{VZ} [meV]	λ_{R} [meV]	ΔE [eV]
Bi_2Te_3								
0	-10.85	5.554	180	2.257	0.528	0.786	1.037	0.529
0	6.98	-3.399	180	0.037	-0.022	3.026	2.054	0.510
4.3	8.22	-3.838	181	0.034	-0.024	3.126	1.791	0.471
4.7	1.54	-2.199	171	-1.936	-0.002	1.254	0.852	0.444
8.9	-3.93	0.247	199	-0.001	0.008	0.050	0.438	0.442
10.9	16.72	-6.171	50	0.109	-0.082	9.562	3.574	0.407
13.9	-1.1	-0.145	-133	0.010	0.006	-0.467	0.183	0.418
17.5	8.22	-3.624	54	0.014	-0.028	-1.568	0.531	0.458
19.1	1.08	-2.406	-45	-0.001	0.005	-1.320	0.143	0.114
19.1	17.93	-5.656	59	-0.034	-0.035	8.578	7.467	0.396
19.1	-5.66	1.797	-48	0.007	0.006	-2.720	0.636	0.427
30	2.94	-0.771	-	0.000	-8.413	0.000	2.703	0.324
Bi_2Se_3								
0	-15.79	-	-	-	-	-	-	-
0	1.05	0.074	180	0.003	-0.007	1.204	0.881	0.692
4.3	2.22	-1.36	-175	0.004	-0.010	1.344	0.879	0.695
4.7	-4.09	1.05	-174	-0.001	0.000	0.369	0.447	0.592
10.9	10.25	-4.114	56	0.054	-0.018	5.016	1.554	0.644
13.9	-6.58	2.216	-148	0.003	0.004	-0.331	0.330	0.664
17.5	2.22	-1.354	-150	0.006	-0.017	-1.490	0.281	0.692
19.1	11.4	-3.624	53	0.003	-0.035	3.197	3.146	0.622
19.1	-4.52	-0.098	-124	0.000	0.000	-0.935	0.315	0.706
20.8	-0.17	-1.313	-85	-0.008	-0.031	-2.194	0.819	0.669
21.1	4.78	-2.36	23	-0.005	-0.074	0.844	2.809	0.632
30	-2.77	0.617	-	0.000	0.049	0.000	1.091	0.700

7 Twist-angle dependent proximity spin-orbit coupling in heterostructures of graphene and $NbSe_2$

In Chap. 5 we already discussed proximity spin-orbit coupling (SOC) in graphene/transition-metal dichalcogenide (TMDC) heterostructures. There, all employed TMDCs (MoS_2, $MoSe_2$, WS_2 and WSe_2) were semiconducting. Using the metallic TMDC $NbSe_2$ instead, can bring about new challenges, but also different physics entailing new possible applications. The most apparent feature of $NbSe_2$ is its superconductivity [109, 110], which can be transferred to graphene via proximity effects [111, 112, 113, 66]. The DFT calculations presented in this chapter are used to reveal the proximity SOC in graphene, but do not describe any superconductivity. However, the flavour of SOC has significant ramifications on the superconductivity. On the one hand, valley-Zeeman SOC (also known as Ising SOC) combined with superconductivity will result in Ising superconductivity, which is very robust against in-plane magnetic fields, as the valley-Zeeman SOC can extend the Pauli limit [207, 109, 208, 209, 210]. Rashba SOC, on the other hand, will result in Rashba-type superconductivity, which is needed in order to realize the superconducting diode effect (SDE) [114, 115, 116, 117, 118]. In the SDE, the interplay of superconductivity, SOC and an external magnetic field in a Josephson junction creates a situation where a supercurrent can flow only in one direction. While tuning the magnitude of the Rashba SOC can be used to tune this effect to a certain degree, especially control of the Rashba angle can be used to realize the radial SDE [211]. In graphene/$NbSe_2$ heterostructures, both SOC and superconductivity can be induced (and tuned by the twist angle) simultaneously in graphene, offering a platform for such effects. $NbSe_2$ additionally displays a charge density wave (CDW) [119, 120, 106] state, where a periodic modulation of the electron ground state density and the atomic lattice occurs, with a typical periodicity of a 3×3 supercell. Whether this can have an effect on the proximity effects on graphene is not clearly known yet. For graphene/1T-TaS_2 heterostructures, the CDW of 1T-TaS_2 in fact seems to heavily impact the proximity SOC [212, 213, 214]. Hence, investigating these structures can be a worthwhile endeavour. Furthermore, there is experimental evidence for the Rashba-Edelstein effect (REE) and unconventional REE (UREE) in graphene/$NbSe_2$ heterostructures [107, 72], with charge-to-spin conversion (CSC) occurring in the proximitized graphene in Ref. [72]. In order to give estimates for CSC efficiencies in the proximitized graphene from theory, we follow a Kubo formula approach with SOC parameters from DFT as input. As other DFT calculations are sparse [111, 215, 216] and do not extract any SOC parameters, there is a definitive need for such an analysis. In order to obtain collinear CSC via the UREE as in Ref. [72], twisted structures need to be considered. We therefore extract the proximity SOC for several different twisted supercells, mapping out the twist-angle dependence of the SOC parameters. However, there are also challenges, which especially the metallic states of NbSe$_2$ entail: If there are NbSe$_2$ states at the same energy and momentum as the graphene Dirac cone, they might hybridize strongly with it and distort it, so that the Dirac cone can no longer accurately be described with a simple model Hamiltonian. Furthermore, even if the Dirac cone stays intact, transport through the heterostructure most likely occurs in both layers. Hence, in order to correctly interpret experimental results, a scheme is required that can disentangle the transport and correctly predict through which layer transport is occurring.

The chapter is based on Ref. [66] and structured in the following way: First, we introduce the twisted supercells used for the calculations in Sec. 7.1. The DFT band structures of the heterostructures and their band offsets are discussed in Sec. 7.2. Challenges regarding the metallic nature of the NbSe$_2$ states are addressed in Sec. 7.3. We extract SOC parameters using a model Hamiltonian and show their twist-angle dependence in Sec. 7.4. Finally, in Sec. 7.5 CSC efficiencies are discussed.

7.1 Twisted supercells

We create the twisted supercell heterostructures by following the scheme in Sec. 4.1. The parameters (n,m) (for the graphene layer) and (n',m') (for the NbSe$_2$ layer) are given in Tab. 7.1. It also lists the strain ϵ, necessary to form commensurate heterostructure supercells, and the interlayer twist angle Θ, which depends on (n,m) and (n',m') and can be determined using the formula, derived in Sec. 4.1:

$$\Theta = \Theta_{(n',m')} - \Theta_{(n,m)} = \arctan\left(\frac{\sqrt{3}m'}{2n'+m'}\right) - \arctan\left(\frac{\sqrt{3}m}{2n+m}\right). \tag{7.1}$$

Contrary to our approach in Chap. 5 and Chap. 6, we also include heterostructure supercells with $n - m = 3 \cdot k, k \in \mathbb{Z}$, even though in such a case the Dirac cones of K and K' fold back on top of each other, making the correct assignment of the sign of λ_{VZ} impossible. These cases are marked with an asterisk in Tab. 7.1. As lattice constants, we used $a_{\mathrm{Gr}} = 2.46$ Å and $a_{\mathrm{NbSe_2}} = 3.48$ Å [111, 217]. The NbSe$_2$ has a thickness of $d_{\mathrm{XX}} = 3.358$ Å [111] and the employed interlayer distance is $d = 3.3$ Å. As previously discussed, strain ϵ is necessary for the formation of commensurate heterostructure supercells; this strain is put on the graphene in all cases, since it is more resilient to strain [79, 80, 144, 145, 146]. Fig. 7.1(a)-(c) illustrate the graphene/NbSe$_2$ heterostructure supercells.

Table 7.1: Structural information of the investigated $NbSe_2$/graphene heterostructures. Integer attributes (n, m) (graphene) and (n', m') ($NbSe_2$) are listed as well as the corresponding strain ϵ (imposed on graphene), twist angle Θ between graphene and $NbSe_2$ and the number of atoms N_{at} in the supercell. If a (n, m) is marked by an asterisk, this indicates that for this supercell it holds $n - m = 3 \cdot k, k \in \mathbb{Z}$ and therefore the Dirac cone is folded back to Γ. Additionally, we list the k-mesh densities of the $n_k \times n_k \times 1$ meshes employed in the self-consistent calculations.

Θ [°]	(n, m)	(n', m')	ϵ [%]	N_{at}	n_k
0.00000	(4 0)	(3 0)	6.0976	59	30
0.00000	(7 0)	(5 0)	1.0453	173	3
1.87177	(3 4)	(2 3)	1.3725	131	6
3.30431	(6 1)	(4 1)	-1.1402	149	6
5.20872	(3 1)	(2 1)	3.8058	47	30
5.20872	(2 4)	(1 3)	-3.6090	95	15
8.94828	(1 5)	(0 4)	1.6303	110	12
10.89339	(2 1)	(1 1)	-7.3905	23	30
11.30178	(4 3)	(2 3)	1.3725	131	6
12.51983	(7 1)*	(4 2)	-0.8516	198	3
13.89789	(2 6)	(0 5)	-1.9128	179	3
13.89789	(5 0)	(3 1)	2.0107	89	12
16.10211	(6 2)	(3 3)	1.9352	185	3
16.10211	(3 3)*	(1 3)	-1.8401	93	15
19.10661	(4 0)	(2 1)	-6.4308	53	18
19.10661	(1 2)	(0 2)	6.9363	26	30
20.48466	(5 2)*	(2 3)	-1.2610	135	6
23.41322	(2 3)	(0 3)	-2.6382	65	21
26.99551	(4 2)	(1 3)	-3.6089	95	15
26.99551	(3 1)	(1 2)	3.8058	47	30
30.00000	(5 0)	(2 2)	-1.9913	86	12
30.00000	(4 4)*	(0 5)	2.0924	171	3

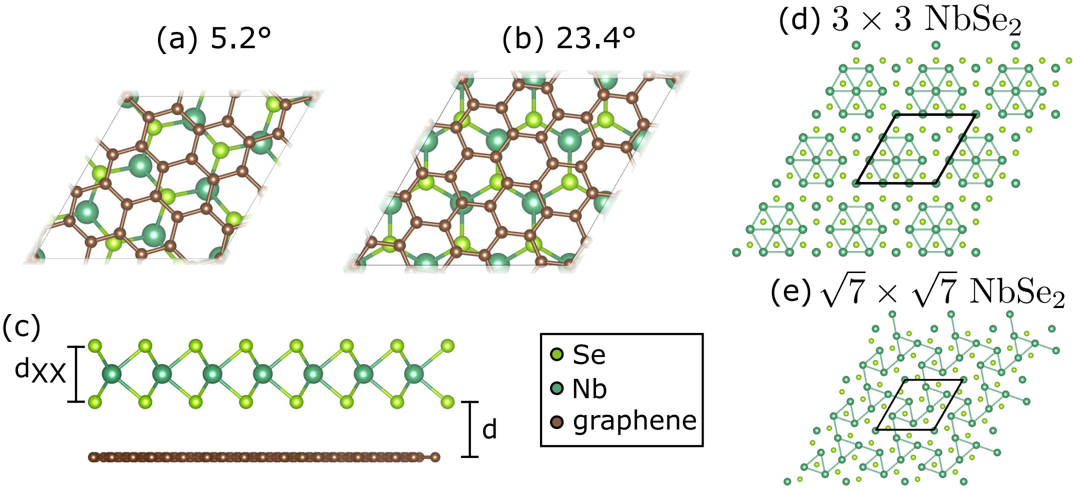

Figure 7.1: Crystal structure of different graphene/NbSe$_2$ commensurate heterostructures. (a)-(b) Bottom view of the 5.2° and 23.4° supercells. (c) Side view of a heterostructure with indicated interlayer distance d and NbSe$_2$ thickness d_{XX}. (d)-(e) Relaxed structures for two examples of graphene/NbSe2 heterostructures, with different underlying NbSe$_2$ supercells (3×3 and $\sqrt{7} \times \sqrt{7}$). The graphene sheet is not shown to better visualize the NbSe$_2$ CDW. To show the subtle atomic reconstructions in the two supercells, we only plot bonds between Nb atoms, if they are less than 3.48 Å apart. The black lines indicate the (3×3 or $\sqrt{7} \times \sqrt{7}$) NbSe$_2$ supercell.

In the main calculations, we do not employ prior structural relaxation, as argued for in Sec. 4.5. However, NbSe$_2$ exhibits a CDW, which comes with an atomic reconstruction with the periodicity of a 3×3 supercell [119, 120, 106]. In order to check, whether the nearby graphene layer has an influence on this reconstruction and also whether the reconstruction has an influence on the Dirac cone of the graphene, we performed additional relaxation calculations on two of the heterostructure supercells. Fig. 7.1(d) and (e) show the relaxed structures. The first one has a twist angle of $\Theta = 0°$ and an underlying 3×3 NbSe$_2$ supercell. Here, the same lattice reconstruction occurs that we witness in the freestanding 3×3 NbSe$_2$ monolayer. Although the filled hexagonal structure is not congruent with the triangular one commonly seen in literature, it is one of the many possible configurations [218]. Most importantly, we see that the graphene layer has barely any influence on the formation of the atomic rearrangement typical for CDW. The other heterostructure supercell has a twist angle of $\Theta = 5.2°$ and an underlying $\sqrt{7} \times \sqrt{7}$ NbSe$_2$ supercell. The rearrangement witnessed in this supercell is much more subtle, with a maximal difference in Nb-Nb bond length of 7.66 mÅ. This is an order of magnitude smaller than the one of the 3×3 supercell (72.44 mÅ). We assume that the formation of this subtle reconstruction is caused by the influence of the graphene layer. Moreover, the relaxation calculations reveal that we underestimated the interlayer distance d by about 3.5%. The effects of the atomic reconstruction on the graphene Dirac cone and the extracted SOC parameters will be presented in Sec. 7.4.

7.2 Band structures & energetic alignments

The DFT band structures are shown in Fig. 7.2(a) and (b) for two different heterostructure supercells. In most situations the Dirac cone (black lines) is energetically located within the $\mathrm{NbSe_2}$ bands (grey dots). This situation corresponds to a negative band offset $E_D - E_\Gamma < 0$ (the fix points for measuring the band offsets are defined in Fig. 7.2(e)). For some cases the Dirac cone is located above these $\mathrm{NbSe_2}$ bands, i.e. the band offset $E_D - E_\Gamma$ is positive. However, these cases are nevertheless not fundamentally different, as the $\mathrm{NbSe_2}$ states showing substantial interlayer interaction with the Dirac cone are located further down in energy (see blue circles in Fig. 7.2(a) and (b)). This will be discussed in more detail in Sec. 7.3. In Fig. 7.2(c) we show this band offset $E_D - E_\Gamma$ plotted against the strain ϵ in graphene. For small strains the linear behaviour of the band offset is less prominent than it was for the heterostructures in Chap. 5 and Chap. 6. Nevertheless, we can establish a decent linear fit providing us with a zero-strain band offset $\Delta E_0 = -109$ meV. However, contrary to Chap. 5 and Chap. 6, we do not use external electric fields to adjust the band offsets to match this zero-strain band offset. The reason is, that we only use heterostructure supercells with $|\epsilon| < 5\%$ for the determination of the SOC parameters. This is different to Chap. 5 and Chap. 6, where the limit was set at $|\epsilon| < 10\%$, allowing for much more strain induced change in band offsets. Hence, we chose not to utilize the electric field band offset correction scheme.

One could alternatively define the band offsets using the band edge of the bands stemming from the $\mathrm{NbSe_2}$ K point (from the 1st Brillouin zone (BZ) corresponding to the primitive $\mathrm{NbSe_2}$ unit cell). This would largely yield the same results. However, it would in fact deviate, as surprisingly the strain ϵ in graphene also bends the $\mathrm{NbSe_2}$ band structure. This can be captured in the 'internal band offset' $E_K - E_\Gamma$, illustrated in Fig. 7.2(e). Plotting this 'internal band offset' against the strain ϵ reveals a similar linear trend, see Fig. 7.2(d). The zero-strain band offset is $\Delta E_{0,\mathrm{internal}} \approx 0$, meaning that $E_K - E_\Gamma$ can be tuned to be positive (K-bands above Γ-bands) for compressive strain $\epsilon < 0$ or negative (Γ-bands above K-bands) for tensile strain $\epsilon > 0$. This behaviour can be explained by the fact that the states of the $\mathrm{NbSe_2}$ Γ-bands are localized more out-of-plane, while the states of the $\mathrm{NbSe_2}$ K-bands are more in-plane. Hence, they react differently to a more dense or less dense graphene sheet.

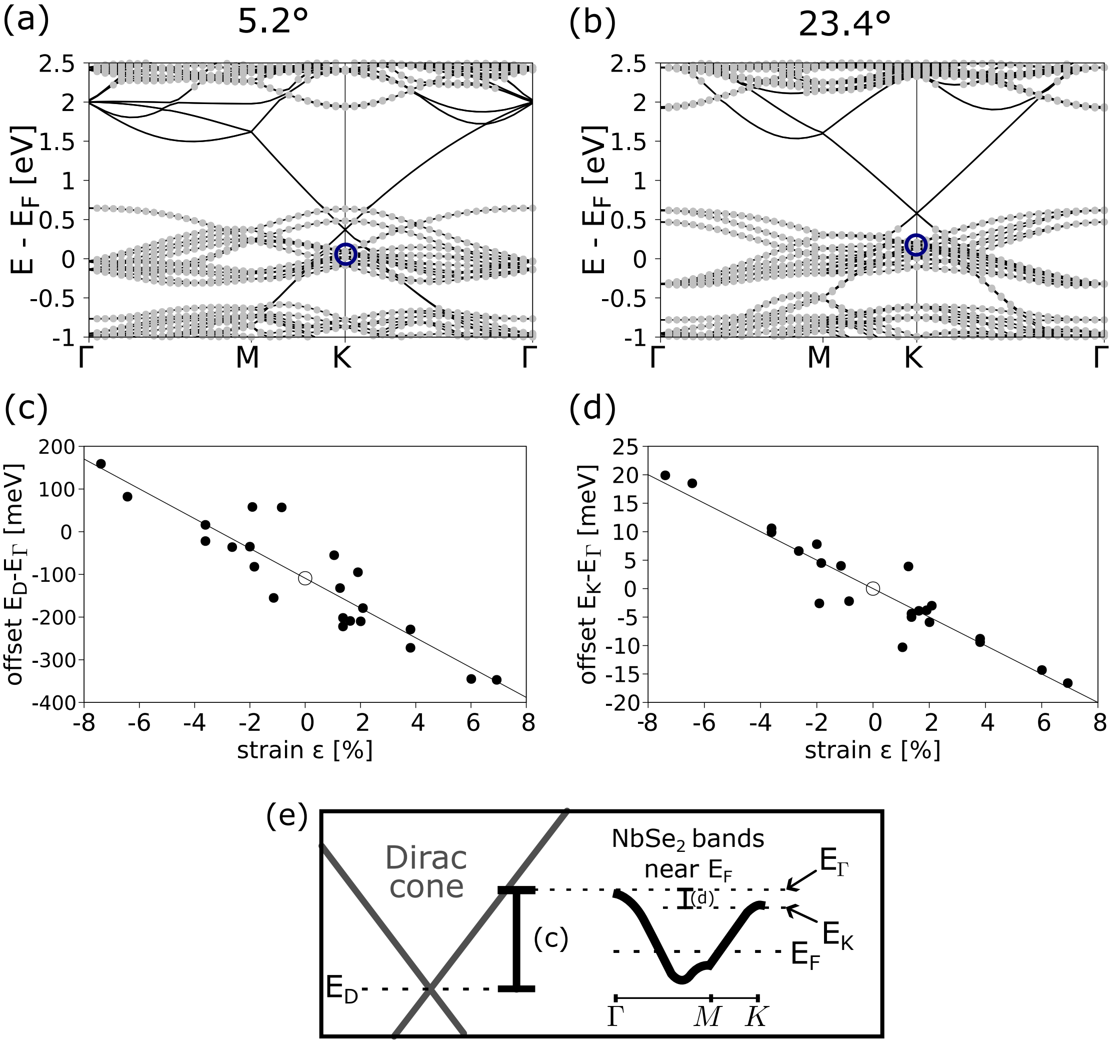

Figure 7.2: (a)-(b) DFT band structures of two different heterostructure supercells with $\Theta = 5.2°$ and $\Theta = 23.4°$. The blue circles indicate the NbSe$_2$ bands closest to the Dirac cone, which interact with it through 'first order' interlayer interaction. (c)-(d) Band offsets as function of the strain in graphene with linear fit (solid line) and estimated zero-strain band offset (empty circle). In (c) the band offset $E_D - E_\Gamma$ between the graphene Dirac cone and the band edge of the NbSe$_2$ Γ-bands is shown. In (d) the 'internal band offset' $E_K - E_\Gamma$ between the band edges of the NbSe$_2$ K-bands and Γ-bands is shown. (e) Illustration of the different fix points of the band structures. The simplified NbSe$_2$ band structure shows the bands near the Fermi level, which can be found in more detail in Fig. 7.3(c).

7.3 Challenges regarding the metallic states

$NbSe_2$ is different to the conventionally employed TMDCs discussed in Chap. 5 in many ways. First and foremost, it is a metal, which means that in a graphene/$NbSe_2$ heterostructure, the Dirac cone is in most cases at the same energy as the $NbSe_2$ bands and not located within a band gap, as it is the case for the semiconducting TMDCs. Nevertheless, we find that for all situations the Dirac cone shows crossings (not anti-crossings) with nearby $NbSe_2$ bands. This implies that, apparently, although the Dirac cone resides at the same energy and is folded back to the same k point (in the heterostructure supercell's 1st BZ) as these nearby $NbSe_2$ bands, it does not hybridize strongly with them. In terms of the interlayer interaction theory introduced in Sec. 4.4, this would indicate they are not connected through a 'first order' interaction, but only through a 'second order' or higher order interaction. Although this is detrimental to the proximity SOC yield, it is beneficial in the way that the Dirac cone is not distorted and can still be described within the model Hamiltonian. In order to analyze the situation in detail, we examined where the energetically closest $NbSe_2$ bands are, which hybridize with the Dirac cone through actual 'first order' interaction. Fig. 7.3(a) shows the 'first order path of interaction' the Dirac cone takes through the $NbSe_2$ 1st BZ, when tuning the twist angle between $\Theta = 0°$ and $\Theta = 30°$. Fig. 7.3(b) then shows the energies of the $NbSe_2$ states along this path. As the strain of graphene influences the path, we show both the path and the energies of the states for three cases with different strain (blue, black and red). From the fit in Fig. 7.2(c), we can estimate the position of the Dirac cone for the three situations as well (horizontal lines). This analysis tells us that the closest $NbSe_2$ bands, which are actually interacting with the Dirac cone through 'first order' interaction, are always separated from it by at least 200 meV. There are surely more $NbSe_2$ states along this path, however, these are even further away energetically. Fig. 7.3(d) additionally shows the orbital decomposition of the states along the path for the case of $\epsilon = 0$. It shows that they mostly consists of p- and d-orbitals with a slight shift towards more d-orbitals towards increasing Θ.

Although we now know that the $NbSe_2$ bands are not directly distorting the Dirac cone, the metallic states still present a problem for transport. While for heterostructures of graphene and semiconducting TMDCs, transport could only occur through the proximitized Dirac cone and not through the TMDC, this is not the case for graphene/$NbSe_2$. In any experiment, transport might occur through either of the layers or through both of them at the same time in some ratio. This issue affects graphene/$NbSe_2$ as well as graphene/TI heterostructures. In order to distinguish the transport channels, one can utilize the strong gate dependence of spin phenomena in the graphene Dirac cone [190, 205, 197, 204, 139]. Most effectively, this is used in determining the origin of charge-spin interconversion effects [107, 205, 204]. If the Fermi level is moved from the graphene conduction band to the graphene valence band (or vice versa), the sign of the charge-spin interconversion should swap, as the spin texture in the Dirac cone is anti-symmetric (except for the special case of graphene/TI structures with $\Theta = 30°$; see Sec. 6.4).

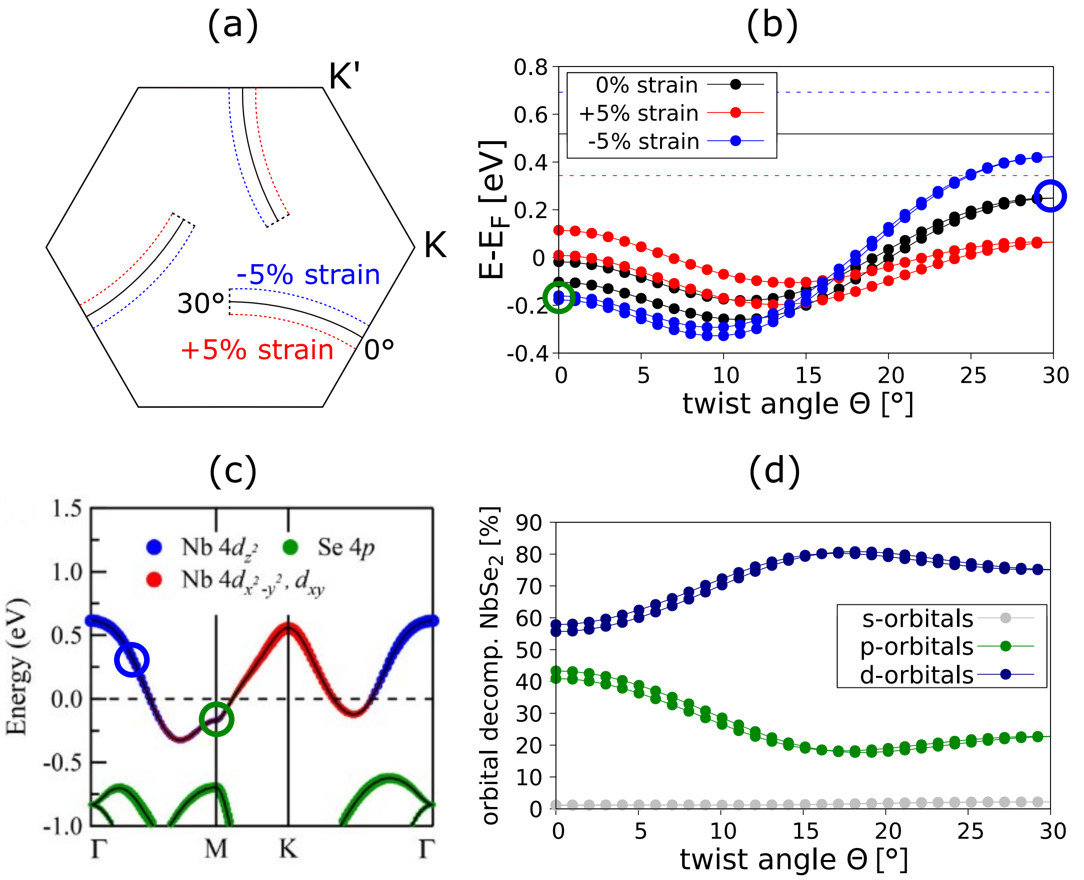

Figure 7.3: NbSe$_2$ states along the 'path of interaction' (see Sec. 4.4) interacting with the Dirac cone in 'first order'. (a) NbSe$_2$ 1st BZ with indicated 'path of first order interaction' of the Dirac cone for twist-angle range $0° \leq \Theta \leq 30°$. Three different cases with different strain are considered (blue: $\epsilon = -5\%$, black: $\epsilon = 0\%$, red: $\epsilon = +5\%$). (b) Energies of states close in energy to the Dirac cone along the 'path of first order interaction' for the three cases. Horizontal lines indicate the position of the Dirac cone for the three cases as determined by the fit in Fig. 7.2(c). To better illustrate where these bands lie energetically in the NbSe$_2$ band structure, we marked two states with circles (green corresponding to $\Theta = 0°, \epsilon = -5\%$; blue corresponding to $\Theta = 30°, \epsilon = 0\%$). Due to their position at high-symmetry points, these can be found in the band structure depicted in (c). (c) NbSe$_2$ band structure along high-symmetry lines; adapted from Ref. [106]. We additionally indicate, where the states marked with a green/blue circle in (b) are located in this band structure. (d) Orbital decomposition of the states along the 'path of first order interaction' for the case of $\epsilon = 0\%$.

7.4 Extracted SOC parameters

After fitting the Dirac cones of the DFT band structures to the model Hamiltonian from Eq. (4.43), we are again left with the twist-angle dependence of the SOC parameters, which are listed in Tab. 7.2 and can be seen in Fig. 7.4(a) and (b). The staggered potential Δ and the Kane-Mele SOC λ_{KM} are negligibly small for all twist angles, as it was already the case in Chap. 5 and Chap. 6. At $\Theta = 0°$ the valley-Zeeman SOC λ_{VZ} and the Rashba SOC λ_{R} start at roughly the same magnitude just under 1 meV. Both parameters stay at approximately this level until at $\Theta \approx 15°$. After this point, λ_{R} increases massively and reaches its maximal value at $\Theta = 30°$ with almost 3 meV magnitude. At the same time λ_{VZ} decreases and reaches $\lambda_{\mathrm{VZ}} = 0$ at $\Theta = 30°$, which is demanded by symmetry (see Subsec. 4.4.4). The Rashba angle Φ starts out at $\Phi = 0°$ (as demanded by symmetry) and only starts to increase at $\Theta \approx 15°$, reaching its maximum value at $\Theta \approx 23°$, only to decline rapidly again to zero at $\Theta = 30°$ (as again demanded by symmetry). This maximum value is $\Phi = -24°$, meaning there is some potential for UREE, albeit at a very low magnitude. Since for both plots the upward and downward triangles mark negative and positive values of strain, respectively, one can gauge how much and in what direction strain causes the parameters' values to deviate. In Fig. 7.4(c) the orbital decomposition of the graphene Dirac cones' $\mathrm{NbSe_2}$ contribution is depicted, i.e. the projection of the Dirac cone states onto the different (s, p and d) $\mathrm{NbSe_2}$ orbitals. When comparing it to Fig. 7.3(d), one can see that both plots show a very similar behaviour. Namely, a very small s-orbital contribution and p- and d-orbitals with comparable sizes, but with d-orbitals increasingly relevant for bigger twist angles Θ. While Fig. 7.3(d) presents the orbital composition of the $\mathrm{NbSe_2}$ states, which most likely provide the hybridization (and therefore the SOC), Fig. 7.4(c) presents the actual hybridization, which can be witnessed in the graphene Dirac cone. It therefore makes sense that Fig. 7.4(c) resembles Fig. 7.3(d) very closely, with one difference being the bias towards p-orbitals in the former one. This can readily be explained by the fact that the Se atoms (dominated by p-orbitals) are closer to the graphene layer in real space. The resemblance of the two plots furthermore supports our assumption that the states depicted in Fig. 7.3(b) are predominantly responsible for the proximity SOC.

This leads us to a plausible explanation of the twist-angle dependency depicted in Fig. 7.4(a): For this, let us evaluate the behaviour of the relevant contributing bands for zero strain (see black curve in Fig. 7.3(b)), when going from $\Theta = 0°$ to $\Theta = 30°$. One can see two features:

1. They generally move towards the Dirac cone in energy. This enhances overall SOC, as it allows the bands to hybridize with the Dirac cone more easily.

2. Their internal spin splitting (spin up and down) decreases, vanishing at $\Theta = 30°$, where the bands are degenerate. Since the valley-Zeeman SOC is driven by such a spin splitting, λ_{VZ} decreases and vanishes at $\Theta = 30°$.

Although these general trends seem to align well with the behaviour of the SOC, witnessed

Table 7.2: Parameters extracted from fitting the DFT band structures. For all heterostructure supercells, we list the twist angle Θ, strain ϵ (in graphene), the extracted fitting parameters and the band offset $\Delta E = E_D - E_\Gamma$ of the Dirac cone with respect to the NbSe$_2$ Γ band (see Fig. 7.2(e)). The fitting parameters are staggered potential Δ, Kane-Mele SOC λ_{KM}, valley-Zeeman SOC λ_{VZ}, magnitude of the Rashba SOC λ_{R} and Rashba angle Φ. For some of the supercells the Dirac cone is folded back to Γ (if $n - m = 3 \cdot k, k \in \mathbb{Z}$); they are marked with an asterisk in Tab. 7.1. As a consequence, the sign of the λ_{VZ} cannot be determined unambiguously and is presented with a ±.

Θ[°]	ϵ [%]	Φ [°]	Δ [meV]	λ_{KM} [meV]	λ_{VZ} [meV]	λ_{R} [meV]	ΔE [eV]
0.0	6.10	0	0.081	-0.001	0.913	0.846	-0.345
0.0	1.05	0	0.045	0.002	0.817	0.681	-0.055
1.9	1.37	0	0.013	-0.005	0.902	0.791	-0.202
3.3	-1.14	-1	0.049	0.003	0.925	0.716	-0.155
5.2	-3.61	-3	0.021	0.002	0.807	0.538	-0.022
5.2	3.81	2	0.060	0.019	0.619	0.934	-0.272
8.9	1.63	1	0.039	0.010	0.601	0.833	-0.209
10.9	-7.39	-19	-0.016	0.003	0.452	0.225	0.159
11.3	1.37	0	0.036	0.012	0.542	0.848	-0.222
12.5	-0.85	-7	0.023	0.002	±0.555	0.481	0.057
13.9	-1.91	-12	0.019	0.003	0.524	0.433	0.058
13.9	2.01	-2	0.028	0.021	0.460	0.937	-0.210
16.1	1.94	-7	0.017	0.010	±0.507	0.877	-0.095
16.1	-1.84	-14	0.015	0.004	0.516	0.619	-0.082
19.1	6.93	-10	-0.002	0.035	-0.438	1.973	-0.347
19.1	-6.43	-33	0.009	0.006	0.315	0.467	0.082
20.5	-1.26	-23	-0.014	0.015	±0.438	1.361	-0.132
23.4	-2.64	-24	0.018	0.067	0.366	1.726	-0.036
27.0	-3.61	-14	0.009	0.043	0.214	2.17	0.016
27.0	3.81	-15	-0.019	0.054	-0.249	2.562	-0.229
30.0	-2.00	0	0.000	0.053	0.000	2.468	-0.035
30.0	2.09	0	-0.173	0.052	±0.134	2.638	-0.179

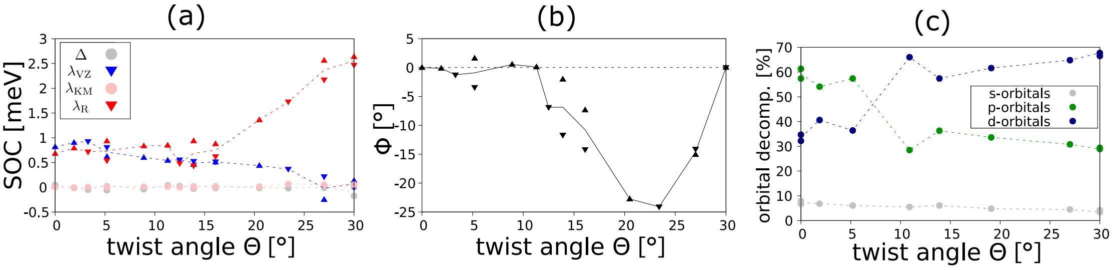

Figure 7.4: Twist-angle dependences of Dirac cone properties: (a) SOC parameters $\lambda_R, \lambda_{VZ}, \lambda_{KM}$ and staggered potential Δ, (b) Rashba angle Φ and (c) orbital decomposition of the $NbSe_2$ states featured in the Dirac states. Upward and downward pointing triangles indicate data points with tensile ($\epsilon > 0$) and compressive ($\epsilon < 0$) strain, respectively. The dotted lines in (a) and (c) and solid line in (b) are merely a guide to the eyes. If the Dirac cone was backfolded to Γ, the sign of λ_{VZ} cannot be determined. For such data points λ_{VZ} is assumed to be positive in accordance with the other supercells.

in the Dirac cone, it cannot be considered a full explanation of the behaviour, as it is not accounting for any possible changes in orbital decomposition and therefore overlap of the states. Although the steep increase in Rashba SOC can be rationalized in parts, it nevertheless exceeds the expectations associated with this simple picture. Also, the behaviour of the Rashba angle, which arises from a complex interference of Rashba contributions from different bands, cannot be explained within this argument.

Lastly, we analyze the SOC parameters of the two relaxed heterostructure supercells shown in Fig. 7.1(d) and (e). For this, we compare the extracted SOC parameters for the relaxed and unrelaxed structures. They are listed in Tab. 7.3. As already mentioned, the relaxed structures adopt a slightly larger interlayer distance. In fact, most of the change in SOC parameters (overall decrease of about 35%) can be traced back to this increased interlayer distance and is congruent with what one can expect from such an increased

(n,m)	(n',m')	Θ [°]	ϵ [%]	relaxed	Φ [°]	Δ [meV]	λ_{KM} [meV]	λ_{VZ} [meV]	λ_R [meV]	$\frac{\lambda_{VZ}}{\lambda_R}$
(4,0)	(3,0)	0.0	6.10	no	0	0.081	-0.001	0.913	0.846	1.079
(4,0)	(3,0)	0.0	6.10	yes	0	-0.649	-0.018	0.559	0.571	0.979
(3,1)	(2,1)	5.2	3.81	no	2	-0.060	0.019	0.619	0.934	0.663
(3,1)	(2,1)	5.2	3.81	yes	2	0.491	-0.091	0.409	0.604	0.677

Table 7.3: Comparison of the fitting parameters of the two heterostructures shown in Fig. 7.1(d) and (e) for both the relaxed and the idealized (unrelaxed) structure. The first two lines describe the structure with a 3×3 $NbSe_2$ supercell (Fig. 7.1(d)), while the last two lines describe the structure with a $\sqrt{7} \times \sqrt{7}$ $NbSe_2$ supercell (Fig. 7.1(e)).

interlayer distance (see for example the dependence of the SOC on the interlayer distance presented in Ref. [14]). Another effect is the onset of non negligible λ_{KM} and Δ. However, this effect is commonly occurring in relaxed structures (see Refs. [13, 14, 163, 67, 64]) and likely arises due to a rippling in graphene. Apart from these predictable effects of the relaxation, only a slight change of the ratio $\frac{\lambda_{\mathrm{VZ}}}{\lambda_{\mathrm{R}}}$ is witnessed. This effect is more pronounced, but still not major, for the structure based on the 3×3 supercell than the one based on the $\sqrt{7} \times \sqrt{7}$ supercell.

7.5 Charge-to-spin conversion

Let us now evaluate the potential for CSC (REE and UREE) for the different twisted supercell heterostructures, employing the method discussed in Sec. 4.6. One example of a graphene Dirac cone and its CSC efficiencies for different Fermi level positions is shown in Fig. 7.5(a). For this particular heterostructure supercell, the UREE and REE efficiencies are comparable in size. In Fig. 7.5(b), we show the (U)REE efficiencies as function of the twist angle. We find that the results are very much in line with what can be expected from the extracted SOC parameters. This means that

1. The potential for the REE follows the trend of λ_{R}, with a roughly constant value at $0° \leq \Theta \leq 15°$ and then rising, reaching its maximal value at $\Theta = 30°$.
2. The potential for UREE follows the trend of the Rashba angle Φ, showing a maximum at about $\Theta \approx 25°$ and vanishing at $\Theta = 0°$ and $\Theta = 30°$. Overall, the values of the UREE efficiencies never surpass those of the REE, as the maximal absolute value of Φ is only $|\Phi|_{\mathrm{max}} = 24°$.

The only minute difference is that the peak UREE efficiency is at a slightly higher twist angle than the peak of Φ, as the Rashba SOC shows a steep increase towards $\Theta = 30°$.

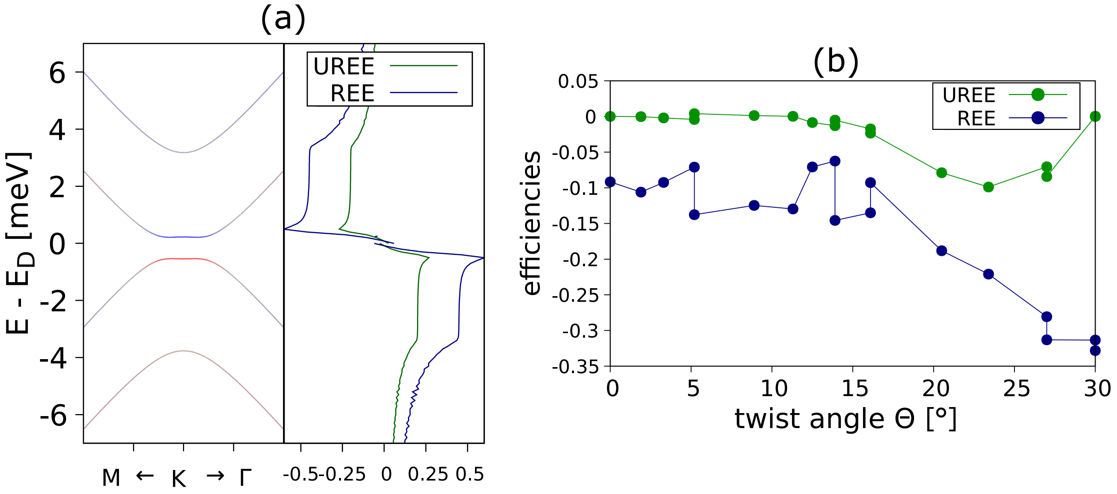

Figure 7.5: CSC in graphene/NbSe$_2$ heterostructures. (a) The left side shows the graphene Dirac cone for the $\Theta = 23.4°$ heterostructure supercell with color coded spin-z. The right side shows the REE and UREE efficiencies (x-axis) for the Fermi level set to a certain energy near the Dirac cone (y-axis). (b) (U)REE efficiencies plotted against the twist angle (averaged over a Fermi energy range, see Sec. 4.6).

7.6 Summary

We performed DFT calculations on multiple twisted graphene/NbSe$_2$ heterostructure supercells. Examining the energetic alignments of their band structures reveals, that the band offset between the NbSe$_2$ and graphene band structures exhibits a linear behaviour with the strain ϵ applied to graphene. Additionally, the 'internal band offset' of the NbSe$_2$ band structure shows the same linear trend (albeit to a lesser degree), even though no strain was applied to the NbSe$_2$ layer. Furthermore, we observed that the graphene Dirac cone stays intact for all twist angles and strains, although metallic NbSe$_2$ states reside at the same energy and momentum. This feature can be readily explained within the theory of interlayer interaction, as introduced by Koshino in Ref. [22]. Fitting the Dirac cones to a model Hamiltonian provides us with SOC parameters for various twist angles. These extracted SOC parameters show a tripling of the Rashba SOC at $\Theta = 30°$ and a peak of the Rashba angle at $\Theta \approx 23°$. Calculating CSC efficiencies within linear response theory confirms that these two features translate into a large peak REE yield at $\Theta = 30°$ and a smaller peak UREE yield at $\Theta \approx 24°$. These findings can be used to rationalize experimental findings. Moreover, we analyzed the effects of atomic relaxation for two exemplary heterostructure supercells. Our findings indicate that the atomic reconstruction of the 3×3 NbSe$_2$ supercell associated with the CDW is neither effected by the nearby graphene layer, nor does it affect the graphene Dirac cone in any substantial way.

A Proving the inverse of the statement about backfolding from Subsec. 4.4.2

In Subsec. 4.4.2, we proved that k points of two different layers connected by the matching condition Eq. (4.58), always fold back to the same k point in the heterostructure supercell's 1st Brillouin zone (BZ). We stated that, for minimal heterostructure supercells, i.e. if the heterostructure cannot be viewed as a supercell of another heterostructure supercell, the inverse is also correct. This means, as long as two k points fold back to the same k point in the heterostructure supercell's 1st BZ, they automatically fulfill the matching condition Eq. (4.58). Demanding that $\mathbf{k}$ and $\tilde{\mathbf{k}}$ fold back to the same point $\mathbf{k}^S$ is equal to demanding, that general reciprocal lattice vectors $\mathbf{G}_1^S$ and $\mathbf{G}_2^S$ of the supercell system exist, so that

$$\mathbf{k} = \mathbf{k}^S + \mathbf{G}_1^S \tag{A.1}$$

$$\tilde{\mathbf{k}} = \mathbf{k}^S + \mathbf{G}_2^S. \tag{A.2}$$

If we can find the right $\mathbf{G}$ and $\tilde{\mathbf{G}}$ to add to the equations, i.e.

$$\mathbf{k} + \mathbf{G} = \mathbf{k}^S + (\mathbf{G}_1^S + \mathbf{G}) \tag{A.3}$$

$$\tilde{\mathbf{k}} + \tilde{\mathbf{G}} = \mathbf{k}^S + (\mathbf{G}_2^S + \tilde{\mathbf{G}}) \tag{A.4}$$

so that

$$(\mathbf{G}_1^S + \mathbf{G}) = (\mathbf{G}_2^S + \tilde{\mathbf{G}}), \tag{A.5}$$

then the matching condition is fulfilled. Joining $\mathbf{G}_1^S$ and $\mathbf{G}_2^S$ into one general supercell reciprocal lattice vector, which we name $\mathbf{G}^S$, we can rewrite it as:

$$\mathbf{G}^S := (\mathbf{G}_1^S - \mathbf{G}_2^S) = \tilde{\mathbf{G}} - \mathbf{G}. \tag{A.6}$$

If we can now prove that for every $\mathbf{G}^S$, we can find $\mathbf{G}$ and $\tilde{\mathbf{G}}$, fulfilling this equation, the proof is complete. We can prove this by using explicit reciprocal lattice vectors in the (n, m) notation, introduces in Sec. 4.1. The unit cell of layer 1 forms a (n, m) supercell, which is matching the $(\tilde{n}, \tilde{m})$ supercell of layer 2. Inverting the matrix implicitly given in Eq. (4.13) and Eq. (4.14), we can formulate a general form of the reciprocal lattice vectors $\mathbf{b}_{1/2}$ of the primitive unit cell as linear combination of the supercell's reciprocal lattice vectors:

$$\begin{aligned}\mathbf{b}_1 &= n\mathbf{b}_1^S - m\mathbf{b}_2^S && \text{(A.7)}\\ \mathbf{b}_2 &= m\mathbf{b}_1^S + (n+m)\mathbf{b}_2^S. && \text{(A.8)}\end{aligned}$$

This holds true for both layer 1 ($\mathbf{b}_{1/2}$) and layer 2 ($\tilde{\mathbf{b}}_{1/2}$), so we can also write:

$$\begin{aligned}\tilde{\mathbf{b}}_1 &= n\mathbf{b}_1^S - m\mathbf{b}_2^S && \text{(A.9)}\\ \tilde{\mathbf{b}}_2 &= \tilde{m}\mathbf{b}_1^S + (\tilde{n}+\tilde{m})\mathbf{b}_2^S. && \text{(A.10)}\end{aligned}$$

Using this, we can write Eq. (A.6) as

$$\begin{aligned}\mathbf{G}^S =& \tilde{\mathbf{G}} - \mathbf{G} && \text{(A.11)}\\ l\mathbf{b}_1^S + k\mathbf{b}_2^S =& \tilde{s}\tilde{\mathbf{b}}_1 + \tilde{t}\tilde{\mathbf{b}}_2 - s\mathbf{b}_1 - t\mathbf{b}_2 && \text{(A.12)}\\ =& \tilde{s}\left(\tilde{n}\mathbf{b}_1^S - \tilde{m}\mathbf{b}_2^S\right) + \tilde{t}\left(\tilde{m}\mathbf{b}_1^S + (\tilde{n}+\tilde{m})\mathbf{b}_2^S\right) && \text{(A.13)}\\ &- s\left(n\mathbf{b}_1^S - m\mathbf{b}_2^S\right) - t\left(m\mathbf{b}_1^S + (n+m)\mathbf{b}_2^S\right), && \text{(A.14)}\end{aligned}$$

with integers $l, k, s, t, \tilde{s}, \tilde{t}, n, m, \tilde{n}, \tilde{m} \in \mathbb{Z}$. This leaves us with two equations (one for $\mathbf{b}_1^S$ and one for $\mathbf{b}_2^S$):

$$\begin{aligned}l =& \tilde{s}\tilde{n} + \tilde{t}\tilde{m} - sn - tm && \text{(A.15)}\\ k =& -\tilde{s}\tilde{m} + \tilde{t}(\tilde{n}+\tilde{m}) + sm - t(m+n). && \text{(A.16)}\end{aligned}$$

Apart from the non-physical case where $n = m = 0$ or $\tilde{n} = \tilde{m} = 0$, we need to show that

$$\forall l, k, n, m, \tilde{n}, \tilde{m} \in \mathbb{Z} \quad \exists s, t, \tilde{s}, \tilde{t} \in \mathbb{Z} \tag{A.17}$$

so that both equations can be fulfilled. As all cases can effectively be reduced to the case where $m = 0$ and $\tilde{m} = 0$ (i.e. a $n \times n$ supercell on top of a $\tilde{n} \times \tilde{n}$ supercell), we will only discuss this case. Here the Eq. (A.15) and Eq. (A.16) reduce to:

$$\begin{aligned}l &= \tilde{s}\tilde{n} - sn && \text{(A.18)}\\ k &= \tilde{t}\tilde{n} - tn. && \text{(A.19)}\end{aligned}$$

Let us assume $l = k = 1$, since, if it is true for this case, it is as well for all integers, as we can simply adjust $\{s, t, \tilde{s}, \tilde{t}\}$ by scaling it with l and k, i.e. $\{s, t, \tilde{s}, \tilde{t}\} \rightarrow \{ls, kt, l\tilde{s}, k\tilde{t}\}$. We can now use Bezout's identity [219], which states that

$$\forall a, b \in \mathbb{Z} \;\; \exists x, y \in \mathbb{Z}: \quad ax + by = d, \tag{A.20}$$

with d the greatest common denominator of a and b. We can now utilize the assumption we made, that the heterostructure supercell we constructed is the smallest possible one, i.e. that it is not a 'supercell of a supercell'. With this assumption, it is clear that the greatest common denominator of n and $\tilde{n}$ is $d = 1$, concluding the proof.

B Derivation of the Bloch function based linear response susceptibilities in the weak disorder limit

In the following, we transform the Green's functions based Fermi-surface (Eq. (4.89)) and Fermi-sea (Eq. (4.90)) susceptibilities of the Bonbien decomposition to the ones based on Bloch states (Eq. (4.91) and Eq. (4.92)). For this, we first take the traces:

$$\chi_A^{\text{surf}} = \frac{\hbar}{4\pi} \sum_{n,m} \int d\epsilon \frac{\partial f(\epsilon)}{\partial \epsilon} \text{Re}\Big(\langle n| \hat{A}(\hat{G}^r - \hat{G}^a) |m\rangle \langle m| \hat{B}(\hat{G}^r - \hat{G}^a) |n\rangle \Big) \tag{B.1}$$

$$\chi_A^{\text{sea}} = \frac{\hbar}{2\pi} \sum_{n,m} \int d\epsilon f(\epsilon) \text{Re}\Big(\langle n| \hat{A}(\hat{G}^r - \hat{G}^a) |m\rangle \langle m| \hat{B}(\frac{\partial \hat{G}^r}{\partial \epsilon} + \frac{\partial \hat{G}^a}{\partial \epsilon}) |n\rangle \Big), \tag{B.2}$$

where $|n\rangle \equiv |n\mathbf{k}\rangle$ and $\epsilon_n \equiv \epsilon_{n,\mathbf{k}}$ are the eigenstate and eigenenergy of the Hamiltonian $H(\mathbf{k})$ with band number n at a certain position $\mathbf{k}$ in k space. We omit the $\mathbf{k}$-dependence for this derivation. ϵ_F is the Fermi energy. Next, we insert the Greens functions $\hat{G}^{r/a} = \lim_{\gamma\to\infty} \frac{1}{\epsilon - \hat{H} \pm i\gamma}$. In the calculation of χ_A^{sea}, we will explicitly take the limit of γ going to zero, while for χ_A^{surf} we reinterpret γ as a constant weak scattering, omit the limit and see the formula as only valid for small γ. Using Bloch states as basis, we can rewrite

$$(\hat{G}^r - \hat{G}^a) |n\rangle = \Big(\frac{1}{\epsilon - \hat{H} + i\gamma} - \frac{1}{\epsilon - \hat{H} - i\gamma} \Big) |n\rangle \tag{B.3}$$

$$= \Big(\frac{1}{(\epsilon - \epsilon_n) + i\gamma} - \frac{1}{(\epsilon - \epsilon_n) - i\gamma} \Big) |n\rangle \tag{B.4}$$

$$= \frac{-2i\gamma}{(\epsilon - \epsilon_n)^2 + \gamma^2} |n\rangle , \tag{B.5}$$

with the limit

$$\lim_{\gamma\to 0} (\hat{G}^r - \hat{G}^a) |n\rangle = -2i\pi\delta(\epsilon - \epsilon_n) |n\rangle . \tag{B.6}$$

Inserting Eq. (B.5) into Eq. (B.1) and Eq. (B.6) into Eq. (B.2) gives us:

$$\chi_A^{\text{surf}} = \frac{\hbar}{4\pi}\sum_{n,m}\int d\epsilon \frac{\partial f(\epsilon)}{\partial \epsilon} \frac{-4\gamma^2 \text{Re}\Big(\langle n|\,\hat{A}\,|m\rangle \langle m|\,\hat{B}\,|n\rangle\Big)}{\Big((\epsilon-\epsilon_n)^2+\gamma^2\Big)\Big((\epsilon-\epsilon_m)^2+\gamma^2\Big)} \tag{B.7}$$

$$\chi_A^{\text{sea}} = \frac{\hbar}{2\pi}\sum_{n,m}\int d\epsilon (2\pi\delta(\epsilon-\epsilon_m)) f(\epsilon) \text{Im}\Big(\langle n|\,\hat{A}\,|m\rangle \langle m|\,\hat{B}(\frac{\partial \hat{G}^r}{\partial \epsilon}+\frac{\partial \hat{G}^a}{\partial \epsilon})\,|n\rangle\Big) \tag{B.8}$$

Using $\frac{\partial f(\epsilon)}{\partial \epsilon} = -\delta(\epsilon-\epsilon_F)$ we can eliminate the integral and arrive at the final result for χ_A^{surf}:

$$\chi_A^{\text{surf}} = \frac{\hbar}{\pi}\sum_{n,m} \frac{\gamma^2 \text{Re}\Big(\langle n|\,\hat{A}\,|m\rangle \langle m|\,\hat{B}\,|n\rangle\Big)}{\Big((\epsilon_F-\epsilon_n)^2+\gamma^2\Big)\Big((\epsilon_F-\epsilon_m)^2+\gamma^2\Big)} \tag{B.9}$$

For the Fermi-sea term we additionally need to rewrite:

$$\Big(\frac{\partial \hat{G}^r}{\partial \epsilon}+\frac{\partial \hat{G}^a}{\partial \epsilon}\Big)|n\rangle = (-(\hat{G}^r)^2-(\hat{G}^a)^2)\,|n\rangle \tag{B.10}$$

$$= \Big(\frac{-1}{(\epsilon-\epsilon_n+i\gamma)^2}+\frac{-1}{(\epsilon-\epsilon_n-i\gamma)^2}\Big)|n\rangle \tag{B.11}$$

$$= \Big(\frac{-1}{(\epsilon-\epsilon_n+i\gamma)^2}+\frac{-1}{(\epsilon_n-\epsilon+i\gamma)^2}\Big)|n\rangle, \tag{B.12}$$

which after inserting to Eq. (B.8) and integrating gives us

$$\chi_A^{\text{sea}} = \hbar\sum_{n,m}\text{Im}\Bigg(\langle n|\,\hat{A}\,|m\rangle \langle m|\,\hat{B}\,|n\rangle \Bigg(\frac{-f(\epsilon_m)}{(\epsilon_m-\epsilon_n+i\gamma)^2}+\frac{-f(\epsilon_m)}{(\epsilon_n-\epsilon_m+i\gamma)^2}\Bigg)\Bigg). \tag{B.13}$$

Since $\hat{A}$ and $\hat{B}$ are hermitian, switching the notation of n and m in the first part of the addition yields an extra minus sign. Thus we arrive at the final result after taking γ to zero:

$$\chi_A^{\text{sea}} = \hbar\sum_{n,m}(f(\epsilon_n)-f(\epsilon_m))\frac{\text{Im}\Big(\langle n|\,\hat{A}\,|m\rangle \langle m|\,\hat{B}\,|n\rangle\Big)}{(\epsilon_n-\epsilon_m)^2}, \tag{B.14}$$

References

[1] A. K. Geim and I. V. Grigorieva. Van der Waals heterostructures. *Nature*, 499(7459),419, 2013.

[2] K. S. Novoselov, A. K. Geim, S. V. Morozov, D. Jiang, Y. Zhang, S. V. Dubonos, I. V. Grigorieva, and A. A. Firsov. Electric Field Effect in Atomically Thin Carbon Films. *Science*, 306(5696),666–669, 2004.

[3] A. H. Castro Neto, F. Guinea, N. M. R. Peres, K. S. Novoselov, and A. K. Geim. The electronic properties of graphene. *Rev. Mod. Phys.*, 81,109–162, Jan 2009.

[4] S. Das Sarma, Shaffique Adam, E. H. Hwang, and Enrico Rossi. Electronic transport in two-dimensional graphene. *Rev. Mod. Phys.*, 83,407–470, May 2011.

[5] Y J Zhang, M Yoshida, R Suzuki, and Y Iwasa. 2D crystals of transition metal dichalcogenide and their iontronic functionalities. *2D Materials*, 2(4),044004, 2015.

[6] Sajedeh Manzeli, Dmitry Ovchinnikov, Diego Pasquier, Oleg V. Yazyev, and Andras Kis. 2D transition metal dichalcogenides. *Nature Reviews Materials*, 2(8),17033, Jun 2017.

[7] Igor Žutić, Jaroslav Fabian, and S. Das Sarma. Spintronics: Fundamentals and applications. *Review of Modern Physics*, 76,323, 2004.

[8] Wei Han, Roland K Kawakami, Martin Gmitra, and Jaroslav Fabian. Graphene spintronics. *Nat. Nanotechnol.*, 9(10),794, 2014.

[9] A. Avsar, H. Ochoa, F. Guinea, B. Özyilmaz, B. J. van Wees, and I. J. Vera-Marun. Colloquium: Spintronics in graphene and other two-dimensional materials. *Rev. Mod. Phys.*, 92,021003, Jun 2020.

[10] Simranjeet Singh, Jyoti Katoch, Jinsong Xu, Cheng Tan, Tiancong Zhu, Walid Amamou, James Hone, and Roland Kawakami. Nanosecond spin relaxation times in single layer graphene spin valves with hexagonal boron nitride tunnel barriers. *Appl. Phys. Lett.*, 109(12),122411, 2016.

[11] Marc Drögeler, Christopher Franzen, Frank Volmer, Tobias Pohlmann, Luca Banszerus, Maik Wolter, Kenji Watanabe, Takashi Taniguchi, Christoph Stampfer, and Bernd Beschoten. Spin Lifetimes Exceeding 12 ns in Graphene Nonlocal Spin Valve Devices. *Nano Lett.*, 16(6),3533, 2016.

[12] P. Hohenberg and W. Kohn. Inhomogeneous Electron Gas. *Phys. Rev.*, 136,B864, 1964.

[13] Martin Gmitra and Jaroslav Fabian. Graphene on transition-metal dichalcogenides: A platform for proximity spin-orbit physics and optospintronics. *Phys. Rev. B*, 92,155403, Oct 2015.

[14] Martin Gmitra, Denis Kochan, Petra Högl, and Jaroslav Fabian. Trivial and inverted Dirac bands and the emergence of quantum spin Hall states in graphene on transition-metal dichalcogenides. *Phys. Rev. B*, 93,155104, Apr 2016.

[15] Yuan Cao, Valla Fatemi, Shiang Fang, Kenji Watanabe, Takashi Taniguchi, Efthimios Kaxiras, and Pablo Jarillo-Herrero. Unconventional superconductivity in magic-angle graphene superlattices. *Nature*, 556(7699),43–50, Apr 2018.

[16] Harpreet Singh Arora, Robert Polski, Yiran Zhang, Alex Thomson, Youngjoon Choi, Hyunjin Kim, Zhong Lin, Ilham Zaky Wilson, Xiaodong Xu, Jiun-Haw Chu, et al. Superconductivity in metallic twisted bilayer graphene stabilized by WSe 2. *Nature*, 583(7816),379–384, 2020.

[17] Petr Stepanov, Ipsita Das, Xiaobo Lu, Ali Fahimniya, Kenji Watanabe, Takashi Taniguchi, Frank HL Koppens, Johannes Lischner, Leonid Levitov, and Dmitri K Efetov. Untying the insulating and superconducting orders in magic-angle graphene. *Nature*, 583(7816),375–378, 2020.

[18] Leon Balents, Cory R Dean, Dmitri K Efetov, and Andrea F Young. Superconductivity and strong correlations in moiré flat bands. *Nature Physics*, 16(7),725–733, 2020.

[19] Yang Li and Mikito Koshino. Twist-angle dependence of the proximity spin-orbit coupling in graphene on transition-metal dichalcogenides. *Phys. Rev. B*, 99,075438, Feb 2019.

[20] Alessandro David, Péter Rakyta, Andor Kormányos, and Guido Burkard. Induced spin-orbit coupling in twisted graphene–transition metal dichalcogenide heterobilayers: Twistronics meets spintronics. *Phys. Rev. B*, 100,085412, Aug 2019.

[21] Csaba G. Péterfalvi, Alessandro David, Péter Rakyta, Guido Burkard, and Andor Kormányos. Quantum interference tuning of spin-orbit coupling in twisted van der Waals trilayers. *Phys. Rev. Research*, 4,L022049, May 2022.

[22] Mikito Koshino. Interlayer interaction in general incommensurate atomic layers. *New Journal of Physics*, 17(1),015014, jan 2015.

[23] Marcin Kurpas, Martin Gmitra, and Jaroslav Fabian. Spin-orbit coupling and spin relaxation in phosphorene: Intrinsic versus extrinsic effects. *Phys. Rev. B*, 94,155423, 2016.

[24] L.D. Landau and E.M. Lifshitz. *Quantum Mechanics: Non-Relativistic Theory*. Teoreticheskaiafizika. Elsevier Science, 2013.

[25] Mitchel Weissbluth. *Atoms and Molecules*. New York: Academic Press (1978), 1978.

[26] W. H. E. Schwarz, A. Rutkowski, and S. G. Wang. Understanding relativistic effects of chemical bonding. *International Journal of Quantum Chemistry*, 57(4),641–653, 1996.

[27] W H Schwarz. *An Introduction to Relativistic Quantum Chemistry*, pages 1–62. 04 2010.

[28] Daniel Huertas-Hernando, F. Guinea, and Arne Brataas. Spin-orbit coupling in curved graphene, fullerenes, nanotubes, and nanotube caps. *Phys. Rev. B*, 74(15),155426, 2006.

[29] Yugui Yao, Fei Ye, Xiao-Liang Qi, Shou-Cheng Zhang, and Zhong Fang. Spin-orbit gap of graphene: First-principles calculations. *Phys. Rev. B*, 75,041401, Jan 2007.

[30] M. Gmitra, S. Konschuh, C. Ertler, C. Ambrosch-Draxl, and J. Fabian. Band-structure topologies of graphene: Spin-orbit coupling effects from first principles. *Phys. Rev. B*, 80,235431, 2009.

[31] S. Konschuh, M. Gmitra, D. Kochan, and J. Fabian. Theory of spin-orbit coupling in bilayer graphene. *Phys. Rev. B*, 85(11),115423, 2012.

[32] J. Sichau, M. Prada, T. Anlauf, T. J. Lyon, B. Bosnjak, L. Tiemann, and R. H. Blick. Resonance Microwave Measurements of an Intrinsic Spin-Orbit Coupling Gap in Graphene: A Possible Indication of a Topological State. *Phys. Rev. Lett.*, 122,046403, 2019.

[33] L. Banszerus, S. Möller, C. Steiner, E. Icking, S. Trellenkamp, F. Lentz, K. Watanabe, T. Taniguchi, C. Volk, and C. Stampfer. Spin-valley coupling in single-electron bilayer graphene quantum dots. *Nature Communications*, 12(1),5250, Sep 2021.

[34] C. L. Kane and E. J. Mele. Quantum Spin hall effect in graphene. *Phys. Rev. Lett.*, 95(22),226801, 2005.

[35] C. L. Kane and E. J. Mele. Z2 topological order and the quantum spin hall effect. *Phys. Rev. Lett.*, 95(14),146802, 2005.

[36] Tobias Frank, Petra Högl, Martin Gmitra, Denis Kochan, and Jaroslav Fabian. Protected Pseudohelical Edge States in $\mathbb{Z}_2$-Trivial Proximitized Graphene. *Phys. Rev. Lett.*, 120,156402, Apr 2018.

[37] S. A. Wolf, D. D. Awschalom, R. A. Buhrman, J. M. Daughton, S. von Molnár, M. L. Roukes, A. Y. Chtchelkanova, and D. M. Treger. Spintronics: A Spin-Based Electronics Vision for the Future. *Science*, 294(5546),1488–1495, 2001.

[38] Conan Weeks, Jun Hu, Jason Alicea, Marcel Franz, and Ruqian Wu. Engineering a Robust Quantum Spin Hall State in Graphene via Adatom Deposition. *Phys. Rev. X*, 1,021001, 2011.

[39] Alessandro Cresti, Dinh Van Tuan, David Soriano, Aron W. Cummings, and Stephan Roche. Multiple Quantum Phases in Graphene with Enhanced Spin-Orbit Coupling: From the Quantum Spin Hall Regime to the Spin Hall Effect and a Robust Metallic State. *Phys. Rev. Lett.*, 113,246603, Dec 2014.

[40] Zhe Wang, Dong-Keun Ki, Hua Chen, Helmuth Berger, Allan H MacDonald, and Alberto F Morpurgo. Strong interface-induced spin-orbit interaction in graphene on WS2. *Nat. Commun.*, 6,8339, 2015.

[41] Kenan Song, David Soriano, Aron W. Cummings, Roberto Robles, Pablo Ordejón, and Stephan Roche. Spin Proximity Effects in Graphene/Topological Insulator Heterostructures. *Nano Lett.*, 18(3),2033, 2018.

[42] Paengro Lee, Kyung-Hwan Jin, Si Jin Sung, Jin Gul Kim, Min-Tae Ryu, Hee-Min Park, Seung-Hoon Jhi, Namdong Kim, Yongsam Kim, Seong Uk Yu, Kwang S. Kim, Do Young Noh, and Jinwook Chung. Proximity Effect Induced Electronic Properties of Graphene on Bi2Te2Se. *ACS Nano*, 9(11),10861–10866, 2015. PMID: 26549323.

[43] Wendong Cao, Rui-Xing Zhang, Peizhe Tang, Gang Yang, Jorge Sofo, Wenhui Duan, and Chao-Xing Liu. Heavy Dirac fermions in a graphene/topological insulator hetero-junction. *2D Materials*, 3(3),034006, sep 2016.

[44] Thomas Naimer and Jaroslav Fabian. Twist-angle dependent proximity induced spin-orbit coupling in graphene/topological insulator heterostructures. *Phys. Rev. B*, 107,195144, May 2023.

[45] K. Hatsuda, H. Mine, T. Nakamura, J. Li, R. Wu, S. Katsumoto, and J. Haruyama. Evidence for a quantum spin Hall phase in graphene decorated with Bi_2Te_3 nanoparticles. *Science Advances*, 4(11),eaau6915, 2018.

[46] Markus König, Steffen Wiedmann, Christoph Brüne, Andreas Roth, Hartmut Buhmann, Laurens W. Molenkamp, Xiao-Liang Qi, and Shou-Cheng Zhang. Quantum Spin Hall Insulator State in HgTe Quantum Wells. *Science*, 318(5851),766–770, 2007.

[47] Seongshik Oh. The Complete Quantum Hall Trio. *Science*, 340(6129),153–154, 2013.

[48] Aron W. Cummings, Jose H. Garcia, Jaroslav Fabian, and Stephan Roche. Giant Spin Lifetime Anisotropy in Graphene Induced by Proximity Effects. *Phys. Rev. Lett.*, 119,206601, Nov 2017.

[49] Talieh S. Ghiasi, Josep Ingla-Aynés, Alexey A. Kaverzin, and Bart J. Van Wees. Large Proximity-Induced Spin Lifetime Anisotropy in Transition-Metal Dichalcogenide/Graphene Heterostructures. *Nano Lett.*, 17(12),7528, 2017.

[50] L. Antonio Benítez, Juan F. Sierra, Williams Savero Torres, Aloïs Arrighi, Frédéric Bonell, Marius V. Costache, and Sergio O. Valenzuela. Strongly anisotropic spin relaxation in graphene-transition metal dichalcogenide heterostructures at room temperature. *Nat. Phys.*, 14(3),303, 2018.

[51] Simon Zihlmann, Aron W. Cummings, Jose H. Garcia, Máté Kedves, Kenji Watanabe, Takashi Taniguchi, Christian Schönenberger, and Péter Makk. Large spin relaxation anisotropy and valley-Zeeman spin-orbit coupling in WSe_2/graphene/*h*-BN heterostructures. *Phys. Rev. B*, 97,075434, 2018.

[52] Wilhelm Hanle. Über magnetische Beeinflussung der Polarisation der Resonanzfluoreszenz. *Zeitschrift für Physik*, 30(1),93–105, Dec 1924.

[53] T. Kuczmik, M. Oltscher, A. Bayer, D. Schuh, D. Bougeard, M. Ciorga, and D. Weiss. Hanle spin precession in a two-dimensional electron system. *Phys. Rev. B*, 95,195315, May 2017.

[54] S. Omar and B. J. van Wees. Graphene-WS_2 heterostructures for tunable spin injection and spin transport. *Phys. Rev. B*, 95,081404, 2017.

[55] Martin Gmitra and Jaroslav Fabian. Proximity Effects in Bilayer Graphene on Monolayer WSe_2: Field-Effect Spin Valley Locking, Spin-Orbit Valve, and Spin Transistor. *Phys. Rev. Lett.*, 119,146401, Oct 2017.

[56] J. O. Island, X. Cui, C. Lewandowski, J. Y. Khoo, E. M. Spanton, H. Zhou, D. Rhodes, J. C. Hone, T. Taniguchi, K. Watanabe, L. S. Levitov, M. P. Zaletel, and A. F. Young. Spin–orbit-driven band inversion in bilayer graphene by the van der Waals proximity effect. *Nature*, 571(7763),85, 2019.

[57] Priya Tiwari, Saurabh Kumar Srivastav, and Aveek Bid. Electric-Field-Tunable Valley Zeeman Effect in Bilayer Graphene Heterostructures: Realization of the Spin-Orbit Valve Effect. *Phys. Rev. Lett.*, 126,096801, Mar 2021.

[58] Supriyo Datta and Biswajit Das. Electronic analog of the electrooptic modulator. *Appl. Phys. Lett.*, 56(7),665, 1990.

[59] Michel I Dyakonov. Spin Hall Effect. 2010.

[60] V.M. Edelstein. Spin polarization of conduction electrons induced by electric current in two-dimensional asymmetric electron systems. *Solid State Communications*, 73(3),233–235, 1990.

[61] Manuel Offidani, Mirco Milletari, Roberto Raimondi, and Aires Ferreira. Optimal Charge-to-Spin Conversion in Graphene on Transition-Metal Dichalcogenides. *Phys. Rev. Lett.*, 119,196801, 2017.

[62] A. Dyrdał, J. Barnaś, and V. K. Dugaev. Current-induced spin polarization in graphene due to Rashba spin-orbit interaction. *Phys. Rev. B*, 89,075422, Feb 2014.

[63] L Smrcka and P Streda. Transport coefficients in strong magnetic fields. *Journal of Physics C: Solid State Physics*, 10(12),2153, jun 1977.

[64] Seungjun Lee, D. J. P. de Sousa, Young-Kyun Kwon, Fernando de Juan, Zhendong Chi, Fèlix Casanova, and Tony Low. Charge-to-spin conversion in twisted graphene/WSe_2 heterostructures. *Phys. Rev. B*, 106,165420, Oct 2022.

[65] Jakub Železný, Yang Zhang, Claudia Felser, and Binghai Yan. Spin-Polarized Current in Noncollinear Antiferromagnets. *Phys. Rev. Lett.*, 119,187204, Nov 2017.

[66] Thomas Naimer, Martin Gmitra, and Jaroslav Fabian. Tuning proximity spin-orbit coupling in graphene/$NbSe_2$ heterostructures via twist angle. *Phys. Rev. B*, 109,205109, May 2024.

[67] Klaus Zollner, Simão M. João, Branislav K. Nikolić, and Jaroslav Fabian. Twist- and gate-tunable proximity spin-orbit coupling, spin relaxation anisotropy, and charge-to-spin conversion in heterostructures of graphene and transition metal dichalcogenides. *Phys. Rev. B*, 108,235166, Dec 2023.

[68] Alessandro Veneri, David T. S. Perkins, Csaba G. Péterfalvi, and Aires Ferreira. Twist angle controlled collinear Edelstein effect in van der Waals heterostructures. *Phys. Rev. B*, 106,L081406, Aug 2022.

[69] Kapildeb Dolui, Marko D. Petrović, Klaus Zollner, Petr Plecháč, Jaroslav Fabian, and Branislav K. Nikolić. Proximity Spin–Orbit Torque on a Two-Dimensional Magnet within van der Waals Heterostructure: Current-Driven Antiferromagnet-to-Ferromagnet Reversible Nonequilibrium Phase Transition in Bilayer CrI3. *Nano Letters*, 20(4),2288–2295, Apr 2020.

[70] B. Dieny, I. L. Prejbeanu, K. Garello, P. Gambardella, P. Freitas, R. Lehndorff, W. Raberg, U. Ebels, S. O. Demokritov, J. Akerman, A. Deac, P. Pirro, C. Adelmann, A. Anane, A. V. Chumak, A. Hirohata, S. Mangin, Sergio O. Valen-

zuela, M. Cengiz Onbaşlı, M. d'Aquino, G. Prenat, G. Finocchio, L. Lopez-Diaz, R. Chantrell, O. Chubykalo-Fesenko, and P. Bortolotti. Opportunities and challenges for spintronics in the microelectronics industry. *Nature Electronics*, 3(8),446–459, Aug 2020.

[71] Mark Stiles and J Miltat. *Spin Transfer Torque and Dynamics*. Spin Dynamics in Confined Magnetic Structures III: Topics in Applied Physics 101, Springer Berlin / Heidelberg, Heidelberg, DE, 2006-11-01 2006.

[72] Josep Ingla-Aynés, Inge Groen, Franz Herling, Nerea Ontoso, C K Safeer, Fernando de Juan, Luis E Hueso, Marco Gobbi, and Fèlix Casanova. Omnidirectional spin-to-charge conversion in graphene/NbSe$_2$ van der Waals heterostructures. *2D Materials*, 9(4),045001, jun 2022.

[73] Min Yi and Zhigang Shen. A review on mechanical exfoliation for the scalable production of graphene. *J. Mater. Chem. A*, 3,11700–11715, 2015.

[74] Maria Losurdo, Maria Michela Giangregorio, Pio Capezzuto, and Giovanni Bruno. Graphene CVD growth on copper and nickel: role of hydrogen in kinetics and structure. *Phys. Chem. Chem. Phys.*, 13(46),20836, 2011.

[75] Claudia Backes, Amr M Abdelkader, Concepción Alonso, Amandine Andrieux-Ledier, Raul Arenal, Jon Azpeitia, Nilanthy Balakrishnan, Luca Banszerus, Julien Barjon, Ruben Bartali, Sebastiano Bellani, Claire Berger, Reinhard Berger, M M Bernal Ortega, Carlo Bernard, Peter H Beton, André Beyer, Alberto Bianco, Peter Bøggild, Francesco Bonaccorso, Gabriela Borin Barin, Cristina Botas, Rebeca A Bueno, Daniel Carriazo, Andres Castellanos-Gomez, Meganne Christian, Artur Ciesielski, Tymoteusz Ciuk, Matthew T Cole, Jonathan Coleman, Camilla Coletti, Luigi Crema, Huanyao Cun, Daniela Dasler, Domenico De Fazio, Noel Díez, Simon Drieschner, Georg S Duesberg, Roman Fasel, Xinliang Feng, Alberto Fina, Stiven Forti, Costas Galiotis, Giovanni Garberoglio, Jorge M García, Jose Antonio Garrido, Marco Gibertini, Armin Gölzhäuser, Julio Gómez, Thomas Greber, Frank Hauke, Adrian Hemmi, Irene Hernandez-Rodriguez, Andreas Hirsch, Stephen A Hodge, Yves Huttel, Peter U Jepsen, Ignacio Jimenez, Ute Kaiser, Tommi Kaplas, HoKwon Kim, Andras Kis, Konstantinos Papagelis, Kostas Kostarelos, Aleksandra Krajewska, Kangho Lee, Changfeng Li, Harri Lipsanen, Andrea Liscio, Martin R Lohe, Annick Loiseau, Lucia Lombardi, Maria Francisca López, Oliver Martin, Cristina Martín, Lidia Martínez, Jose Angel Martin-Gago, José Ignacio Martínez, Nicola Marzari, Álvaro Mayoral, John McManus, Manuela Melucci, Javier Méndez, Cesar Merino, Pablo Merino, Andreas P Meyer, Elisa Miniussi, Vaidotas Miseikis, Neeraj Mishra, Vittorio Morandi, Carmen Munuera, Roberto Muñoz, Hugo Nolan, Luca Ortolani, Anna K Ott, Irene Palacio, Vincenzo Palermo, John Parthenios, Iwona Pasternak, Amalia Patane, Maurizio Prato, Henri Prevost, Vladimir Prudkovskiy, Nicola Pugno, Teófilo Rojo, Antonio Rossi, Pascal

Ruffieux, Paolo Samorì, Léonard Schué, Eki Setijadi, Thomas Seyller, Giorgio Speranza, Christoph Stampfer, Ingrid Stenger, Wlodek Strupinski, Yuri Svirko, Simone Taioli, Kenneth B K Teo, Matteo Testi, Flavia Tomarchio, Mauro Tortello, Emanuele Treossi, Andrey Turchanin, Ester Vazquez, Elvira Villaro, Patrick R Whelan, Zhenyuan Xia, Rositza Yakimova, Sheng Yang, G Reza Yazdi, Chanyoung Yim, Duhee Yoon, Xianghui Zhang, Xiaodong Zhuang, Luigi Colombo, Andrea C Ferrari, and Mar Garcia-Hernandez. Production and processing of graphene and related materials. *2D Materials*, 7(2),022001, jan 2020.

[76] Marco Bieri, Matthias Treier, Jinming Cai, Kamel Aït-Mansour, Pascal Ruffieux, Oliver Gröning, Pierangelo Gröning, Marcel Kastler, Ralph Rieger, Xinliang Feng, Klaus Müllen, and Roman Fasel. Porous graphenes: two-dimensional polymer synthesis with atomic precision. *Chem. Commun.*, pages 6919–6921, 2009.

[77] K.I. Bolotin, K.J. Sikes, Z. Jiang, M. Klima, G. Fudenberg, J. Hone, P. Kim, and H.L. Stormer. Ultrahigh electron mobility in suspended graphene. *Solid State Communications*, 146(9),351–355, 2008.

[78] Xu Du, Ivan Skachko, Anthony Barker, and Eva Y. Andrei. Approaching ballistic transport in suspended graphene. *Nature Nanotechnology*, 3(8),491–495, Aug 2008.

[79] Chen Si, Zhimei Sun, and Feng Liu. Strain engineering of graphene: a review. *Nanoscale*, 8,3207–3217, 2016.

[80] Seon-Myeong Choi, Seung-Hoon Jhi, and Young-Woo Son. Effects of strain on electronic properties of graphene. *Phys. Rev. B*, 81,081407, Feb 2010.

[81] Caterina Soldano, Ather Mahmood, and Erik Dujardin. Production, properties and potential of graphene. *Carbon*, 48(8),2127, 2010.

[82] Jean-Christophe Charlier, Xavier Blase, and Stephan Roche. Electronic and transport properties of nanotubes. *Rev. Mod. Phys.*, 79,677–732, May 2007.

[83] Poulomi Bhakta and Bhavna Barthunia. Fullerene and its applications: A review. *Journal of Indian Academy of Oral Medicine and Radiology*, 32(2), 2020.

[84] Yanping Liu, Yuanji Gao, Siyu Zhang, Jun He, Juan Yu, and Zongwen Liu. Valleytronics in transition metal dichalcogenides materials. *Nano Research*, 12(11),2695–2711, Nov 2019.

[85] John R. Schaibley, Hongyi Yu, Genevieve Clark, Pasqual Rivera, Jason S. Ross, Kyle L. Seyler, Wang Yao, and Xiaodong Xu. Valleytronics in 2D materials. *Nature Reviews Materials*, 1(11),16055, Aug 2016.

[86] F. Langer, C. P. Schmid, S. Schlauderer, M. Gmitra, J. Fabian, P. Nagler, C. Schüller, T. Korn, P. G. Hawkins, J. T. Steiner, U. Huttner, S. W. Koch, M. Kira, and R. Huber. Lightwave valleytronics in a monolayer of tungsten diselenide. *Nature*, 557(7703),76–80, May 2018.

[87] E. Blundo, M. Felici, T. Yildirim, G. Pettinari, D. Tedeschi, A. Miriametro, B. Liu, W. Ma, Y. Lu, and A. Polimeni. Evidence of the direct-to-indirect band gap transition in strained two-dimensional WS_2, MoS_2, and WSe_2. *Phys. Rev. Res.*, 2,012024, Jan 2020.

[88] Klaus Zollner, Paulo E. Faria Junior, and Jaroslav Fabian. Strain-tunable orbital, spin-orbit, and optical properties of monolayer transition-metal dichalcogenides. *Phys. Rev. B*, 100,195126, 2019.

[89] Kartikey Thakar and Saurabh Lodha. Optoelectronic and photonic devices based on transition metal dichalcogenides. *Materials Research Express*, 7(1),014002, jan 2020.

[90] Kin Fai Mak and Jie Shan. Photonics and optoelectronics of 2D semiconductor transition metal dichalcogenides. *Nature Photonics*, 10(4),216–226, Apr 2016.

[91] Yaxu Wei, Chunguang Hu, Yanning Li, Xiaotang Hu, Kaihao Yu, Litao Sun, Michael Hohage, and Lidong Sun. Initial stage of MBE growth of MoSe2 monolayer. *Nanotechnology*, 31(31),315710, may 2020.

[92] C.N.R. Rao and Urmimala Maitra. Inorganic Graphene Analogs. *Annual Review of Materials Research*, 45(Volume 45, 2015),29–62, 2015.

[93] Gang Wang, Alexey Chernikov, Mikhail M. Glazov, Tony F. Heinz, Xavier Marie, Thierry Amand, and Bernhard Urbaszek. Colloquium: Excitons in atomically thin transition metal dichalcogenides. *Rev. Mod. Phys.*, 90,021001, Apr 2018.

[94] Tomasz Woźniak, Paulo E. Faria Junior, Gotthard Seifert, Andrey Chaves, and Jens Kunstmann. Exciton g factors of van der Waals heterostructures from first-principles calculations. *Phys. Rev. B*, 101,235408, Jun 2020.

[95] Kai-Qiang Lin, Paulo E. Faria Junior, Jonas M. Bauer, Bo Peng, Bartomeu Monserrat, Martin Gmitra, Jaroslav Fabian, Sebastian Bange, and John M. Lupton. Twist-angle engineering of excitonic quantum interference and optical nonlinearities in stacked 2D semiconductors. *Nature Communications*, 12(1),1553, Mar 2021.

[96] Kai-Qiang Lin, Chin Shen Ong, Sebastian Bange, Paulo E. Faria Junior, Bo Peng, Jonas D. Ziegler, Jonas Zipfel, Christian Bäuml, Nicola Paradiso, Kenji Watanabe, Takashi Taniguchi, Christoph Strunk, Bartomeu Monserrat, Jaroslav Fabian,

Alexey Chernikov, Diana Y. Qiu, Steven G. Louie, and John M. Lupton. Narrow-band high-lying excitons with negative-mass electrons in monolayer WSe2. *Nature Communications*, 12(1),5500, Sep 2021.

[97] Kai-Qiang Lin. A roadmap for interlayer excitons. *Light: Science & Applications*, 10(1),99, May 2021.

[98] Ying Jiang, Shula Chen, Weihao Zheng, Biyuan Zheng, and Anlian Pan. Interlayer exciton formation, relaxation, and transport in TMD van der Waals heterostructures. *Light: Science & Applications*, 10(1),72, Apr 2021.

[99] Kai-Qiang Lin, Paulo E. Faria Junior, Ruven Hübner, Jonas D. Ziegler, Jonas M. Bauer, Fabian Buchner, Matthias Florian, Felix Hofmann, Kenji Watanabe, Takashi Taniguchi, Jaroslav Fabian, Alexander Steinhoff, Alexey Chernikov, Sebastian Bange, and John M. Lupton. Ultraviolet interlayer excitons in bilayer WSe2. *Nature Nanotechnology*, 19(2),196–201, Feb 2024.

[100] Chirag C. Palekar, Paulo E. Faria Junior, Barbara Rosa, Frederico B. Sousa, Leandro M. Malard, Jaroslav Fabian, and Stephan Reitzenstein. Amplification of interlayer exciton emission in twisted $WSe_2/WSe_2/MoSe_2$ heterotrilayers. 2023.

[101] Archana Raja, Andrey Chaves, Jaeeun Yu, Ghidewon Arefe, Heather M. Hill, Albert F. Rigosi, Timothy C. Berkelbach, Philipp Nagler, Christian Schüller, Tobias Korn, Colin Nuckolls, James Hone, Louis E. Brus, Tony F. Heinz, David R. Reichman, and Alexey Chernikov. Coulomb engineering of the bandgap and excitons in two-dimensional materials. *Nature Communications*, 8(1),15251, May 2017.

[102] Archana Raja, Lutz Waldecker, Jonas Zipfel, Yeongsu Cho, Samuel Brem, Jonas D. Ziegler, Marvin Kulig, Takashi Taniguchi, Kenji Watanabe, Ermin Malic, Tony F. Heinz, Timothy C. Berkelbach, and Alexey Chernikov. Dielectric disorder in two-dimensional materials. *Nature Nanotechnology*, 14(9),832–837, Sep 2019.

[103] Lutz Waldecker, Archana Raja, Malte Rösner, Christina Steinke, Aaron Bostwick, Roland J. Koch, Chris Jozwiak, Takashi Taniguchi, Kenji Watanabe, Eli Rotenberg, Tim O. Wehling, and Tony F. Heinz. Rigid Band Shifts in Two-Dimensional Semiconductors through External Dielectric Screening. *Phys. Rev. Lett.*, 123,206403, Nov 2019.

[104] David Tebbe, Marc Schütte, Kenji Watanabe, Takashi Taniguchi, Christoph Stampfer, Bernd Beschoten, and Lutz Waldecker. Tailoring the dielectric screening in WS2–graphene heterostructures. *npj 2D Materials and Applications*, 7(1),29, Apr 2023.

[105] Paulo E Faria Junior, Thomas Naimer, Kathleen M McCreary, Berend T Jonker, Jonathan J Finley, Scott A Crooker, Jaroslav Fabian, and Andreas V Stier.

Proximity-enhanced valley Zeeman splitting at the WS2/graphene interface. *2D Materials*, 10(3),034002, may 2023.

[106] Chao-Sheng Lian, Chen Si, and Wenhui Duan. Unveiling Charge-Density Wave, Superconductivity, and Their Competitive Nature in Two-Dimensional NbSe2. *Nano Letters*, 18(5),2924–2929, May 2018.

[107] Anamul Md. Hoque, Bing Zhao, Dmitrii Khokhriakov, Prasanta Muduli, and Saroj P. Dash. Charge to spin conversion in van der Waals metal NbSe2. *Applied Physics Letters*, 121(24),242404, 12 2022.

[108] Lukáš Nádvorník, Oliver Gueckstock, Lukas Braun, Chengwang Niu, Joachim Gräfe, Gunther Richter, Gisela Schütz, Hidenori Takagi, Mahmoud Zeer, Tom S. Seifert, Peter Kubaščík, Avanindra K. Pandeya, Abdelmadjid Anane, Heejun Yang, Amilcar Bedoya-Pinto, Stuart S. P. Parkin, Martin Wolf, Yuriy Mokrousov, Hiroyuki Nakamura, and Tobias Kampfrath. Terahertz Spin-to-Charge Current Conversion in Stacks of Ferromagnets and the Transition-Metal Dichalcogenide NbSe2. *Advanced Materials Interfaces*, 9(36),2201675, 2022.

[109] Xiaoxiang Xi, Zefang Wang, Weiwei Zhao, Ju-Hyun Park, Kam Tuen Law, Helmuth Berger, Laszlo Forro, Jie Shan, and Kin Fai Mak. Ising pairing in superconducting NbSe2 atomic layers. *Nature Physics*, 12(2),139–143, Feb 2016.

[110] Hong Wang, Xiangwei Huang, Junhao Lin, Jian Cui, Yu Chen, Chao Zhu, Fucai Liu, Qingsheng Zeng, Jiadong Zhou, Peng Yu, Xuewen Wang, Haiyong He, Siu Hon Tsang, Weibo Gao, Kazu Suenaga, Fengcai Ma, Changli Yang, Li Lu, Ting Yu, Edwin Hang Tong Teo, Guangtong Liu, and Zheng Liu. High-quality monolayer superconductor NbSe2 grown by chemical vapour deposition. *Nature Communications*, 8(1),394, Aug 2017.

[111] Yohanes S. Gani, Hadar Steinberg, and Enrico Rossi. Superconductivity in twisted graphene NbSe_2 heterostructures. *Phys. Rev. B*, 99,235404, Jun 2019.

[112] Rai Moriya, Naoto Yabuki, and Tomoki Machida. Superconducting proximity effect in a NbSe_2/graphene van der Waals junction. *Phys. Rev. B*, 101,054503, Feb 2020.

[113] Zhiming Zhang, Kenji Watanabe, Takashi Taniguchi, and Brian J. LeRoy. Local characterization and engineering of proximitized correlated states in graphene/NbSe_2 vertical heterostructures. *Phys. Rev. B*, 102,085429, Aug 2020.

[114] Jiangping Hu, Congjun Wu, and Xi Dai. Proposed Design of a Josephson Diode. *Phys. Rev. Lett.*, 99,067004, Aug 2007.

[115] Kun Jiang and Jiangping Hu. Superconducting diode effects. *Nature Physics*, 18(10),1145–1146, Oct 2022.

[116] C Baumgartner, L Fuchs, A Costa, Jordi Picó-Cortés, S Reinhardt, S Gronin, G C Gardner, T Lindemann, M J Manfra, P E Faria Junior, D Kochan, J Fabian, N Paradiso, and C Strunk. Effect of Rashba and Dresselhaus spin–orbit coupling on supercurrent rectification and magnetochiral anisotropy of ballistic Josephson junctions. *Journal of Physics: Condensed Matter*, 34(15),154005, feb 2022.

[117] Andreas Costa, Jaroslav Fabian, and Denis Kochan. Microscopic study of the Josephson supercurrent diode effect in Josephson junctions based on two-dimensional electron gas. *Phys. Rev. B*, 108,054522, Aug 2023.

[118] Christian Baumgartner, Lorenz Fuchs, Andreas Costa, Simon Reinhardt, Sergei Gronin, Geoffrey C. Gardner, Tyler Lindemann, Michael J. Manfra, Paulo E. Faria Junior, Denis Kochan, Jaroslav Fabian, Nicola Paradiso, and Christoph Strunk. Supercurrent rectification and magnetochiral effects in symmetric Josephson junctions. *Nature Nanotechnology*, 17(1),39–44, Jan 2022.

[119] Miguel M. Ugeda, Aaron J. Bradley, Yi Zhang, Seita Onishi, Yi Chen, Wei Ruan, Claudia Ojeda-Aristizabal, Hyejin Ryu, Mark T. Edmonds, Hsin-Zon Tsai, Alexander Riss, Sung-Kwan Mo, Dunghai Lee, Alex Zettl, Zahid Hussain, Zhi-Xun Shen, and Michael F. Crommie. Characterization of collective ground states in single-layer NbSe2. *Nature Physics*, 12(1),92–97, Jan 2016.

[120] Xiaoxiang Xi, Liang Zhao, Zefang Wang, Helmuth Berger, László Forró, Jie Shan, and Kin Fai Mak. Strongly enhanced charge-density-wave order in monolayer NbSe2. *Nature Nanotechnology*, 10(9),765–769, Sep 2015.

[121] M. Z. Hasan and C. L. Kane. Colloquium: Topological insulators. *Rev. Mod. Phys.*, 82,3045, 2010.

[122] Tong Zhang, Peng Cheng, Xi Chen, Jin-Feng Jia, Xucun Ma, Ke He, Lili Wang, Haijun Zhang, Xi Dai, Zhong Fang, Xincheng Xie, and Qi-Kun Xue. Experimental Demonstration of Topological Surface States Protected by Time-Reversal Symmetry. *Phys. Rev. Lett.*, 103,266803, 2009.

[123] D. Hsieh, Y. Xia, D. Qian, L. Wray, F. Meier, J. H. Dil, J. Osterwalder, L. Patthey, A. V. Fedorov, H. Lin, A. Bansil, D. Grauer, Y. S. Hor, R. J. Cava, and M. Z. Hasan. Observation of Time-Reversal-Protected Single-Dirac-Cone Topological-Insulator States in Bi_2Te_3 and Sb_2Te_3. *Phys. Rev. Lett.*, 103,146401, Sep 2009.

[124] Wenchao Tian, Wenbo Yu, Jing Shi, and Yongkun Wang. The Property, Preparation and Application of Topological Insulators: A Review. *Materials (Basel).*, 10(7),814, 2017.

[125] Nikesh Koirala, Matthew Brahlek, Maryam Salehi, Liang Wu, Jixia Dai, Justin Waugh, Thomas Nummy, Myung-Geun Han, Jisoo Moon, Yimei Zhu, Daniel Dessau, Weida Wu, N. Peter Armitage, and Seongshik Oh. Record Surface State

Mobility and Quantum Hall Effect in Topological Insulator Thin Films via Interface Engineering. *Nano Lett.*, 15(12),8245, 2015.

[126] Yi Zhang, Ke He, Cui Zu Chang, Can Li Song, Li Li Wang, Xi Chen, Jin Feng Jia, Zhong Fang, Xi Dai, Wen Yu Shan, Shun Qing Shen, Qian Niu, Xiao Liang Qi, Shou Cheng Zhang, Xu Cun Ma, and Qi Kun Xue. Crossover of the three-dimensional topological insulator Bi 2 Se 3 to the two-dimensional limit. *Nat. Phys.*, 6(8),584, 2010.

[127] B. Andrei Bernevig, Taylor L. Hughes, and Shou-Cheng Zhang. Quantum Spin Hall Effect and Topological Phase Transition in HgTe Quantum Wells. *Science*, 314(5806),1757–1761, 2006.

[128] Haijun Zhang, Chao Xing Liu, Xiao Liang Qi, Xi Dai, Zhong Fang, and Shou Cheng Zhang. Topological insulators in Bi 2 Se 3, Bi 2 Te 3 and Sb 2 Te 3 with a single Dirac cone on the surface. *Nat. Phys.*, 5(6),438, 2009.

[129] Rui Sun, Shijia Yang, Xu Yang, Eric Vetter, Dali Sun, Na Li, Lei Su, Yan Li, Yang Li, Zi-zhao Gong, Zong-kai Xie, Kai-yue Hou, Qeemat Gul, Wei He, Xiang-qun Zhang, and Zhao-hua Cheng. Large Tunable Spin-to-Charge Conversion Induced by Hybrid Rashba and Dirac Surface States in Topological Insulator Heterostructures. *Nano Letters*, 19(7),4420–4426, 2019. PMID: 31137933.

[130] Hailong Wang, James Kally, Joon Sue Lee, Tao Liu, Houchen Chang, Danielle Reifsnyder Hickey, K. Andre Mkhoyan, Mingzhong Wu, Anthony Richardella, and Nitin Samarth. Surface-State-Dominated Spin-Charge Current Conversion in Topological-Insulator–Ferromagnetic-Insulator Heterostructures. *Phys. Rev. Lett.*, 117,076601, Aug 2016.

[131] A. R. Mellnik, J. S. Lee, A. Richardella, J. L. Grab, P. J. Mintun, M. H. Fischer, A. Vaezi, A. Manchon, E.-A. Kim, N. Samarth, and D. C. Ralph. Spin-transfer torque generated by a topological insulator. *Nature*, 511(7510),449–451, Jul 2014.

[132] Chao-Xing Liu, HaiJun Zhang, Binghai Yan, Xiao-Liang Qi, Thomas Frauenheim, Xi Dai, Zhong Fang, and Shou-Cheng Zhang. Oscillatory crossover from two-dimensional to three-dimensional topological insulators. *Phys. Rev. B*, 81,041307, 2010.

[133] Oleg V. Yazyev, Joel E. Moore, and Steven G. Louie. Spin Polarization and Transport of Surface States in the Topological Insulators Bi_2Se_3 and Bi_2Te_3 from First Principles. *Phys. Rev. Lett.*, 105,266806, 2010.

[134] Kyungwha Park, J. J. Heremans, V. W. Scarola, and Djordje Minic. Robustness of Topologically Protected Surface States in Layering of Bi_2Te_3 Thin Films. *Phys. Rev. Lett.*, 105,186801, 2010.

[135] Jiwon Chang, Leonard F. Register, and Sanjay K. Banerjee. Topological insulator Bi2Se3 thin films as an alternative channel material in metal-oxide-semiconductor field-effect transistors. *Journal of Applied Physics*, 112(12),124511, 12 2012.

[136] Balint Fülöp, Albin Marffy, Simon Zihlmann, Martin Gmitra, Endre Tovari, Balint Szentpeteri, Mate Kedves, Kenji Watanabe, Takashi Taniguchi, Jaroslav Fabian, Christian Schönenberger, Peter Makk, and Szabolcs Csonka. Boosting proximity spin-orbit coupling in graphene/WSe2 heterostructures via hydrostatic pressure. *npj 2D Materials and Applications*, 5(1),82, Sep 2021.

[137] Haozhe Yang, Beatriz Martín-García, Jozef Kimák, Eva Schmoranzerová, Eoin Dolan, Zhendong Chi, Marco Gobbi, Petr Němec, Luis E. Hueso, and Fèlix Casanova. Twist-angle tunable spin texture in $\mathrm{WSe_2}$/graphene van der Waals heterostructures. 2023.

[138] Erwen Zhang, Fanrong Lin, Zhihao Lei, Shuai Qi, Siyuan Ban, Ajayan Vinu, Jiabao Yi, and Yanpeng Liu. Twist the doorknob to open the electronic properties of graphene-based van der Waals structure. *Matter*, 4(11),3444–3482, 2021.

[139] Jonas Kiemle, Lukas Powalla, Katharina Polyudov, Lovish Gulati, Maanwinder Singh, Alexander W. Holleitner, Marko Burghard, and Christoph Kastl. Gate-Tunable Helical Currents in Commensurate Topological Insulator/Graphene Heterostructures. *ACS Nano*, 16(8),12338–12344, 2022. PMID: 35968692.

[140] Wenhui Dang, Hailin Peng, Hui Li, Pu Wang, and Zhongfan Liu. Epitaxial heterostructures of ultrathin topological insulator nanoplate and graphene. *Nano Lett.*, 10(8),2870, 2010.

[141] Daniel S Koda, Friedhelm Bechstedt, Marcelo Marques, and Lara K Teles. Coincidence lattices of 2D crystals: heterostructure predictions and applications. *The Journal of Physical Chemistry C*, 120(20),10895–10908, 2016.

[142] Stephen Carr, Shiang Fang, and Efthimios Kaxiras. Electronic-structure methods for twisted moiré layers. *Nature Reviews Materials*, 5(10),748–763, 2020.

[143] Zilu Wang, Qian Chen, and Jinlan Wang. Electronic Structure of Twisted Bilayers of Graphene/MoS2 and MoS2/MoS2. *The Journal of Physical Chemistry C*, 119(9),4752–4758, 2015.

[144] Gui Gui, Jin Li, and Jianxin Zhong. Band structure engineering of graphene by strain: First-principles calculations. *Phys. Rev. B*, 78,075435, Aug 2008.

[145] D. Grassano, M. D'Alessandro, O. Pulci, S. G. Sharapov, V. P. Gusynin, and A. A. Varlamov. Work function, deformation potential, and collapse of Landau levels in strained graphene and silicene. *Phys. Rev. B*, 101,245115, Jun 2020.

[146] Changgu Lee, Xiaoding Wei, Jeffrey W. Kysar, and James Hone. Measurement of the Elastic Properties and Intrinsic Strength of Monolayer Graphene. *Science*, 321(5887),385–388, 2008.

[147] Paolo Giannozzi and et al. QUANTUM ESPRESSO: a modular and open-source software project for quantum simulations of materials. *J. Phys.: Cond. Mat.*, 21(39),395502, 2009.

[148] E. Engel and R.M. Dreizler. *Density Functional Theory: An Advanced Course*. Theoretical and Mathematical Physics. Springer Berlin Heidelberg, 2011.

[149] Tobias Frank. Ab initio studies of extrinsic spin-orbit coupling effects in graphene and quantum Monte Carlo simulations of phosphorene, März 2019.

[150] S. Cottenier. *Density Functional Theory and the family of (L)APW-methods: a step-by-step introduction*. 2002.

[151] W. Kohn and L. J. Sham. Self-Consistent Equations Including Exchange and Correlation Effects. *Phys. Rev.*, 140,A1133, 1965.

[152] D. M. Ceperley and B. J. Alder. Ground State of the Electron Gas by a Stochastic Method. *Phys. Rev. Lett.*, 45,566–569, Aug 1980.

[153] Aron J. Cohen, Paula Mori-Sánchez, and Weitao Yang. Challenges for Density Functional Theory. *Chemical Reviews*, 112(1),289–320, Jan 2012.

[154] John P. Perdew, Kieron Burke, and Matthias Ernzerhof. Generalized Gradient Approximation Made Simple. *Phys. Rev. Lett.*, 77,3865, 1996.

[155] Frank Jensen. *Introduction to Computational Chemistry*. John Wiley & Sons, 2001.

[156] Hendrik J. Monkhorst and James D. Pack. Special points for Brillouin-zone integrations. *Phys. Rev. B*, 13,5188–5192, Jun 1976.

[157] P. E. Bloechl. Projector augmented-wave method. *Phys. Rev. B*, 50,17953–17979, Dec 1994.

[158] Stefan Grimme. Semiempirical GGA-type density functional constructed with a long-range dispersion correction. *J. Comput. Chem.*, 27(15),1787, 2006.

[159] Stefan Grimme, Jens Antony, Stephan Ehrlich, and Helge Krieg. A consistent and accurate ab initio parametrization of density functional dispersion correction (DFT-D) for the 94 elements H-Pu. *J. Chem. Phys.*, 132(15),154104, 2010.

[160] Vincenzo Barone, Maurizio Casarin, Daniel Forrer, Michele Pavone, Mauro Sambi, and Andrea Vittadini. Role and effective treatment of dispersive forces in materials: Polyethylene and graphite crystals as test cases. *J. Comput. Chem.*, 30(6),934, 2009.

[161] Sergey Mikhailov. Nonlinear Electrodynamic Properties of Graphene and Other Two-Dimensional Materials, 2018.

[162] Denis Kochan, Susanne Irmer, and Jaroslav Fabian. Model spin-orbit coupling Hamiltonians for graphene systems. *Phys. Rev. B*, 95,165415, 2017.

[163] Thomas Naimer, Klaus Zollner, Martin Gmitra, and Jaroslav Fabian. Twist-angle dependent proximity induced spin-orbit coupling in graphene/transition metal dichalcogenide heterostructures. *Phys. Rev. B*, 104,195156, Nov 2021.

[164] Tobias Frank, Paulo E. Faria Junior, Klaus Zollner, and Jaroslav Fabian. Emergence of radial Rashba spin-orbit fields in twisted van der Waals heterostructures. *Phys. Rev. B*, 109,L241403, Jun 2024.

[165] Lujun Wang, Andreas Baumgartner, Péter Makk, Simon Zihlmann, Blesson Sam Varghese, David I. Indolese, Kenji Watanabe, Takashi Taniguchi, and Christian Schönenberger. Global strain-induced scalar potential in graphene devices. *Communications Physics*, 4(1),147, Jun 2021.

[166] Sergej Konschuh, Martin Gmitra, and Jaroslav Fabian. Tight-binding theory of the spin-orbit coupling in graphene. *Phys. Rev. B*, 82,245412, 2010.

[167] Klaus Zollner and Jaroslav Fabian. Heterostructures of Graphene and Topological Insulators Bi2Se3, Bi2Te3, and Sb2Te3. *physica status solidi (b)*, 258(1),2000081, 2021.

[168] Siyao Hou, Lihong Han, Liyuan Wu, Ruge Quhe, and Pengfei Lu. Robust quasi-ohmic contact against angle rotation in noble transition-metal-dichalcogenide/graphene heterobilayers. *RSC Adv.*, 7,45896–45901, 2017.

[169] Armando Pezo, Zeila Zanolli, Nils Wittemeier, Pablo Ordejón, Adalberto Fazzio, Stephan Roche, and Jose H Garcia. Manipulation of spin transport in graphene/transition metal dichalcogenide heterobilayers upon twisting. *2D Materials*, 9(1),015008, nov 2021.

[170] D Di Felice, E Abad, C González, A Smogunov, and Y J Dappe. Angle dependence of the local electronic properties of the graphene/MoS2interface determined byab initiocalculations. *Journal of Physics D: Applied Physics*, 50(17),17LT02, mar 2017.

[171] Klaus Zollner and Jaroslav Fabian. Single and bilayer graphene on the topological insulator Bi_2Se_3: Electronic and spin-orbit properties from first principles. *Phys. Rev. B*, 100,165141, 2019.

[172] Kyung-Hwan Jin and Seung-Hoon Jhi. Proximity-induced giant spin-orbit interaction in epitaxial graphene on a topological insulator. *Phys. Rev. B*, 87,075442, 2013.

[173] Igor Popov, Mauro Mantega, Awadhesh Narayan, and Stefano Sanvito. Proximity-induced topological state in graphene. *Phys. Rev. B*, 90,035418, Jul 2014.

[174] Peter Blaha, Karlheinz Schwarz, Fabien Tran, Robert Laskowski, Georg K. H. Madsen, and Laurence D. Marks. WIEN2k: An APW+lo program for calculating the properties of solids. *The Journal of Chemical Physics*, 152(7),074101, 02 2020.

[175] G. Kresse and J. Furthmüller. Efficient iterative schemes for ab initio total-energy calculations using a plane-wave basis set. *Phys. Rev. B*, 54,11169–11186, Oct 1996.

[176] José M Soler, Emilio Artacho, Julian D Gale, Alberto García, Javier Junquera, Pablo Ordejón, and Daniel Sánchez-Portal. The SIESTA method for ab initio order-N materials simulation. *Journal of Physics: Condensed Matter*, 14(11),2745, mar 2002.

[177] James P. Lewis, Pavel Jelínek, José Ortega, Alexander A. Demkov, Daniel G. Trabada, Barry Haycock, Hao Wang, Gary Adams, John K. Tomfohr, Enrique Abad, Hong Wang, and David A. Drabold. Advances and applications in the FIREBALL ab initio tight-binding molecular-dynamics formalism. *physica status solidi (b)*, 248(9),1989–2007, 2011.

[178] R. Kubo. A general expression for the conductivity tensor. *Canadian Journal of Physics*, 34(12A),1274–1277, 1956.

[179] Ryogo Kubo. Statistical-Mechanical Theory of Irreversible Processes. I. General Theory and Simple Applications to Magnetic and Conduction Problems. *Journal of the Physical Society of Japan*, 12(6),570–586, 1957.

[180] A. Crépieux and P. Bruno. Theory of the anomalous Hall effect from the Kubo formula and the Dirac equation. *Phys. Rev. B*, 64,014416, Jun 2001.

[181] Varga Bonbien and Aurélien Manchon. Symmetrized decomposition of the Kubo-Bastin formula. *Phys. Rev. B*, 102,085113, Aug 2020.

[182] Frank Freimuth, Stefan Blügel, and Yuriy Mokrousov. Spin-orbit torques in Co/Pt(111) and Mn/W(001) magnetic bilayers from first principles. *Phys. Rev. B*, 90,174423, 2014.

[183] Abdulrhman M. Alsharari, Mahmoud M. Asmar, and Sergio E. Ulloa. Proximity-induced topological phases in bilayer graphene. *Phys. Rev. B*, 97,241104, 2018.

[184] Jun Yong Khoo, Alberto F. Morpurgo, and Leonid Levitov. On-Demand Spin-Orbit Interaction from Which-Layer Tunability in Bilayer Graphene. *Nano Lett.*, 17(11),7003, 2017.

[185] A Avsar, J Y Tan, T Taychatanapat, J Balakrishnan, G. K. W. Koon, Y Yeo, J Lahiri, A Carvalho, A S Rodin, E. C. T. O'Farrell, G Eda, A H Castro Neto, and B. Özyilmaz. Spin–orbit proximity effect in graphene. *Nat. Commun.*, 5,4875, 2014.

[186] Bowen Yang, Min-Feng Tu, Jeongwoo Kim, Yong Wu, Hui Wang, Jason Alicea, Ruqian Wu, Marc Bockrath, and Jing Shi. Tunable spin–orbit coupling and symmetry-protected edge states in graphene/WS 2. *2D Mater.*, 3(3),031012, 2016.

[187] Zhe Wang, Dong-Keun Ki, Jun Yong Khoo, Diego Mauro, Helmuth Berger, Leonid S. Levitov, and Alberto F. Morpurgo. Origin and Magnitude of 'Designer' Spin-Orbit Interaction in Graphene on Semiconducting Transition Metal Dichalcogenides. *Phys. Rev. X*, 6(4),041020, 2016.

[188] Tobias Völkl, Tobias Rockinger, Martin Drienovsky, Kenji Watanabe, Takashi Taniguchi, Dieter Weiss, and Jonathan Eroms. Magnetotransport in heterostructures of transition metal dichalcogenides and graphene. *Phys. Rev. B*, 96,125405, Sep 2017.

[189] CK Safeer, Josep Ingla-Aynés, Franz Herling, José H Garcia, Marc Vila, Nerea Ontoso, M Reyes Calvo, Stephan Roche, Luis E Hueso, and Fèlix Casanova. Room-temperature spin Hall effect in graphene/MoS_2 van der Waals heterostructures. *Nano Lett.*, 19(2),1074, 2019.

[190] Franz Herling, C. K. Safeer, Josep Ingla-Aynés, Nerea Ontoso, Luis E. Hueso, and Fèlix Casanova. Gate tunability of highly efficient spin-to-charge conversion by spin Hall effect in graphene proximitized with WSe2. *APL Materials*, 8(7),071103, 2020.

[191] S. Omar and B. J. van Wees. Spin transport in high-mobility graphene on WS_2 substrate with electric-field tunable proximity spin-orbit interaction. *Phys. Rev. B*, 97,045414, 2018.

[192] Julia Amann, Tobias Völkl, Tobias Rockinger, Denis Kochan, Kenji Watanabe, Takashi Taniguchi, Jaroslav Fabian, Dieter Weiss, and Jonathan Eroms. Counterintuitive gate dependence of weak antilocalization in bilayer graphene/WSe_2 heterostructures. *Phys. Rev. B*, 105,115425, Mar 2022.

[193] Lorenzo Camosi, Josef Světlík, Marius V Costache, Williams Savero Torres, Iván Fernández Aguirre, Vera Marinova, Dimitre Dimitrov, Marin Gospodinov, Juan F Sierra, and Sergio O Valenzuela. Resolving spin currents and spin densities generated by charge-spin interconversion in systems with reduced crystal symmetry. *2D Materials*, 9(3),035014, jun 2022.

[194] Nerea Ontoso, C. K. Safeer, Franz Herling, Josep Ingla-Aynés, Haozhe Yang, Zhendong Chi, Beatriz Martin-Garcia, Iñigo Robredo, Maia G. Vergniory, Fernando de Juan, M. Reyes Calvo, Luis E. Hueso, and Fèlix Casanova. Unconventional Charge-to-Spin Conversion in Graphene/$MoTe_2$ van der Waals Heterostructures. *Phys. Rev. Appl.*, 19,014053, Jan 2023.

[195] Etienne Lorchat, Luis E. Parra López, Cédric Robert, Delphine Lagarde, Guillaume Froehlicher, Takashi Taniguchi, Kenji Watanabe, Xavier Marie, and Stéphane Berciaud. Filtering the photoluminescence spectra of atomically thin semiconductors with graphene. *Nature Nanotechnology*, 15(4),283–288, Apr 2020.

[196] Can-Li Song, Yi-Lin Wang, Ye-Ping Jiang, Yi Zhang, Cui-Zu Chang, Lili Wang, Ke He, Xi Chen, Jin-Feng Jia, Yayu Wang, Zhong Fang, Xi Dai, Xin-Cheng Xie, Xiao-Liang Qi, Shou-Cheng Zhang, Qi-Kun Xue, and Xucun Ma. Topological insulator Bi2Se3 thin films grown on double-layer graphene by molecular beam epitaxy. *Appl. Phys. Lett.*, 97(14),143118, 2010.

[197] Dmitrii Khokhriakov, Aron W. Cummings, Kenan Song, Marc Vila, Bogdan Karpiak, André Dankert, Stephan Roche, and Saroj P. Dash. Tailoring emergent spin phenomena in Dirac material heterostructures. *Sci. Adv.*, 4(9),eaat9349, 2018.

[198] Zhuonan Lin, Wei Qin, Jiang Zeng, Wei Chen, Ping Cui, Jun-Hyung Cho, Zhenhua Qiao, and Zhenyu Zhang. Competing Gap Opening Mechanisms of Monolayer Graphene and Graphene Nanoribbons on Strong Topological Insulators. *Nano Letters*, 17(7),4013–4018, 2017. PMID: 28534404.

[199] Wenliang Liu, Xiangyang Peng, Xiaolin Wei, Hong Yang, G. Malcolm Stocks, and Jianxin Zhong. Surface and substrate induced effects on thin films of the topological insulators Bi_2Se_3 and Bi_2Te_3. *Phys. Rev. B*, 87,205315, May 2013.

[200] Shivani Rajput, Yao-Yi Li, Michael Weinert, and Lian Li. Indirect Interlayer Bonding in Graphene–Topological Insulator van der Waals Heterostructure: Giant Spin–Orbit Splitting of the Graphene Dirac States. *ACS Nano*, 10(9),8450–8456, 2016. PMID: 27617796.

[201] S. Jafarpisheh, A. W. Cummings, K. Watanabe, T. Taniguchi, B. Beschoten, and C. Stampfer. Proximity-induced spin-orbit coupling in graphene/Bi1.5Sb0.5Te1.7Se1.3 heterostructures. *Phys. Rev. B*, 98(24),241402, 2018.

[202] H. Steinberg, L. A. Orona, V. Fatemi, J. D. Sanchez-Yamagishi, K. Watanabe, T. Taniguchi, and P. Jarillo-Herrero. Tunneling in graphene–topological insulator hybrid devices. *Phys. Rev. B*, 92,241409, 2015.

[203] A. Zalic, T. Dvir, and H. Steinberg. High-density carriers at a strongly coupled interface between graphene and a three-dimensional topological insulator. *Phys. Rev. B*, 96,075104, 2017.

[204] Dmitrii Khokhriakov, Anamul Md. Hoque, Bogdan Karpiak, and Saroj P. Dash. Gate-tunable spin-galvanic effect in graphene-topological insulator van der Waals heterostructures at room temperature. *Nature Communications*, 11(1),3657, Jul 2020.

[205] Md. Anamul Hoque, Lars Sjöström, Dmitrii Khokhriakov, Bing Zhao, and Saroj Prasad Dash. Room temperature nonlocal detection of charge-spin interconversion in a topological insulator. *npj 2D Materials and Applications*, 8(1),10, Feb 2024.

[206] Seizo Nakajima. The crystal structure of $Bi_2Te_{3-x}Se_x$. *Journal of Physics and Chemistry of Solids*, 24(3),479–485, 1963.

[207] Yu Saito, Yasuharu Nakamura, Mohammad Saeed Bahramy, Yoshimitsu Kohama, Jianting Ye, Yuichi Kasahara, Yuji Nakagawa, Masaru Onga, Masashi Tokunaga, Tsutomu Nojima, Youichi Yanase, and Yoshihiro Iwasa. Superconductivity protected by spin–valley locking in ion-gated MoS2. *Nature Physics*, 12(2),144–149, Feb 2016.

[208] Hemian Yi, Lun-Hui Hu, Yuanxi Wang, Run Xiao, Jiaqi Cai, Danielle Reifsnyder Hickey, Chengye Dong, Yi-Fan Zhao, Ling-Jie Zhou, Ruoxi Zhang, Anthony R. Richardella, Nasim Alem, Joshua A. Robinson, Moses H. W. Chan, Xiaodong Xu, Nitin Samarth, Chao-Xing Liu, and Cui-Zu Chang. Crossover from Ising- to Rashba-type superconductivity in epitaxial Bi2Se3/monolayer NbSe2 heterostructures. *Nature Materials*, 21(12),1366–1372, Dec 2022.

[209] Sergio C. de la Barrera, Michael R. Sinko, Devashish P. Gopalan, Nikhil Sivadas, Kyle L. Seyler, Kenji Watanabe, Takashi Taniguchi, Adam W. Tsen, Xiaodong Xu, Di Xiao, and Benjamin M. Hunt. Tuning Ising superconductivity with layer and spin–orbit coupling in two-dimensional transition-metal dichalcogenides. *Nature Communications*, 9(1),1427, Apr 2018.

[210] J. M. Lu, O. Zheliuk, I. Leermakers, N. F. Q. Yuan, U. Zeitler, K. T. Law, and J. T. Ye. Evidence for two-dimensional Ising superconductivity in gated MoS_2. *Science*, 350(6266),1353–1357, 2015.

[211] Wun-Hao Kang, Michael Barth, Aitor Garcia-Ruiz, Alina Mreńca-Kolasińska, Ming-Hao Liu, and Denis Kochan. Magnetotransport Signatures of the Radial Rashba Spin-Orbit Coupling in Proximitized Graphene, 2024.

[212] Karol Szałowski, Marko Milivojević, Denis Kochan, and Martin Gmitra. Spin–orbit and exchange proximity couplings in graphene/1T-TaS2 heterostructure triggered by a charge density wave. *2D Materials*, 10(2),025013, feb 2023.

[213] Maedeh Rassekh, Marko Milivojević, and Martin Gmitra. Proximity Induced Spin Currents and Spin-orbit Torques in Graphene on 1T-TaS2. In *2023 IEEE 13th International Conference Nanomaterials: Applications & Properties (NAP)*, pages TPNS02–1–TPNS02–5, 2023.

[214] Zhendong Chi, Seungjun Lee, Haozhe Yang, Eoin Dolan, C. K. Safeer, Josep Ingla-Aynés, Franz Herling, Nerea Ontoso, Beatriz Martín-García, Marco Gobbi, Tony Low, Luis E. Hueso, and Fèlix Casanova. Control of Charge-Spin Interconversion in van der Waals Heterostructures with Chiral Charge Density Waves. *Advanced Materials*, 36(18),2310768, 2024.

[215] Jeri Berlyn D Linganay and Darwin B Putungan. Adsorption and diffusion properties of calcium ions at the van der Waals interface of NbSe2-graphene 2D heterostructure for multivalent battery applications: density functional theory calculations. *Materials Research Express*, 9(9),095506, sep 2022.

[216] Sergio Fuentes Moyado Donald Homero Galvan, Joel Antúnez-García. Electronic Properties of NbSe2 over Graphene: A Meticulous Theoretical Analysis. *Open Access Library Journal*, 4(5),1–9, 2017.

[217] Jun Ding, Zhenhua Qiao, Wanxiang Feng, Yugui Yao, and Qian Niu. Engineering quantum anomalous/valley Hall states in graphene via metal-atom adsorption: An ab-initio study. *Phys. Rev. B*, 84,195444, 2011.

[218] Bogdan Guster, Carmen Rubio-Verdú, Roberto Robles, Javier Zaldívar, Paul Dreher, Miguel Pruneda, José Ángel Silva-Guillén, Deung-Jang Choi, José I. Pascual, Miguel M. Ugeda, Pablo Ordejón, and Enric Canadell. Coexistence of Elastic Modulations in the Charge Density Wave State of 2H-NbSe2. *Nano Letters*, 19(5),3027–3032, May 2019.

[219] Étienne Bézout. *Théorie Générale des Équations Algébriques*. Paris, Impr. de Ph.-D. Pierres, 1764.

List of publications

1. ’Twist-angle dependent proximity induced spin-orbit coupling in graphene/transition metal dichalcogenide heterostructures’,
   Phys. Rev. B 104, 195156 (2021),
   Thomas Naimer, Klaus Zollner, Martin Gmitra and Jaroslav Fabian
2. ‘Twist-angle dependent proximity induced spin-orbit coupling in graphene/topological insulator heterostructures’,
   Phys. Rev. B 107, 195144 (2023),
   Thomas Naimer and Jaroslav Fabian
3. ‘Proximity-enhanced valley Zeeman splitting at the WS_2/graphene interface’,
   2D Mater. 10 034002 (2023),
   Paulo E Faria Junior, **Thomas Naimer**, Kathleen M McCreary, Berend T Jonker, Jonathan J Finley, Scott A Crooker, Jaroslav Fabian and Andreas V Stier
4. ’Tuning proximity spin-orbit coupling in graphene/$NbSe_2$ heterostructures via twist angle’,
   Phys. Rev. B 109, 205109 (2024),
   Thomas Naimer, Martin Gmitra and Jaroslav Fabian

Acknowledgements

I would like to thank everyone supporting me during my PhD. First and foremost, I thank Professor Jaroslav Fabian for giving me the opportunity to work in his group. Special thanks go to Klaus Zollner, Paulo E. Faria Junior, Marco Milivojević, Jordi Picó Cortés, Luca Magazzù and Martin Gmitra for proofreading of the thesis. Moreover, Martin deserves extra thanks, since he mentored me in my first steps in DFT as one of my former Bachelor thesis advisors and also for hosting my visit in Košice. In this context, I additionally want to thank all other friendly people from Košice, who made the stay there so enjoyable.

I would also like to thank Christoph Brückner, Moritz Frankerl, Jordi Picó Cortés and Luca Magazzù for their companionship during the PhD and Florian Feldmeier, Ansgar Graf and Hermann Angerer for their companionship in my prior physics education. Finally I would like to thank my non-physicist friends and family, especially my girlfriend Nina and our cat Knubbel for their support.

I further acknowledge funding by the FLAG ERA JTC 2021 project 2DSOTECH, the European Union Horizon 2020 Research and Innovation Program 881603 (Graphene Flagship), the International Doctorate Program Topological Insulators of the Elite Network of Bavaria, the Deutsche Forschungsgemeinschaft (DFG, German Research Foundation), SFB 1277 (Project-ID 314695032) and SPP 2244 (project no. 443416183).